Global-scale observations of changes in ionospheric echo occurrence and convection during periods of increased solar wind activity and increased geomagnetic activity

A Thesis Submitted to the
College of Graduate Studies and Research
in Partial Fulfillment of the Requirements
for the degree of Doctor of Philosophy
in the Department of Physics and Engineering Physics
University of Saskatchewan
Saskatoon

By

D. M. Gillies

Permission to Use

In presenting this thesis in partial fulfilment of the requirements for a Postgraduate degree from the University of Saskatchewan, I agree that the Libraries of this University may make it freely available for inspection. I further agree that permission for copying of this thesis in any manner, in whole or in part, for scholarly purposes may be granted by the professor or professors who supervised my thesis work or, in their absence, by the Head of the Department or the Dean of the College in which my thesis work was done. It is understood that any copying or publication or use of this thesis or parts thereof for financial gain shall not be allowed without my written permission. It is also understood that due recognition shall be given to me and to the University of Saskatchewan in any scholarly use which may be made of any material in my thesis.

Requests for permission to copy or to make other use of material in this thesis in whole or part should be addressed to:

Head of the Department of Physics and Engineering Physics
116 Science Place
University of Saskatchewan
Saskatoon, Saskatchewan
Canada
S7N 5E2

Abstract

This thesis presents an investigation of ionospheric plasma convection and HF radar echoes during periods of enhanced geomagnetic activity. The work was split into two studies: the ionospheric response to periods of prolonged geomagnetic activity in the form of geomagnetic storms and to abrupt changes in geomagnetic activity during sudden commencement (SC) events. A new statistical analysis technique was developed and applied to ionospheric plasma velocity measurements to categorize sunward and antisunward ionospheric plasma drifts. The global effects on the ionosphere during periods of abrupt changes in geomagnetic activity were investigated using the Super Dual Auroral Radar Network (SuperDARN).

The first study investigated 136 geomagnetic storms. The influences of the main and recovery phase of geomagnetic storms on HF radar echoes and ionospheric plasma velocities were examined. It is important to study the HF radar echoes because they reveal important information regarding the state of the ionosphere. The geomagnetic storms were divided into three storm classes, and a superposed epoch analysis was performed. It was found that the number of SuperDARN echoes varied during the storm. For weak-moderate and strong storms, the number of echoes decreased during the main phase until well into the recovery phase. In contrast, the intense storms exhibited a marked increase in the number of echoes seen during the main phase in the 09-15 MLT sector and a reduction in the 21-03 MLT sector. SuperDARN recorded faster antisunward velocities in the 09-15 MLT sector before and during the main phase. A very good correlation between the minimum Sym-H at the end of the main phase and the minimum IMF B_z that occurred roughly 1 hour earlier was found. This indicated a continuum of storm intensities that suggested the division of geomagnetic storms into classes based on intensity is arbitrary and unnecessary. The ring current decay time calculated using the high time resolution Sym-H index for the 136 geomagnetic storms was T=7.2 hours. This agreed with the *Burton et al.* (1975) value of T=7.7 hours.

The second study focused on 205 SC events. The SC events were identified using

ground-based magnetometer data from the years 2000 through 2007. Irrespective of whether or not the SC was followed by a geomagnetic storm, there was excellent correlation between the strength of SC events and the magnitude of the jump in the solar wind dynamic pressure. HF radar velocities and echo occurrence rates in the noon sector increased in response to the jump in solar wind dynamic pressure. In contrast, the number of SuperDARN echoes in the midnight sector decreased as the solar wind dynamic pressure increased, although the average drift speed in the midnight sector increased. The ionosphere and ring current evolved differently following the arrival of the solar wind pressure pulses. The Sym-H index, which represents changes in both the magnetopause and ring currents responded immediately and either rapidly returned to pre-SC values or progressed into the main phase of a geomagnetic storm. The SuperDARN velocities were affected for a much longer time period. This research revealed that the ring current reacts to a sudden compression of the magnetosphere on a time scale of 10 minutes, while the ionospheric convection velocities and echo occurrence was affected for as long as the increase in solar wind dynamic pressure was sustained, or until a geomagnetic storm was triggered.

Acknowledgements

First and foremost I offer my deepest gratitude to my supervisors, Dr. Jean-Pierre St.-Maurice and Dr. Kathryn McWilliams, who have guided and supported me throughout this degree. Their patience was boundless and they provided me with opportunities to excel in the field of space physics. Without their support, extensive knowledge, and encouragement, this thesis would not have been possible.

Aside from my supervisors, I am grateful for the help I received from the members of the SuperDARN group at the University of Saskatchewan. Thank you to Dr. George Sofko, Dr. Sasha Koustov, and Dr. Glenn Hussey for their valuable comments and suggestions. Thank you to Dieter André, Dr. Pasha Ponomarenko, and Dr. Chad Bryant for helpful discussions, programming advice, and various programs used in this thesis. I am indebted to my fellow past and present graduate students for their constant support, including: Dr. Rob Gillies, Dr. Robyn Fiori, and Gareth Perry. I am grateful to the members of the Radio and Space Plasma Physics group at the University of Leicester, UK, for providing me with the opportunity to study with their group for three months in 2008. In particular I am grateful to my supervisor Dr. Steve Milan for providing guidance and direction with my research project.

I would like to thank the various agencies for providing data used in this thesis, specifically the World Data Center in Kyoto, Japan, for providing the Sym-H indices, NASA GSFCs Space Physics Data Facility's OMNIWeb service for the use of OMNI data, and the Observatori de l'Ebre for providing the SC listings. Special thank you to the principal investigators of the SuperDARN radars used in this study. I am also grateful to Dr. Luis F. Alberca for his helpful discussions. Funding for this research was provided through NSERC, operating funds from CRC, and by the EU Marie Curie Early Stage Training in Space, Planetary, and Astrophysical Sciences (SPARTAN) programme. I would like to thank the Department of Physics and Engineering Physics for providing me with financial assistance through numerous scholarships.

Dedication

This thesis is primarily dedicated to my father, Herbert Hargrove, who always stood behind me and knew I would succeed in whatever I did with grace and dignity. Thank you for taking me out at three in the morning in the middle of a freezing Winnipeg winter just to see the aurora because you knew I'd love it. Thank you for helping me with my homework, spending hours researching for my first telescope, and then taking me out into the country so I could use it whenever I asked no matter how busy you were. Thank you for teaching me to draw and paint, for always reminding me how important the pursuit of knowledge is, and how vital it is to never stop questioning things. I wish you could still be here with us to see the result of all your hard work and sacrifice.

I'd also like to dedicate this thesis to my family. To my mother, Debbie, whose unwavering support and encouragement have lead me to where I am today. To my siblings Jennifer, Sarah, and Andrew. They have supported me in whatever endeavor I embarked on from a very early age, no matter how 'nerdy' it appeared to be, and this thesis would not be possible without them.

And finally this thesis is dedicated to my beloved husband Rob and my beautiful daughter Kara. To Rob, words simply cannot express the love and gratitude I have for your endless dedication and patience. You were always there to give advice, help with the baby, and be a shoulder to lean on when things were rough. To Kara, well, you're just awesome. You remind me why I do the things that I do even when I think there is nothing left to give. No matter how frustrated I would get you'd always be there with a smile and a cuddle and it made everything else seem small in comparison to the joy you give me just by being you. Thank you.

Contents

List of Tables

List of Figures

List of Abbreviations

AACGM	Altitude Adjusted Corrected Geomagnetic Coordinates
ACE	Advance Composition Explorer
ACF	Auto Correlation Function
AIA	Atmospheric Imaging Assembly
AU	Astronomical Unit
CARISMA	Canadian Array for Realtime Investigations of Magnetic Activity
CIR	Corotating Interaction Region
CME	Coronal Mass Ejection
DMSP	Defense Meteorological Satellite Program
Dst	Disturbed Storm Time
FAC	Field Aligned Current
FBI	Farley Buneman Instability
FOV	Field of View
FSIM	Fort Simpson (magnetometer station)
GC	Gradually Commencing (geomagnetic storm)
GDI	Gradient Drift Instability
GSM	Geocentric Solar Magnetospheric System
HCS	Heliospheric Current Sheet
HF	High Frequency
HMB	Heppner-Maynard boundary
IAGA	International Association of Geomagnetism and Aeronomy
IEF	Interplanetary Electric Field
IMF	Interplanetary Magnetic Field
IR	Interaction Region
LASCO	Large Angle and Spectrometric Coronagraph
l-o-s	line-of-sight
MLT	Magnetic Local Time
RC	Ring Current
Re	Radius of the Earth
SC	Sudden Commencement
SDO	Solar Dynamic Observatory
SI	Sudden Impulse
SOHO	Solar and Heliospheric Observatory
Sq	Solar quiet
SSC	Storm Sudden Commencement
SuperDARN	Super Dual Auroral Radar Network
Sym-H	Symmetric H-component (of the geomagnetic field)
UT	Universal Time

Chapter 1

Introduction

The Sun and Earth represent a coupled dynamic system that is the current focus of much research. The space between the Sun and Earth is filled with hot plasma and magnetic fields streaming from the Sun which will encounter the Earth's magnetosphere. The effects of this interaction are frequently referred to as 'Space Weather'. With increases in satellite communications, number of trans-polar flights, and space exploration, space weather and how it affects the near-space environment is becoming an increasingly important topic of research. The upper atmosphere of the Earth contains the ionosphere, a region of ionized particles. During periods of enhanced ionization, the electron density in the lower E region (where the collision frequency is high) becomes large. When this occurs, HF radio waves can be absorbed or reflected instead of propagating to the F region which is necessary for communication relay. This absorption or reflection of the HF radio waves can lead to ionospheric scintillation of the signal which causes changes in the propagation path. Communication between ground-satellite systems such as GPS navigation, rely on accurate propagation paths to determine position. Ionospheric scintillation can result in miscommunication in signal location and errors in navigation can occur. Large fluxes of highly energetic particles from the Sun can damage communication satellites which are orbiting the Earth. This can interfere with ground communications. Extreme space weather can pose a danger to those traveling on polar flights and in low-Earth orbits where exposure to energetic particles and X-rays can be damaging. Nearer to the surface, geomagnetically induced currents can form in power lines and pipelines as a result of magnetic disturbances. Typical consequences of this phenomenon include loss of signal to GPS units, large scale power outages, and corrosion of pipelines

due to oxidization. One prime example of this is the Quebec Hydro disaster in 1989 which left 6 million people without power for over 9 hours. Extreme space weather is a topic of great interest to researchers as we approach solar maximum.

Geomagnetic storms fall into the category of extreme space weather. Geomagnetic storms are defined as periods of intense geomagnetic activity (*Akasofu and Chapman*, 1963a,b; *Perreault and Akasofu*, 1978). These periods of enhanced geomagnetic activity are the result of large increases in magnetospheric current systems that are observed by ground-based magnetometers. With the advent of *in situ* solar wind data from spacecraft, geomagnetic storms have been related to interactions of the magnetosphere with the solar wind. Southward interplanetary magnetic field and solar wind pressure pulses (defined and discussed in Chapter 2) are now understood to be key phenomena that cause changes in the magnetospheric current systems. Geomagnetic storms have been tied to solar phenomena such as coronal mass ejections and corotating interaction regions (*Tsurutani and Gonzalez*, 1997; *Correia and de Souza*, 2005; *Denton et al.*, 2006; *Richardson et al.*, 2006, 2001) (to be discussed in Chapter 2).

The interplanetary origins of extreme space weather are beginning to be understood. A global scale study of the effect of solar wind on the Earth's ionosphere is a current topic of interest. Changes in geomagnetic activity can have a profound effect on ionospheric properties such as convection patterns of HF radar echoes.

This thesis studies geomagnetic storms during the declining phase of solar cycle 23 and the solar wind and interplanetary magnetic field properties prior to, and during, the geomagnetic storm. The first goal of this thesis is to characterize the ionospheric response to storms on a global scale. To achieve this goal, the first statistical study to determine the effects, if any, of the arrival of a geomagnetic storm on ionospheric properties such as radio echo occurrence rates and convection pattern is performed. Statistical studies of the effect of storms on the ionospheric convection pattern have now become feasible due to the marked expansion of the area covered by the Super Dual Auroral Radar Network (SuperDARN) (*Greenwald et al.*, 1995; *Ruohoniemi and Baker*, 1998; *Chisham et al.*, 2007) radars. SuperDARN radars have proven

to be a very useful tool for the study of substorms (*Grocott et al.*, 2009; *Wild and Grocott*, 2008). Previous studies on the main and recovery phases of geomagnetic storms include the work done by *Kane and Makarevich* (2010) who investigated the ionospheric response to geomagnetic storms using data from six low-latitude SuperDARN stations. They note a change in the ionospheric convection pattern immediately after the start of the geomagnetic storm that is followed by longer term signatures of enhanced convection. More recently, *Hutchinson et al.* (2011a) performed an analysis similar to that used in this thesis to study geomagnetic storms during the last solar cycle (Schwabe Cycle 23). *Hutchinson et al.* (2011b) created a novel way to look at SuperDARN data using a superposed latitude-time-velocity (LTV) technique. *Hutchinson et al.* (2011b) separates gridded SuperDARN plasma drift measurements into two horizontal components - north towards the geomagnetic pole and east. These components are placed in a grid that is fixed relative to the Sun-Earth line. *Hutchinson et al.* (2011b) used the LTV method to determine the mean convection pattern during weak CME-driven storms during solar cycle 23. The LTV method reveals low-latitude return flow and an increase in high velocity ionospheric plasma drifts during the beginning of the main phase. Chapter 5 of this thesis expands the earlier SuperDARN storm studies by studying a large number of storms of various intensity levels, and by using all available radar data from the northern hemisphere SuperDARN radars. Interplanetary parameters (such as interplanetary magnetic field conditions, solar wind pressure and velocity parameters, and the geomagnetic response to these properties) and HF radar data (such as echo occurrence rates, ionospheric velocity distributions, and convection patterns) are analyzed in an effort to understand how geomagnetic storms evolve and how they influence the near-space environment.

The second goal of this thesis is to characterize the ionospheric response to sudden commencement events, characterized by abrupt sharp increases in geomagnetic activity, on a global scale. These are caused by the arrival of a solar wind dynamic pressure pulse, a common feature in coronal mass ejections and corotating interaction regions and generally indicate the start of a geomagnetic storm. At its most basic, a

sudden increase in the solar wind dynamic pressure compresses the magnetosphere on the dayside and the magnetic pressure in the magnetosphere balances the plasma pressure in the magnetosheath (*Shue et al.*, 1997). This compression of the magnetosphere causes perturbation to the geomagnetic field strength which is monitored by ground-based magnetometers and is called a sudden commencement (SC). SCs can be subdivided into two groups: Sudden Impulses (SI) and Storm Sudden Commencements (SSC), the later being SCs followed by a geomagnetic storm. Chapter 5 of this thesis presents the radar data properties of sudden commencements. The focus is on the global-scale ionospheric response to SCs using SuperDARN. This is not the first time that the effect of SCs on SuperDARN radar echoes has been studied (*Coco et al.*, 2005; *Boudouridis et al.*, 2007; *Kane and Makarevich*, 2010). This thesis undertakes a comprehensive study focusing on the local and global ionospheric responses to a sudden increase in the solar wind dynamic pressure. All the northern hemisphere SuperDARN radar data, and all cataloged sudden commencements from ground-based magnetometers during from 2000 to 2007, inclusive, are used to investigate the ionospheric response as a function of magnetic latitude and MLT to a sudden increase in the solar wind dynamic pressure. The increase in the solar wind dynamic pressure was confirmed by satellite data for all SC (both SSC and SI) events.

1.1 Outline

Chapter 2 discusses introductory background information outlining the basic principles covered in this thesis. Properties of the Sun, solar wind, interplanetary magnetic field, and the Earth's magnetospheric system are discussed. Particular attention is paid to high latitude plasma motion and ionospheric convection patterns and properties. Chapter 3 outlines the key instruments used in this thesis. A description of satellite data systems and ground-based magnetometers is presented. The Super Dual Auroral Radar Network, a key instrument used in this study, is discussed in detail. Chapter 4 discusses the methodology for the statistical epoch analysis tech-

nique including the automated classification of line-of-sight plasma drifts. Chapter 5 presents the results of the statistical epoch analysis of the ionospheric response to geomagnetic storms and HF radar data. Chapter 6 presents the results of the statistical epoch analysis of sudden commencement events and HF radar data. In Chapter 7 conclusions and suggestions for future work are provided.

Chapter 2

Background

2.1 The Sun and Solar Wind

The Sun's atmosphere consists of three layers. The lowest layer, the photosphere is a thin (500 km) dense (n=10^{23} m^{-3}) region which emits most of the Sun's light (*Priest*, 1997). At the bottom of the photosphere the temperature is roughly 6600 K, cooling to 4300 K at the top (*Priest*, 1997). The bottom of the photosphere is also considered the visual 'surface' of the Sun. Below this layer alternative methods, such as helioseismology, are required to map the solar structure. Above the photosphere lies the chromosphere. This region is transparent to the human eye, the average density is around 10^{17} m^{-3}, and it is much hotter than the photosphere with temperatures reaching $\sim 1 \times 10^6$ K (*Priest*, 1997). Beyond the chromosphere is the corona. This layer extends radially outwards into interplanetary space far beyond our solar system's orbit. It is extremely hot, reaching temperatures near $2{\times}10^6$ K close to the Sun (*Priest*, 1997).

To the human eye each layer of the Sun's atmosphere is visually quite different. The photosphere reveals the granulated structure of the underlying convection zone and resembles boiling water when viewed with a telescope. Sunspots are another visual phenomenon which can be seen on the solar 'surface'. Sunspots consist of a dark cool ($\sim$ 4100 K) central region, reaching sizes of $\sim 20{\times}10^6$ m, with a strong magnetic field (up to 0.3 T), surrounded by a penumbra of dark and light filament-like structures (*Priest*, 1997). Sunspots typically appear in pairs with a leading sunspot and a trailing sunspot. In most cases, the nearly vertical magnetic field emerging from one umbra closes in the leading (or trailing) umbra. The chromosphere, when

viewed through an H_α filter, also shows a great deal of structure. There are sometimes bright regions around sunspots, called plages, and these are associated with solar prominences (which appear as thin dark lines in the H_α images) and solar flares. Solar prominences may appear as dark lines stretching across the chromosphere but they are actually large sheets of vertical plasma much cooler and less dense than the surrounding corona. The corona is much dimmer than the photosphere and can only be viewed with the naked eye during solar eclipses, but when visible it gives spectacular view of solar flares, prominences and other phenomena.

The Sun is magnetically active with activity levels that have a roughly 11 year cycle. During the 11 year cycle, the Sun's magnetic field reverses polarity. A full solar cycle, known as a Hale cycle, is roughly 22 years in duration with two magnetic reversals. Because of their high visibility, sunspots have historically been used to monitor the activity level of the Sun. During the 11 year cycle, sunspot numbers will peak (solar maximum) and then drop (solar minimum). The emergence of new sunspots with opposite polarity generally heralds the start of the next solar cycle. Solar cycle 23 began in May 1996 and ended in December 2008 (*Richardson and Kane*, 2010). During this cycle the peak number of sunspots was 122 during solar maximum (*Kane*, 2001). During solar maximum, solar phenomena, such as sunspots seen in the photosphere, solar prominences, solar flares, coronal mass ejections, and high speed solar wind streams are much more common. During this time the Sun is considered 'active' and the near-Earth environment can be greatly affected.

The Sun's magnetic field has a very complicated and dynamic structure. Emerging from the photosphere, the magnetic field consists of an apparently random series of looping field lines connecting from one umbra to another. Figure 2.1 is a superposition of images taken at three different wavelengths overlaid with a model of the Sun's magnetic field structure at that particular time. These were recorded the Solar Dynamic Observatory (SDO) using their Atmospheric Imaging Assembly (AIA) instrument, which takes images of the Sun in ten wavelengths every ten seconds. The magnetic field lines emerge from deep within the solar structure, looping out into the solar corona before returning to the surface. Where sunspots are not present

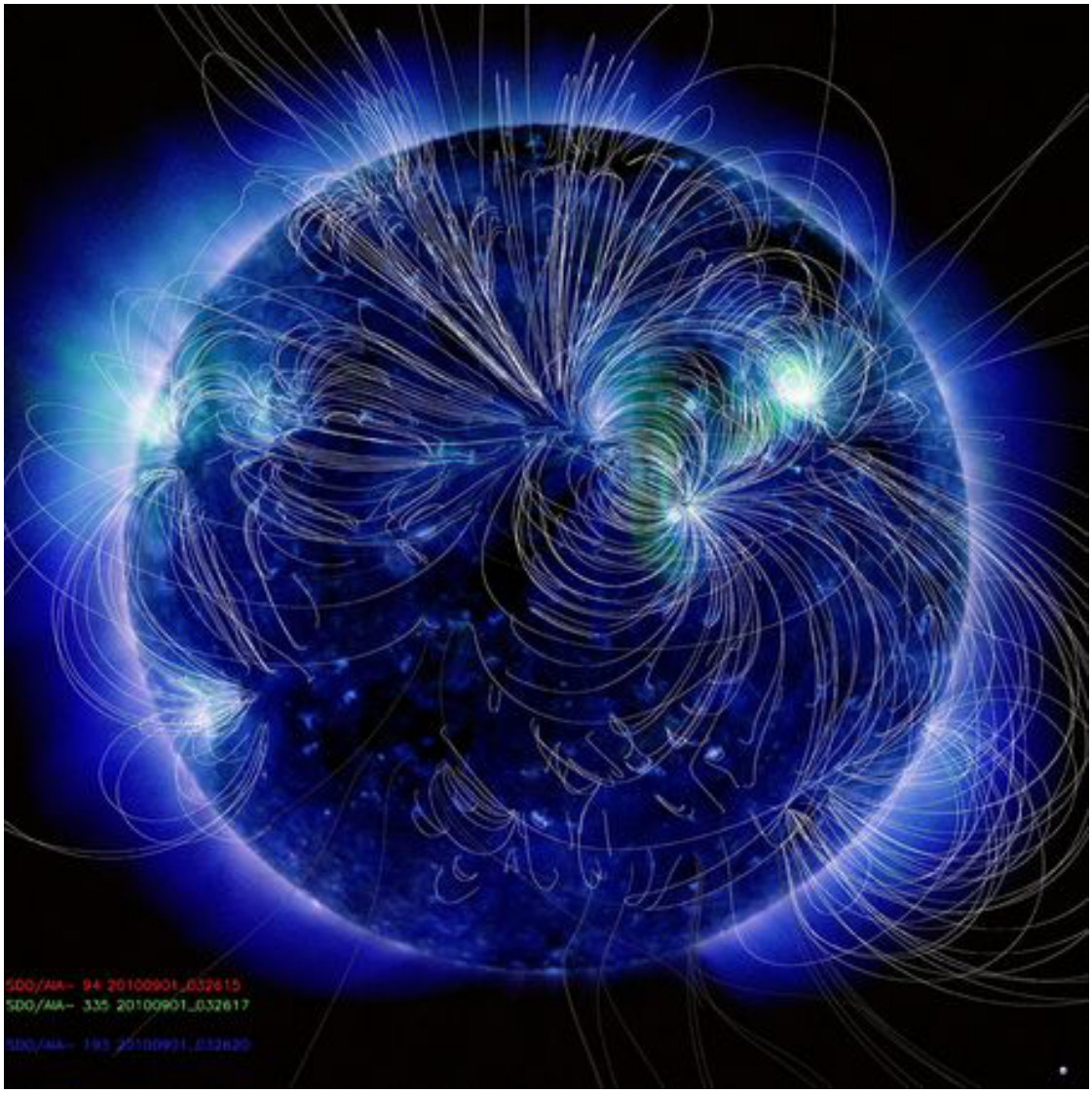

Figure 2.1: Implied magnetic field structure of the Sun (http://sdo.gsfc.nasa.gov/). Image shows mapped magnetic field lines emerging from the Sun overlaid on a composite image taken at three different wavelengths: 9.4 nm (characteristic temperature of 6.3×10^6 K), 33.5 nm (characteristic temperature of 2.5×10^6 K), and 19.3 nm (characteristic temperature of 1.2×10^6 K and 2×10^7 K).

the Sun's magnetic field extends far into interplanetary space before closing in the opposite hemisphere. This happens mainly near the solar poles. The magnetic field lines above and below the equatorial plane are in opposite directions. The heliospheric current sheet (HCS) is present near the solar equator between the regions of oppositely directed magnetic field lines.

Interplanetary space is filled with the solar wind, which is made up of gasses flowing out from the corona. The solar wind is a highly structured plasma streaming radially outward from the corona at supersonic speeds (*Brueckner and Bartoe*, 1983). The existence of a pressure gradient between the solar atmosphere and interplanetary space creates the outflow of plasma. Due to the highly conducting nature of the solar wind plasma, the Sun's extended magnetic field is carried by the plasma and travels with it through interplanetary space. The typical speed of particles flowing from the solar corona is of the order of 400 km/s. This constitutes a supersonic flow with respect to the acoustic speed of the solar wind plasma, which is roughly 120 km/s, as it leaves the corona (*Brueckner and Bartoe*, 1983). This solar wind is referred to as the 'slow' solar wind by some authors (*Heber et al.*, 1999; *Alves et al.*, 2006; *Webb and Howard*, 1994). By the time it reaches the Earth, the typical density of the solar wind is roughly several protons/cm^3. The particles are moderately energetic, with ion energies of about 5 eV and electron energies of about 10 eV (*Newbury and Russell*, 1998).

The presence of the solar wind gives the Sun's extended magnetic field a unique twisted shape known as the Parker spiral. Once the magnetic field leaves the immediate vicinity of the Sun, it is called the interplanetary magnetic field (IMF). The spiral pattern, shown in blue and red in Figure 2.2, is best described as similar to a spinning lawn sprinkler. In this figure, the observer is looking down on the Sun into the equatorial plane with the solid lines indicating the IMF structure with the Sun at the center. Although the magnetic field flows radially outward, the outflowing solar wind and rotating solar surface create a twisting effect which creates the spiral shape. The IMF structure is typically broken into sectors composed of field lines going towards (blue) or away (red) from the Sun. The sector boundaries are

outlined in green. Near the solar surface the magnitude of the IMF is near 50 μT. At the orbital distance of the Earth, the magnitude of the IMF has decreased to several nT. Typical IMF magnitudes are of the order of 1 or 10 nT, the latter occurring during more active periods. The occurrence of solar flares, sun spots, and prominences greatly affects the solar wind.

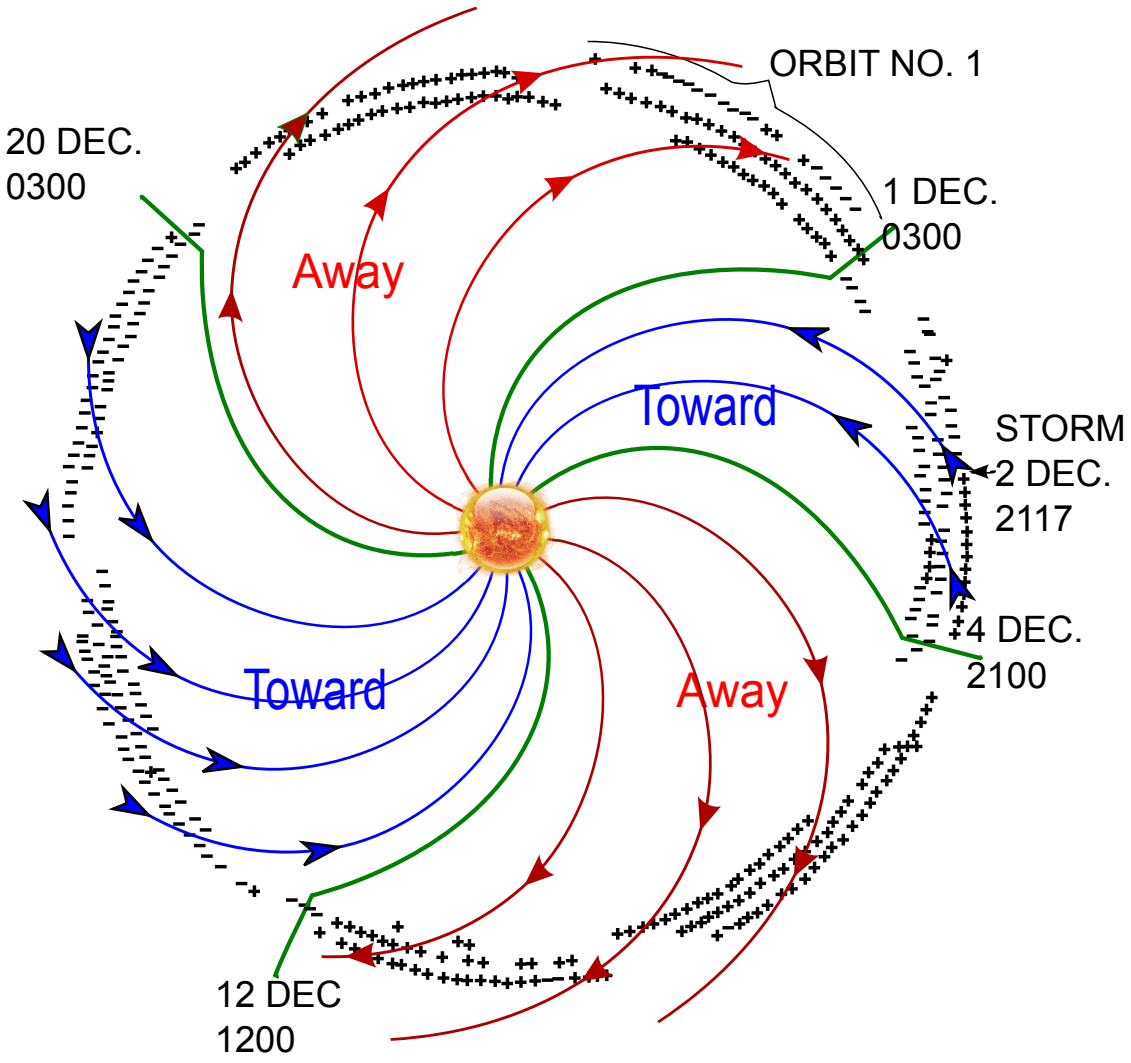

Figure 2.2: Solar sector boundary crossings and Parker spiral behavior, adapted from *Wilcox and Ness* (1965). Magnetic field lines are displayed in blue (towards the Sun) and red (away from the Sun). Sector crossings are illustrated in green.

2.1.1 Coronal Mass Ejections

Coronal mass ejections (CMEs) are eruptions of high energy plasma into interplanetary space from the solar corona. A majority of CMEs originate from an area with many sunspots (*Cliver and Ling*, 2001). The frequency of CMEs is highly dependent upon the solar cycle. CMEs occur most often during solar maximum when sunspots are most prevalent (*Cliver and Ling*, 2001; *Webb and Howard*, 1994; *Alves et al.*, 2006). A CME can contain a few billion tons of plasma and strong magnetic fields from the corona (*Webb and Howard*, 1994; *Temmer et. al.*, 2010). CMEs are one of the most explosive phenomena in the solar system, releasing on average $1{\times}10^{31}$ ergs of kinetic energy (*Webb and Howard*, 1994), but not much is known about the physics of their origin. The standard model (*Webb and Howard*, 1994) suggests a CME originates from an expanding solar prominence in the corona, as depicted in Figure 2.3. As the prominence expands outwards, the coronal magnetic field line lengthens creating a vertical current sheet. As the oppositely opposed magnetic field lines intersect, it creates a region of zero magnetic field strength commonly referred to as a x-type neutral line. The magnetic field lines are 'cut' and then reconnect in the horizontal plane, effectively detaching the CME from the chromosphere. The coronal mass detaches from the corona and is ejected into interplanetary space at high velocities. A study by *Temmer et. al.* (2010) suggests that a significant amount of the energy stored in the magnetic fields is transferred to the plasma particles. The particles are then accelerated along the newly closed magnetic field lines into the lower chromosphere. This is observed as enhanced UV and H_α radiation. Another portion of the energy expended is transferred to the CME acceleration. During solar cycle 23, the CME plasma ranged in speed from 500 km/s to 2700 km/s measured at a distance of 1 astronomical unit (AU) from the Sun (*Zhang et al.*, 2007). When a CME is directed towards the Earth it is called a "halo" CME. This nomenclature is derived from the ring like structure (halo) of light observed by observing satellites positioned between the Earth and the Sun.

The typical structure of a CME has 3 regions: bright white leading edges, a

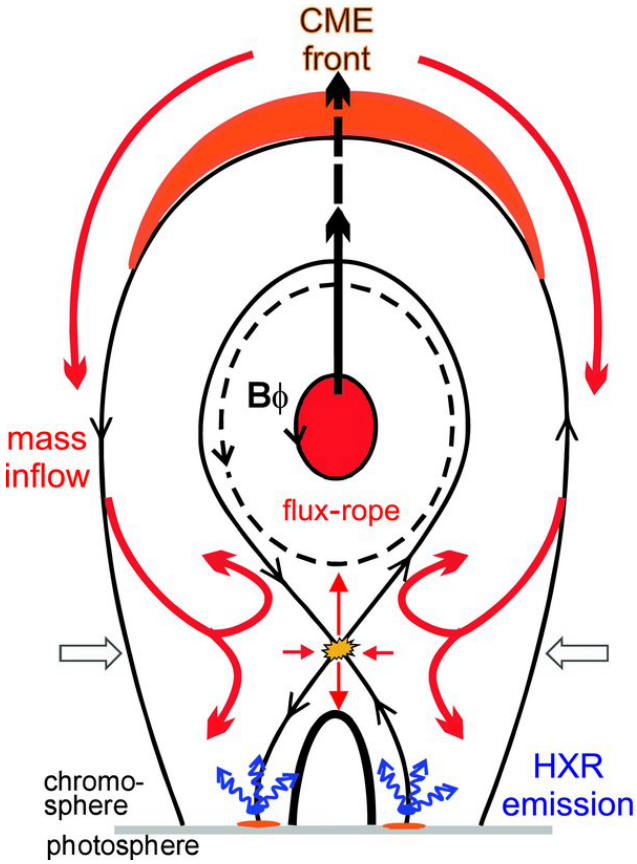

Figure 2.3: Schematic of the structure of the origin of a coronal mass ejection (*Temmer et. al.*, 2010).

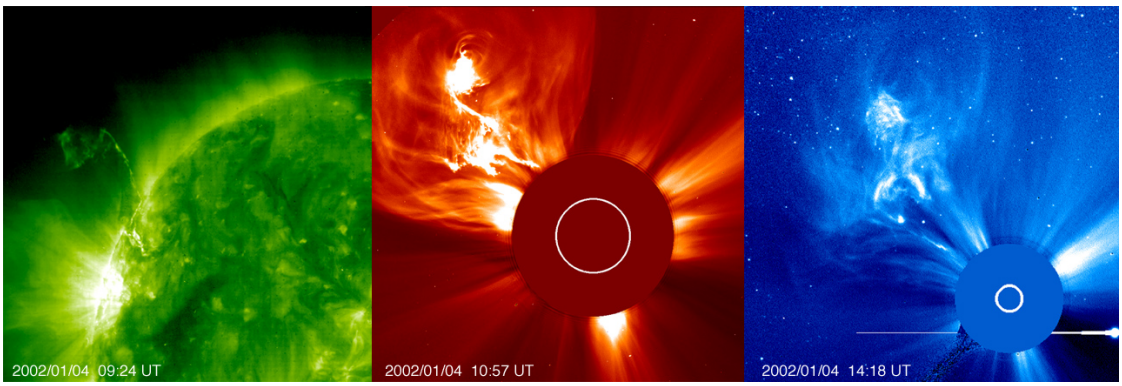

Figure 2.4: Compilation of a coronal mass ejection which occurred on January 4^{th}, 2002. Panels (i)-(iii) show an ultraviolet image of the solar corona, an image taken by LASCO C2 imager, and an image taken by the LASCO C3 imager. Images courtesy of the Solar and Heliospheric Observatory (*SOHO*).

dense core, and a dark cavity with low electron density (*Illing and Hundhausen*, 1983; *Tokman and Bellan*, 2002). The image of a CME that occurred on January 4^{th}, 2002 and was recorded by the Solar and Heliospheric Observatory (SOHO) is depicted in Figure 2.4 (*SOHO*). Panel (i) is an ultraviolet image of the solar corona. On the left hand side a filament-like structure emanates from the solar corona. Panel (ii) is an image taken by the Large Angle and Spectrometric Coronagraph (LASCO) C2 imager of the coronal mass separating from the solar corona. The image in panel (iii) is the same CME, at a later time, as imaged by the LASCO C3 imager. The corona is the bright plasma emitted radially away from the occulting disk in the second and third panels. The CME results in the formation of a coronal hole. Coronal holes are low temperature, low luminosity, and low density regions in the corona with magnetic field densities as low as 1% of those in the surrounding corona (*Zirker*, 1977).

2.1.2 Corotating Interaction Regions

Coronal holes are linked to another solar wind structure called corotating interaction regions (CIRs). As mentioned in the previous section, sun spots, solar prominences, flares, and CMEs occur more frequently near solar maximum. Up to and during solar minimum coronal holes are the more active phenomenon. Coronal holes are regions of the Sun with extremely low densities and temperatures (5×10^{11} m^{-3} and 1.6×10^{6} K at a distance of 1 solar radius) compared to the surrounding medium (*Priest*, 1997). Very little light is emitted from these regions which appear dark when viewed at x-ray wavelengths (*Alves et al.*, 2006). During solar maximum, the heliospheric polar region is reduced in area, and the coronal holes are confined to high solar latitudes. Coronal holes can and do form at lower latitudes, usually as a result of a CME (*Richardson*, 2004). During the declining phase of the solar cycle, the holes are at their largest and extend to lower latitudes close to the ecliptic equator (*Alves et al.*, 2006; *Heber et al.*, 1999). Close to the Sun, the magnetic field structure of coronal holes appear to have a single polarity, either directed inward or outward, emerging into interplanetary space (*Heber et al.*, 1999; *Alves et al.*, 2006). This

'open' field line reaches far into interplanetary space. Coronal holes are the primary source for the high speed component of the solar wind plasma, having an average speed of 800 km/s (*Heber et al.*, 1999; *Priest*, 1997; *Alves et al.*, 2006). This 'fast' solar wind flows radially outward from the coronal hole. As the coronal hole rotates this fast solar wind stream will reappear every 27 days at low equatorial latitudes (*Heber et al.*, 1999) when viewed from Earth. This fast solar wind can catch up to the slower moving solar wind. The interaction will increase the density in the slow solar wind region and increase the thermal energy of the plasma in the fast solar wind (*Alves et al.*, 2006). At distances greater than 1.5 AU this will create a shock formation in the solar wind. At distances of roughly 1 AU, shocks are not typically seen. Instead, discontinuities defined as abrupt increases or decrease in the solar wind velocity and density are observed (*Alves et al.*, 2006; *Heber et al.*, 1999).

The solar wind interaction described above is displayed in Figure 2.5. The Sun is situated at the bottom of the figure and the Earth's orbit is represented by the dotted green line arching across the top of the figure. The slow moving solar wind is emitted at a time t_1 at position p which is located in a stationary reference frame with the Sun at the center. As the coronal hole rotates past position p, the fast solar wind particles are emitted at time t_2. The fast solar wind will catch up to the slow solar wind creating an interaction region (IR), also called a stream interface, which is shown by the shaded purple zone looping out from the Sun (*Borovsky and Denton*, 2010; *Alves et al.*, 2006; *Heber et al.*, 1999). If this interaction region is stable and reappears in interplanetary space through several synodic rotations then it is labelled a CIR (*Heber et al.*, 1999; *Alves et al.*, 2006). When the coronal holes, and subsequent CIRs, are situated at low heliographic latitudes the Earth's orbit crosses the high speed stream approximately once every 27 days and an ensuing periodic activity in the near Earth-space environment is observed. In the situation depicted in Figure 2.5, a geomagnetic storm (described in section 2.7.1) is likely to occur when the Earth's orbit crosses the IR. During the declining phase of the solar cycle, CMEs are less frequent and CIRs occur more frequently (*Heber et al.*, 1999).

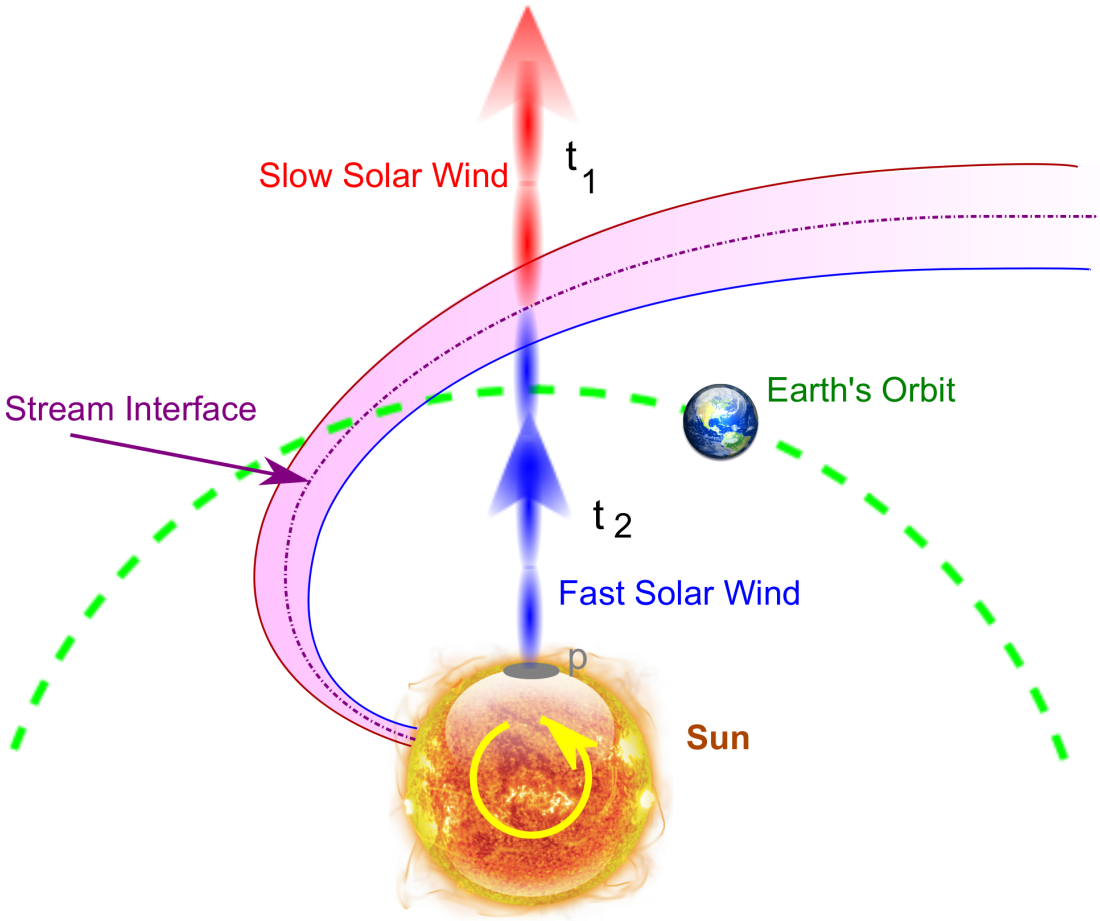

Figure 2.5: Sketch of an idealized CIR stream in the equatorial plane, adapted from (*Borovsky and Denton*, 2010). The Sun is situated at the bottom of the figure, and the Earth's orbit is represented by the dotted green line arching across the top of the figure. The interaction region (stream interface) is depicted by the shaded purple region spiralling out from the Sun.

2.2 Magnetosphere

The Earth is largely shielded from the influence of the solar wind by the presence of the magnetosphere. The geomagnetic field impedes the stream of energetic solar wind particles from reaching the Earth. The size and shape of the magnetospheric cavity is largely determined by the geomagnetic field, the solar wind and the IMF. The geomagnetic field approximates a magnetic dipole close to the Earth's surface. The orientation of the Earth's dipole magnetic moment is tilted with respect to the rotation axis of the Earth by roughly 11 degrees. The geomagnetic field strength, B, can be represented by the dipole approximation:

$$B = \frac{M(1 + 3\cos^2(\theta))^{1/2}}{r^3}, \tag{2.1}$$

where M is the dipole magnetic moment, r is the radial distance from the center of the Earth, and θ is the dipole colatitude. The effect that the solar wind and IMF have on the magnetospheric cavity can be seen in Figure 2.6. The incoming solar wind and IMF compress the magnetosphere on the sunward side and lengthen the magnetic field lines on the nightside creating the magnetotail region.

As the supersonic solar wind approaches the Earth, it encounters the geomagnetic field. It is possible to approximate the location of the magnetopause boundary sunward of the Earth by considering the pressure balance between the geomagnetic field and the solar wind. The main portion of the solar wind's energy is kinetic, the contribution of the solar wind's dynamic pressure can be approximated by $P_{dyn} = (1/2)n_{sw}u_{sw}^2$, where n_{sw} and u_{sw} are the proton density and flow speed, respectively. By balancing the solar wind dynamic pressure with the magnetic pressure exerted by the geomagnetic field the approximate location of the dayside boundary is (*Walker and Russell*, 1997):

$$L_{mp}(R_e) = 107.4(n_{sw}u_{sw}^2)^{-1/6}. \tag{2.2}$$

Typically this distance is around 10 Re upstream of the Earth. When deflected by the geomagnetic field, incoming solar wind particles create a current sheet called the magnetopause current, illustrated in green in Figure 2.6.

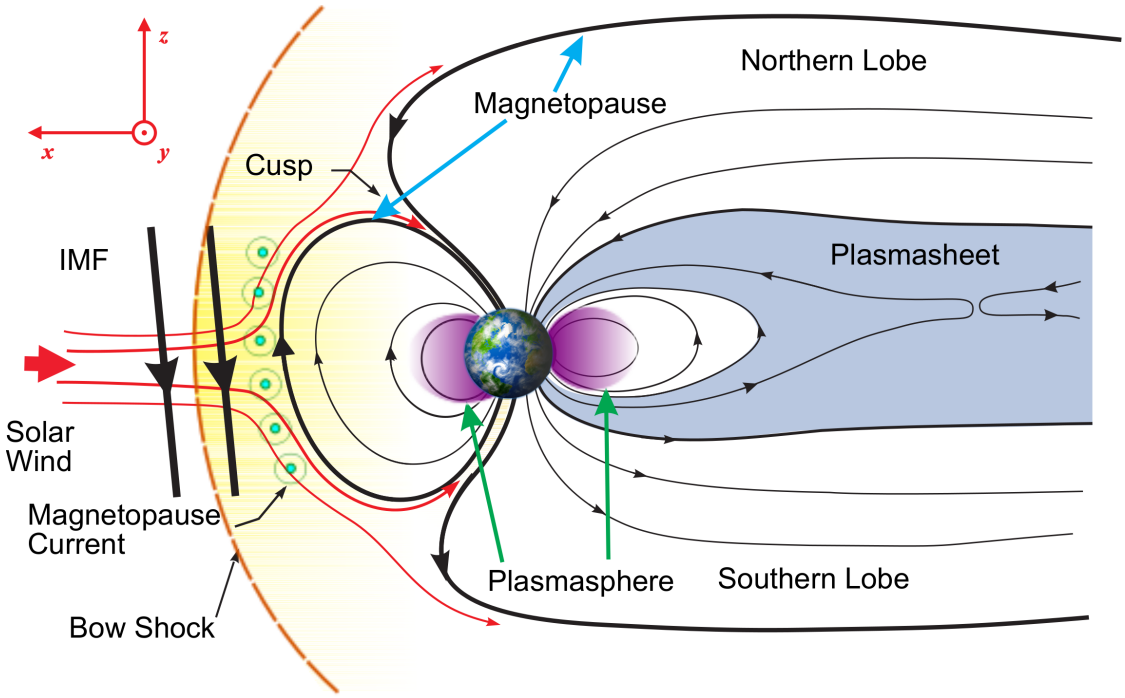

Figure 2.6: Cross-section of the north and south hemisphere of the Magnetosphere as viewed from the side. Various Magnetospheric Regions and current systems are labelled with the GSM coordinate system shown. Image adapted from original schematic by K. McWilliams.

Consider a simplified model where $\mathbf{B}_{sw} \approx 0$ and solar wind particles encounter the geomagnetic field, as shown in Figure 2.7. The system is described using the geocentric solar elliptical co-ordinate system (GSE): the x-axis points towards the Sun, the y-axis points towards dusk, and the z-axis is oriented to complete the right hand coordinate system. This simplified solar wind consists of electrons and protons traveling in the -x direction and the geomagnetic field ($\mathbf{B}\sim$ B$\hat{\mathbf{z}}$) points out of the figure. As the particles approach the magnetic field they experience the Lorentz force, $\mathbf{F}_B$,

$$\mathbf{F}_B = q(\mathbf{v} \times \mathbf{B}), \tag{2.3}$$

where q is the particle charge, $\mathbf{v}$ is the particle velocity, and $\mathbf{B}$ is the geomagnetic field. The Lorentz force deflects the ions towards dusk (+y direction) and the electrons towards dawn (-y direction). This relative motion between the ions and the electrons generates the magnetopause current, and it flows from dawn to dusk along the magnetopause. The magnetopause current is consistent with a lower geomagnetic field strength sunward of the magnetopause boundary and an enhanced geomagnetic field strength on the earthward side. Changes in the solar wind dynamic pressure change the strength of the magnetopause current.

The solar wind is slowed down to subsonic speeds by the formation of a collisionless shock in a region called the bow shock. The standoff distance of the nose of the bow shock sunward of the Earth is roughly 14 Re (*Cairns and Lazarus*, 1995) and is illustrated by the dotted orange line in Figure 2.6. At the bow shock, the particles slow down and their temperatures dramatically increase (*Quest*, 1998). Directly between the bow shock and the magnetopause is a region known as the magentosheath, depicted by the shaded yellow region in Figure 2.6. When the supersonic solar wind plasma crosses the bow shock, it is slowed to approximately 250 km/s (*Hargreaves*, 1992). The kinetic energy lost in this transition is converted into thermal energy making the average temperature of the plasma in the magentosheath approximately 5×10^6 K (*Hargreaves*, 1992).

The antisunward portion of the magnetospheric cavity extends into interplanetary space and is known as the magnetotail. The general shape of the magnetotail

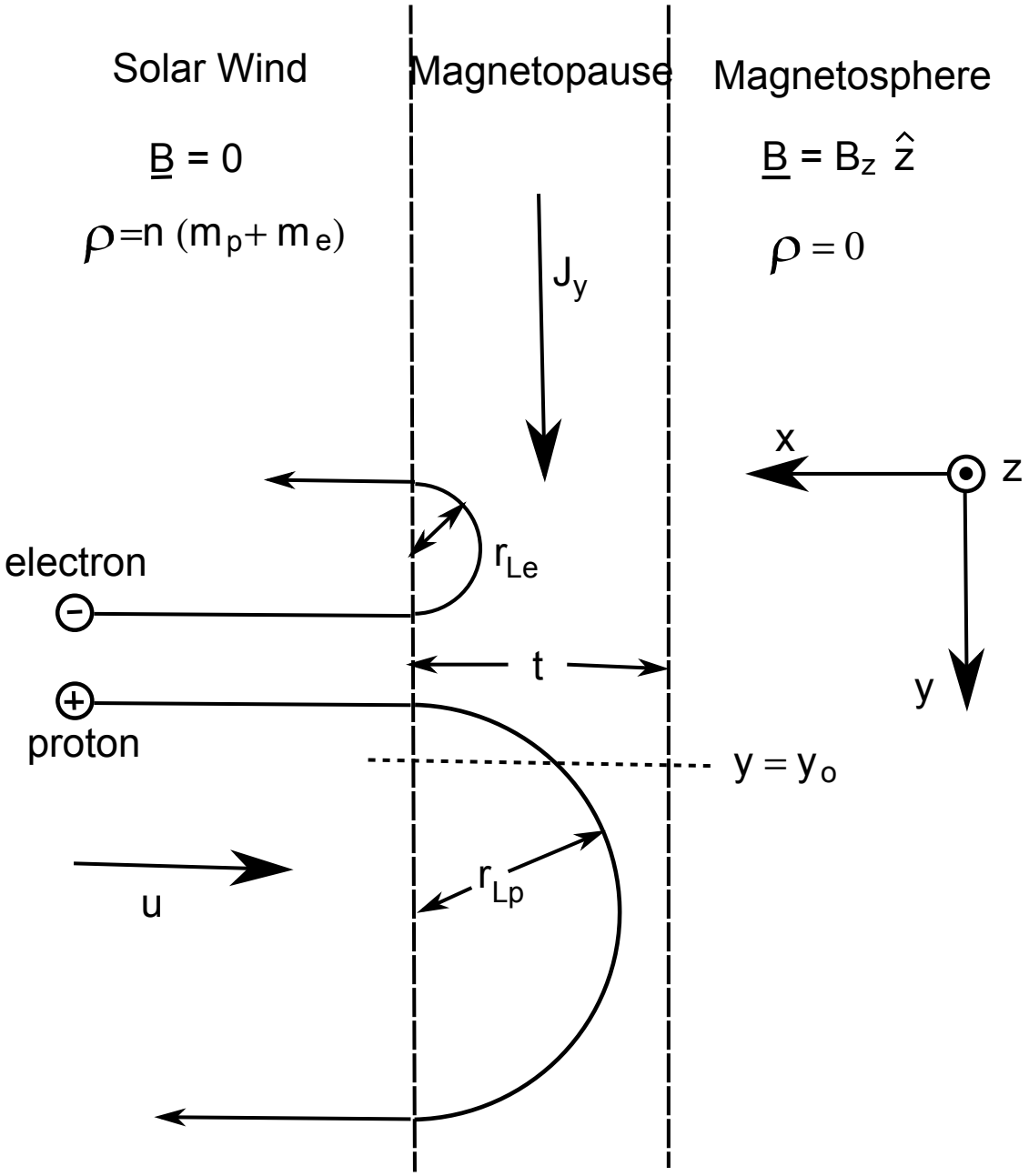

Figure 2.7: Magnetopause current system as viewed from the equatorial plane. Sun is located in the -x direction and Earth to the +x direction. Image courtesy of *Hughes* (1997).

approximates a solenoid divided into north and south regions or 'lobes'. The north lobe contains magnetic field lines directed towards the Earth, while the south lobe contains magnetic field lines directed away from the Earth, as shown in Figure 2.6. The magnetotail's north and south lobes are separated by the plasma sheet. The plasma sheet is roughly 5-10 Re thick and contains dense energetic particles. Particle densities in this region range from 0.1 to 1 cm^{-3} with energies on the order of 1 or 10 keV (*Hargreaves*, 1992). The plasmasphere is a region of cold dense plasma (0.1 eV, 10^3 cm^{-3}) that rotates with the Earth (*Baumjohann and Treumann*, 2006). The plasmasphere is contained close to the Earth, within 3-5 Re, where the geomagnetic field is most dipole-like.

2.3 Magnetospheric Convection

The solar wind plasma and IMF are coupled to each other. In collisionless plasma, such as the solar wind, the conductivity can be so large that Ohm's law can only be satisfied if:

$$\mathbf{E} + \mathbf{v} \times \mathbf{B} = 0, \tag{2.4}$$

where $\mathbf{E}$ is the electric field, $\mathbf{v}$ is the plasma velocity, and $\mathbf{B}$ is the magnetic field. Despite the simplicity of equation 2.4 it carries strong implications for solar wind plasma and IMF interaction. It can be shown from equation 2.4 that the magnetic flux through a given volume must remain constant. With respect to the solar wind plasma and IMF, it means that as the solar wind flows through interplanetary space, the IMF must go with it to ensure constant flux along the field line. The implication is that the plasma is 'frozen' to the IMF that passes through it and cannot cross from one field line to another. The 'frozen-in' plasma is also referred to as flux tubes and they propagate from the Sun towards the Earth.

As the flux tubes propagate through interplanetary space they encounter the geomagnetic field. The interaction between a predominately southward IMF ($B_z < 0$) and the magnetosphere is illustrated in Figure 2.8. In this figure, the Sun is located to

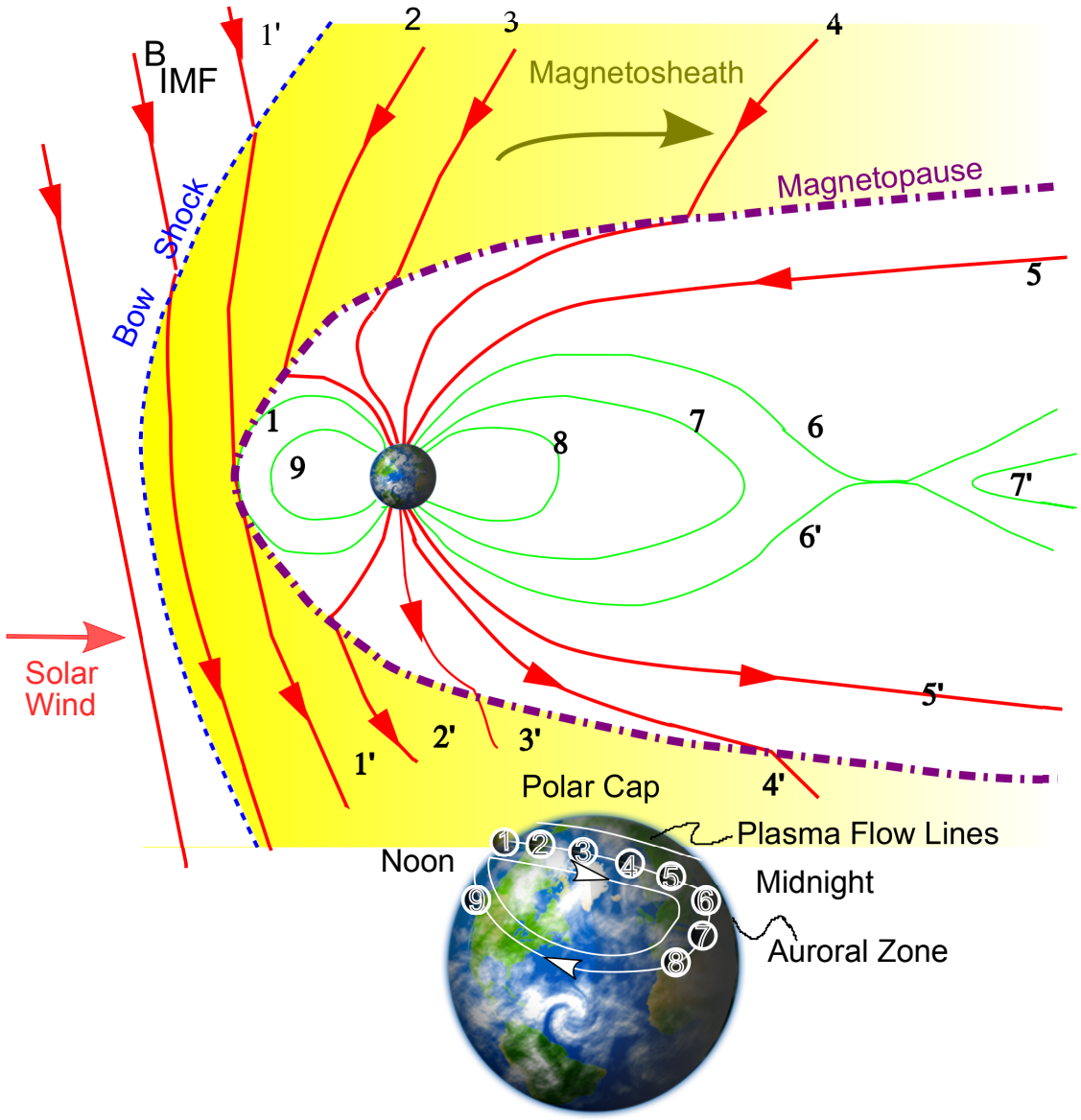

Figure 2.8: Magnetospheric plasma flow driven by magnetic reconnection and associated ionospheric plasma convection associated with the IMF footprint. Image from schematic by *Hughes* (1997).

the left of the page and the geomagnetic north pole is located towards the top of the page. The dashed lines represent the bow shock (blue) and the magnetopause (purple), and they are labelled accordingly. As the southward IMF (line 1') approaches the northward geomagnetic field (line 1), the IMF and geomagnetic field lines merge. This merging process creates 'open' magnetic field lines. Open magnetic field lines connect the IMF to the geomagnetic field lines. The solar wind continues to flow through interplanetary space dragging the newly opened flux tubes anti-sunward, as illustrated by the sequence of lines 2-4. As the flux tubes extend into the tail region (field line 5) the oppositely directed open field lines (line 6 and 6') merge and form the closed geomagnetic field line (line 7) and purely IMF (line 7') field line. The closed geomagnetic field then contracts earthward to a more dipole-like configuration (lines 7 and 8).

The inset in Figure 2.8 shows how the reconnection drives plasma convection in the high latitude ionosphere. The ionospheric footprint of the flux tube motion across the polar cap drives the ionospheric plasma, that is also frozen-in to a large extend, antisunward from the noon sector (point 1 in the inset) towards the midnight sector (point 6). This two cell convection pattern is completed when the newly closed geomagnetic flux tubes on the nightside return towards dawn or the dusk (points 7 and 8) at lower latitudes towards the dayside.

Different IMF configurations will result in different plasma convection patterns in the high latitude ionosphere. Convection patterns for various IMF orientations for quiet solar wind conditions are summarized in Figure 2.9 (*Ruohoniemi and Baker*, 1998). The pattern for a strongly southward oriented IMF ($B_y \sim 0$) is in the middle bottom convection pattern. The IMF $B_y < 0$ tilts the flow around the polar cap region. The dusk cell dominated ($B_y < 0$) pattern is in the middle left convection pattern and the slightly dawn cell dominated ($B_y > 0$) is in the middle right convection pattern.

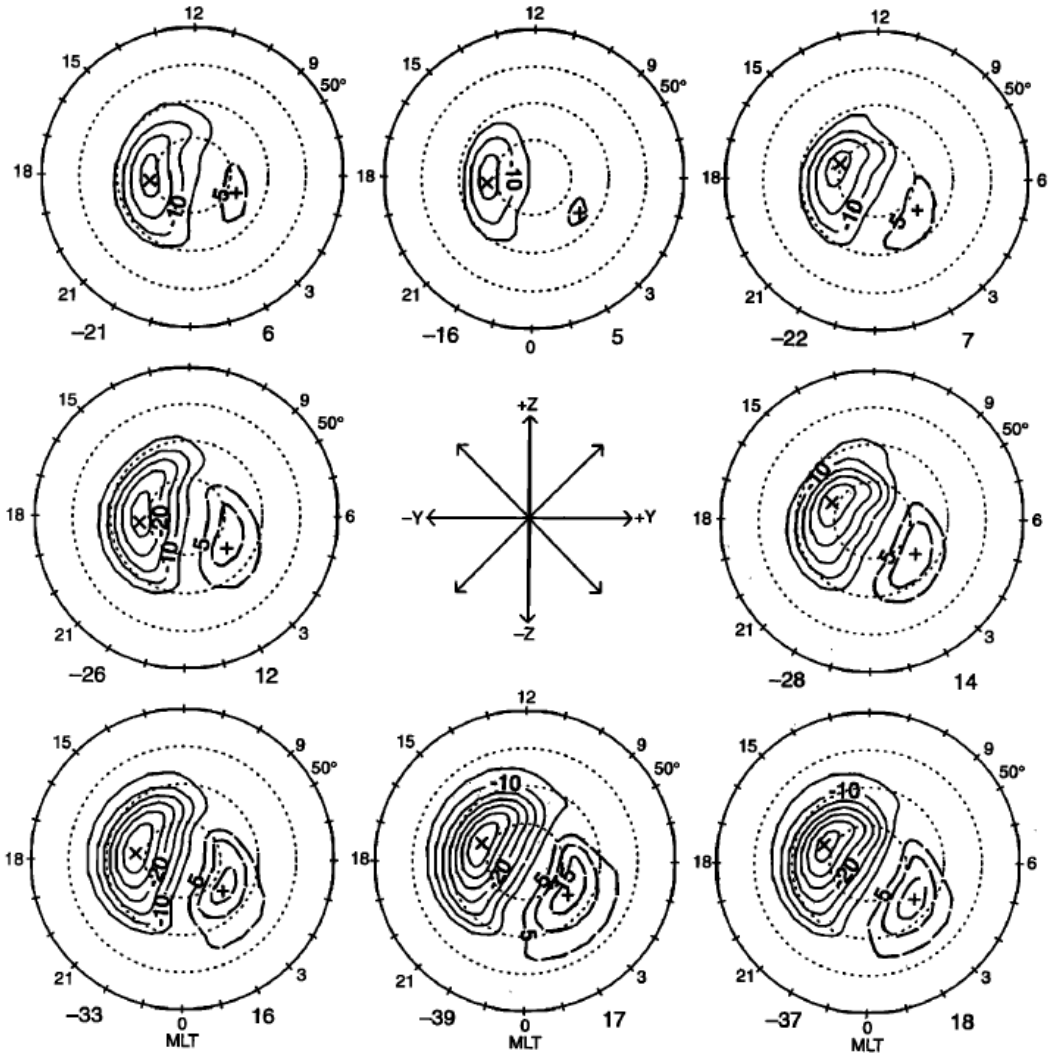

Figure 2.9: Convection patterns sorted by IMF angle for IMF magnitude in the interval $0 \leq B_T \leq 4$ nT (*Ruohoniemi and Baker*, 1998). GSM coordinate system defined in center.

2.4 High Latitude Plasma Motion

In addition to flux tube motion and the electric field applied from the solar wind, plasma motion in the lower high latitude ionosphere is highly affected by collisions and the neutral wind. Below 500 km, the Earth's neutral atmosphere is comprised mainly of O, N_2, and O_2. The distribution of these three dominant neutrals is displayed in Figure 2.10. Above 200 km O dominates while N_2 is the main atmospheric constituent lower down. O_2 is only found in large quantities below 105 km. At altitudes roughly above 80 km, particle precipitation and photoionization free electrons from the neutrals and create a region of ionized plasma called the ionosphere. Figure 2.11 shows a vertical profile of electron density versus altitude in the presence of photoionization (*Hargreaves*, 1992). The ionosphere is separated into three layers loosely defined by the shape of their electron density profiles (outlined in Figure 2.11): the D-region (∼80 to 100 km), the E-region (∼100km to 150 km), and the F-region (∼150 to upwards of 1000 km) (*Hargreaves*, 1992). The boundaries of each region are described differently in various literature sources and there is no official upper limit to the F-region although a good approximation is between 1000 and 2000 km, beyond which begins the start of the magnetosphere.

The motion of the electrons and the ions at the various altitudes is described by the fluid equation of motion which reads (*Schunk and Nagy*, 2000):

$$m_\alpha \frac{d\mathbf{v}_\alpha}{dt} = q_\alpha(\mathbf{E}+\mathbf{v}_\alpha\times\mathbf{B}) - \nu_{\alpha n} m_\alpha(\mathbf{v}_\alpha - \mathbf{U}_n) - \frac{\nabla(n_\alpha T_\alpha)}{n_\alpha} \pm m_\alpha \nu_{ei}(\mathbf{v}_e - \mathbf{v}_i) + m_\alpha \mathbf{g}, \quad (2.5)$$

where $\mathbf{E}$ is the electric field, q_α is the charge of the particle α, $\mathbf{B}$ is the geomagnetic field, $\mathbf{U}_n$ is the neutral wind speed, ν_{ei} is the electron-ion collision frequency, $\mathbf{g}$ is the acceleration due to gravity, and $\nu_{\alpha n}$, m_α, $\mathbf{v}_\alpha$, T_α (measured in eV), and n_α are the momentum transfer collision (α-neutral) frequency, mass, velocity, temperature and number density of the particle α. In the above equation the term which describes Coulomb collisions between electrons and ions was eliminated under the assumption $\nu_{\alpha n} >> \nu_{ei}$ which is valid below 200 km. It can be shown that for electric fields in excess of a few mV/m, gravity and the pressure gradient normally introduce only

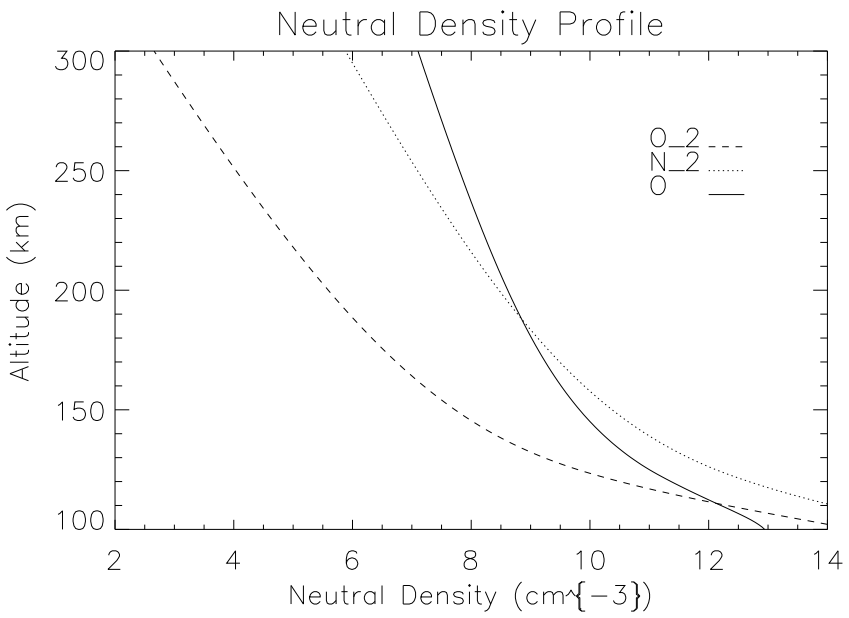

Figure 2.10: Neutral density profile for April 3^{rd}, 2000. The three main ionospheric neutral densities (O, O_2, N_2) are potted against altitude. Data obtained using the MSIS-E-90 Atmosphere Model courtesy of Virtual Ionosphere, Thermosphere, Mesosphere Observatory (VITMO).

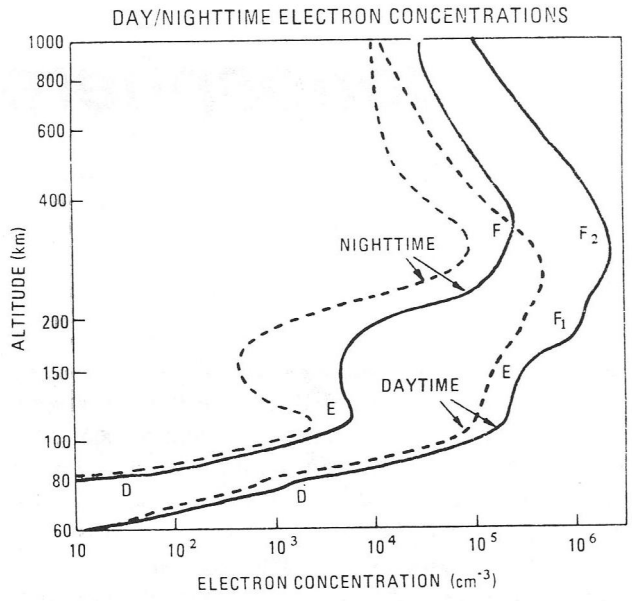

Figure 2.11: Ionospheric electron density profiles obtained for mid-latitudes for both day and night (*Hargreaves*, 1992). Dashed and solid lines represent data obtained during sunspot minimum and maximum, respectively.

second order corrections to the leading order balance. The general equation of motion of the particle α simplifies to (*Kelley*, 1989):

$$\mathbf{v}_{\alpha\perp} = \frac{1}{1+(\frac{\nu_\alpha}{\Omega_\alpha})^2}\left[\frac{\nu_{\alpha n}}{\Omega_\alpha}\frac{\mathbf{E'}_\perp}{B} + \frac{\mathbf{E'}_\perp \times \mathbf{B}}{B^2}\right], \tag{2.6}$$

where $\Omega_\alpha (= \frac{q_\alpha B}{m_\alpha})$ is the gyrofrequency of the particle α, and $\mathbf{E'}_\perp = \mathbf{E}_\perp + \mathbf{U}_n \times \mathbf{B}$. The gyrofrequency, Ω_α, is charge dependent, so the first term on the right hand side of equation 2.6 is negative for the electrons. This enables relative drift between the ions and electrons if $\nu_{\alpha n}$ is high enough. Equation 2.6 is essential when describing high-latitude particle motion. The first term describes the motion of particles along the electric field, **E**, direction and the second term describes the particle motion produced by the crossed electric and magnetic fields. The magnitude and direction of the ion or electron drift is greatly affected by the ratio of the particle-neutral collision frequency to the particle gyrofrequency.

The neutral collision frequency and gyrofrequency, in the E-region are shown in Figure 2.12. The neutral collision frequencies for both electrons and ions were calculated using the equations found in *Schunk and Nagy* (2000). The gyrofrequencies for the ion and electrons are independent of altitude over this range at 160 Hz and 1.7×10^6 Hz, respectively. At roughly 150 km, the electron-neutron collision frequency, ν_{en} is quite low, at roughly 10^3 Hz. As altitude decreases, there is an exponential increase in ν_{en}, until it becomes equal with the gyrofrequency at ∼70 km, reaching a value of $\sim 10^7$ Hz by approximately 60 km. The ion-neutral collision frequency is quite low (50 Hz) at 150 km. It increases with decreasing altitude, equalling the gyrofrequency at 120 km, before reaching 5×10^6 Hz by 60 km.

According to equation 2.6, the electron and ion motion is strongly related to the ratio of ν_α/Ω_α. Below roughly 100 km the density of the ionized particles is typically too low to cause appreciable current (*Baumjohann and Treumann*, 2006). Above 100 km the gyrofrequency of the electrons is much greater than the collision frequency (Figure 2.12), and the second term in equation 2.6 therefore dominates so that the electrons acquire a $\mathbf{E} \times \mathbf{B}$ motion. For ions, above 120 km, the ratio of ν_i/Ω_i is smaller, and the ions drift with the electrons with an $\mathbf{E} \times \mathbf{B}$ motion. Below

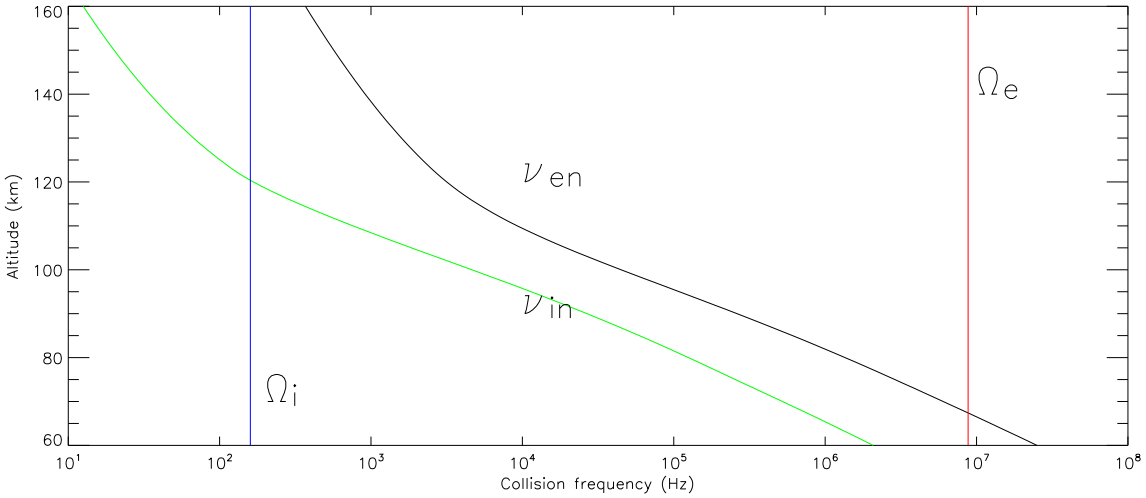

Figure 2.12: Collision collision frequency and gyrofrequency at mid-latitude plotted as a function of altitude for the March equinox, 2002.

$\sim$ 120 km, the ion-neutral collision frequency dramatically increases with decreasing altitude. As a result, the ions are no longer as strongly bound to the magnetic field lines; collisions with neutrals will tend to free it from the magnetic field line. The resulting ion, no longer bound to the magnetic field, is free to drift with a component of motion along the direction of **E**.

The F region is the ionospheric layer directly above the E region upwards of 150 km with a peak electron density of roughly 10^6 cm^{-3}. In the F region, the ions and electrons are highly magnetized, or 'frozen-in' to the magnetic field. This magnetization is due to the gyrofrequency of the ions and the electrons being much greater than that of the collision frequency ($\nu_\alpha << \Omega_\alpha$). We can simplify equation 2.6 to establish that the general motion of both the ions and the electrons is, to a good degree of approximation:

$$\mathbf{V_E} = \frac{\mathbf{E} \times \mathbf{B}}{B^2}, \tag{2.7}$$

where $\mathbf{V_E}$ is also known as the $\mathbf{E} \times \mathbf{B}$ drift.

The relative motion of the ions and electrons at the different altitudes will create a system of currents in the E region. The various motion of the ions and electrons and the associated currents are displayed in Figure 2.13. The magnetic field is oriented in the z-direction, electric field is oriented in the y-direction and the x-direction completes the right hand coordinate system. The motion of the ions and electrons

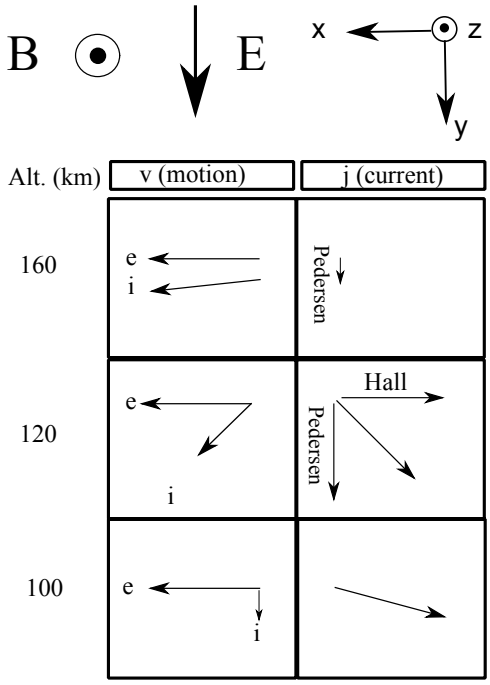

Figure 2.13: Cartoon of ion and electron motion, and resulting ionospheric currents, as a function of altitude, adapted from *Richmond and Thayer* (2000).

at the altitudes 100 km, 120 km, and 160 km is illustrated in Figure 2.13. At 100 km, repeated collisions result in the ions having a small component of $\mathbf{v}$ along the y-axis (along $\mathbf{E}$) and the electrons in the direction of $\mathbf{V_E}$. This creates a current nearly opposing the $\mathbf{E} \times \mathbf{B}$ drift. Between 110 and 150 km, collisions with the neutrals enable the ions to move in a direction other than the $\mathbf{V_E}$ direction. This results in a current with a component along the $\mathbf{E}$ and the $\mathbf{E} \times \mathbf{B}$ directions. Intensification of the current generated in the E region will cause deflections of the geomagnetic field which can be detected by ground-based magnetometers which will be discussed further in section 2.7. The component of the current moving parallel the electric field is called the Pedersen current. The component moving perpendicular to both the magnetic and electric fields is called the Hall current. At 160 km, the ions and the electrons are moving together and there is only a weak Pedersen current. Pedersen currents, though small, become important for the generation of F-region instabilities discussed in section 3.4. In the high altitude F region, the electric field ($\mathbf{E}$) seen is

a result of the plasma convection discussed in section 2.3.

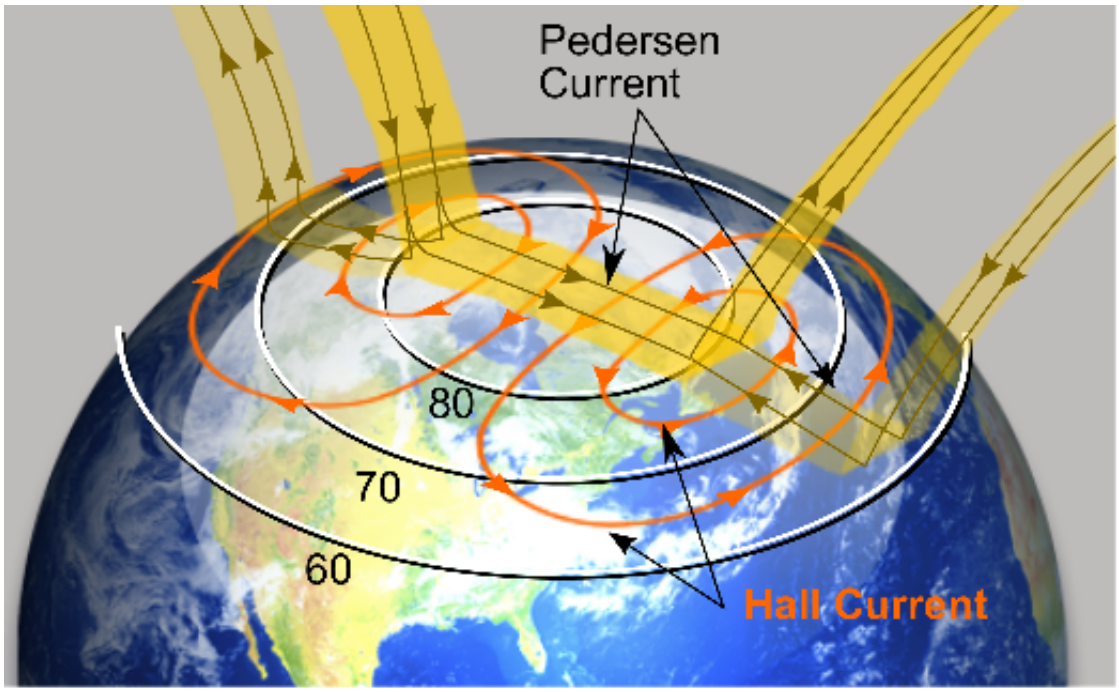

Figure 2.14: Global representation of the ionospheric Hall and Pedersen current systems coupled to the FAC current system as viewed from above. Image courtesy of MetEd (*https* : *//www.meted.ucar.edu/index.php*).

The Hall currents flow in a direction perpendicular to both the electric and the magnetic fields, and form a closed current loop inside the ionosphere, at least in principle. The Pedersen currents, on the other hand, flow in the direction of **E** and therefore must close outside of the ionosphere (illustrated in Figure 2.14). The Birkeland currents, flowing into and out of the ionosphere, meet this need.

2.5 Field Aligned Currents (FAC)

Field-aligned currents (FAC), also known as Birkeland currents, are an integral part of magnetosphere-ionosphere coupling (*Cowley*, 2000). Early statistical distributions were obtained from magnetic field observations using the Triad satellite in a circular polar orbit at an altitude of ∼800 km, the results of which are displayed in Figure 2.15. The FAC distributions are displayed in a magnetic local time (MLT) and

magnetic latitude coordinate system, with magnetic local noon (12 MLT) located at the top of the plot and dawn (6 MLT) to the right. Concentric circles of magnetic latitude for 60^o, 70^o, and 80^o are centered on the magnetic north pole. Figure 2.15 illustrates the direction of currents going into and out of the ionosphere and their locations during both quiet and disturbed geomagnetic activity levels. Region 1 currents are directed upward on the dusk side and downward on the dawn side. Region 1 currents connect the ionosphere to the magnetospheric plasma sheet and boundary layers. The currents equatorward of Region 1 are known as Region 2 currents (*Iijima and Potemra*, 1978), and they are directed downward on the dusk side and upward on the dawn side. When magnetic activity intensifies, the currents increase in area and move equatorward, reaching to nearly 60^o magnetic latitude in the dusk sector. In the midnight sector, the Region 2 current also extends into the the pre-dawn sector moving from 0 MLT to 1 MLT.

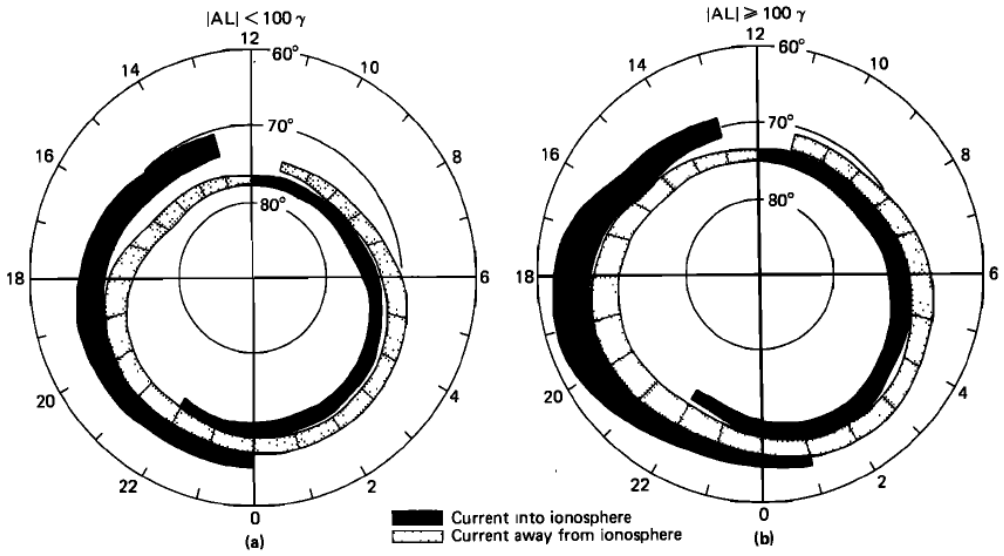

Figure 2.15: Birkeland Current pattern showing Region 1 and Region 2 currents for both quiet (left) and disturbed (right) geomagnetic conditions (*Iijima and Potemra*, 1978). Geomagnetic activity levels are determined by the AL index.

In Figure 2.16 the region 1 and 2 currents are overlaid with the high-latitude electric fields. The regions where the currents tend to flow into the ionosphere

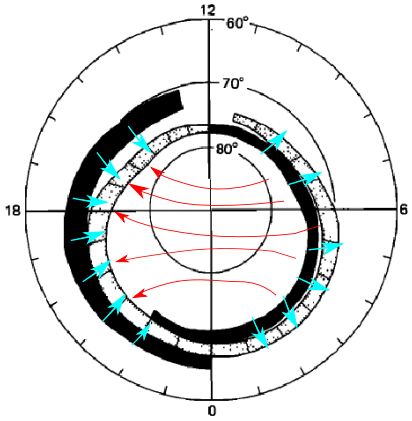

Figure 2.16: High latitude parallel current systems and associated electric fields. Adapted from (*Iijima and Potemra*, 1978; *Wolf*, 1997; *Baumjohann and Treumann*, 2006). Dark regions represent regions of positive charge accumulation and blocked in white regions represent areas of negative charge accumulation. Red arrows indicate polar cap electric field and blue arrows represent dusk to dawn electric field.

are charged positively (dark region) whereas regions of upward current flow are negatively charged (light regions). In the regions near 6 and 18 MLT, this creates a dusk-to-dawn electric field at equatorward latitudes as shown by blue arrows. Across the polar cap region a dawn-to-dusk electric field, which is represented by the red arrows, connects the Region 1 currents. This is known as the polar cap electric field.

2.6 The ring current

After reconnection has occurred in the tail, a plasma of solar wind and terrestrial origins is formed in the newly closed terrestrial flux tubes. Particles drifting in the near-Earth space environment encounter a gradient in the geomagnetic field as they get closer to the Earth. This magnetic field gradient causes the ions and the electrons to undergo curvature-gradient drift according to (*Baumjohann and Treumann*, 2006):

$$\mathbf{v}_{\nabla BR} = \frac{mv_{\perp}^2}{2qB}\frac{\mathbf{B}\times\nabla B}{B^2} + \frac{mv_{\parallel}^2}{qR_c^2}\frac{\mathbf{R}_c\times\mathbf{B}}{B^2}, \tag{2.8}$$

where $\mathbf{R}_c$ is the radius of curvature, $\mathbf{B}$ is the magnetic field, q is the charge of the particle, and $v_\perp$ and $v_\parallel$ are the components of the particle velocity perpendicular and parallel to the magnetic field lines. In the tail region, according to equation 2.8, the ions flow to the dusk side and the electrons flow to the dawn side. The curvature-gradient drift generates a westward current circling the Earth (*Wolf*, 1997), known as the ring current. The Dessler-Parker-Sckopke relationship (*Wolf*, 1997) shows the relationship between the decrease in the surface geomagnetic field at low-latitudes and the energy of particles in the ring current:

$$\frac{\Delta \mathbf{B}_{particles}}{B_o} = -\frac{2}{3}\frac{W_{particles}}{W_{mag}}\hat{\mathbf{e}}_z, \tag{2.9}$$

where B_o is the magnetic field strength of the dipole at the Earth's equator, $\hat{\mathbf{e}}_z$ is oriented along the northward magnetic field direction, $W_{particles}$ is the total energy of the particles, and W_{mag} is the total energy of the dipole magnetic field at the Earth's equator. The ring current contains 10-200 keV ions and electrons and exists at an average distance of 2-7 Re. There is a change in the ring current intensity as it travels around the Earth due to the ring current connection to the ionosphere.

During periods of prolonged southward IMF there is an increase in reconnection. This increase in reconnection results in the entry of more solar wind particles into the magnetosphere which is ultimately deposited into the ring current. The increase in particles intensifies the existing ring current resulting in a decrease in the geomagnetic field strength earthward of the current ring current position. When the IMF returns to a northward orientation, the ring current slowly returns to pre-disruption levels. As the ring current returns to normal strength, the geomagnetic field strength earthward of the ring current strengthens, returning to equilibrium values.

2.6.1 The Partial Ring Current

There is an asymmetric component to the ring current system called the partial ring current. A cut of the magnetosphere in the equatorial plane is illustrated in Figure 2.17 with the hot plasmasphere plasma depicted in light blue. For the ring current system described above, in a closed system with no reconnection, the ions

would curvature gradient drift westward and the electrons eastward. There would be no charge separation of the hot plasma population and a symmetric westward current would flow around the Earth (Figure 2.17(a)). In the presence of reconnection, plasma is removed from the dayside and an $\mathbf{E} \times \mathbf{B}$ drift will drive plasma in the subsolar region, bringing cold equatorial plane plasma closer to the dayside magnetopause (shown by the displacement of the white area in Figure 2.17). The dawn to dusk electric field introduces a charge build up of ions on the dusk side and of electrons on the dawn side (*Cowley*, 2000). In order to neutralize this build up of charge, and maintain current continuity, electrons need to flow into the ionosphere on the dusk side and ions out of the ionosphere on the dawn side. This creates a westward asymmetric, or partial ring, current which flows in the midnight sector as illustrated by Figure 2.17(b). It is connected to the ionosphere through the FAC current systems.

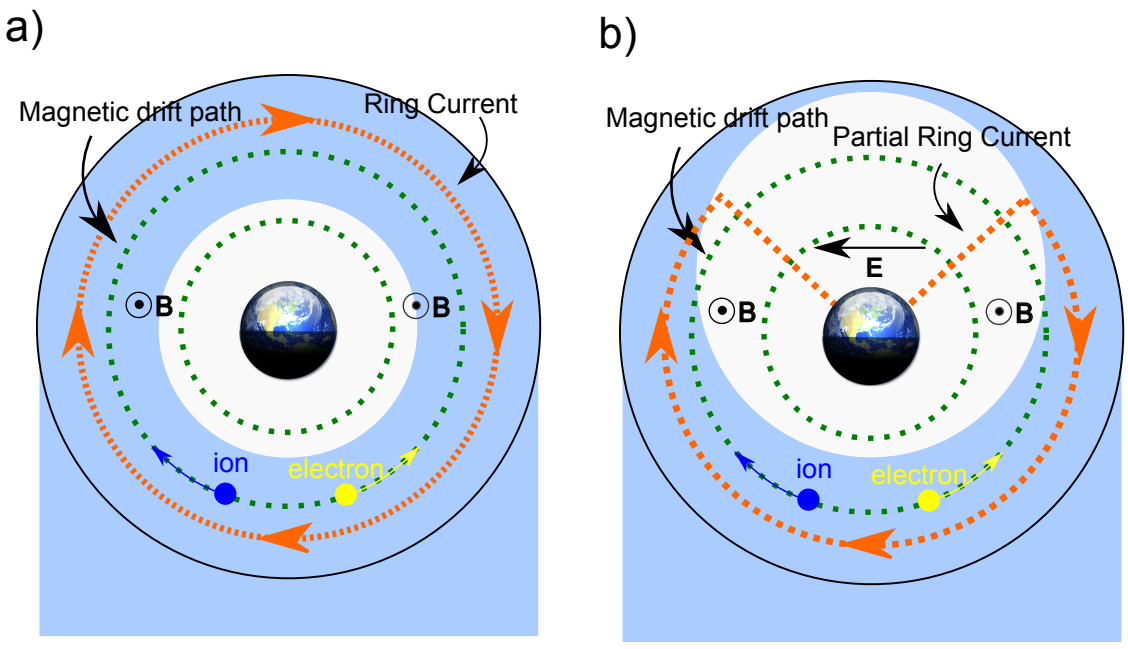

Figure 2.17: Simplified model of the partial ring current adapted from *Cowley*.

2.7 Magnetic Disturbances

Magnetospheric-ionospheric current systems have a profound effect on the geomagnetic field, and this can be detected from the ground. Intensification of the magnetopause current increases the geomagnetic field strength, while intensification in the ring current decreases the geomagnetic field within the ring. Large scale variations in the geomagnetic field can be monitored from the ground with magnetometers positioned around the globe. Magnetometers measure the magnitude and direction of the local magnetic field. One of the simpler and more common methods of measuring magnetic fields is by using a fluxgate magnetometer. Fluxgate magnetometers on the ground measure the three geographic components of the geomagnetic field: x (geographic north), y (geographic east), and z (down). A fluxgate magnetometer is composed of two ferromagnetic bars placed close together. The two bars are wrapped with a wire called the "primary" coil. This wire is wrapped clockwise around one core and counterclockwise around the second coil. A "sensing", or secondary, wire is then wrapped around both cores. An alternating current (AC) is then passed through the primary coil. This causes the core to become alternately saturated and unsaturated. The resulting varying field creates a current in the secondary coil. It is feasible to extract the strength and direction of the background magnetic field from the currents induced in the secondary coil. Shown in Figure 2.18 is a sample magnetometer output from the Fort Simpson (FSIM) magnetometer of the CARISMA magnetometer chain for the period of one day. The top panel contains the magnetometer data for the x-component of the magnetic field while the bottom panel contains the y-component of the geomagnetic field. Prior to roughly 6 UT, the value of the geomagnetic field is constant. At approximately 6 UT there is a brief increase in both the x- and y-components of the geomagnetic field before an overall sharp decrease. After a minimum is reached there is a gradual return to equilibrium values. The Fort Simpson magnetometer responds to both ionospheric and magnetospheric currents. Occasionally, this variation in geomagnetic field strength is recorded by magnetometers around the globe simultaneously. This is what a geomagnetic storm

is, by definition.

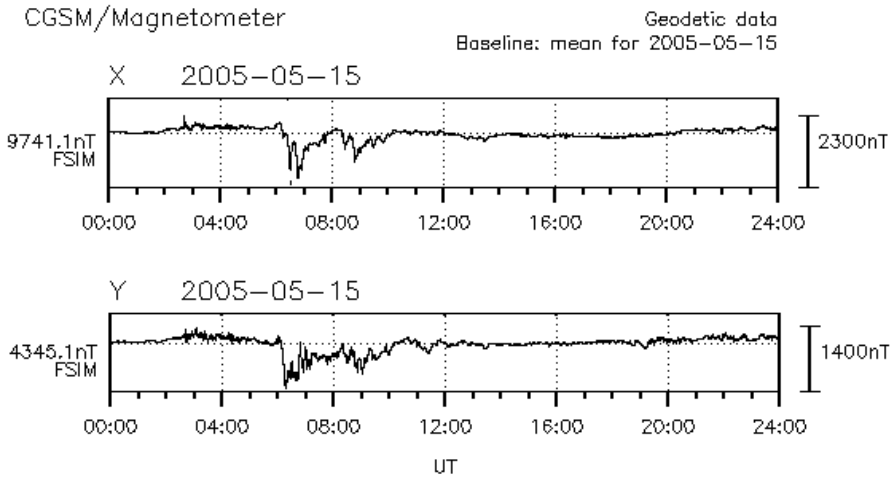

Figure 2.18: Fort Simpson (FSIM) magnetometer data for May 15^{th}, 2005 courtesy of the CARISMA Magnetometer Chain.

2.7.1 Geomagnetic storms

Geomagnetic storms are defined as periods of enhanced geomagnetic activity on a global scale (*Akasofu and Chapman*, 1963a,b; *Perreault and Akasofu*, 1978). These periods are the result of large increases in magnetospheric current systems. With the advent of in situ solar wind data from spacecraft, geomagnetic storms have been shown to relate to interactions of the magnetosphere with the solar wind. A 'standard' geomagnetic storm has three stages: an initial phase, a main phase, and a recovery phase (e.g., *Perreault and Akasofu* (1978)). These phases are described by their geomagnetic activity profiles described by the Disturbed Storm Time (Dst) index. The Dst index is derived from an array of low-to-mid latitude magnetometers (discussed further in Chapter 3), and Dst is widely used for monitoring geomagnetic storms (e.g., *Wanliss and Showalter* (2006); *Wang et al.* (2009); *Burton et al.* (1975)). An example of an intense geomagnetic storm is shown in Figure 2.19 through its Dst index profile for the date of May 15^{th}, 2005. A "standard" geomagnetic storm begins abruptly with a Storm Sudden Commencement (SSC) (*Akasofu and Chapman*,

1963a). The SSC is a sharp increase in the Dst index. The SSC marks the beginning of a period of increased geomagnetic field strength that can last for several hours. This period of increased geomagnetic strength is called the initial phase, and it is a result of an increase of the magnetopause current. This increase indicates a strengthening in the poloidal component of the geomagnetic field in response to a compression of the dayside magnetosphere from its typical position of $\sim$ 10 Re. During particularly severe storms, the compression can reach as close as 6 Re (*Walter D. Gonzalez*, 1999). Not all storms have this initial Dst enhancement, indicating that not all storms are associated with a marked compression of the magnetopause on the dayside (*McPherron*, 1997). Gradually commencing (GC) type geomagnetic storms lack the SSC feature and subsequent initial phase of the geomagnetic storm. The initial phase (if present) is followed immediately by the main phase of the geomagnetic storm. The main phase is marked by a steep, mostly linear, decline in the Dst value over a time scale of hours. During this phase the Dst index drops steeply reaching negative values of hundreds of nTs. This decrease is caused by the intensification of the ring current.

The main phase is followed by the recovery phase. This phase can be the longest, lasting from several hours up to several days. During this phase the Dst value gradually returns to a normal, pre-storm, value. To do this, the ring current begins to dissipate, presumably through scattering of the ring current ions into the loss cone (as a result of cold ionospheric plasma present in the newly expanding plasmasphere) or through recombination of ring current ions forming cold neutral hydrogen (*Walter D. Gonzalez*, 1999). During the recovery phase, the IMF has returned to a more normal range of values indicating that magnetic merging on the dayside has slowed down considerably.

Storms are traditionally identified and classified using the Dst index (*Perreault and Akasofu*, 1978; *Wanliss and Showalter*, 2006; *Wang et al.*, 2009). Storm intensity classification is based on the deepest Dst minimum reached during the main phase of the storm. For instance, *Tsurutani and Gonzalez* (1997) have classified geomagnetic storms into four categories: 'small' (-50 nT $\leq$ Dst $\leq$ -30 nT), 'moderate' (-100 nT

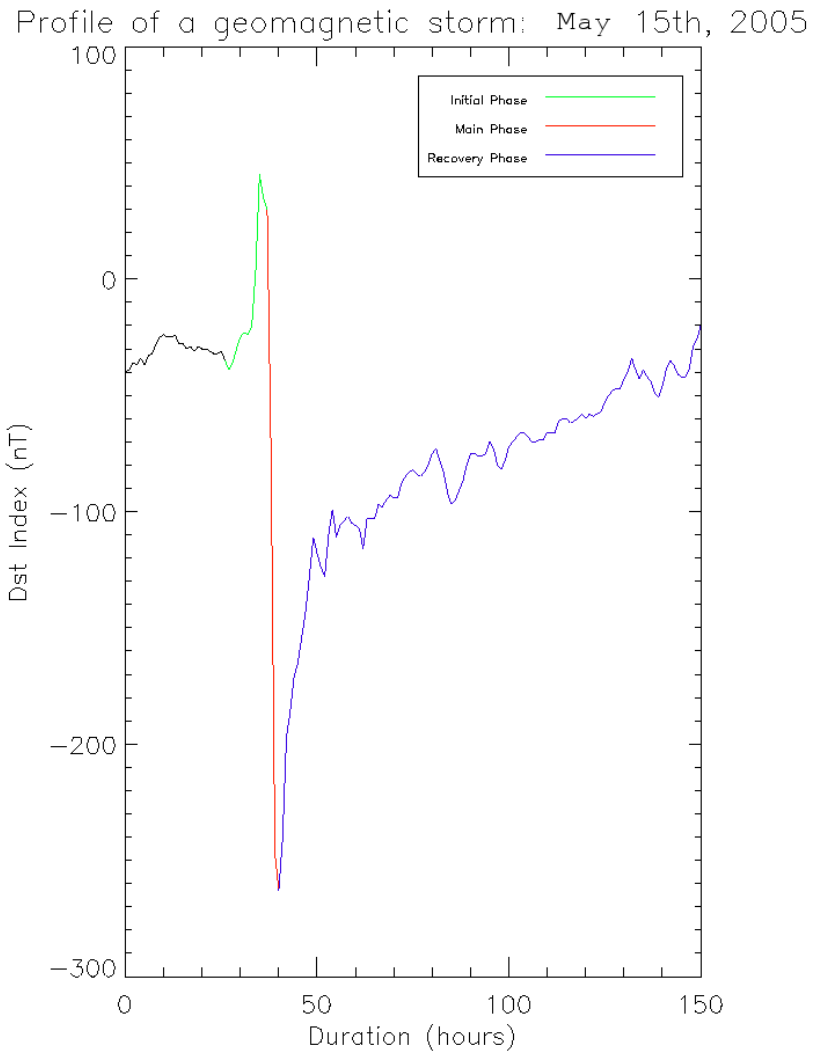

Figure 2.19: Dst index profile for the geomagnetic storm occurring on May 15^{th}, 2005. The initial phase is outlined in green, the main phase in red, and the recovery phase in blue.

$\leq$ Dst $\leq$ -50 nT), 'intense' (-200 nT $\leq$ Dst $\leq$ -100 nT), and 'big' ($\leq$-200 nT).

Phenomenon	CME-Driven Storms	CIR-Driven Storms
Phase of the solar cycle when dominant	solar maximum	declining phase
Occurrence pattern	irregular	27-day repeating
Calm before the storm	sometimes	usually
Storm sudden commencement (SSC)	common	infrequent
Mach number of the bow shock	moderate	high
Spacecraft surface charging	less severe	more severe
Ring current (Dst)	stronger	weaker
Dipole distortion	very strong	strong
Great aurora	sometimes	rare

Table 2.1: Abridged findings of characteristics of geomagnetic storms triggered by CMEs and CIRs analyzed by *Borovsky and Denton* (2006)

The interplanetary conditions related to geomagnetic storms have been extensively studied for the last two solar cycles. The storms where the main phase reaches Dst values below -100 nT and their associated solar wind conditions have been cataloged in numerous studies, e.g. *Zhang et al.* (2007); *Richardson et al.* (2006). Coronal mass ejections (CMEs) and corotating interaction regions (CIRs) have long been identified as the interplanetary causes of intense (Dst $\leq$-100 nT) geomagnetic storms (*Tsurutani and Gonzalez*, 1997; *Correia and de Souza*, 2005; *Denton et al.*, 2006; *Richardson et al.*, 2006, 2001). *Borovsky and Denton* (2006) presented a study of the solar wind and IMF parameters of two solar wind phenomena: CMEs and CIRs. Their main findings are summarized in Table 2.1. They observed that CME-driven geomagnetic storms are shorter in duration, have strong ring currents, tend to occur more often during solar maximum, and are more likely to include the presence of a SSC signature in the Dst profile. In contrast, CIR-driven storms are longer, have a weaker ring current, are unlikely to have an SSC signature or initial phase, and are more likely to be seen at solar minimum.

2.7.2 Substorms

Magnetospheric substorms are similar to geomagnetic storms. During times of heightened reconnection, open flux on the dayside is transported to the tail region. During this time the polar cap (the ionospheric foot print of the open flux) will increase in size. The plasma sheet thins and the tail current moves closer to the Earth. Increased reconnection in the thinned plasma sheet causes bursts of highly energized plasma to be accelerated back towards the Earth. This energized plasma is injected into the ring current, where it can be accelerated along the magnetic field lines into the ionosphere creating the visual aurora. Similar to geomagnetic storms, substorms also have three phases: the growth phase, the expansion phase, and the recovery phase. Unlike their larger geomagnetic storm counter parts which are a global phenomenon and can be seen everywhere at once, substorms are more localized. Substorms also tend to be shorter in duration and weaker in magnitude (according to the Dst profile), lasting minutes to hours instead of days. Substorms frequently (although not always) occur during the recovery phase of a geomagnetic storm when reconnection in the tail has slowed and open flux has built up in the tail. However, substorms are also seen in the absence of storm activity.

Chapter 3

Data Sets and Instruments

Three data sets are used in this study of geomagnetic storms from both an interplanetary and an Earth-based view point. To quantify the storm time geomagnetic activity level, the Dst index is commonly used e.g. *Akasofu and Chapman* (1963a,b); *Perreault and Akasofu* (1978). However, in this thesis the Symmetric-H (Sym-H) index, which is a proxy for the Dst, has been used because of its higher temporal resolution. The ionospheric convection velocities during storms, the Super Dual Auroral Radar Network (SuperDARN) (*Greenwald et al.*, 1995; *Ruohoniemi and Baker*, 1998; *Chisham et al.*, 2001) was utilized. To identify the solar wind and IMF features, the OMNIweb database (*http://nssdc.gsfc.nasa.gov/omniweb*) was used. Each of these systems is described below in detail.

3.1 Solar wind and IMF observations

The interplanetary data were obtained from the OMNIweb database. The OMNIweb database contains multi-spacecraft data spanning a 36 year interval. The database provides key parameters such as the IMF and the solar wind proton velocity. OMNIweb provides data that have been processed using the phase front propagation technique of *Weimer et al.*(2003, 2004) that time-shifts the spacecraft data to 17 R_e upstream of Earth, close to the nose of the bow shock. This enables better comparisons of upstream solar wind and IMF measurements and geomagnetic observations. The data for the present study included the main instruments used to measure solar wind and IMF parameters from the ACE, WIND, and IMP 8 satellites. In 2000, the magnetometers aboard the IMP8 satellite failed, and WIND and ACE became

the main providers of IMF information. The ACE satellite is positioned at the L1 Lagrangian point while the WIND satellite's orbit is much more complex ranging from the L1 position to the L2 position.

The time shifted IMF and solar wind data are available for public usage through the Space Physics Data Facility ($http://cdaweb.gsfc.nasa.gov/istp\_public/$). The key IMF and solar wind parameters of interest to this thesis are: IMF components, solar wind proton flow speed, solar wind dynamic pressure (calculated using $P_{dyn} = 2 \times 10^{-6} \times N_p \times V_p^2$ where the subscript p denotes protons, N is the density and V is the flow speed), bow shock position, and the calculated interplanetary electric field.

3.2 Ground-based Magnetic Sensing

As described in the previous chapter, magnetometers measure the geomagnetic field in a localized area. Chains of magnetometers are stationed across the globe to enable large scale observations of changes in the ionospheric current systems by recording the changes in the geomagnetic field strength. Since the ionospheric current system is closely coupled to the magnetosphere, fluctuations in the solar wind and IMF can greatly affect the ionospheric currents.

It is useful to understand what the global magnetic field strength is in order to determine if the measured geomagnetic activity comes from a localized disruption or a global change. A localized region of geomagnetic activity will not appear in an index that is an average of globally placed magnetometers of similar latitudes. Until recently, the most common tool for monitoring large scale changes in the geomagnetic field was the Dst index. However, the higher resolution Sym-H index is now used with increasing frequency.

3.2.1 The Disturbed Storm Time Index

The Dst is used to monitor the changes in the horizontal component (H-component) of the geomagnetic field. The Dst index, which has 1 hour time resolution, is derived from 4 mid-latitude magnetometers (shown in black in Figure 3.1 with locations

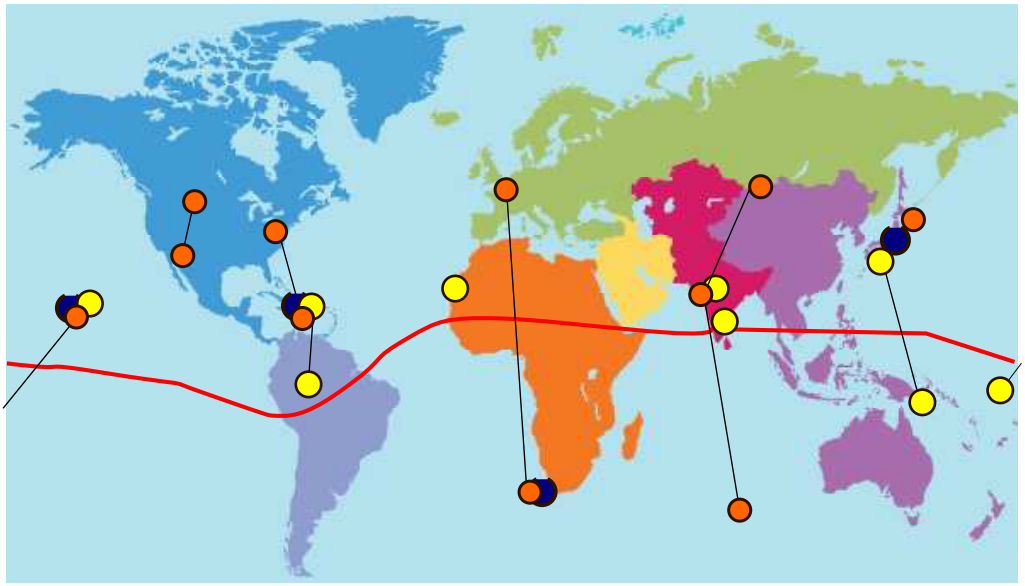

Figure 3.1: Geographical locations of the Dst, Sym-H, and SC magnetic observatories. Magnetic equator is represented by the solid red line bisecting the image. Observatories reporting for the Dst index calculation are shown by the blue dots, Sym-H by orange dots, and the SC observatories by the yellow dots. The black line connecting pairs of observatories indicates the conjugate observatory used in the event data are missing from the primary observing location.

outlined in Table 3.1). The annual baseline H-component value is calculated from the 5 magnetically 'quietest' days of the year. The hourly change in the H-component is then calculated by subtracting the baseline (mean) value from the average value observed by a given observatory during that hour.

$$\Delta H(t) = H_{obs} - H_{base}(t) \tag{3.1}$$

The solar quiet time current, S_q, is a current generated by tidal motion and, while always present, is a prominent feature in quiet geomagnetic conditions. Its perturbation of the geomagnetic field must be removed from the data from each observatory. The baseline S_q is calculated each month for the five quietest days of the month from all contributing observatories. The disturbance variation, D(t), is then calculated by removing the S_q variation from the observed change in the H-component:

Dst Observatory	Geographic longitude	Geographic latitude
Hermanus	19.22^o	-34.40^o
Honolulu	201.98^o	21.32^o
Kakioka	140.18^o	36.23^o
San Juan	293.88^o	18.11^o

Table 3.1: Magnetic observatory locations used in the calculation of the global magnetic activity Dst index.

$$D(t) = \Delta H(t) - S_q(t) \tag{3.2}$$

The mean value D(t) value of the 4 contributing observatories is then normalized to the magnetic dipole equator and summed to calculate the Dst value:

$$Dst(t) = \sum_{i=1}^{i=4} \frac{D_i(t)}{\cos(\phi_i)} \tag{3.3}$$

where ϕ_i is the latitude. Traditionally, the Dst index is used to observe the magnetospheric ring current variations that are a feature of geomagnetic storms.

3.2.2 The Symmetric-H component index

A higher resolution H-component profiling is available using the 1-minute Symmetric Disturbance index (*Wanliss and Showalter*, 2006). This Sym-H index has become an acceptable alternative to the Dst index for high resolution monitoring (*Menvielle et al.*, 2011). Both indices are derived in the same manner from stations that are similar in latitude. The advantage of using the Sym-H index over the Dst resides in the much higher temporal resolution the Sym-H index provides. Sym-H uses six mid-latitude magnetometers. The six magnetometers are shown in orange in Figure 3.1 and their geographic coordinates are listed in Table 3.2. In the event that the magnetometer from a primary magnetic observatory is not recording data (due to maintenance or repair) data from a conjugate magnetic observatory is used.

Observatory	Geographic longitude	Geographic latitude
Fredericksburg	38.200^o	282.630^o
Boulder	38.2^o	282.63^o
Tucson	32.17^o	249.27^o
Memambetsu	43.91^o	144.189^o
Urumqi	43.80^o	87.7^o
Alibag	18.638^o	72.872^o
Martin de Vives	-37.796^o	19.225^o
Chambon-la-Foret	48.025^o	2.261^o
Hermanus	19.22^o	-34.40^o
Honolulu	201.98^o	21.32^o
San Juan	293.85^o	18.11^o

Table 3.2: Magnetic Observatory locations used in the calculation of the global magnetic activity Sym-H index.

These conjugate observatories are represented in Figure 3.1 as a line connecting the observatories. The derivation of the Sym-H component is nearly identical to the Dst. The main difference between the two indices, aside from temporal resolution, is that the Sym-H index uses the dipole coordinate system and 6 magnetometers are considered instead of just 4 (*Wanliss and Showalter*, 2006).

3.2.3 Sudden Commencement Events

Abrupt, on the order of minutes, changes in the geomagnetic indices due to changes in the magnetospheric or ionospheric current systems are quite common. Changes in the Dst and Sym-H can arise from changes in the auroral or equatorial currents. Similarly, shocks in the solar wind dynamic pressure can also cause global increases in the H-component of the geomagnetic field. The phases of a geomagnetic storm were explained in section 2.7.1 and the start of the initial phase was defined as

a storm sudden commencement (SSC). From an interplanetary viewpoint, sudden commencements (SCs) are a result of a jump in the solar wind dynamic pressure impacting the front of the magnetosphere. Solar wind dynamic pressure (ΔP_{dyn}) pulses compress the dayside magnetosphere and cause the magnetopause current to intensify and move earthward (*Akasofu and Chapman*, 1963a,b; *Perreault and Akasofu*, 1978). This increase in the magnetopause current increases the intensity of the geomagnetic field on the dayside. This increase is evident by the sharp positive increase in the Dst (and Sym-H) index. The 1-hour temporal resolution of the Dst index is not sufficient to accurately measure the arrival of the SC, which occurs in a matter of minutes. Furthermore, the position of the Dst magnetic observatories at low, almost equatorial, latitudes increases their chance of observing changes in ionospheric currents which may be mistaken for a SC. The Sym-H index is also subject to errors for the determination of SC events. Although the Sym-H index has the appropriate time resolution, its magnetic observatories are situated at mid-latitudes. Occasionally, changes in ionospheric currents seen at mid-latitudes could be mistaken for SC events.

To remedy the above difficulties, the actual SC determination is made instead from magnetograms recorded at low-latitude observatories far enough from the equator to avoid contamination from equatorial current systems. The low-latitude region is this way predominately removed from disturbances caused by currents in the auroral (mid-high latitude) and equatorial zones. A SC is a global phenomenon and should appear in all magnetic observatories, regardless of longitude. In order to measure a SC, five low-latitude observatories are positioned at approximately equally spaced longitudes around the globe. The positions of the five primary observatories are shown in Figure 3.1 in yellow. If the characteristic 'step-like' perturbation of the H-component during a SC is detected in the magnetograms from at least 3 of the 5 observatories, then it is declared a SC event. If solar wind data are available, a confirmation of the presence of a geomagnetic field compression produced by a solar wind dynamic pressure pulse is used to further validate the event. By requiring 3 out of the 5 observatories to record the event, local disturbances are more likely to

be rejected.

An official list of SC events is calculated by the Observatori de l'Ebre in Spain (*http* : *//www.obsebre.es/php/geomagnetisme/variaciorap.php*). Each month, an additional 30 magnetic observatories share their data with the Observatori de l'Ebre. In the event of a questionable, or unclear, SC, the Observatori de l'Ebre will use these additional magnetograms to augment their data from the five low-latitude observatories. Once the presence of a SC has been firmly established, the Observatori de l'Ebre publishes a monthly listing of all SCs including the SC start time and duration, the mean deflection value, and clarity of event code.

Once the SC event timing has been established, the Dst index can be used to determine the presence of a geomagnetic storm within an hour of the SC. If there is a geomagnetic storm present soon after the SC, the event is labelled a Storm Sudden Commencement (SSC) which then marks the onset of the initial phase of the geomagnetic storm, as outline in section 2.7.1. If no magnetic storm follows the SC, the event is labeled a Sudden Impulse (SI) event. After 2008, SC listings provided to the IAGA by the Ebre Observatory classify SCs as either SIs or SSCs and this step is no longer required.

For further clarification, a cartoon profile of the Sym-H index for both a SSC and a SI type event is presented in Figure 3.2. The SI type event in Figure 3.2(a) is evident as a sharp increase in Sym-H indicating the SC with an elevated Sym-H value for a brief period, generally on the order of hours, before descending back to the baseline value. The SSC event presented in Figure 3.2(b) contains the same initial perturbation profile, except that after the initial increase in Sym-H the index decreases according to the typical profile of a geomagnetic storm, as discussed in section 2.7.1.

Although the Dst and Sym-H indices are not used to identify and classify the SC, they can be used to analyze SC events. As mentioned, the SC is a global phenomenon and appears in all magnetometers at approximately the same time. Once the start time of the SC has been established, a search of Sym-H during the $\pm$ 10 minute interval surrounding the SC identifies the SC in the Sym-H index. Although the SC

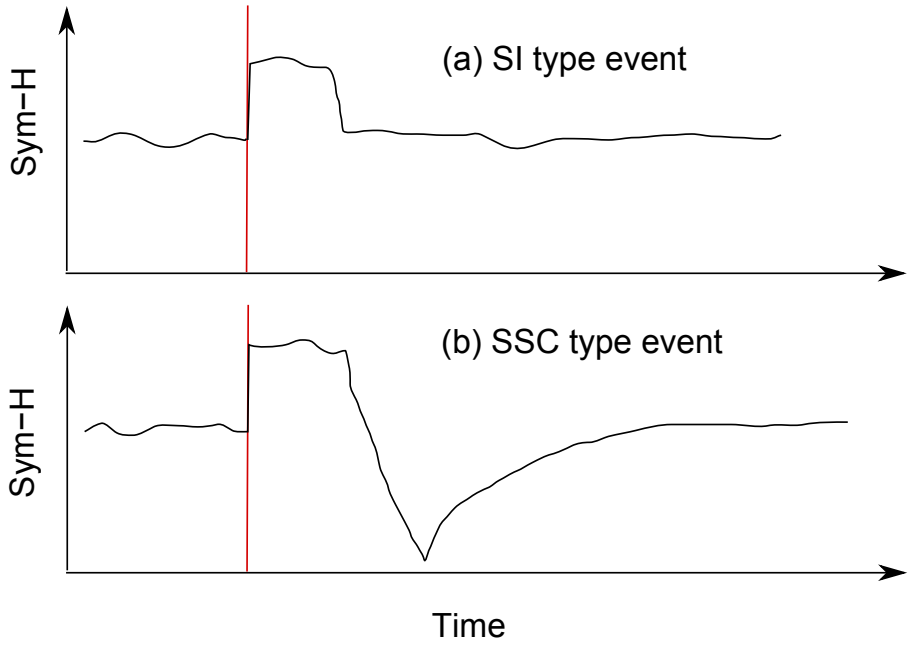

Figure 3.2: Cartoon of a SI and SSC type event using the Sym-H index. Index value is shown on the y-axis and time progresses along the x-axis. The vertical red line indicates the zero epoch reference marker.

signature can also be seen in the Dst index, care should be taken in any detailed analysis of events using this index owing to the Dst's low temporal resolution.

3.3 SuperDARN HF Radars

To study the ionospheric convection velocities during geomagnetic storms SuperDARN (*Greenwald et al.*, 1995; *Chisham et al.*, 2001) was utilized. SuperDARN monitors the mid- to high-latitude ionosphere and provides global ionospheric convection maps of the northern and southern hemispheres. SuperDARN was designed to provide continuous coverage of high-latitude **ExB** ionospheric plasma convection. SuperDARN is a high frequency coherent-scatter radar network capable of operating in the 8-20 MHz range. The data from nine northern hemisphere SuperDARN radars were used in this thesis. Each radar has a field of view (FOV) consisting of 16 sequentially scanned beam positions separated in azimuth by $\sim 3.24^{\circ}$ providing a full field

of view of 52^o. In standard operating mode, each beam consists of 75 range gates, each 45 km in length, with the first range gate starting 180 km from the radar site. Situated a short distance ahead or behind the main antenna array are 4 more antennas which allow for the determination of elevation angle of arrival of the returned signal using interferometry. The standard dwell time for each beam is 3 seconds, or 7 seconds depending on the scan mode, which enables a full 16-beam sweep every 1 or 2 minutes, respectively. This short dwell time is one of the primary benefits of these coherent scatter radars. Using a short dwell time enables maps of the plasma flow on a global scale every 1 to 2 minutes. The ionospheric signal received at the radar occurs from the scattering of radio waves from decameter ionospheric irregularities that are aligned with the geomagnetic field lines. The information received from each sounding pulse is then converted into the auto correlation function (ACF). From the ACF it is possible to determine ionospheric parameters such as Doppler shift, back scattered power, and spectral width. The Doppler shift of the received radar signal provides an estimate of the line-of-sight (l-o-s) velocity measurement. The l-o-s velocity data from all radars are processed and a global scale convection pattern is produced every one or two minutes (*Baker and Wing*, 1989; *Ruohoniemi and Baker*, 1998).

In the ionosphere, waves and structures produced in the plasma propagate perpendicular to the geomagnetic field lines. At E- and F-region heights in the high latitude ionosphere, the geomagnetic field is nearly vertical. Since the irregularities are aligned with the geomagnetic field, in order for the transmitted SuperDARN radio waves to be scattered back to the co-located receiver the radio wave needs to propagate perpendicular to the magnetic field lines. The SuperDARN radars achieve this by transmitting a signal in the 8-20 MHz frequency range. At this frequency, the radar waves refract in the ionosphere, and they can approach the irregularities perpendicularly to the geomagnetic field at ionospheric altitudes. At F-region heights, these irregularities drift at the **ExB** plasma velocity. SuperDARN provides a global view of convection patterns and structures. Optimally the SuperDARN radars are constructed in pairs with overlapping FOVs to enable the determination of the full

Radar Station	Geographic Coords		Geomagnetic Coords	
	latitude (^{o})	longitude (^{o})	latitude (^{o})	longitude (^{o})
Goose Bay	53.32N	60.46W	61.94N	23.02E
Kapuskasing	49.39N	82.32W	60.06	N 9.22W
Saskatoon	52.16N	106.53W	61.34N	45.26W
Prince George	53.98N	122.59W	59.88N	65.67W
Kodiak	57.60N	152.2W	57.17N	96.28W
Pykkvibaer	63.86N	19.20W	64.59N	69.65E
Hankasalmi	62.32N	26.61E	59.78N	105.53E
King Salmon	58.68N	156.65W	57.43N	100.51E
Wallops Island	37.93N	75.47W	30.63N	75.52E
Hokkaido	43.53N	143.61E	38.14N	145.67W
Inuvik	68.42N	133.5W	72.96N	28.17W
Rankin Inlet	62.82N	93.11W	72.96N	28.17W

Table 3.3: Geographic and geomagnetic coordinates for the nine northern hemisphere SuperDARN radars operating between the years 2000 and 2007 inclusive.

velocity vector. In practice, there are missing data, due either to the lack of radar coverage in the continental Russian sector or propagation effects, so an algorithm is used to fit the convection to an estimated harmonics model in order to construct overall flow patterns. The locations of the nine radars used in this thesis are outlined in table 3.3 and the FOVs of the radars are displayed in Figure 3.3.

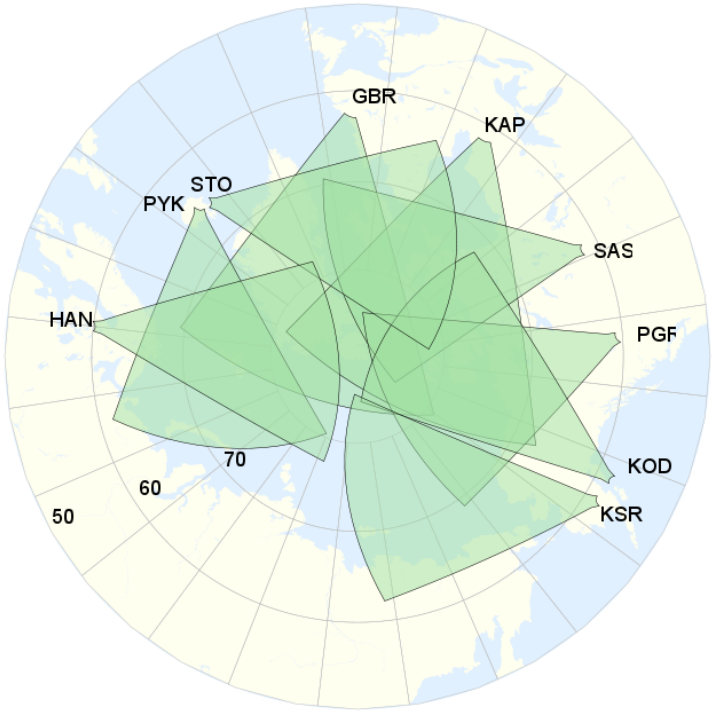

Figure 3.3: Field-of-view (FOV) of the nine SuperDARN radars operating in the northern hemisphere used during the time period of this study. Solid grey lines represent concentric lines of magnetic latitude of 50, 60, and 70 degrees. Radar ID corresponding to: Saskatoon (SAS), Goose Bay (GBR), Kapuskasing (KAP), Stokkseyri (STO), Hankasalmi (HAN), Pykkvibaer (PYK), Prince George (PGR), Kodiak (KOD), King Salmon (KSR).

3.3.1 FitACF theory and application

In order to determine spectral parameters such as Doppler shift, spectral width, and back scattered power of the ionospheric plasma, SuperDARN emits a series of radio

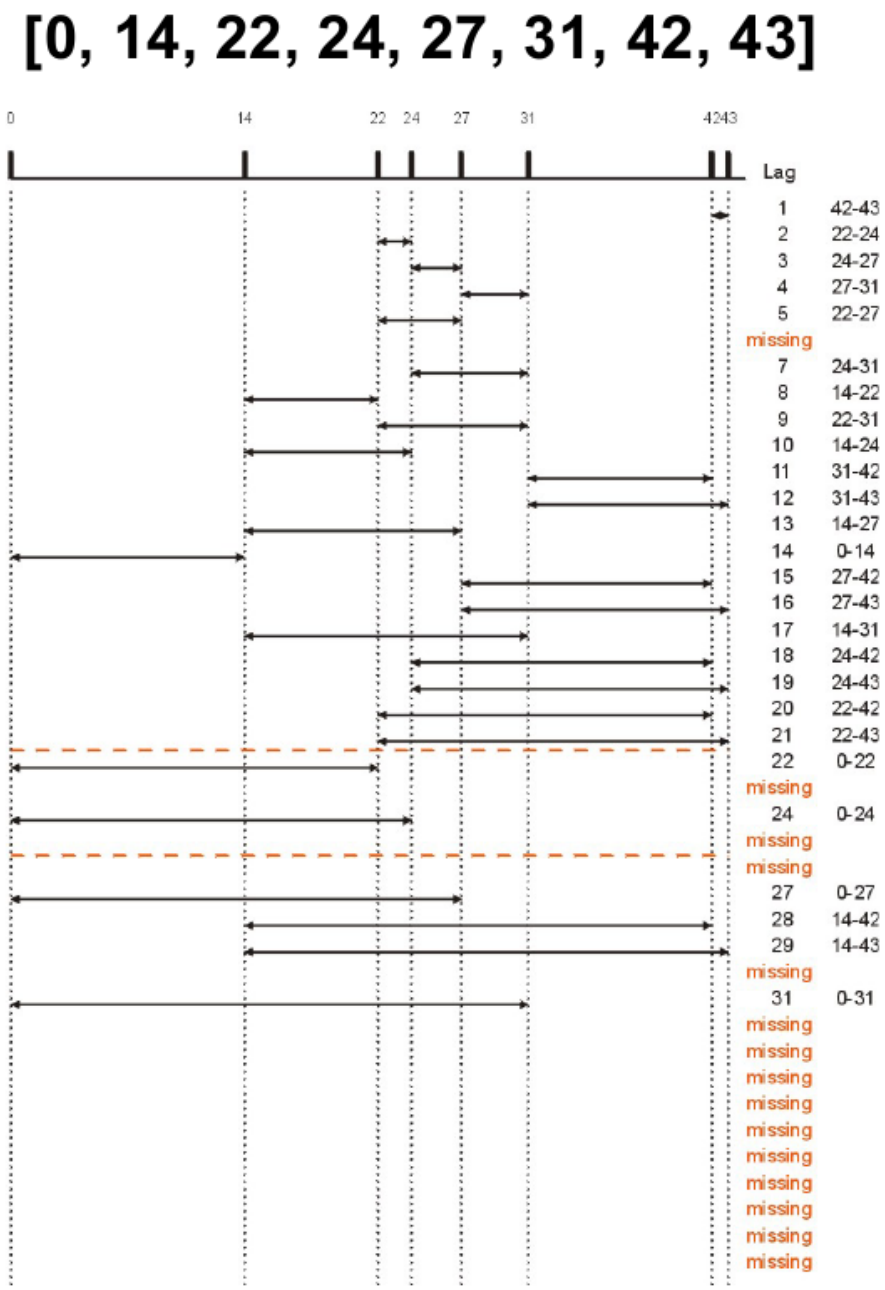

Figure 3.4: Current 8 pulse sequence known as 'katscan'. Transmission time is represented in μ seconds, progressing from the left of the page to the right, lag time increases from the top of the plot to the bottom.

wave pulses. SuperDARN uses an irregularly spaced multi-pulse sequence in order to ensure a sufficiently long decay time for the ACF. The received signal is processed into the ACF. This is a digitalized signal of the form $Ae^{i\omega t-\phi}$ which can be analyzed to determine the ionospheric spectral parameters. Each radar transmits a signal for 300 μs at intervals of t=0, 14, 22, 24, 27, 31, 42, 43 μs with a standard pulse separation (lag) time of $\tau = 1.8$ ms. This pulse sequence, and lag determination, is shown in Figure 3.4. This pulse sequence is repeated approximately 70 times for each beam position in a 2 minute scan. The multipulse sequence enables a high quality averaged ACF for processing. A program called 'fitacf' is used to determine spectral parameters such as Doppler shift, spectral width and back scattered power from the ACF without the need for a Fourier transform of the returned signal. Figure 3.5 shows the ACF for the Kapuskasing radar on November 24, 1998 on Beam 3, range gate 59 at 11:21 UT. The real and imaginary components of the ACF signal are presented in Figure 3.5(a) plotted against lag time. The decay envelope of the signal is outlined in red. The envelope decays with increasing lag. Figure 3.5(b) shows the phase of the ACF, $\Phi = \arctan(Im/Re)$ (where Im denotes the imaginary portion of the signal and Re the real portion), plotted against lag time. The slope of the phase is used to determine the Doppler velocity $< v_D >$ of the signal. From this it is possible to determine the phase (ϕ), the l-o-s Doppler velocity $< v_D >$, and the spectral width (w):

$$\Phi =< \omega_D > k\tau \tag{3.4}$$

$$< v_D >= \frac{c < \omega_D >}{4\pi f_{radar}} \tag{3.5}$$

$$w = \frac{2\beta c}{4\pi f_{radar}}, \tag{3.6}$$

where c is the speed of light,$< \omega_D >$ is the Doppler frequency, k is the wave number, β is a characteristic decay, and f_{radar} is the frequency used by the radar during a particular scan. Since the transmitter and receiver are co-located, the system cannot transmit a signal at the same time as it receives a signal. The pulse sequence has

a long time delay between the first transmitted pulse and the second transmitted pulse, approximately 14 τ. This time delay allows the antenna to receive echoes from the first pulse for all range gates before transmitting the second pulse. The first missing lags do not occur until lags 6τ and 23τ. This enables optimal sampling of the ACF signal and thus good determination of the Doppler shift, back scattered power, and spectral width of the plasma irregularities. Range aliasing can occur when the transmitted signal from two different range gates is received at the same time. In such cases the range gate with the highest lag zero power is used to determine from which range gate the signal is being returned and the other ACF sample is discarded.

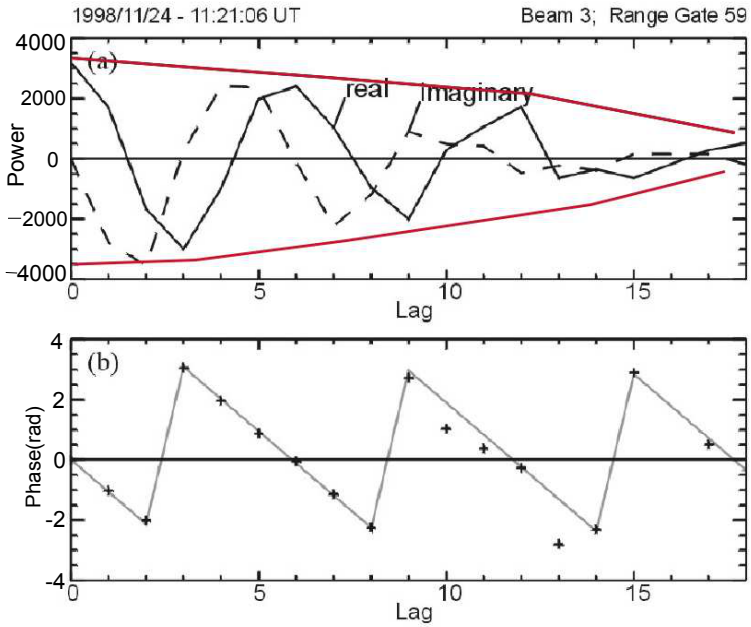

Figure 3.5: The auto correlation function. Panel (a) displays the real and imaginary part of the returned signal as a function of lag time. Panel (b) displays the phase of the ACF plotted against lag time.

The maximum, or 'alias', velocity that the radar can register is determined by the frequency of the transmitted pulse. The Doppler velocity is measured using the slope of the ACF phase. As seen in Figure 3.5(b), Φ can vary by $\pm\pi$. The maximum resolvable velocity is therefore $v_D = \frac{c}{4\pi f_{radar}}$. For example, the maximum velocity

that can be detected by a radar operating at a frequency of 10 MHz with a lag time, τ, of 1.5 ms would be $v = 4900$ m/s. A Lorentzian or Gaussian fit is applied to the ACF. The backscattered power of the signal is determined by the lag zero power of this fit. The spectral width is fitted to the decaying envelope of the ACF signal using either model with the help of equation 3.4.

3.3.2 Line-of-sight velocity mapping

Once the returned signal's ACF has been analyzed and key parameters such as Doppler shift, spectral width, and back scattered power are determined for each beam and range gate of the radar, the values are stored in a "fitacf" file in order to undergo further processing. As mentioned in Chapter 2, the backscatter observed is the result of coherent scatter from irregularities with wavelengths 1/2 the radar wavelength in a region where the signal propagates orthogonally to the geomagnetic field lines. The Doppler shift provides an estimate of the line-of-sight (l-o-s) **ExB** velocity along the beam direction. The backscatter data derived from the ACFs can be further processed and mapped directly onto a gridded geomagnetic map in 1 or 2 minute intervals. This gridded map is defined by a spatial scale of 1^o latitude which is the equivalent of 111 km projected onto the Earth's surface. The number of gridded cells for each latitude is determined by $n(\theta) = 360^\circ \sin(\theta)$, where θ is the magnetic co-latitude, and n is rounded off to the nearest integer (*Ruohoniemi and Baker*, 1998). Only scatter from ionospheric sources are included as ground scatter has been flagged and rejected at this point in the processing technique. The first 10 range gates were removed at this stage in the process due to the dominance of non $\mathbf{E} \times \mathbf{B}$ drifting E-region echoes in range gates 1-10. Echoes between 180 to 450 km from radar are statistically more likely to be E-region echoes as the radio waves pass through to the F region. L-o-s velocity data from each station are averaged to an altitude-adjusted corrected geomagnetic (AACGM) latitude versus longitude grid and stored in a '*.map' file. Gridded l-o-s vectors on a latitude vs longitude graph are presented in Figure 3.6 for the date of April 7^{th}, 2000 at 00:10 - 00:12 UT. In this figure, the l-o-s velocity vectors from each radar station are overlaid on a magnetic

latitude/magnetic local time (MLT) plot. Magnetic local noon is towards the top of the page and dawn is to the right. The velocity vectors are represented by a dot at the base of the vector and a line emanating in the direction of motion. The color and length of the plotted vector are an indication of flow strength. A color bar indicating the color for each velocity magnitude is shown in the upper left corner of the map. The averaged IMF orientation in the y-z Geocentric Solar Magnetospheric System (GSM) plane during this 2 minute interval is shown in dial in the upper right corner. It is important to note that the IMF orientation has no bearing on the mapping technique at this stage and is shown purely for informational purposes.

To create the 2-D convection maps the gridded l-o-s velocity vectors are then processed using a complex data amalgamation technique. This technique uses statistical convection data to create a convection map that is as similar to the l-o-s velocity measurements as possible. Using spherical harmonic functions, the program undergoes many iterations of the functions coefficients to best fit the convection map data to the original l-o-s velocity measurements. This fitting is constrained by *a priori* statistical convection model parametrized by the orientation of the IMF. This statistical model relies strongly on IMF conditions during the 2 minute interval to determine which type of convection pattern is likely to occur (statistical convection patterns were shown in Figure 2.9). As already seen in Figure 3.3, although SuperDARN FOV covers a large portion of the northern hemisphere, there are wide gaps over continental Russia. In the event of missing data, either from a gap in the radar coverage or absent data from operational radars, the approach used by the model approximates the resulting convection map based on the statistical model. It is therefore important to consider maps with a large number of data points to obtain the most accurate and realistic representation of measured ionospheric convection patterns. Convection maps with just a few measured velocity components should be considered to be largely influenced by the model and not a result of measured ionospheric convection velocities. The convection pattern produced from the gridded l-o-s velocity vectors shown in Figure 3.6 is in Figure 3.7. The solid and dashed black lines represent an equipotential contour overlaid upon the convection with negative

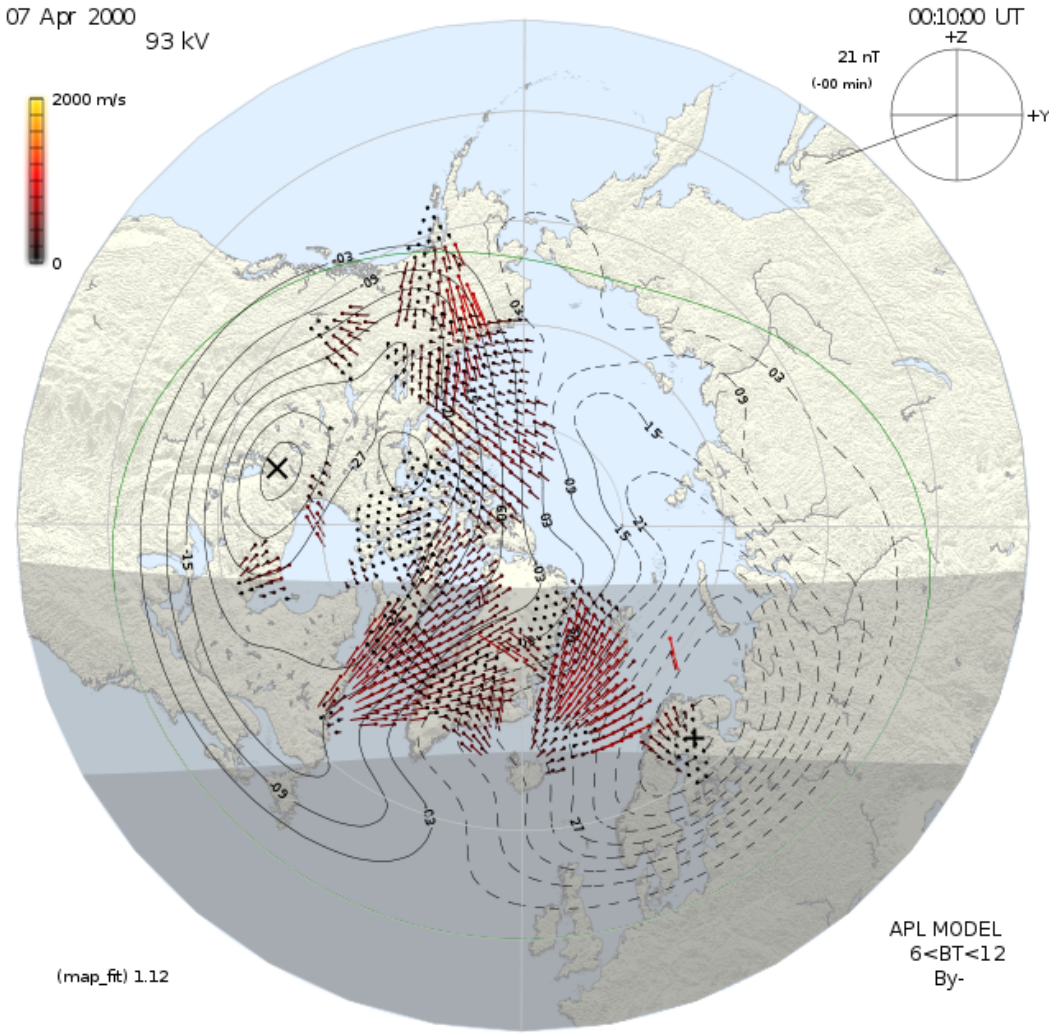

Figure 3.6: Gridded line-of-sight velocity vectors aligned to the AACGM grid for April 7^{th}, 2000 at 00:10 - 00:12 UT.

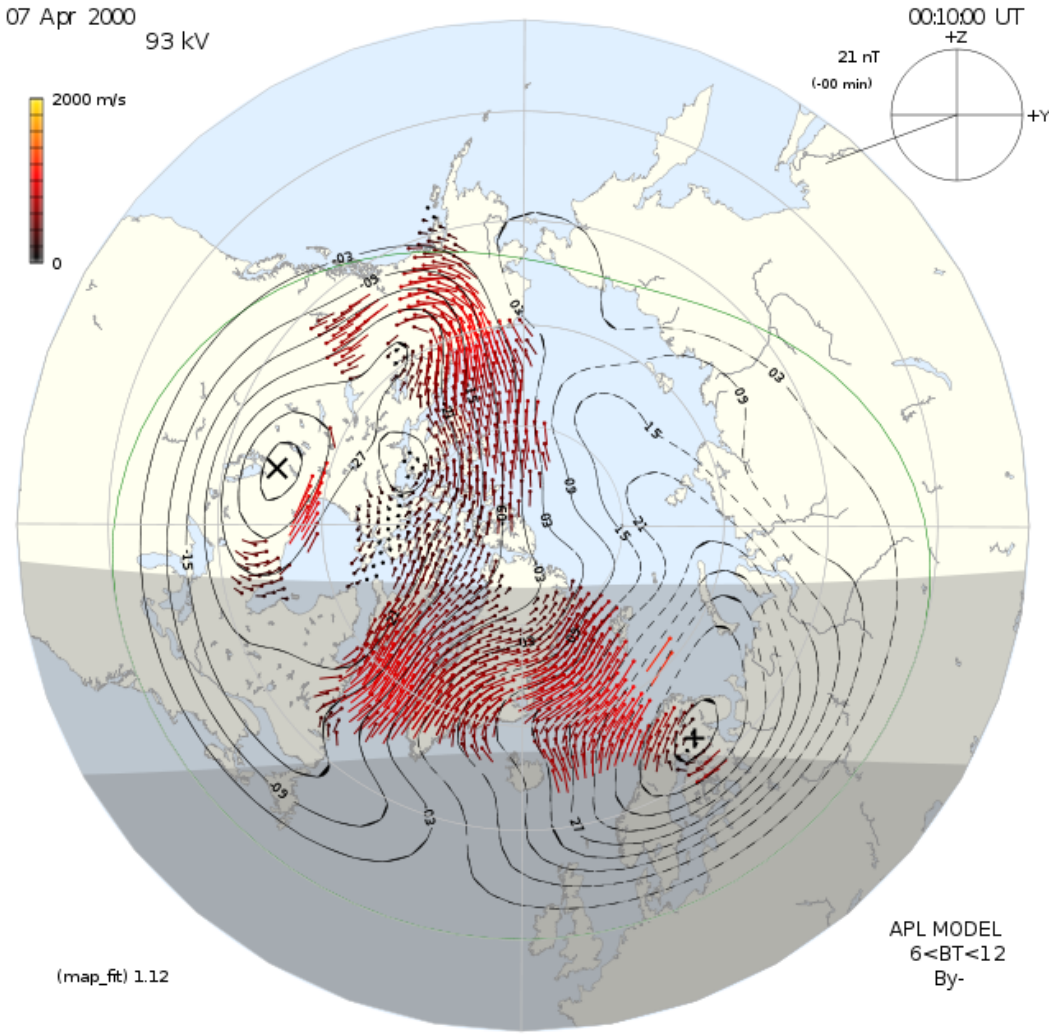

Figure 3.7: Ionospheric convection map for April 7^{th}, 2000 at 00:10 - 00:12 UT.

voltages shown by the solid line and positive voltages shown by the dashed line. The IMF orientation and magnitude used for the convection model is displayed in the upper right hand corner of the map. At this point the IMF has been used in the convection mapping model to constrain, via the a priori statistical convection pattern, the equipotential contours in the region where there are no data available. The SuperDARN cross polar cap potential difference is obtained by subtracting the maximum and minimum voltages in the convection map, in this case the voltages at the center of the positive and negative equipotential contours marked by a plus sign (high V) and an x (low V). In the region where there is a high number of vectors, the fitted contours are well constrained by measurements and are a more reliable representation of the actual convection pattern than the regions where there are no data points. The velocity magnitudes are represented by the color bar in the upper left hand corner of the figure. The green solid line encircling the equipotential map contours is called the Heppner-Maynard boundary (HMB) and represents zero-flow boundary at the equatorward edge of the convection pattern. The HMB is set by the user when performing the convection mapping. These convection maps provide a good estimate of the overall **ExB** ionospheric plasma drift occurring at approximately 300 km altitude in the northern or southern hemisphere.

3.4 E- and F-region Instabilities

As discussed in the previous subsections, SuperDARN relies on the generation of field-aligned irregularities for the generation of echoes scattered by the ionosphere. The main generation mechanism for instabilities in the F region is thought to be the Gradient-drift Instability (GDI). The two main generation mechanisms for irregularity formation in the E region are a different version of the Gradient-drift instability and, for stronger electric fields, the Farley-Buneman instability.

3.4.1 The Gradient Drift Instability

The geometry required to produce the GDI in the F-region is presented in Figure 3.8(a). Consider the interface between 2 regions of different densities with **B** in the positive z-direction out of the page. In the simplest case, an ambient electric field is assumed to be perpendicular to the density gradient. Plasma density enhancements are more electrically conductive and therefore introduce a perturbed electric field, $\mathbf{E}_1$, in a direction opposite to the ambient field. In the presence of the magnetic field, a perturbed drift, $\mathbf{E}_1 \times \mathbf{B}$, then occurs towards the bottom of the page for the geometry in Figure 3.8. The higher density plasma then moves into the lower density region. As seen in Figure 3.8(c), for an initial sinusoidal perturbation the perturbed electric field causes the larger structure to break down into narrow 'fingers'. Given enough time, these elongated fingers will separate, forming multiple high density 'blobs' in the low density regions and 'holes' in the high density regions. If the high density region has moved far enough into the low density, the density contrast is high. This is said to be an "unstable" process. As radars are Fourier analyzing the plasma, the steeper the slope, the more visible the blobs and holes are to coherent systems such as SuperDARN.

Mathematically, the F-region GDI (also called the Interchange or Universal instability) can be derived as follows. As is usually done, chemistry will be neglected (*Kelley*, 1989; *Keskinen and Ossakow*, 1982). This is acceptable because changes in chemistry occur on a much longer timescale than growth rate times for the instability. First consider the continuity equation:

$$\frac{\partial n_\alpha}{\partial t} + \nabla \cdot (n_\alpha \mathbf{v}_\alpha) = 0, \tag{3.7}$$

where α represents either ions or electrons, n refers to density, and $\mathbf{v}$ refers to drift velocity. The orientation of the density gradient, magnetic field, and electric field are those that were considered in the above description of the GDI process. $\mathbf{E}$, n, and $\mathbf{v}$ are perturbed such that $n = n_o + n_1$, $\mathbf{E} = \mathbf{E_o} + \mathbf{E_1}$, and $\mathbf{v} = \mathbf{v_0} + \mathbf{v_1}$. The subscript α has been dropped for this derivation and only electrons need to be considered

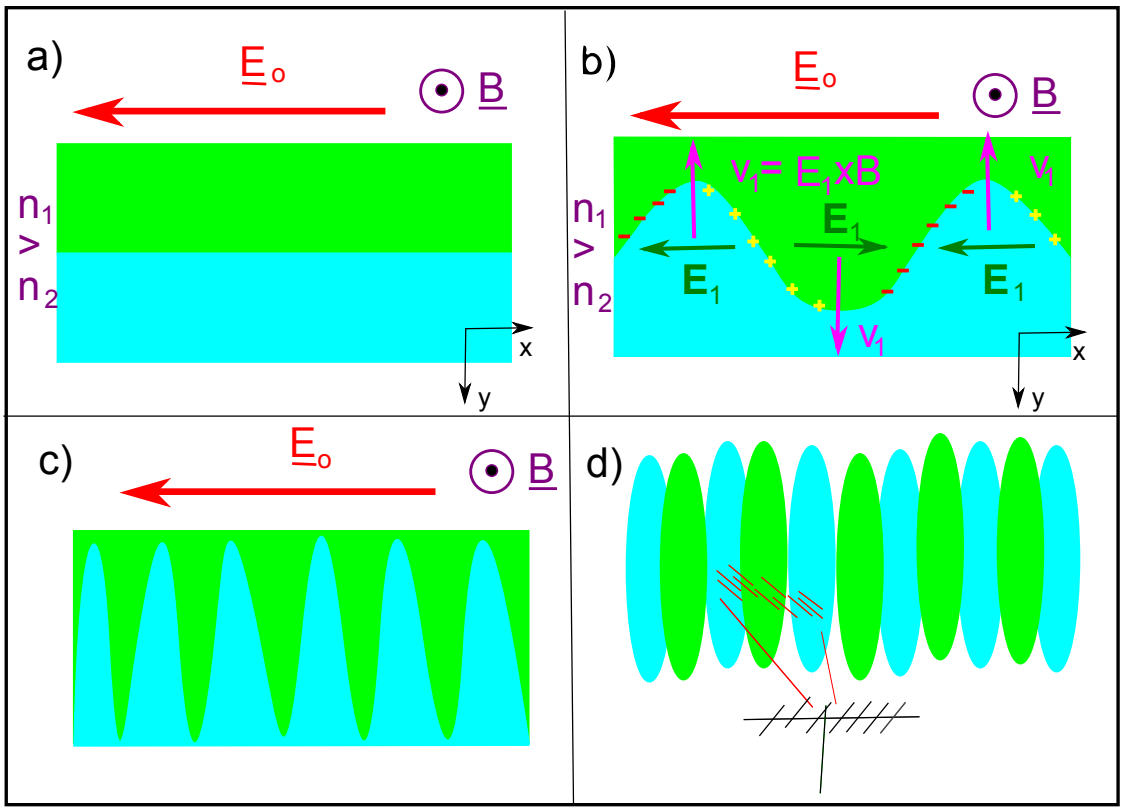

Figure 3.8: Physical mechanism for the Gradient-drift instability. A) t=t_o: Two regions of differing plasma density with $n_1 > n_2$. B) t=t_1: A perturbation has been applied to the plasma interface creating a perturbation electric field, $\mathbf{E}_1$. This electric field coupled with the ambient magnetic field causes region of low density plasma (n_2) to move into regions of higher density plasma (n_1) and vice versa. c) t=t_2: at a later time the plasma begins to mix into elongated blob-like structures. d) Coherent radars transmit signals that are scattered off the edges of the blob-like structures.

initially. Let $\mathbf{v_0} = (\mathbf{E_0} \times \mathbf{b})/B$ where $\mathbf{b}$ is a unit vector along the magnetic field, $|\mathbf{v_0}| >> |\mathbf{v_1}|$, and $n_0 >> n_1$. Note that $\nabla \cdot \mathbf{v}_o = 0$.

Consider the first order perturbation, neglecting nonlinear terms:

$$\frac{\partial}{\partial t}(n_1) + \nabla \cdot (n_1 \mathbf{v_0} + n_0 \mathbf{v_1}) = 0$$

$$\frac{\partial}{\partial t}(n_1) + \cancelto{0}{n_1 \nabla \cdot \mathbf{v_0}} + \mathbf{v_0} \cdot \nabla n_1 + n_0 \nabla \cdot \mathbf{v_1} + \mathbf{v_1} \cdot \nabla n_0 = 0$$

Next, divide through by n_0:

$$\frac{1}{n_0}\frac{\partial}{\partial t}(n_1) + \mathbf{v_0}\cdot\frac{\nabla n_1}{n_0} + \nabla\cdot\mathbf{v_1} + \mathbf{v_1}\cdot\frac{\nabla n_0}{n_0} = 0 \tag{3.8}$$

Let $\mathbf{H} = \frac{\nabla n_0}{n_0}$. Consider a change of variables from n_1 to n_1/n_0:

$$\nabla\left(\frac{n_1}{n_0}\right) = \frac{1}{n_0}\nabla n_1 - \frac{n_1}{n_0}\left(\frac{\nabla n_0}{n_0}\right)$$
$$\frac{\nabla n_1}{n_0} = \nabla\left(\frac{n_1}{n_0}\right) + \left(\frac{n_1}{n_0}\right)\frac{\nabla n_0}{n_0} = \nabla\left(\frac{n_1}{n_0}\right) + \left(\frac{n_1}{n_0}\right)\mathbf{H} \tag{3.9}$$

Similarly:

$$\frac{\partial}{\partial t}\left(\frac{n_1}{n_0}\right) = \frac{1}{n_0}\frac{\partial}{\partial t}n_1 - \left(\frac{n_1}{n_0}\right)\left(\frac{1}{n_0}\frac{\partial}{\partial t}n_0\right)$$
$$\frac{1}{n_0}\frac{\partial}{\partial t}n_1 = \frac{\partial}{\partial t}\left(\frac{n_1}{n_0}\right) + \left(\frac{n_1}{n_0}\right)\left(\frac{1}{n_0}\frac{\partial}{\partial t}n_0\right) \tag{3.10}$$

The zeroth order balance of equation 3.7 becomes:

$$\frac{\partial}{\partial t}(n_0) + \nabla\cdot(n_0\mathbf{v_0}) = 0$$
$$\frac{\partial}{\partial t}(n_0) = -\cancelto{0}{n_0\nabla\cdot\mathbf{v_0}} - \mathbf{v_0}\cdot\nabla n_0$$
$$\frac{\partial}{\partial t}(n_0) = -\mathbf{v_0}\cdot\nabla n_0 \tag{3.11}$$

Next, substitute equation 3.11 into equation 3.10:

$$\frac{1}{n_0}\frac{\partial}{\partial t}n_1 = \frac{\partial}{\partial t}\left(\frac{n_1}{n_0}\right) + \frac{n_1}{n_0}\left(\frac{1}{n_0}\right)(-\mathbf{v_0}\cdot\nabla n_0)$$
$$\frac{1}{n_0}\frac{\partial}{\partial t}n_1 = \frac{\partial}{\partial t}\left(\frac{n_1}{n_0}\right) - \frac{n_1}{n_0}(\mathbf{v_0}\cdot\mathbf{H}) \tag{3.12}$$

Substituting equations 3.9 and 3.12 into equation 3.8 yields:

$$\left[\frac{\partial}{\partial t} + \mathbf{v_0}\cdot\nabla\right]\left(\frac{n_1}{n_0}\right) = -\nabla\cdot\mathbf{v_1} - \mathbf{v_1}\cdot\mathbf{H} \tag{3.13}$$

Consider the first term on the right hand side of equation 3.13 : $\nabla\cdot\mathbf{v_1}$

$$\mathbf{v_1} = -\frac{\nu_e}{\Omega_e}\frac{\mathbf{E_1}}{B} + \frac{\mathbf{E_1}\times\mathbf{B}}{B^2}$$
$$\nabla\cdot\mathbf{v_1} = \frac{\nu_e}{\Omega_e}\nabla\cdot\frac{\mathbf{E_1}}{B} + \nabla\cdot\cancelto{0}{\left(\frac{\mathbf{E_1}\times\mathbf{B}}{B^2}\right)} \cong 0 \tag{3.14}$$

Applying equation 3.14 to equation 3.13 and using $\frac{\nu_e}{\Omega_e} << 1$ gives:

$$\left[\frac{\partial}{\partial t} + \mathbf{v_0} \cdot \nabla\right]\left(\frac{n_1}{n_0}\right) = -\mathbf{v_1} \cdot \mathbf{H} = -\frac{\mathbf{E_1} \times \mathbf{B}}{B^2} \cdot \mathbf{H} \tag{3.15}$$

3.4.2 Divergence of J = 0

In order to determine the relationship between the perturbed electric field, $\mathbf{E}_1$, and the perturbed density, n_1, a little further explanation is needed. Consider the divergence of the current $\mathbf{J}$:

$$\begin{aligned}
\frac{\nabla \cdot \mathbf{J}}{q} &= \nabla \cdot (n(\mathbf{v}_i - \mathbf{v}_e)) \\
&= \nabla \cdot (n_0(\mathbf{v}_{i1} - \mathbf{v}_{e1}) + n_1(\mathbf{v}_{i0} - \mathbf{v}_{e0})) \\
&= (\mathbf{v}_{i1} - \mathbf{v}_{e1}) \cdot \nabla n_o + n_o \nabla \cdot (\mathbf{v}_{i1} - \mathbf{v}_{e1}) \\
&\quad + n_1 \nabla \cdot (\mathbf{v}_{i0} - \mathbf{v}_{e0}) + (\mathbf{v}_{i0} - \mathbf{v}_{e0}) \cdot \nabla n_1
\end{aligned} \tag{3.16}$$

The first term on the right hand side of the above equation is proportional to $\frac{\nu_i^2}{\Omega_i^2}$, which is small in the F-region can be neglected. The three other terms in the above equation can be simplified to:

$$\begin{aligned}
n_o \nabla \cdot (\mathbf{v}_{i1} - \mathbf{v}_{e1}) &= n_o \nabla \cdot (\mathbf{v}_{i1}) \\
&= \frac{\nu_i}{\Omega_i} n_o \nabla \cdot \frac{\mathbf{E}_1}{B} \\
n_1 \nabla \cdot (\mathbf{v}_{i0} - \mathbf{v}_{e0}) &= n_1 \nabla \cdot (\mathbf{v}_{i0}) \\
&= \frac{\nu_i}{\Omega_i} n_1 \nabla \cdot \frac{\mathbf{E}_o}{B} \\
(\mathbf{v}_{i0} - \mathbf{v}_{e0}) \cdot \nabla n_1 &= \frac{\nu_i}{\Omega_i} \frac{\mathbf{E}_o}{B} \cdot \nabla n_1
\end{aligned} \tag{3.17}$$

Substituting these approximations back into equation 3.16 yields:

$$\begin{aligned}
\frac{\nabla \cdot \mathbf{J}}{q} &= \frac{\nu_i}{\Omega_i} n_o \nabla \cdot \frac{\mathbf{E}_1}{B} + \frac{\nu_i}{\Omega_i} n_1 \nabla \cdot \frac{\mathbf{E}_o}{B} + \frac{\nu_i}{\Omega_i} \frac{\mathbf{E}_o}{B} \cdot \nabla n_1 \\
&= \frac{\nu_i}{\Omega_i} \left[n_o \nabla \cdot \frac{\mathbf{E}_1}{B} + n_1 \nabla \cdot \frac{\mathbf{E}_o}{B} + \frac{\mathbf{E}_o}{B} \cdot \nabla n_1 \right] \\
&= \frac{\nu_i}{\Omega_i} \left[\nabla \cdot \left[n_o \frac{\mathbf{E}_1}{B} \right] + \nabla \cdot \left[n_1 \frac{\mathbf{E}_o}{B} \right] - \frac{\mathbf{E}_1}{B} \cdot \nabla n_o \right] \\
&= \frac{\nu_i}{\Omega_i} \left[\nabla \cdot \left[n_o \frac{\mathbf{E}_1}{B} + n_1 \frac{\mathbf{E}_o}{B} \right] \right] \\
&= 0
\end{aligned} \tag{3.18}$$

The result of equation 3.18 is the following relationship:

$$\mathbf{E}_1 = -\frac{n_1}{n_0} \mathbf{E}_o \tag{3.19}$$

Equation 3.19 can be used in equation 3.15 to complete the derivation. It should be noted that the result is only valid as long as $\mathbf{E}_1 \perp \nabla n_o$.

3.4.3 Returning to derivation

For the F-region electrons where $\mathbf{v_1} \perp \mathbf{E_1}$, substituting equation 3.19 into equation 3.15 yields:

$$\mathbf{v_1} = \frac{\mathbf{E_1} \times \mathbf{b}}{B} = -\frac{\mathbf{E_0} \times \mathbf{b}}{B} \left(\frac{n_1}{n_0} \right) \tag{3.20}$$

Replacing equation 3.20 into equation 3.15 yields:

$$\left[\frac{\partial}{\partial t} + \mathbf{v_0} \cdot \nabla \right] \left(\frac{n_1}{n_0} \right) = \left[\frac{\mathbf{E_0} \times \mathbf{b}}{B} \cdot \frac{\nabla n_0}{n_0} \right] \left(\frac{n_1}{n_0} \right) \tag{3.21}$$

This states that while a structure moves at a velocity $\mathbf{v}_o$, the magnitude of n_1/n_o grows exponentially at the rate given by:

$$\gamma = \frac{\mathbf{E_0} \times \mathbf{b}}{B} \cdot \frac{\nabla n_0}{n_0} \tag{3.22}$$

3.4.4 The plane wave approach for the GDI derivation

From the above derivation one can see that a plane wave approach is not needed to obtain the desired growth rate. For more complicated geometry it is nonetheless

preferable to derive an oscillation frequency and growth rate of the GDI through Fourier analysis of the equations. In this more comprehensive treatment, pressure gradients are included and a more general orientation is considered (Figure 3.9) while still maintaining a uniform **E** and **B** fields. For simplicity, the limiting case of $k_{//} = 0$ is still considered.

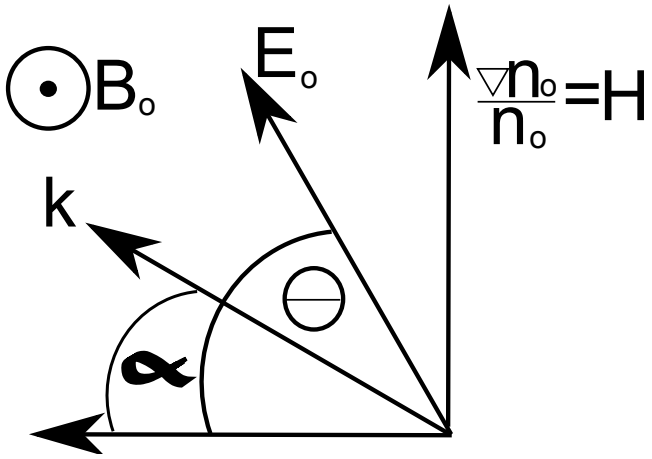

Figure 3.9: Gradient-drift instability geometry.

The momentum equation, including pressure gradients and collisions, reads:

$$\frac{d\mathbf{v}_\alpha}{dt} = \frac{q}{m_\alpha}\left(\mathbf{E} + \mathbf{v}_\alpha \times \mathbf{B}\right) - \frac{\nabla P_\alpha}{\rho_\alpha} - \nu_{\alpha n}\mathbf{v}_\alpha \tag{3.23}$$

A sinusoidal perturbation proportional to $e^{i(-\omega t + \mathbf{k}\cdot\mathbf{r})}$ is applied to the perturbed electric field (**E**), density (n), and particle velocity ($\mathbf{v}_\alpha$). It is assumed that the perturbations are much smaller than the initial property, i.e. $|\mathbf{E}_1| << |\mathbf{E}|$, the plasma is quasi-neutral ($n_e = n_i = n_o$), and the medium is isothermal (T=constant). A brief note on notation is necessary: the perturbation of the density, n_1, is an abbreviated form of $n_{k\omega}$. Essentially, the perturbation is tied to the wave number **k** such that $n_1 e^{-i\omega t + i\mathbf{k}\cdot\mathbf{r}} \propto n_{k\omega} e^{-i\omega t + i\mathbf{k}\cdot\mathbf{r}}$, similarly for $\mathbf{E_1} \propto \mathbf{E}_{k\omega}$, etc.

By using the electron continuity equation (3.7), the momentum (equation 3.23) equations for both ions and electrons, and the current continuity equation, the fol-

lowing four linear equations are obtained:

$$\left(\frac{n_1}{n_0}\right)\left[\omega - \mathbf{b}\cdot\frac{\mathbf{k}\times\mathbf{E_0}}{B}\right] = -i\mathbf{H}\cdot\mathbf{v_{e1}} \tag{3.24}$$

$$\mathbf{v_{e1}} = -i\mathbf{k}\times\mathbf{b}\left[\frac{\phi}{B} + \left(\frac{n_1}{n_0}\right)\left(\frac{k_B T_e}{qB}\right)\right] \tag{3.25}$$

$$\mathbf{v_{i1}} = -i\left(\frac{\nu_i}{\Omega_i}\right)\left[\mathbf{k} + \frac{\Omega_i}{\nu_i}\mathbf{k}\times\mathbf{b}\right]\left[\frac{\phi}{B} + \left(\frac{n_1}{n_0}\right)\left(\frac{k_B T_i}{qB}\right)\right] \tag{3.26}$$

$$\left(\frac{n_1}{n_0}\right) i\mathbf{k}\cdot(\mathbf{v}_{oi} - \mathbf{v}_{oe}) + \cancelto{\sim 0}{\mathbf{H}\cdot(\mathbf{v}_{i1} - \mathbf{v}_{e1})} = -i\mathbf{k}\cdot\mathbf{v}_{i1} \tag{3.27}$$

where $\mathbf{H} = \frac{\nabla n_0}{n_0}$ and ϕ is the perturbed electrostatic potential.

The approximation made in equation 3.27 is based on the fact that the term $\mathbf{H}\cdot(\mathbf{v}_{i1} - \mathbf{v}_{e1})$ can be dropped because, for the plane wave decomposition to make sense, $|\mathbf{k}| >> |\mathbf{H}|$. Also, note that diamagnetic currents have been omitted since they are divergence free.

After inserting equation 3.25 into 3.24, another useful equation is obtained:

$$\left(\frac{n_1}{n_0}\right)\left[\omega - \mathbf{b}\cdot\left(\frac{\mathbf{k}\times\mathbf{E_0}}{B} - (\mathbf{H}\times\mathbf{k})\frac{k_B T_e}{qB}\right)\right] = -\mathbf{b}\cdot(\mathbf{H}\times\mathbf{k})\left[\frac{\phi}{B}\right] \tag{3.28}$$

Placing equation 3.28 into equations 3.26 and 3.27, and using $w = w_r + i\gamma$, yields the following dispersion equation:

$$-\frac{\mathbf{k}\cdot\mathbf{E_0}}{B} = \frac{-ik^2C_s^2}{\Omega_i} - ik^2\left[\frac{\mathbf{b}\cdot(\mathbf{k}\times\mathbf{E_0})}{B(\mathbf{b}\cdot(\mathbf{H}\times\mathbf{k}))}\right] + ik^2\omega_r\left(\frac{1}{\mathbf{b}\cdot(\mathbf{H}\times\mathbf{k})}\right) + \gamma k^2\left(\frac{1}{\mathbf{b}\cdot(\mathbf{H}\times\mathbf{k})}\right), \tag{3.29}$$

where the ion acoustic speed, $C_s = \sqrt{\frac{k_B(T_e+T_i)}{m_i}}$, has been introduced.

Separating equation 3.29 into real and imaginary parts produces the growth rate (γ) and the oscillation frequency (ω_r):

$$\gamma = \mathbf{b}\cdot(\mathbf{H}\times\mathbf{k})\left[\frac{1}{k^2}\right]\left(\mathbf{k}\cdot\frac{\mathbf{E_0}}{B}\right) \tag{3.30}$$

$$= H\frac{E_o}{B}\cos(\alpha)\cos(\theta-\alpha) \tag{3.31}$$

$$\omega_r = \left[\frac{\mathbf{b}\cdot(\mathbf{k}\times\mathbf{E_0})}{B}\right] + \mathbf{b}\cdot(\mathbf{H}\times\mathbf{k})\left[\frac{C_s^2}{\Omega_i}\right] \tag{3.32}$$

$$= k\frac{E_o}{B}\sin(\theta-\alpha) + \frac{C_s^2}{\Omega_i}Hk\cos(\alpha) \tag{3.33}$$

Under the appropriate geometry, equation 3.22 can be recovered from equation 3.30. SuperDARN radars assume that the first term of equation 3.32 is all that matters to measure the l-o-s component of the **E**x**B** plasma drift. The second term in equation 3.32 is mildly interesting. To demonstrate this, consider equation 3.32 in the following form:

$$\frac{\omega_r}{k} = \frac{E_o}{B}\sin(\theta - \alpha) + \frac{1}{L}\frac{C_s^2}{\Omega_i}\cos(\alpha), \tag{3.34}$$

where H=1/L. Under normal circumstances, the second term of equation 3.34 should be considered as quite small and can be neglected. For example, consider the following ionospheric values: a gradient scale of L=10 km, Ω_i =150 rads/s, E_o = 20 mV/m, B=0.5 G, and $C_s \simeq 400$ m/s. Placing these values into equation 3.34 will yield an estimate of:

$$\frac{\omega_r}{k} = 400 \;\; m/s + 0.1 \;\; m/s. \tag{3.35}$$

The ion-acoustic portion (second term) is negligible. However, if there are strong gradients, L=100 m and a slightly higher ion-acoustic speed, C_s = 800 m/s, then the second term becomes $\sim$ 40 m/s, which is a significant contribution to the phase velocity ω_r/k particularly for $\alpha = 0$ and $\theta = \alpha$ (line-of-sight along E_o and in direction perpendicular to the ambient density gradient).

The resulting generalized growth rate (equation 3.30) was presented in the work done by *Keskinen and Ossakow* (1982) where they too neglected parallel perturbation fields. Using equation 3.30 the angle of maximum growth relative to the ambient electric field can be determined and is given by (*Keskinen and Ossakow*, 1982):

$$\alpha = \frac{\theta}{2}, \tag{3.36}$$

where θ is the angle between the ambient electric and the direction perpendicular to the density gradient, as seen in Figure 3.9. This stated, *Keskinen and Ossakow* (1982) primarily applied their growth rate to a slab geometry. For a more general solution, consider Figure 3.10(a) where the ambient electric field points to the right, the ambient density gradient points to the top of the page and the magnetic field

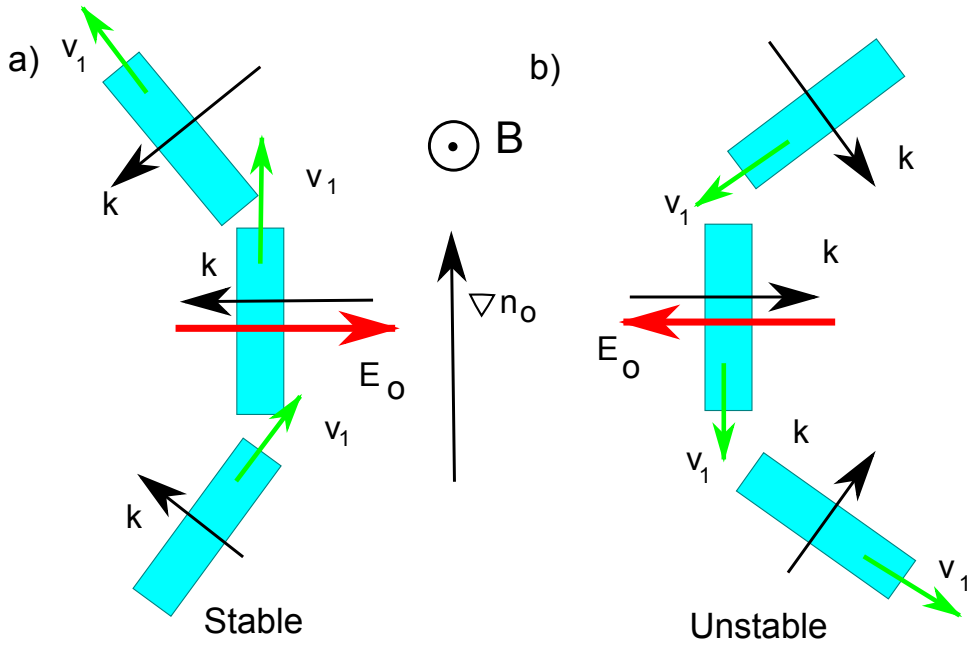

Figure 3.10: Various orientations of F region patches to illustrate stablility. The "dominant **k** vector" is perpendicular to the long axis of the patch. a) Three separate cases that illustrate "stable" orientations. b) Three separate cases that illustrate "unstable" orientations.

orientation is out of the page. It is also important to note that the **k** vector discussed here is the "dominant wave vector". This "dominant wave vector" is perpendicular to the long axis of the structures. For the particular configuration of Figure 3.10(a), the plasma is stable: the perturbed $\mathbf{E}_1$x$\mathbf{B}$ drift ($\mathbf{v}_1$) vector takes the enhanced density plasma into a region of higher density, thus creating a stable situation. There is therefore no growth for this orientation of the ambient electric field and the density gradient.

Alternately, if the ambient electric field is pointing towards the left of the page, as seen in Figure 3.10(b), the patch becomes unstable for all **k** vectors as the $\mathbf{E}_1 \times \mathbf{B}$ drift moves the higher density patch into a region of lower density, causing a growth in n_1/n_0. For this geometry, the plasma is unstable for all **k** directions except for $\mathbf{k} \parallel \nabla n_o$ where the growth rate is zero. This statement applies to all **k** vectors associated with the structure, not just the dominant one.

There are two special cases for which there is neither growth nor decay. The first

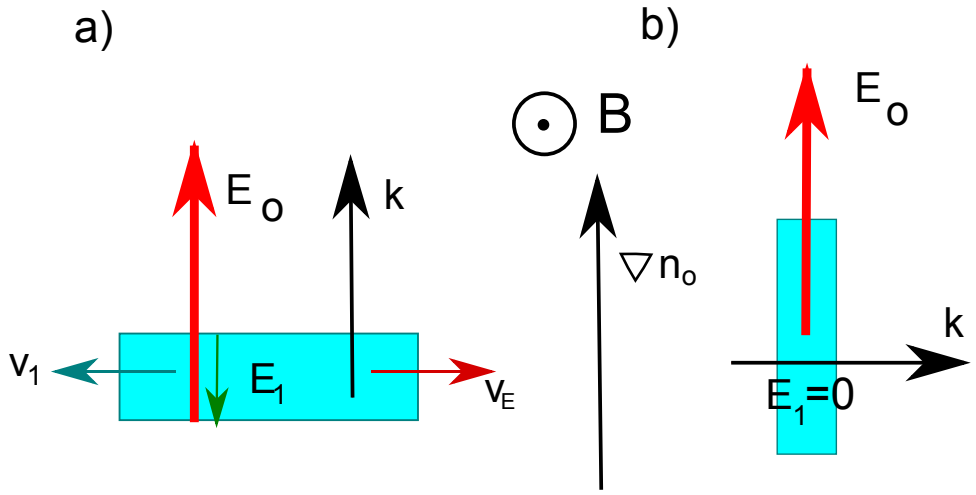

Figure 3.11: Geometry for unique orientations for which there is either no plasma growth or decay.

case concerns $\mathbf{k} \parallel \nabla n_o$, as shown in Figure 3.11(a). For this situation, the perturbed electric field moves the plasma along the density isocontour. Since the plasma is moving along a density isocontour n_1/n_o it neither grows nor decays. However, even a small tilt in $\mathbf{k}$ results in the growth or instability as shown in Figure 3.10. The second case, as seen in Figure 3.11(b), is the case of $\mathbf{k} \perp \mathbf{E_o}$. For this geometry there is no polarization and thus no movement at all. Therefore, the system is once again neither stable nor unstable.

It is of interest to apply the above analysis to auroral arc geometry. The ideal geometry of an auroral arc can be seen in Figure 3.12(a). The arc makes an elongated, high density plasma structure with density gradients pointing to the center on either edge of the arc. Auroral arc lengths can be tens of km across but are typically made of substructures 100 m to 1 km in size (*Johansson et. al.*, 2007). The ambient electric field typically stretches across the arc and a magnetic field points into the page. This means that an elongated narrow structure of high density plasma resides in a region where an ambient electric field, $\mathbf{E}_o$ crosses the arc, being parallel to the density gradient along one edge and anti-parallel along the other edge. For maximum growth, the polarization electric field will cause n_1/n_o to grow at a 45^o angle away from the edges of the arc, as shown in Figure 3.12(b).

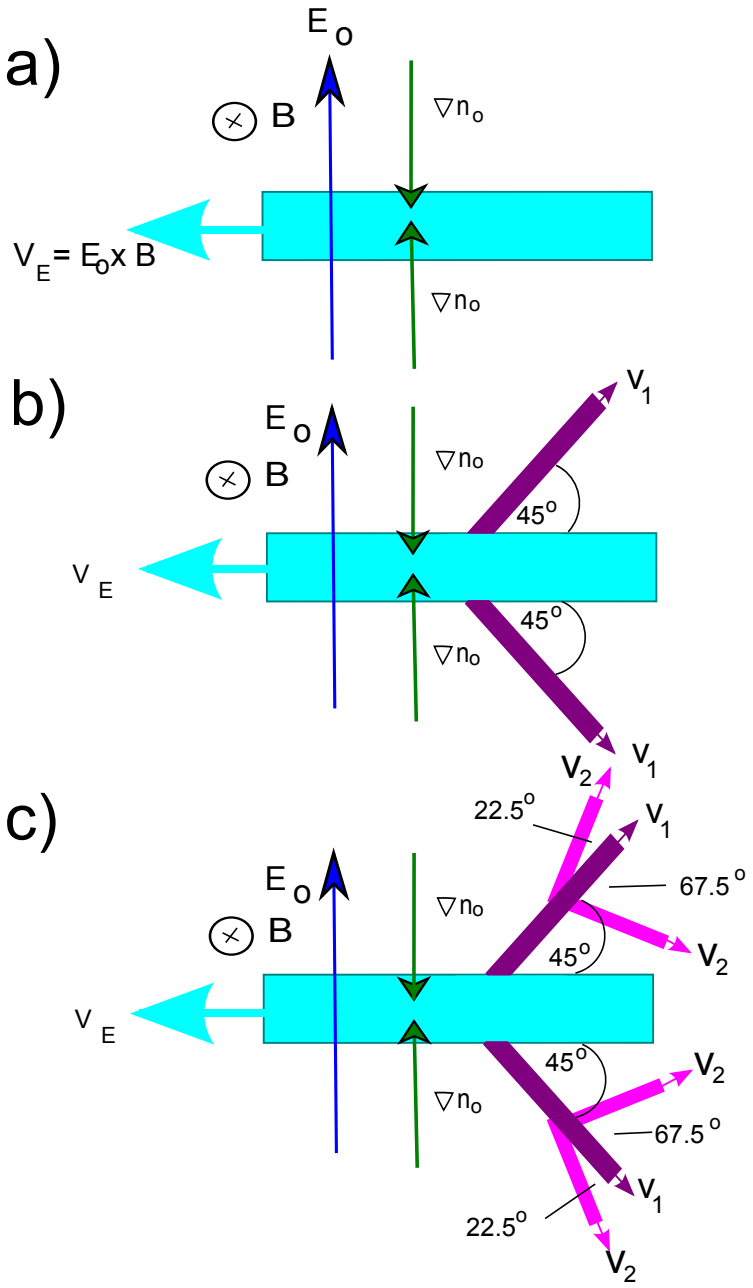

Figure 3.12: Geometry for unstable auroral arc (depicted in light blue) - irregularities can form under these conditions. a) shows the initial plasma distribution. b) A small perturbation is applied to the system causing secondary fingers to grow at 45 degree angles from the initial plasma structure. c) Tertiary fingers continue to evolve at appropriate angles resulting in structures off which coherent radars such as SuperDARN scatter transmitted waves.

The relative amplitude of these large primary scale fingers will grow as they propagate away from the auroral arc. Once they have propagated far enough away, these primary large scale fingers can generate their own steep plasma density gradients perpendicular to their edges. Small scale secondary finger growth will therefore be triggered through the GDI mechanism again. The angles of the primary and secondary fingers have been calculated and shown in Figure 3.12(b) and (c). As seen in Figure 3.12(b), the secondary fingers propagate at right angles to each other, a phenomenon which will become important in the detection of abundant echoes by SuperDARN. If the SuperDARN radar look direction is into the arc (along the $\mathbf{E}_o$ direction for the case presented in Figure 3.12), it catches slow moving echoes from the "dominant" wave vector on both sides of the arc. These slow moving echoes are associated with the tertiary fingers nearly perpendicular to $\mathbf{E}_o$ in Figure 3.12(c). When looking along the arc (along the $\mathbf{E}_o \times \mathbf{B}$ direction for the case presented in Figure 3.12) the plasma flow is dominated by the ambient $\mathbf{E}_o \times \mathbf{B}$ drift of the plasma. However, the echoes are not as strongly generated by the primary irregularity (Figure 3.12(b)) as they are by the secondary structures seen developing in Figure 3.12(c).

The above considerations show that the gradient-drift mechanism works for almost any direction of the electric field and plasma-density gradient through a recursive two step process. By contrast, *Carlson and Moen* (2007) suggested a need for a new process involving the generation of a shear instability at first, followed by the gradient drift instability to generate the decameter F-region irregularities. The approach suggested here can use the GDI alone to create the necessary structures. This approach also expands on work that was only applied to a slab geometry (*Keskinen and Ossakow*, 1982) and can be expanded to vortex configurations (not discussed here). Therefore, based on the generalized growth rate discussed here, the GDI can operate in most directions. It is this unique property of GDI that makes it ideal for studying plasma motion in the high latitude ionosphere. Coherent scatter radar systems such as SuperDARN are able to measure the l-o-s velocity of ionospheric plasma drifts to infer the ionospheric convection.

3.4.5 E-region Instabilities: Farley-Buneman Mechanism

Irregularities generated in the E region can also be detected by SuperDARN. As mentioned in section 2.6, in the E region the electrons are magnetized ($\Omega_e >> \nu_e$) while the ions are demagnetized ($\Omega_i << \nu_i$). As a result, in the lower E region the electrons $\mathbf{E} \times \mathbf{B}$ drift, while the ions move mostly along the electric field direction. This creates a net current that has components along the electric field direction (Pedersen current) and along the direction transverse to both the electric and magnetic field directions (Hall current). Consider a high-latitude E region where the magnetic field is oriented anti-parallel to the z-direction, the electric field is along the x-direction, and there is a density gradient parallel to the electric field. Use a plane wave decomposition for the background electric field ($\mathbf{E}_1$), density (n_1), and particle velocity ($\mathbf{v}_{\alpha 1}$) of the form $e^{(i\mathbf{k}\cdot\mathbf{r}-iwt)}$. The equation of motion (equation 2.5) and the continuity equation (equation 3.7) for the quasi-neutral plasma can be reduced to the following set of linear equations:

$$i\omega\left(\frac{n_1}{n_o}\right) - i\mathbf{k}\cdot\mathbf{v}_{\alpha\mathbf{o}}\left(\frac{n_1}{n_o}\right) - i\mathbf{k}\cdot\mathbf{v}_{\alpha\mathbf{1}} = 0, \tag{3.37}$$

$$-i\omega\mathbf{v}_{\alpha\mathbf{1}} = -\frac{e}{m_\alpha}i\mathbf{k}\phi - \Omega_\alpha\mathbf{v}_{\alpha\mathbf{1}}\times\hat{e_z} - \nu_\alpha\mathbf{v}_{\alpha 1} - \frac{T_\alpha i\mathbf{k}}{m_\alpha}\left(\frac{n_1}{n_o}\right), \tag{3.38}$$

where $\mathbf{v}_{\alpha 1}$ is the particle speed, Ω_α is the gyrofrequency, T_α is the temperature in energy units (with $\alpha = i, e$), ϕ is the perturbed electrostatic potential, ω is the frequency, and $\mathbf{k}$ is the wave vector. It has been assumed here that the perturbations are much smaller than the initial quantity, i.e. $n_1 << n_o$, and temperature fluctuations have been neglected.

Assume that the ions are initially moving parallel to the electric field ($\nu_i >> \Omega_i$) and the electrons are Hall drifting transverse to the magnetic and electric field ($\nu_e << \Omega_e$). Separating equations 3.37 and 3.38 for ions and electrons yields four equations and four unknowns: $\frac{n_1}{n_0}$, $\mathbf{v}_{i1}$, $\mathbf{v}_{e1}$, and ϕ. Solving for the perturbed ion and electron velocities yields the dispersion relation (*Sudan*, 1983; *Kelley*, 1989):

$$(\omega - \mathbf{k}\cdot\mathbf{v}_{oe}) = -\frac{\Psi}{\nu_i}\left((-i\omega+\nu_i)(\omega-\mathbf{k}\cdot\mathbf{v}_{oi}) + ik^2c_s^2\right), \tag{3.39}$$

where $\Psi = \psi\left(\frac{k_\perp^2}{k^2} + \frac{\Omega_e^2}{\nu_e^2}\frac{k_\parallel^2}{k^2}\right)$, $\psi = \frac{\nu_e\nu_i}{\Omega_e\Omega_i}$, and $c_s = \sqrt{\frac{Ti+Te}{m_i}}$ is the ion acoustic speed. Let $\omega = \omega_r + i\gamma$ (so that positive gamma indicates positive growth). The real part(ω_r) and the growth rate (γ) are:

$$\omega_r = \frac{1}{1+\Psi}(\mathbf{k}\cdot\mathbf{v}_{oe} + \Psi\mathbf{k}\cdot\mathbf{v}_{oi}) \tag{3.40}$$

$$\gamma = \frac{\Psi/\nu_i}{1+\Psi}(\omega_r^2 - k^2c_s^2) \tag{3.41}$$

According to equation 3.41, for the waves to grow the phase velocity of the wave must be greater than the ion acoustic speed ($\omega_r > kc_s$). Consider a blob-like elongated structure once again. As the amplitude of the structure grows, the total electric field inside the structure decreases, causing the growth rate to ultimately become zero (*St.-Maurice and Hamza*, 2009). However, as the growth rate approaches zero, the phase speed approaches the ion acoustic speed. The largest amplitude structures are therefore observed to be moving at the ion acoustic speed by coherent radars such as SuperDARN (*St.-Maurice and Hamza*, 2009, 2001). If there are irregularities moving at the ion acoustic speed and at the **E**x**B** drift, it is much more likely that the higher amplitude ion acoustic waves are going to be registered by the SuperDARN radars. This stated, many other factors can affect the threshold speed at times, such as gradients. Echoes located at lower altitudes that can increase the threshold speed, and thermal effects that can increase electron speed which will in turn affect C_s (*St.-Maurice and Hamza*, 2009, 2001).

Experimental studies by *Koustov et. al.* (2005) have shown that statistically, E-region HF echoes tend to move at a lower speed than the **E**x**B** drift suggested by F-region plasma. In their study, *Koustov et. al.* (2005) compared **E**x**B** F region Defense Meteorological Satellite Program (DMSP) measurements to E-region high frequency (HF) radar echoes from the Stokkseyri radar. They concluded that the overall ratios between the E-region HF echoes and the F-region DMSP drift was 0.35. They further determined that it was even lower, approximately 0.1, for larger

drifts (greater than 1000 m/s) and slightly higher for drifts slower than 400 m/s (approximately 0.4). They also noted that the observed spectra for the short range Stokkseyri echoes were often double peaked. They performed a spectral analysis of the double peaked spectra using an analysis technique called the Burg method which showed that for the slower plasma flows, less than 400 m/s, the high speed component of the spectra closely matched the expected **E**x**B** drift. For plasma drifts greater than 700 m/s, on the other hand, the high speed component of the spectra was in the range of possible c_s values. Unless a spectrum by spectrum analysis was undertaken, it would be quite difficult to determine which echoes were from **E**x**B** drifts and which were from ion acoustic sources. Even then, in the event of double peaked spectra, further analysis would need to be undertaken to extract the appropriate **E**x**B** drift from the spectra. As such, for the purpose of this thesis, removing E-region echoes removes the possibility of data contamination from non **E**x**B** sources which are prevalent in the E region. Since most E region data are confined to shorter ranges, by removing the first 10-15 range gates a large majority of E-region scatter can be removed from the SuperDARN data sets.

Chapter 4

Data Analysis Technique

The focus of this thesis is the study of the effect of CMEs and CIRs on the ionospheric environment. The results of these studies are presented in Chapters 5 and 6 in journal submission format. In particular, this chapter expands on the computer algorithms used and on the processing of the gridded line-of-sight velocity vectors, which are key tools of the analysis. A case study of a geomagnetic storm event is also presented to highlight the investigation and extend the need for performing a statistical analysis instead of a number of case studies.

In order to study the ionospheric response to the arrival of CMEs and CIRs, particularly geoeffective events were chosen. This meant that the events had a strong impact on the geomagnetic environment and on the ionospheric environment. For the purposes of this thesis, CMEs and CIRs were considered geoeffective if they resulted in either an SC or a geomagnetic storm. The first study, presented in Chapter 5, focuses on CMEs and CIRs that resulted in geomagnetic storms. For that study, the main phase and recovery phase was examined using OMNI, Sym-H, and SuperDARN data sets. The second study, presented in Chapter 6, focused on SC events, in particular the sudden increases in solar wind dynamic pressure pulses associated with them, and their effect on the ionospheric convection and SuperDARN backscatter. In both studies the analysis was approached using the same technique, except for the choice of a zero reference marker in the epoch analysis.

4.1 Epoch Interval Selection

Although the onset of a geomagnetic storm (Chapter 5), or SC (Chapter 6), is defined by ground-based geomagnetic activity levels, and the resulting profile determined by the same measurements, it has long been established that geomagnetic activity is caused by disturbances in the solar wind and IMF. It is important to consider the solar wind phenomena that cause disturbed geomagnetic activity levels. To provide the best understanding of the geomagnetic activity process in its entirety a time period of 24 hours prior to the official commencement of the geomagnetic storm (Chapter 5) or SC (Chapter 6) was included in the epoch interval to investigate the solar wind and IMF parameters of the solar wind driver. Data obtained from satellites, such as ACE, are necessary to analyze solar wind and IMF conditions to establish whether a CME, CIR, or other interplanetary solar wind event was the cause of the change in geomagnetic activity. Pre-storm conditions in the ionosphere obtained by coherent radars such as SuperDARN during this time period provide a baseline to analyze changes that are a result from the solar wind phenomenon. A detailed look at the main phase of the geomagnetic storm was necessary to determine the effects of the interplanetary drivers on the magnetospheric-ionospheric system. The recovery phase was also investigated to determine how the ionosphere recovered. As a result, the system's response was monitored for 72 hours after the onset of the geomagnetic storm. The second study focused solely on the SC which occurs on a much shorter time scale (hours) than a geomagnetic storm (days).

The selection of the geomagnetic storms for the first study and the SC events for the second study are clearly outlined in Chapters 5 and 6, respectively, and will therefore not be presented here.

4.2 Line of sight plasma drift direction

Data from SuperDARN are used exclusively to analyze the ionospheric convection velocities and radar backscatter occurrence during storms and following SCs. The

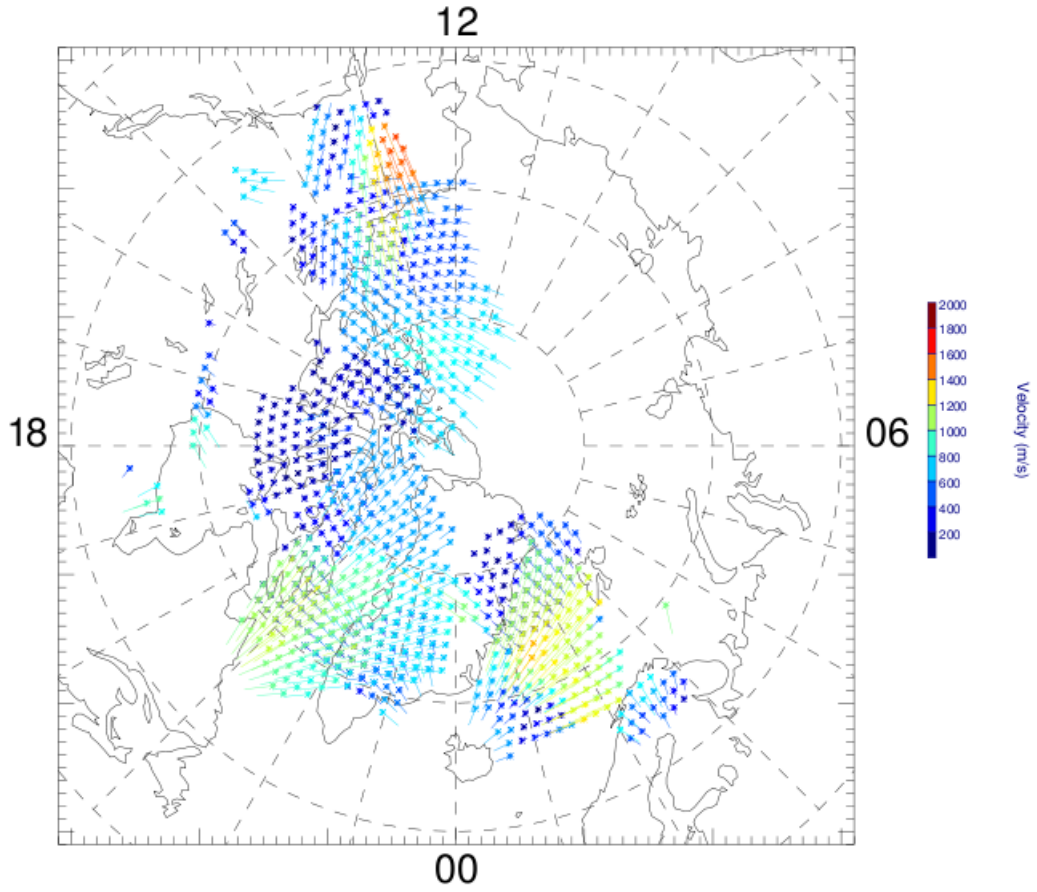

Figure 4.1: A polar plot of gridded velocity vectors aligned to the AACGM grid for April 7^{th}, 2000 at 00:10 - 00:12 UT.

gridded l-o-s velocity data from each radar station (described in section 3.3.2) were used for this study. Each station records l-o-s velocity data containing beam directions, velocity vectors (negative indicates motion away from the radar and positive towards), and magnetic latitude and longitude components. As shown in Figure 3.7, and discussed in section 3.3.2, l-o-s plasma drifts are normally combined in a data assimilation procedure to reconstruct the ionospheric convection pattern. The direction of ionospheric convection can then be inferred visually by the general direction of the mapped vectors. The final stage in the convection mapping model uses *a priori* statistical convection patterns based upon the current IMF conditions to determine what the convection pattern will resemble. When there are few velocity vectors available, the resulting convection velocity vectors have been highly influenced by the model which may not be an accurate representation of the convection pattern. The model is most effective when there are a suitable number of points available, say greater than 300 pts/two minute scan interval. Errors in the time shifting of ACE IMF data could also introduce errors in picking the *a priori* convection pattern and this could introduce further errors when determining flow direction. In a case study the number of vectors affected by this would potentially remain small and not affect the outcome. When performing a statistical study, the results could become swayed by the model. Geoeffective CMEs and CIRs are small in number and therefore this study incorporates a limited number of events. By further limiting the data set to time periods where there was sufficient number of data points would cause the validity of a statistical study to be questionable. The mapping program does not stipulate the flow direction (in either a sunward or antisunward direction). Flow direction was important for the study of plasma convection velocities so a method to determine the direction of the flow, either sunward or antisunward, was needed.

A determination of the geographic co-ordinates of the start and end points of all vectors were the first step to be taken in order to determine the flow direction of the l-o-s velocities. The latitude, longitude, velocity and azimuthal angle of each data point are all stored in the *.map files. If the gridded l-o-s velocity data point was negative, indicating flow away from the radar, the absolute magnitude of data point

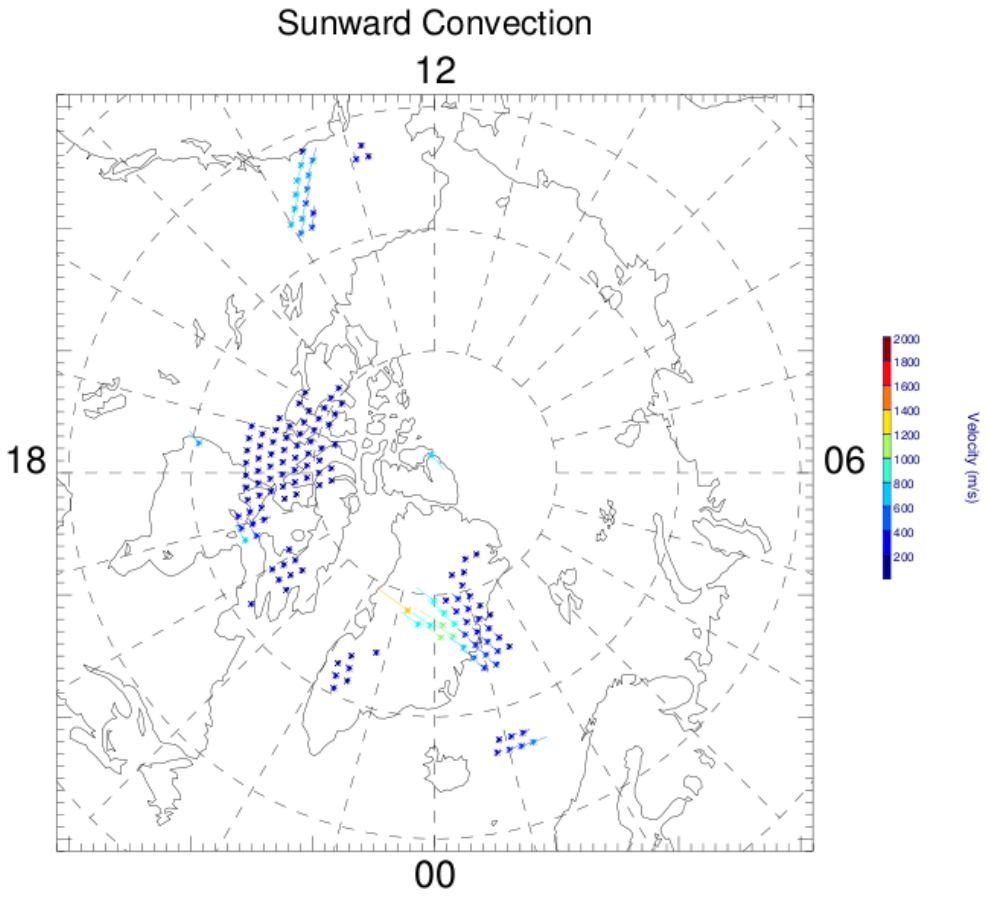

Figure 4.2: Polar plot of sunward flowing gridded velocity vectors aligned to the AACGM grid for April 7^{th}, 2000 at 00:10 - 00:12 UT.

was taken and 180^o added to the azimuthal angle. The geographical coordinates were then converted into magnetic latitude and magnetic local time coordinates. An example of the resulting vectors is shown in Figure 4.1. Similar to the latitude/longitude map seen in Figure 3.7, magnetic local noon (12 MLT) is at the top of the page and dawn (6 MLT) is to the right. The polar plot is centered on the magnetic north pole, as determined by the AACGM coordinate system. Each cell in the grid has a vector with a dot at the base and points in the flow direction. The length of the vector is determined by the magnitude of the flow as does the color seen in the legend located on the right hand side. The IMF orientation dial usually located in the upper right hand corner was omitted in these plots as the IMF model had no bearing

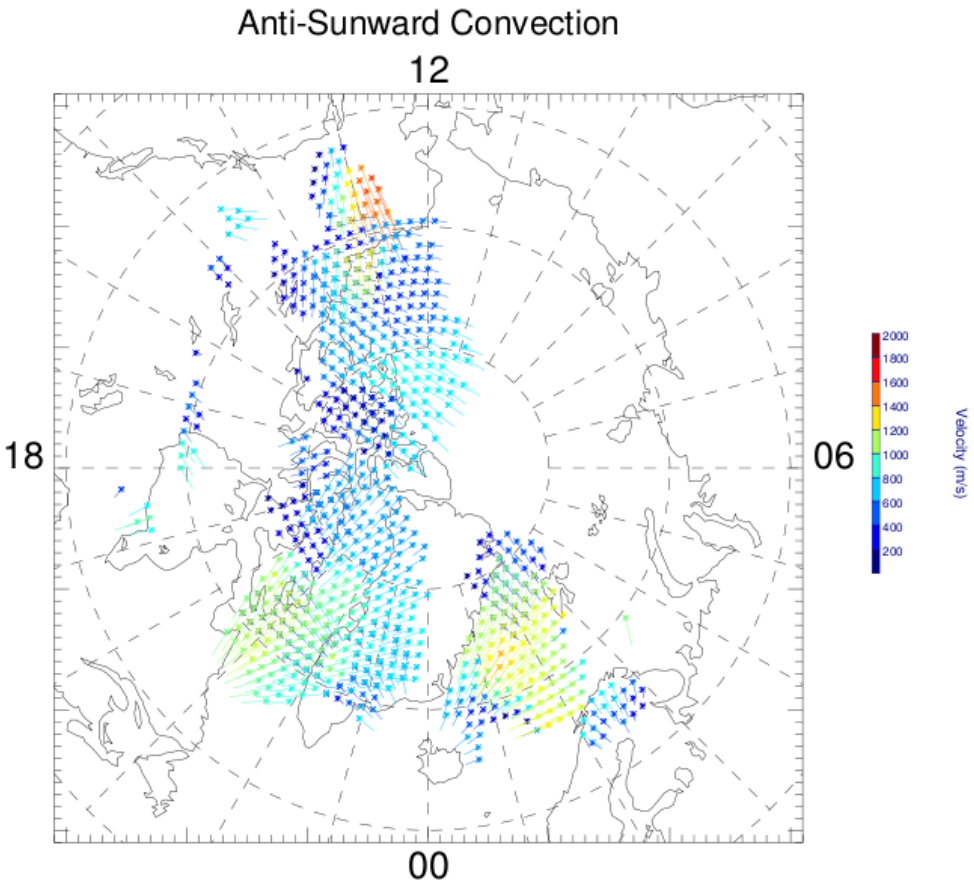

Figure 4.3: Polar plot of antisunward flowing gridded velocity vectors aligned to the AACGM grid for April 7^{th}, 2000 at 00:10 - 00:12 UT.

on this stage in the processing technique. In the example shown in Figure 3.7, there is a predominance of antisunward flow over the noon sector and into the midnight sector (flow from 12 MLT to 0 MLT across the polar cap region). Return sunward flow is seen in the dusk region. One further step was needed in order to determine if a velocity vector was sunward or antisunward. The dot product of the l-o-s velocity vector and a meridian line from midnight to noon MLT was taken. This first order classification only determined two directions - sunward or antisunward. If the flow direction was antisunward, the l-o-s velocity was made negative. If the flow was

sunward then the l-o-s velocity vector remained positive. Using this method it was possible to computationally separate the flow direction and the process was completely automated. Using the MLT/MLAT polar grid system, Figures 4.2 and 4.3 show the results of the directional flow algorithm. Figure 4.2 contains all l-o-s vectors that were found to be sunward and Figure 4.3 all those that were antisunward. The initial classification is applied irrespective of the degree to which a vector is directed sunward or antisunward. If a vector is pointing towards dawn, as long a small component of remains pointing towards 12 MLT, the data point was labelled sunward. At this stage, the focus was on sunward and antisunward flow statistics irrespective of the degree of flow, but future studies can refine the convection flow directions. Once the magnitude and flow direction of each l-o-s data point was determined, a statistical epoch analysis on the SuperDARN data sets could be performed.

4.3 Superposed epoch analysis of geomagnetic storms

Chapter 5 focuses on geomagnetic storms. Once the geomagnetic storm event list and SuperDARN velocity magnitude and flow direction had been established, a superposed epoch analysis was performed. The choice of a zero epoch starting time was key to the study. However, this study encompasses both standard storms (with initial phases) and gradually commencing storms that lack this feature. Regardless of the type of geomagnetic storm, all geomagnetic storms do have a main phase that has a defined end at the most extreme negative Sym-H value, which also signifies the start of the recovery phase. This negative extremum was chosen as the zero reference epoch time for the storm events. The data for 24 hours prior and 72 hours after the zero epoch time was included in the study. Key parameters such as the Sym-H index, the interplanetary electric field (IEF), IMF B_y and B_z GSM components, the solar wind flow speed and dynamic pressure, and the SuperDARN ionospheric backscatter and the convection velocity data were plotted and their evolution analyzed. In order to illustrate the epoch study and the benefits of the approach, a case study is now

presented.

4.3.1 A Case Study: April 6^{th}, 2000

Shown in Figure 4.4 is a case study for a geomagnetic storm that occurred on April 6^{th} to 9^{th}, 2000. The initial phase for this geomagnetic storm began with a storm sudden commencement on April 6^{th} at 16:40 UT. Shown in panels (i)-(iv) are the Sym-H index, the z component of the IMF (GSM coordinates), the solar wind flow speed, and the solar wind dynamic pressure. All are referenced to the zero epoch time indicated by the vertical line at t = 0 hours. The zero epoch marker for this event occurred on April 7^{th} at 00:09 UT. The solar wind and IMF data are shifted to 17 Re upstream in the OMNI database and no further time shifting has been applied.

The Sym-H profile depicts a 'standard' geomagnetic storm with a sharp SSC and an initial phase. The SSC can be seen at approximately t = -7 hours (April 6^{th} at 16:40 UT) and the initial phase lasts for approximately 40 minutes. This SSC is the result of a halo CME event that occurred two days earlier, on April 4^{th}, 2000 at 16:32 UT (*Zhang et al.*, 2007). The main phase commences almost immediately following this increase in the geomagnetic field and can been seen by the rapid decline in Sym-H to near -330 nT. The Sym-H minimum at t = 0 hours indicates the end of the main phase. There is a gradual increase in the Sym-H index during the recovery phase (after t = 0 hours). Seen in panel (ii) is the IMF B_z component for this event. The IMF is strongly negative at SSC and during the SSC and during the initial and main phases. Seen in panels (iii) and (iv) are the discontinuities in the solar wind flow speeds and solar wind dynamic pressure pulse likely the solar wind cause of the SSC. This discontinuity is evidenced by the sudden rise in solar wind dynamic pressure from a steady 1 nPa value to nearly 15 nPa. A simultaneous increase in solar wind flow speed also occurs. Prior to the SSC at t = -7 hours, the solar wind flow speed is steady at approximately 350 km/s. At the SSC there is a rapid step-like increase in the solar wind flow speed to near 600 km/s that is maintained for more than 72 hours.

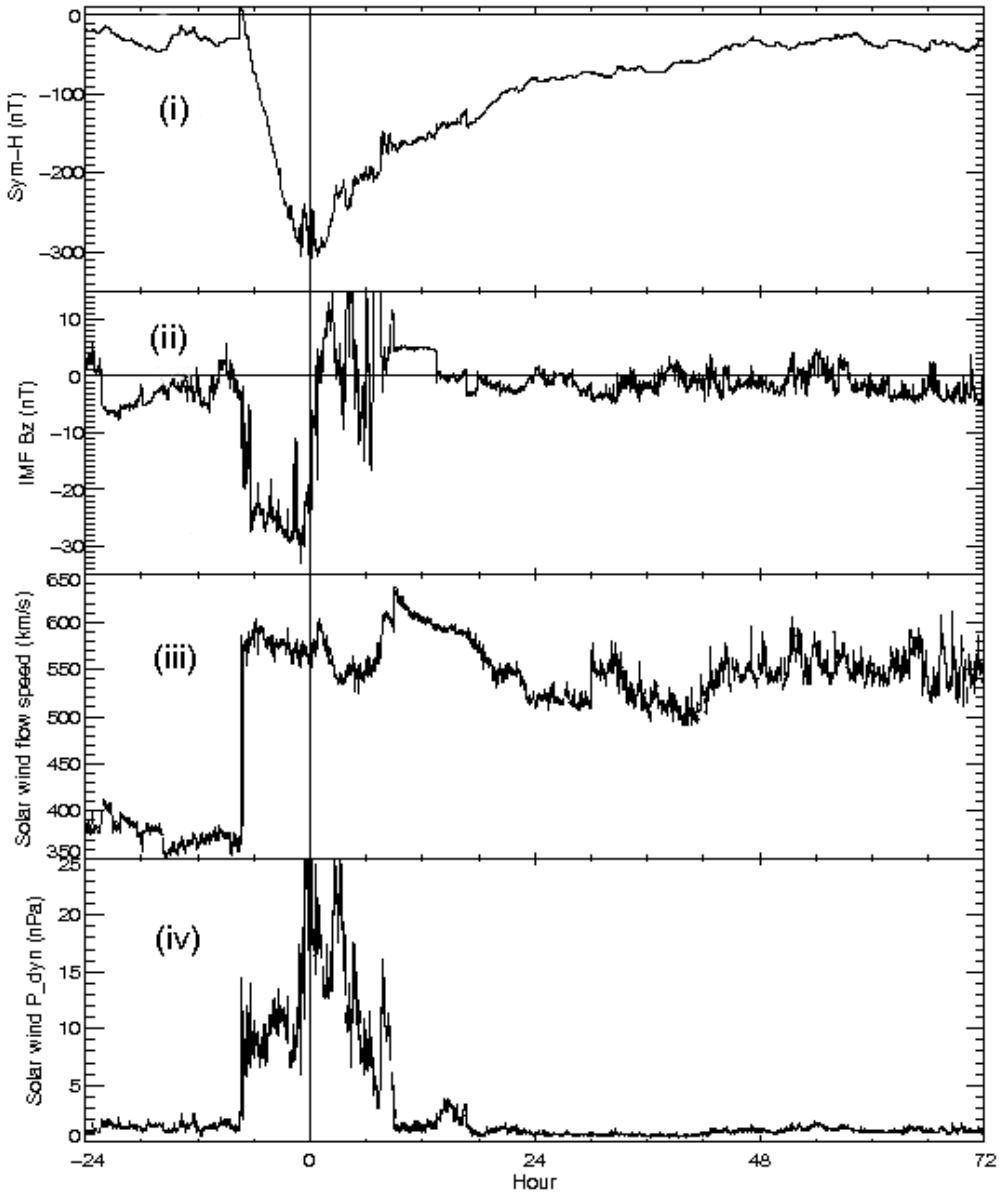

Figure 4.4: Case study of IMF parameters for April 7^{th}, 2000. The Sym-H profile is presented in panel (i), the IMF B_z in panel (ii), the solar wind flow speed in panel (iii) and the solar wind dynamic pressure in panel (iv). The zero epoch time is marked by the black vertical line at $t = 0$.

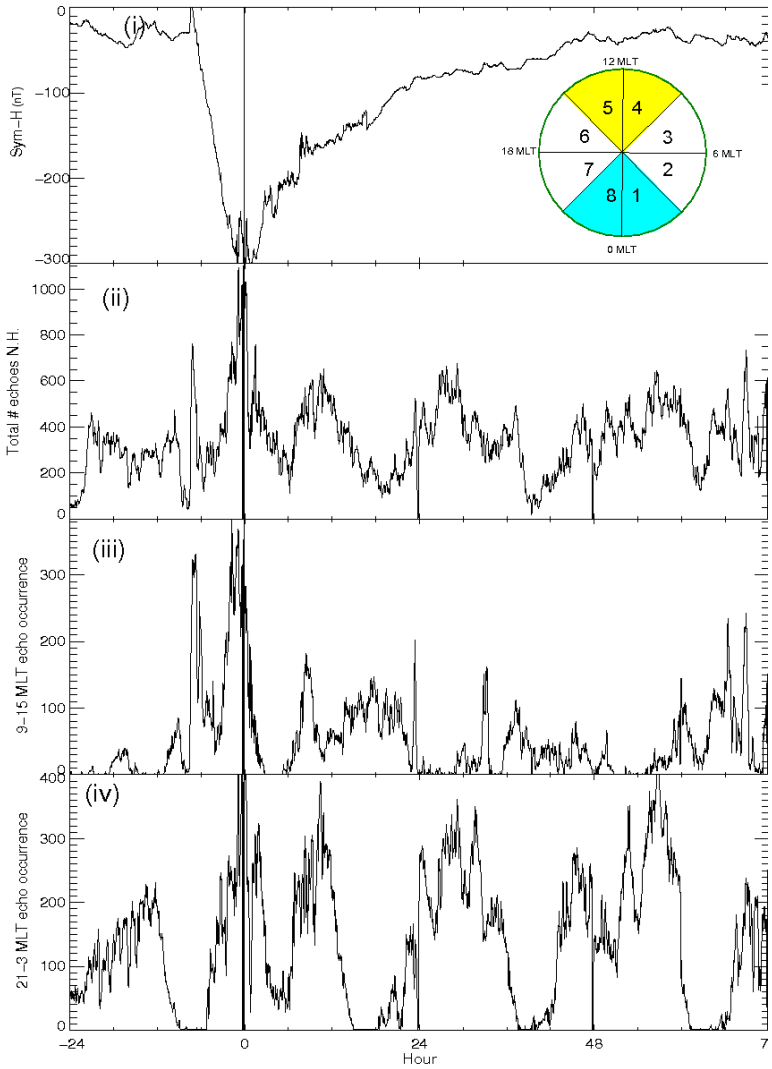

Figure 4.5: Case study of SuperDARN backscatter count parameters for April 7^{th}, 2000. The Sym-H index profile is shown in panel (i). Panel (ii) displays the echo occurrence from all northern hemisphere radars for this event for all MLTs and latitudes. Panel (iii) displays the echo occurrence for the 09-15 MLT (noon) region for this event. Panel (iv) displays the echo occurrence for the 21-03 MLT (midnight). The zero epoch reference marker is shown by the black vertical line at t = 0 hours. The inset dial represents the sections in the algorithm corresponding to each MLT range as described in the text.

The same zero reference epoch time was used for the SuperDARN backscatter data. Shown in Figure 4.5 are the Sym-H index, the total echo occurrence rate for all available radars in the northern hemisphere, the echo occurrence in the 9 to 15 MLT sector, and the echo occurrence in the 21 to 03 MLT sector in panels (i) through (iv), respectively. The inset in the right hand corner of panel (i) illustrates that the MLT sectors were separated into 3 hour time bins. As indicated by the inset, section 1 contains data for 0 to 3 MLT, section 2 contains data for 3 to 6 MLT, etc. The noon sector (9 to 15 MLT) is shaded in yellow and the midnight sector (21 to 03 MLT) is shaded in blue. The Sym-H profile for this event was plotted in panel (i) with the zero reference epoch marker set at t = 0 hours marking the end of the main phase. Although SuperDARN is designed to have nearly global coverage, there are data gaps caused by the distribution of the SuperDARN radars and lack of returned signal due to propagation conditions or the lack of ionospheric irregularities. There is a periodic loss of data in panels (iii) and (iv). To discuss this effect, Figures 4.6 and 4.7 show a map of the l-o-s velocity vectors of the SuperDARN radars for 03:20 -03:22 UT (corresponding to t $\sim$ 3 hours) and 18:30 - 18:32 UT (corresponding to t$\sim$ 18 hours) for the case study. Figure 4.6 shows that at 03:20 - 03:22 UT in the 9 to 15 MLT sector (outlined in red) there is poor radar coverage. This corresponds to the lack of noon sector echoes seen around t = 3 hours in Figure 4.5 (iii). Similarly, at 18:30 -18:32 UT in the midnight sector (outlined in red) in Figure 4.7 the same gap in radar coverage corresponding to the nearly zero echo occurrence in Figure 4.5(iv) seen at t = 18 hours.

The SuperDARN velocity distributions are shown in Figure 4.8. The Sym-H index, IMF B_z component of the IMF and the solar wind dynamic pressure are reproduced in panels (i) to (iii) for comparison. Shown panels (iv) and (v) are the SuperDARN distributions for the noon and midnight sectors. The positive velocities indicate flow towards the sun, and the negative velocities indicate flow away from the sun. There is evidence of SuperDARN's coverage gaps shown in panels (iv) and (v).

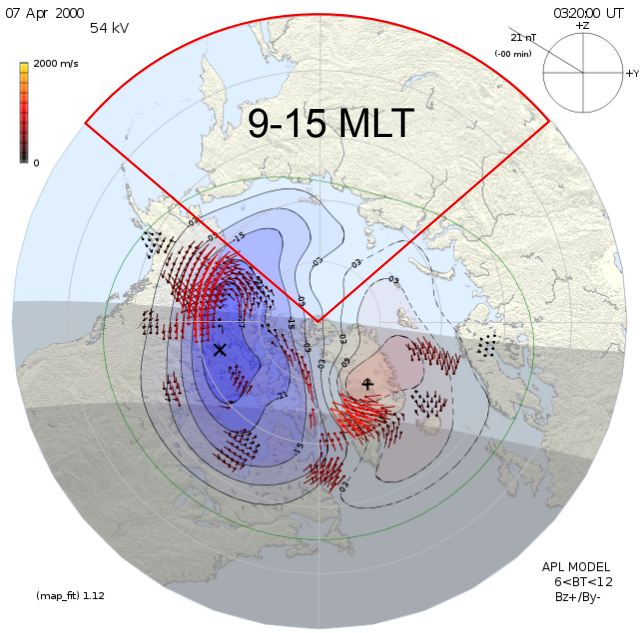

Figure 4.6: SuperDARN l-o-s velocity map for 03:20 - 03:22 UT, April 7^{th}. Outlined in red is the 9 to 15 MLT region.

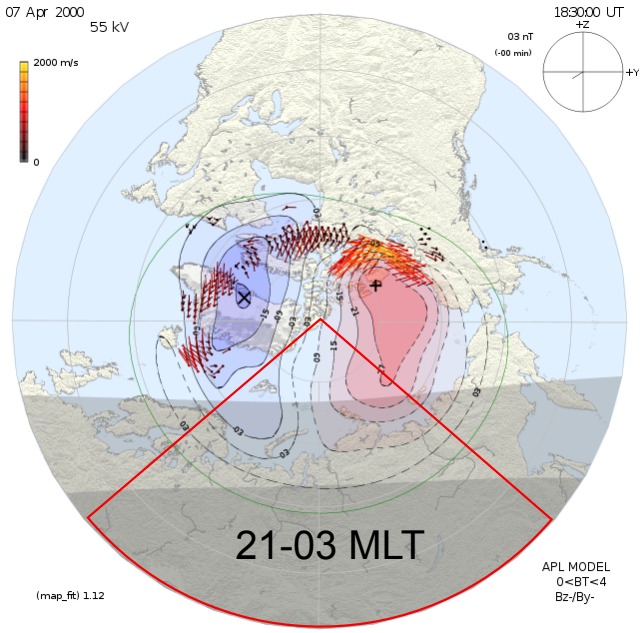

Figure 4.7: SuperDARN l-o-s velocity map for 18:30 - 18:32 UT, April 7^{th}. Outlined in red is the 21 to 03 MLT region.

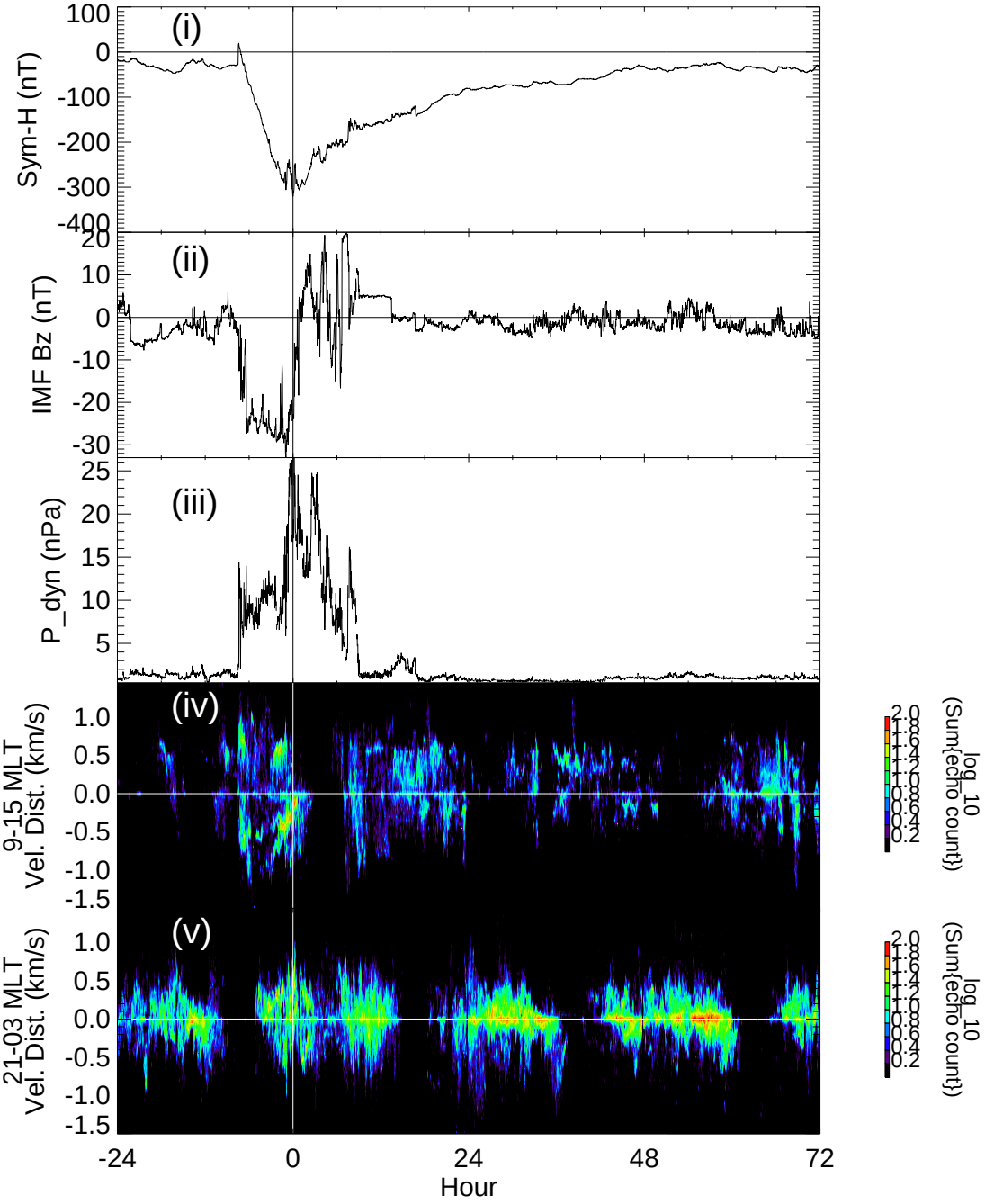

Figure 4.8: Case study of SuperDARN velocity distribution parameters for April 7^{th}, 2000. Panel (i) displays the Sym-H profile, panel (ii) the IMF B_z (GSM coordinates), panel (iii) the solar wind dynamic pressure. Panels (iv) and (v) show the SuperDARN line-of-sight velocity distributions for the 09-15 MLT (noon) and 21-03 MLT (midnight) regions, respectively. L-o-s velocities are binned in 50 m/s bins. Sunward velocity flows are positive and antisunward flows are negative. The zero epoch time is highlighted by the vertical line at t = 0 hours.

One of the benefits of a statistical approach is that if the zero epoch occurs at a random UT the data gaps are effectively removed with a large enough number of events. To achieve this, all of the events need to be superposed. Relative to the end of the main phase , all parameters, which have 1 or 2 minute cadence were averaged. In addition to the end of the main phase being easily identifiable in each event, a previous study performed by *Loewe and Prölss* (1997) showed that choosing the SSC as an epoch zero reference tends to offset the storm profile when averaging. This is due to the varied nature of the time between SSC (if present) and the magnetic storm main phase. By choosing the Sym-H minimum as the zero reference marker the three storm phases remain identifiable upon averaging of the Sym-H profile.

4.4 Superposed epoch analysis of sudden commencements

Chapter 6 focuses on another consequence of CMEs and CIRs, namely, Sudden Commencements. The SC event list discussed in section 3.2.3 was used for the event data set. From 2000 to 2007 the event list was referred to as the 'SSC' listing because, the Observatori de l'Ebre did not make the distinction between SIs and SSCs at the time. From 2008 to present, the tables are named 'SC listings' and the events labeled either SIs or SSCs depending upon their geomagnetic activity levels. For consistency between the storm and SC studies, events between 2000 and 2007 inclusive were used for both. The events were manually separated into SSC (if a geomagnetic storm followed the SC) or SI. There were 99 SI events and 106 SSC events. The zero reference epoch marker was chosen to be the SC. When superposing the events in the epoch study with this reference marker, the Sym-H storm profile blurred considerably for SSCs. Therefore care must be taken when discussing specific timing of the start or end of specific storm phases. The analysis was identical to the geomagnetic storm analysis. To illustrate the difference in zero epoch marker, the Sym-H profile and IMF B_z profile for an SI type event and and SSC type event are shown in Figures 4.9 and 4.10, respectively. In Figure 4.9 the Sym-H profile in panel (i) shows the start of an SI event and is indicated by the vertical line at t = 0 hours. Note the sudden jump in Sym-H at the onset of the SI, which is immediately followed by a brief period of increased magnetic activity before an abrupt return to pre-SI values. Displayed in panel (ii) is the IMF B_z data. Prior to the SC, the IMF B_z component oscillates around 0 nT. During the period of geomagnetic activity (t = 0 hours to t = 6 hours), the IMF B_z component is very strongly northward, at nearly 20 nT. The IMF B_z returns to near zero values as the Sym-H index level returns to pre-SC levels. Figure 4.10 shows a SSC event. Shown in panel (i) is the Sym-H profile of a standard type geomagnetic storm with the SSC at t = 0 hours marked by a dark vertical line followed by the distinct geomagnetic storm profile. Displayed in

panel (ii) is the IMF B_z profile during the event. Prior to the SC, the B_z component oscillates near -5 nT. Immediately following the SC, the B_z turns strongly negative to near -30 nT where it remains for 6 hours. A sharp increase to a strong ($\sim$15 nT) northward orientation is seen.

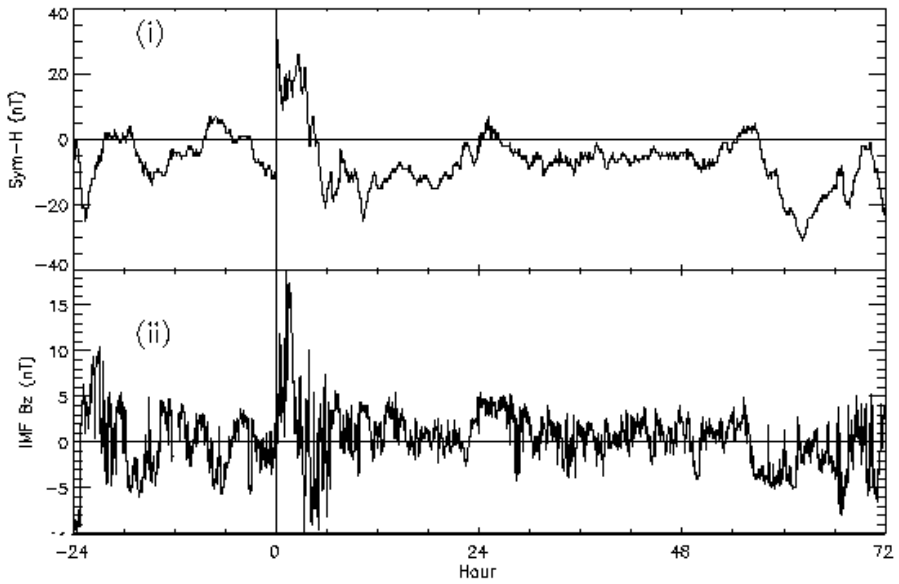

Figure 4.9: An example of an SI type event which occurred on August 27^{th}, 2001. Panel (i) displays the Sym-H profile and panel (ii) the IMF B_z (GSM coordinates). The zero epoch time is highlighted by the vertical line at t = 0 hours.

The next two chapters detail the study of CME and CIR interaction with the ionosphere using the techniques described in this chapter. Chapter 5 focuses on CME and CIR interactions with the magnetosphere and ionosphere which result in a geomagnetic storm. The ionospheric convection and echo occurrence behavior of the main and recovery phases is investigated. Chapter 6 focuses on the solar wind dynamic pressure pulse associated with CMEs and CIRs. In that chapter a study is presented of the SC resulting from a CME or CIR interacting with the magnetosphere using ground based magnetometers and SuperDARN radar data.

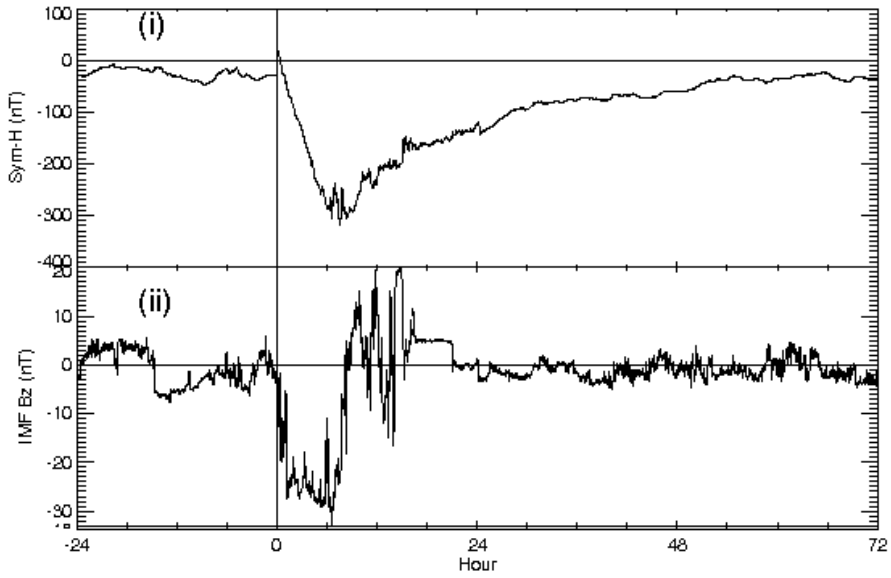

Figure 4.10: An example of an SSC type event which occurred on April 7^{th}, 2000. Panel (i) displays the Sym-H profile and panel (ii) the IMF B_z (GSM coordinates). The zero epoch time is highlighted by the vertical line at t = 0 hours.

Chapter 5

Near-space and global-scale observations during the main and recovery phases of geomagnetic storms

5.1 Introduction

The research presented in this chapter is based upon the following publication:

- Gillies, D. M., K. A. McWilliams, J.-P. St.-Maurice, and S. E. Milan (2011), Global-scale observations of ionospheric convection during geomagnetic storms, *J. Geophys. Res.*, *116*(A12238), doi:10.1029/2011JA017086

This study involved a superposed epoch analysis of 136 geomagnetic storms in the declining phase of solar cycle 23. Magnetic activity and ionospheric convection, velocities, and SuperDARN echo occurrence rates are investigated statistically relative to the start of the recovery phase.

5.2 Results

We present one of the first studies to show geomagnetic storms from the ionospheric convection and HF backscatter perspective. During the declining phase of solar cycle 23, CMEs and CIRs that resulted in geomagnetic storms were investigated using OMNI, SuperDARN, and the Sym-H index. The influence of the main and recovery phases of geomagnetic storms on ionospheric properties such as backscatter occurrence rates, velocity distributions, and convection patterns using a superposed epoch

analysis method were investigated. We found that the evolution of magnetosphere and ionosphere parameters during the storms did not depend on the origin of the storm (e.g., CME versus CIR). Instead, there was a continuum of response to the intensity of the driver. This is one of the first superposed epoch studies to analyze the sunward and antisunward line-of-sight ionospheric convection velocities as a function of MLT for geomagnetic storms of various intensities. In the noon sector, before and during the main phase of the storms, the SuperDARN radars recorded faster antisunward ionospheric plasma drifts, together with a significant increase in the number of ionospheric echoes. The SuperDARN echo occurrence in the noon sector returned to pre-storm values early in the recovery phase. The overall response was similar in the midnight sector, except that the peak echo occurrence for the most intense storms was limited to a narrower time interval centered on the end of the main phase. There were reductions in the strong antisunward flows near local midnight observed during the main phase and early in the recovery phase, particularly for the intense storm class. We also confirmed *Burton et al.*'s ring current decay time constant using an analogous study. We calculated the decay time for the recovery phase of all 136 storms and found the decay time constant to be $T = 7.2$ hours which is in good agreement with *Burton et al.*'s (1975) value of $T = 7.7$ hours. Using geomagnetic storm drivers previously classified (*Zhang et al.*, 2007; *Richardson et al.*, 2006), we determined that CMEs are the sole generators of the intense category geomagnetic storms. This agrees with the *O'Brien and McPherron* (2000) theoretical limit of -181 nT for a CIR driven geomagnetic storm.

5.3 Published Paper

Global-scale observations of ionospheric convection during geomagnetic storms

D. M. Gillies,[1] K. A. McWilliams,[1] J.-P. St. Maurice,[1] and S. E. Milan[2]

Received 19 August 2011; revised 18 October 2011; accepted 21 October 2011; published 31 December 2011.

[1] The global effects on the ionosphere during periods of intense geomagnetic activity associated with geomagnetic storms are investigated using the Super Dual Auroral Radar Network (SuperDARN). The influence of the main and recovery phases of geomagnetic storms on ionospheric properties such as backscatter occurrence rates, velocity distributions, and convection patterns are presented. The evolution of magnetosphere and ionosphere parameters during the storms did not depend on the origin of the storm (e.g., a coronal mass ejection or a corotating interaction region). Instead, there was a continuum of response to the intensity of the driver. For example, we found a clear relationship between the most negative value of the southward component of the interplanetary magnetic field (IMF B_z) and the most negative value of the Sym-H index, which marks the end of the main phase of a storm. This is one of the first superposed epoch studies that analyzes the sunward/antisunward line-of-sight velocity as a function of magnetic local time for geomagnetic storms of various intensities. In the noon sector, before and during the main phase of the storms, the SuperDARN radars recorded faster antisunward ionospheric plasma drifts together with a significant increase in the number of ionospheric echoes. This is consistent with the expected increase in soft particle precipitation in the noon sector and with the reconnection electric field that occurs when the IMF B_z is strongly negative, as is the case during the main phase of storms. The SuperDARN echo occurrence in the noon sector returned to prestorm values early in the recovery phase. The overall response was similar in the midnight sector, except that the peak echo occurrence for the most intense storms was limited to a narrower time interval centered on the end of the main phase. There were reductions in the strong antisunward flows near local midnight observed during the main phase and early in the recovery phase, particularly for the intense storm class. Strong electric fields are applied in the nightside ionosphere during storms, and the decameter structures from which SuperDARN scatter are more easily produced. However, in regions of energetic auroral precipitation and after a long exposure to strong electric fields, there is often a reduction in SuperDARN echoes due to absorption or changes in radio wave propagation.

Citation: Gillies, D. M., K. A. McWilliams, J.-P. St. Maurice, and S. E. Milan (2011), Global-scale observations of ionospheric convection during geomagnetic storms, *J. Geophys. Res.*, *116*, A12238, doi:10.1029/2011JA017086.

1. Introduction

[2] Geomagnetic storms are defined traditionally as periods of intense geomagnetic activity [*Akasofu and Chapman*, 1963a, 1963b; *Perreault and Akasofu*, 1978]. These periods of enhanced geomagnetic activity are the result of large increases in magnetospheric current systems that are reflected in ground-based magnetometer measurements. With the advent of in situ solar wind data from spacecraft, geomagnetic storms have been related to interactions of the magnetosphere with the solar wind. Southward interplanetary magnetic field (IMF) and solar wind pressure pulses are now understood to be key phenomena that cause changes in the magnetospheric current systems. A solar wind dynamic pressure pulse increases the currents at the magnetopause, and thus an increase in geomagnetic field, while a strongly southward directed IMF leads significant enhancement of the ring current due to enhanced reconnection in the tail region. This reconnection enhancement in the tail leads to more plasma being directed into the inner magnetosphere, which leads to an increase in the ring current. This increase in the ring current manifests as a depression of the H (northward) component of the geomagnetic field at equatorial and low latitudes.

[3] A "standard" geomagnetic storm has three stages: the initial phase, the main phase, and the recovery phase [*Perreault*

[1]Institute of Space and Atmospheric Studies, University of Saskatchewan, Saskatoon, Saskatchewan, Canada.
[2]Department of Physics and Astronomy, University of Leicester, Leicester, UK.

0148-0227/11/2011JA017086

and Akasofu, 1978]. A standard storm begins abruptly with a storm sudden commencement (SSC) [*Akasofu and Chapman*, 1963a, 1963b], which launches the initial phase of a storm. A SSC is characterized by a sharp increase in the Dst index in a step function–like manner. During the initial phase, the Dst can remain elevated for several hours [*Perreault and Akasofu*, 1978]. The initial phase is caused by the intensification of the magnetopause currents in response to an elevated solar wind dynamic pressure. "Gradually commencing" (GC) geomagnetic storms lack the initial phase, including the SSC, and they begin directly with the storm main phase [*Perreault and Akasofu*, 1978]. The main phase of a storm is defined by a steady decrease in the Dst. This decrease occurs due to plasma from the magnetotail being injected into the inner magnetosphere which results in an increase of the symmetric ring current. After reaching a minimum, the Dst recovers slowly, over the course of hours to days, to the initial prestorm level, and this final phase is defined as the recovery phase. During the recovery phase the ring current dissipates, presumably through scattering of the ring current ions into the loss cone (as a result of cold ionospheric plasma present in the newly expanding plasmasphere), through recombination of ring current ions forming cold neutral hydrogen [*Gonzalez et al.*, 1999], via electromagnetic ion cyclotron (EMIC) waves [e.g., *Usanova et al.*, 2010; *Sandanger et al.*, 2007], or through charge exchange with the geocorona [*Søraas et al.*, 2003]. The Sym-H index, which indicates the strength of the symmetric H component of the geomagnetic field, is often used as a proxy for Dst [*Wanliss and Showalter*, 2006] since Sym-H has a faster cadence of measurement. Storms are classified according to the maximum negative excursion in the Dst or Sym-H before the start of the recovery phase [e.g., *Perreault and Akasofu*, 1978; *Wanliss and Showalter*, 2006; *Wang et al.*, 2009]. *Tsurutani and Gonzalez* [1997] have classified geomagnetic storms into four categories based on the most extreme negative excursion of the Dst index. The Dst index during "small" storms reaches values between −50 nT and −30 nT at the end of the main phase, during "moderate" storms between −100 nT and −50 nT, during "intense" storms between −200 nT and −100 nT, and during "big" storms below −200 nT.

[4] Coronal mass ejections (CMEs) and corotating interaction regions (CIRs) having long been considered the interplanetary causes of intense (Dst ≤ −100 nT) geomagnetic storms [*Tsurutani and Gonzalez*, 1997; *Correia and de Souza*, 2005; *Denton et al.*, 2006; *Richardson et al.*, 2006, 2001]. *Borovsky and Denton* [2006] studied the solar wind and IMF properties of CMEs and CIRs related to geomagnetic storms. They reported that CME-driven geomagnetic storms are shorter in duration, have stronger ring currents (more negative Dst excursions), occur more frequently during solar maximum, and are more likely to include an SSC signature. In contrast, CIR-driven storms were reported to be longer in duration, unlikely to have an SSC signature, and more likely to occur at solar minimum. They also were reported to have a less negative Dst excursion during the main phase and therefore a weaker ring current perturbation.

[5] Statistical studies of the effect of storms on the global ionospheric convection pattern have now become feasible owing to the marked expansion of the area covered by the Super Dual Auroral Radar Network (SuperDARN) [*Greenwald et al.*, 1995; *Ruohoniemi and Baker*, 1998; *Chisham et al.*, 2007] radars. Even though the SuperDARN radars have proven thus far to be a very useful tool for the study of substorm activity and the ionospheric medium [*Grocott et al.*, 2009; *Wild and Grocott*, 2008], SuperDARN data during geomagnetic storms are only beginning to be examined. Early work has indicated that during geomagnetic storms, the number of SuperDARN echoes is reduced [e.g., *Baker et al.*, 2007]. This reduction in SuperDARN echoes could be the result of the expansion of the auroral zone, where echoes tend to originate, equatorward out of range of the SuperDARN radars used during this study.

[6] More recently, *Hutchinson et al.* [2011a] performed a similar analysis of geomagnetic storms during solar cycle 23 and confirmed the results of *Borovsky and Denton* [2006]. To further this study, *Hutchinson et al.* [2011b] created a novel way to look at SuperDARN data using a superposed latitude-time-velocity (LTV) technique. *Hutchinson et al.* [2011b] separated gridded SuperDARN plasma drift measurements into two horizontal components: north toward the geomagnetic pole and east. These components were placed in a grid that is fixed relative to the Sun-Earth line. *Hutchinson et al.* [2011b] used the LTV method to determine the mean convection pattern during weak CME-driven storms during solar cycle 23. The LTV method reveals low-latitude return flow and an increase in high-velocity ionospheric plasma drifts during the beginning of the main phase.

[7] *Kane and Makarevich* [2010] investigated the ionospheric response to geomagnetic storms using data from six low-latitude SuperDARN stations. They used the SSC as the reference point for a superposed epoch analysis. They found a decrease in SuperDARN echo occurrence beginning about 12 h after the SSC. The ionospheric convection pattern changed immediately after the SSC and was followed by longer-term signatures of enhanced convection.

[8] The present study is a first attempt at characterizing the ionospheric response to storms on a global scale. We have expanded the earlier SuperDARN storm studies by studying a large number of storms of various intensity levels, and by using all available radar data from the Northern Hemisphere SuperDARN radars. We specifically analyzed both interplanetary parameters (such as IMF conditions, solar wind pressure and velocity parameters, and the geomagnetic response to these properties) and ionospheric properties (such as backscatter occurrence rates, velocity distributions, and convection pattern) in an effort to understand how geomagnetic storms evolve and how they influence the near-space environment.

2. Methodology: Data Sets

[9] We have opted to use the Sym-H index to quantify geomagnetic activity levels during storms. We favored the higher resolution magnetic activity monitoring of the 1 min Sym-H over the hourly Dst values to better compare with the 2 min SuperDARN data and the 1 min solar wind data.

[10] The solar wind and IMF data were obtained from the Operating Missions as Nodes on the Internet (OMNI) web-based database (http://nssdc.gsfc.nasa.gov/omniweb). OMNI data are processed using the phase front propagation technique of *Weimer et al.* [2003] and *Weimer* [2004] that time shifts the spacecraft data to 17 Earth radii upstream of Earth. This enables better comparisons of

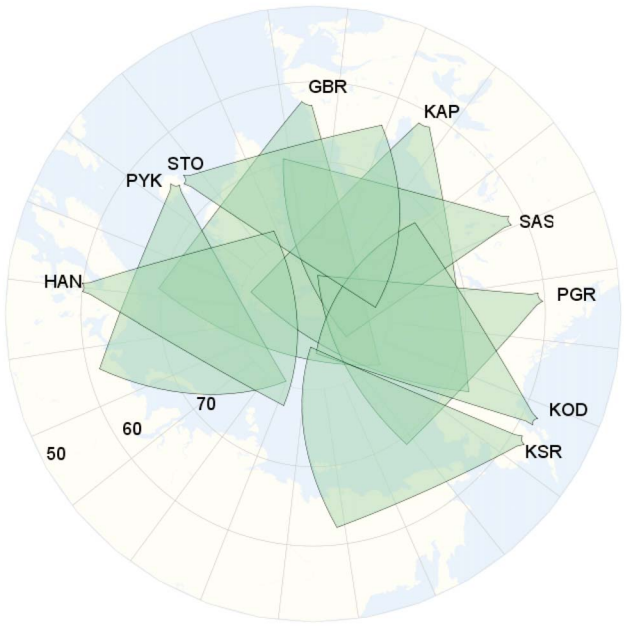

Figure 1. Fields of view for the nine SuperDARN radars operating in the Northern Hemisphere considered during the time period of this study. Solid grey lines represent concentric lines of magnetic latitude starting at 50°, 60°, and 70°. Radars operating as of 2000 are Saskatoon (SAS), Goose Bay (GBR), Kapuskasing (KAP), Stokkseyri (STO), Hankasalmi (HAN), Pykkvibaer (PYK), Prince George (PGR), and Kodiak (KOD). King Salmon (KSR) added in 2001.

upstream solar wind and IMF measurements and geomagnetic observations.

[11] To study the ionospheric convection during geomagnetic storms we have utilized SuperDARN data [*Greenwald et al.*, 1995; *Chisham et al.*, 2007]. SuperDARN monitors convection in the midlatitude to high-latitude ionosphere and provides global ionospheric convection maps of the Northern and Southern Hemispheres. SuperDARN is a high-frequency coherent scatter radar network that operates in the 8–20 MHz range. Every SuperDARN radar can perform a sweep of its entire field of view every 1 or 2 min depending on the scan mode. Each radar has a field of view (FOV) consisting of 16 sequentially scanned beam positions separated in azimuth by ~3.24° providing a full field of view of 52°. In standard operating mode, each beam consists of 75 range gates, each 45 km in length, with the first range gate starting 180 km from the radar site. We show in Figure 1 the FOV of the radars used in the study. In 2000, 8 of the 9 radars were operational: Saskatoon, Goose Bay, Kapuskasing, Stokkseyri, Hankasalmi, Pykkvibaer, Prince George, and Kodiak. In 2001, the King Salmon radar became operational. Radio waves scatter back to the radars from decameter ionospheric irregularities that are aligned with the geomagnetic field lines. The Doppler shift of the received radar signal provides an estimate of the line-of-sight component of the measured $\mathbf{E} \times \mathbf{B}$ convection velocity. When the line-of-sight velocity data from all radars are processed using assimilation techniques, a global-scale convection pattern can be produced every 1 or 2 min [*Baker and Wing*, 1989; *Ruohoniemi and Baker*, 1998].

3. Event Selection and Epoch Analysis

3.1. Storm Identification

[12] We examined both the variation in the number of echoes recorded by the radars and the changes in the measured ionospheric convection velocity. In contrast to *Kane and Makarevich* [2010], we used the beginning of the recovery phase, rather than the SSC, as our zero epoch reference time. We avoided using the SSC as a common marker since not all storms have SSCs. *Loewe and Prölss* [1997] have shown that, due to the varied nature of the time between SSC and the magnetic storm main phase, choosing the SSC as an epoch zero reference tends to offset the storm profile when averaging occurs. We also included gradually commencing storms in our event set and these lack a SSC signature. By choosing the end of the main phase as our zero reference marker the three storm phases remain identifiable. *Hutchinson et al.* [2011a] chose to isolate the geomagnetic storm phases into initial, main, and recovery. They normalized the duration of each of the three storm phases for all 143 storms. Since the main phase of a geomagnetic storm begins gradually, it can be difficult to exactly determine the start of the main phase. In contrast, the most negative excursion at the end of the main phase is easily identifiable in every geomagnetic storm. We separated the geomagnetic storms into three different intensity levels according to the Sym-H value at the end of the main phase: weak–moderate (-100 nT $\leq$ Sym-H < -30 nT), strong (-180 nT $\leq$ Sym-H < -100 nT), and intense (Sym-H < -180 nT).

[13] Our selection criteria required a well-defined main phase during which the Sym-H index drops to -30 nT or lower for at least 1 h. In addition to this, there had to be a clear Sym-H minimum and a clear recovery phase in the storm. An initial phase was not required, meaning that we included gradually commencing storms [*Perreault and Akasofu*, 1978] in the study. These selection criteria are consistent with those established by *Loewe and Prölss* [1997]. We also required that the storm duration exceed 10 h. This was quantified as the time between the storm onset and a return of Sym-H to 20% of prestorm levels during the recovery phase. This criterion was added in an attempt to eliminate large substorms from our event list. Finally, we rejected storms if a subsequent event, defined as the beginning of the main phase of a subsequent storm, occurred within 24 h of the main phase of the initial event so as to eliminate multiple storm effects. A visual inspection of the Sym-H index revealed 136 storms satisfying our selection criteria between 2000 and 2007, inclusive. These events form the basis of our study. For each storm we set the zero epoch time to be the deepest minimum excursion of the Sym-H, which marks the end of the main phase and the beginning of the recovery phase.

[14] *Zhang et al.* [2007] studied geomagnetic storms with a Dst minimum lower than -100 nT that occurred during the years 1996 through 2005. We have cross referenced our Sym-H-derived event set with their Dst-derived event set for storms from 2000 to 2005. Our event list is comprised of 22 intense storms, and 21 events occurred in 2000–2005, inclusive. All 21 events were identified by *Zhang et al.* [2007] as CME-driven

geomagnetic storms. Our remaining event occurred in 2006 and was outside the dates covered by *Zhang et al.* [2007]; however, a study of the IMF and solar wind parameters during this remaining event strongly suggests it was a CME-driven event. Thus, it is with great confidence that our intense storm class is CME-driven.

[15] Our strong geomagnetic storm class consists of 52 storms. *Zhang et al.* [2007] used the Dst index to characterize the geomagnetic activity during storms. The Sym-H index and the Dst index are determined using data from different magnetometers, meaning that the Dst cutoff of −180 nT established by *Zhang et al.* [2007] will produce a slightly different list of storms than those identified using the same value of −180 nT for the Sym-H minimum. The difference, however, was very small. Of the 43 events in our strong storm class that corresponded with the events in the work of *Zhang et al.* [2007], 79% were CME driven, 14% were CIR driven, and 7% were from unclassified sources.

[16] Our weak–moderate class of geomagnetic storms consisted of 62 events. Events of this Sym-H magnitude are usually not included in CME/CIR studies of storms, but due to the slight difference in the Sym-H and Dst near 100 nT, a few weak–moderate events had been included in previous work. *Zhang et al.* [2007] identified three of our weak–moderate events as CME driven and two as CIR driven.

[17] It is clear that all three storm classes include events associated with CMEs. In contrast, only the weak–moderate and the strong storms classes include events associated with CIRs.

3.2. Superposed Epoch Analysis of Storms

[18] We performed a superposed epoch analysis of the data during storms using the end of the main phase as the zero epoch time, t = 0 h. We considered the Sym-H index, the interplanetary electric field ($\mathbf{E} = -\mathbf{v} \times \mathbf{B}$, where **E** is the electric field, **v** is the solar wind flow speed, and **B** is the IMF), the IMF B_y and B_z GSM components, the solar wind flow speed and dynamic pressure, and the SuperDARN ionospheric echo occurrence and convection velocity data. The data for 24 h prior and 72 h after the zero epoch time were analyzed.

4. Results

4.1. Solar Wind and Interplanetary Magnetic Field Data

[19] The first step in our study was to examine how the various interplanetary parameters were related to our three classes of geomagnetic storms. We show in Figure 2 the mean IMF and solar wind data for our three storm categories. No additional time shifting was done to the OMNI data, so all solar wind parameters shown are shifted 17 Earth radii upstream of the Earth. Intense storms are denoted with a blue line, strong storms with a black line, and weak–moderate storms with a red line.

[20] As seen in Figure 2, the weak–moderate (red line) and strong (black line) classes have similar profiles for Sym-H, IMF B_z, P_{dyn}, and flow speed (Figures 2a–2d). The weak–moderate (red line) and strong (black line) storms have similar Sym-H variations. There is very little evidence for an initial phase associated with SSCs in this averaged picture. Instead, both types of storms begin with a relatively steady drop of the Sym-H index similar to a gradually commencing geomagnetic storm. The weak–moderate and strong storms also have similar IMF B_z behavior. Each begins with a near-zero IMF B_z component at $t = -24$ h. The IMF B_z component turns southward, which generally initiates the start of the main phase at $t = -7$ h in both categories. The IMF B_z component turns northward at roughly $t = -0.5$ h in both cases, which ceases loading of the tail due to reconnection. Prior to the weak–moderate storms the solar wind speed is approximately 400 km/s, and the prestorm value for the strong storms is nearly 450 km/s. There is a gradual increase in solar wind speed for both classes to about 500 km/s at $t = 0$ and this speed is maintained for both storm classes for the duration of the event.

[21] The intense geomagnetic storms (blue line) exhibit a solar wind and IMF profile seen in CME-driven geomagnetic storm profiles [*Hutchinson et al.*, 2011a], with characteristics such as sharp increases in solar wind dynamic pressure and flow speed. At $t = -10$ h, there is an increase in Sym-H that lasts for ∼2 h, which is related to SSCs. During all of the main phase and part of the recovery phase there is a very high solar wind dynamic pressure (∼19 nPa) and strongly southward IMF B_z component (∼−30 nT), as seen in Figures 2b and 2d, respectively. Unlike the other storm classes, the increase in solar wind flow speed is more abrupt (increasing from 500 to 700 km/s in 2 h) and reaches higher velocities (700 km/s on average).

4.1.1. What Drives Magnetic Storms?

[22] In Figure 2 there is a clear correspondence between the intensity of the IMF B_z and the intensity of the storm classes, with the minimum in B_z preceding the minimum in the Sym-H index by roughly 2 h. The delay is longest for the intense storms, and shorter for weaker storms. Storm intensity appears to be closely related to how negative the IMF B_z becomes during a storm. A similar conclusion was reached by *Echer et al.* [2008] who studied storms with Dst ≤ −100 nT. They concluded that the east-west component of the interplanetary electric field and the southward component of the IMF were good predictors of the intensity of these very strong storms.

[23] The analysis of *Echer et al.* [2008] only included those storms that would fall into our intense storm class. We repeated the analysis for all three of our storm classes. We found that the most negative value of the IMF B_z component during a storm was well correlated with the Sym-H value at the end of the storm main phase. Our results are shown in Figure 3. The correlation coefficient of the linear fit of the IMF B_z, in Figure 3a, and the Sym-H index was 0.8. The trend was evident in the data from all three of our storm classes, and the correlation coefficient was higher for all three classes (r = 0.81) than for the intense storms alone (r = 0.763). Note that the three storm classes are indistinguishable in Figure 3 suggesting a continuum of response, regardless of system driver. We obtained an equally good correlation coefficient for the linear fit to the *y* component of the interplanetary electric field and the Sym-H index. The minimum Sym-H was better correlated with the IMF B_z and the interplanetary electric field y component (GSM coordinate system) than any other solar wind or IMF parameter. The correlation between the interplanetary electric field y component and Sym-H (r = 0.79), in Figure 3b, suggests that the increased merging rate at the front of the magnetosphere leads to a predictable increase in

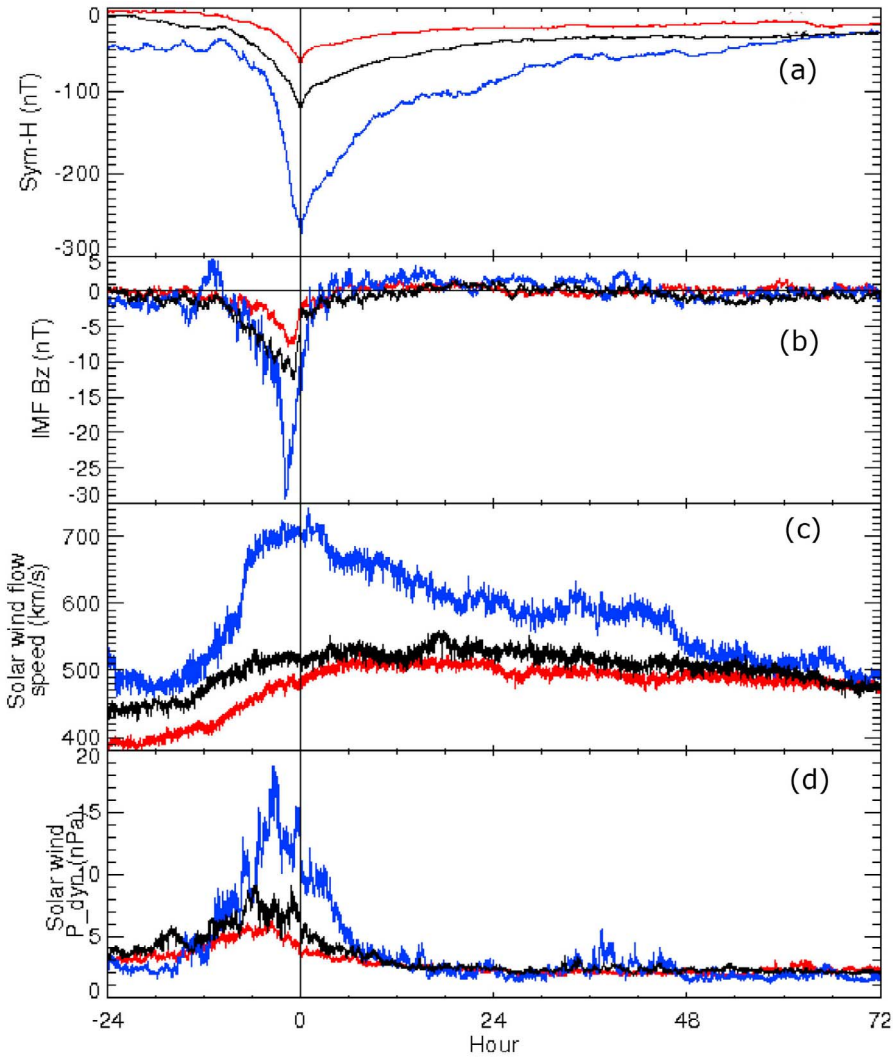

Figure 2. Averaged Sym-H and solar wind data for the three geomagnetic storm intensity categories. The intense, strong, and weak–medium storm categories are plotted using blue, black, and red lines, respectively. (a) The mean Sym-H profile, (b) the mean IMF B_z, (c) mean solar wind flow speed, and (d) the solar wind dynamic pressure. The zero epoch time is marked by the black vertical line at $t = 0$ h.

the diamagnetic ring current, most likely through the injection of current carriers following increased reconnection on the nightside. The duration of the recovery phase is much longer than the rapid return of the IMF B_z to prestorm values, and the Sym-H evidence of the persistent ring current indicates that the mechanism for loss of ring current particles is slower than mechanisms for loading. Mechanisms for the loss of ring current particles have been extensively studied in the past [e.g., *Søraas et al.*, 2002, 2003; *Burton et al.*, 1975].

4.2. SuperDARN Echo Occurrence During Storms

[24] The main focus of this study is to look at the overall changes to ionospheric convection patterns in response to geomagnetic storms of varying intensities. Although SuperDARN covers a large portion of the high-latitude Northern Hemisphere, the individual radars are stationary and their FOV has spatial and temporal limitations. As a geomagnetic storm progresses, an individual radar may move through different regions of the auroral oval, and thus be monitoring different phenomena. It is important to be able to distinguish and properly identify the data in a meaningful way. The uneven distribution of SuperDARN radars around the northern auroral zone and polar cap can be problematic when interpreting changes in the data occurrence rate due to geophysical phenomena. Our objective in considering an epoch analysis of a large number of storms has been to exploit the random distribution of storm onset times to produce geophysically meaningful SuperDARN data in all local time sectors. In that respect our approach differs considerably from the one by *Kane and Makarevich* [2010], where only a small subset of radars was used for the echo occurrence and only one radar was used for a study of the ionospheric convection velocities.

[25] We used the data gridding portion of the convection mapping algorithm of *Ruohoniemi and Baker* [1998] to process the SuperDARN data from all northern SuperDARN

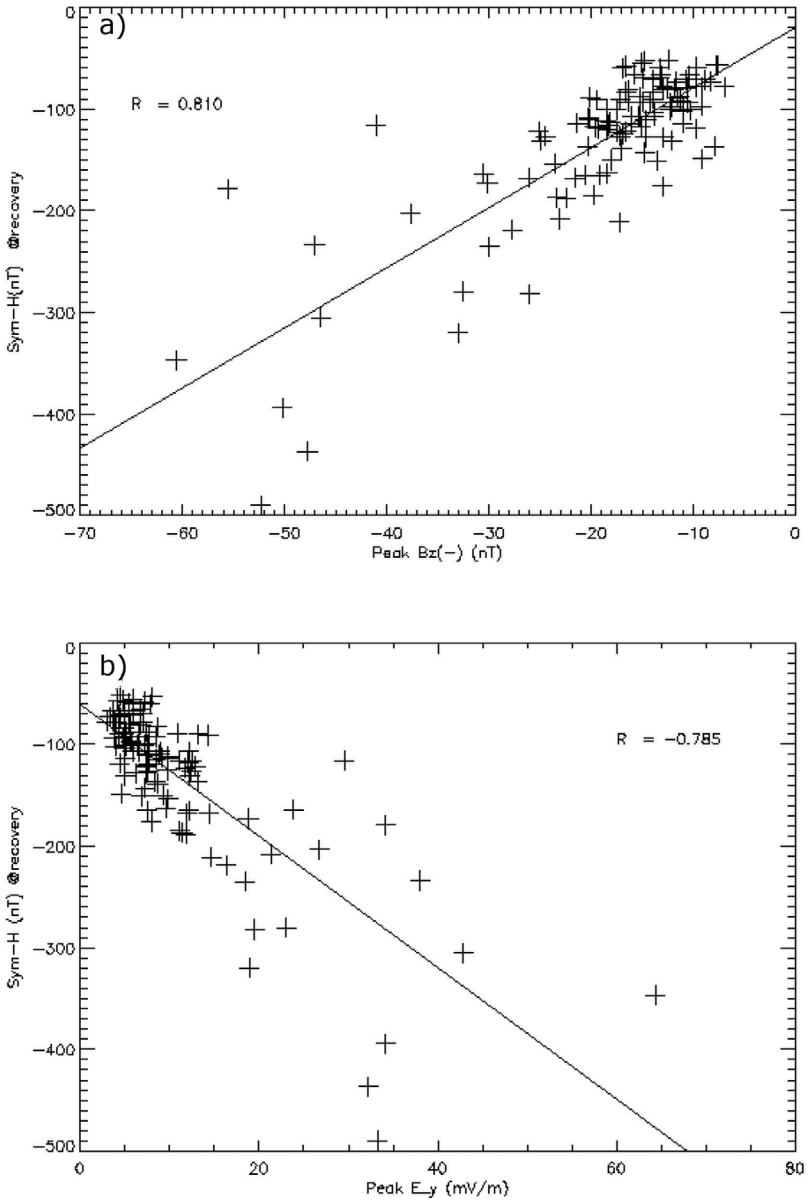

Figure 3. Scatterplots of (a) the most negative IMF B_z excursion versus the most negative Sym-H excursion and (b) the y GSM component of the interplanetary electric field versus Sym-H. Storms from all three classes are included. Superimposed on each is the best fit line from the linear regression.

radars available during the study. This portion of the algorithm places all SuperDARN data from all available radars into an equal-area magnetic local time (MLT)/magnetic latitude grid. This grid is defined by a spatial scale of 1° of latitude, the equivalent of 111 km projected onto the Earth's surface. The integer number of gridded cells n for each latitude is determined by $n(\theta) = 360° \sin(\theta)$, where θ is the magnetic colatitude, and n is rounded off to the nearest integer [*Ruohoniemi and Baker*, 1998]. We used the line-of-sight velocity vectors placed in the equal-area MLT/magnetic latitude grid. Later on in the processing, the antisunward and sunward line-of-sight components are discussed in more detail.

[26] We present the SuperDARN echo occurrence for all northern SuperDARN radars in Figure 4. Only ionospheric echoes were included in our study. Ground scatter has been flagged and rejected by the mapping algorithm [*Ruohoniemi and Baker*, 1998]. Near-range ionospheric echoes were excluded to reduce the likelihood of including E region echoes. Echoes between 180 and 450 km from radar are statistically more likely to be E region echoes as the radio wave passes through to the F region. The SuperDARN echo occurrence is the number of ionospheric echoes recorded by all Northern Hemisphere radars in a 2 min interval. We chose a 2 min interval since the majority of the radars were synchronized to perform scans every 2 min during the years of interest. We used the coordinates at the center of the grid cell to which a data point was assigned as the location of the velocity measurement.

[27] Figure 4a is a repeat of the averaged Sym-H profiles for all three storm classes, for reference. Again, intense storms are plotted in blue, strong storms in black, and weak–

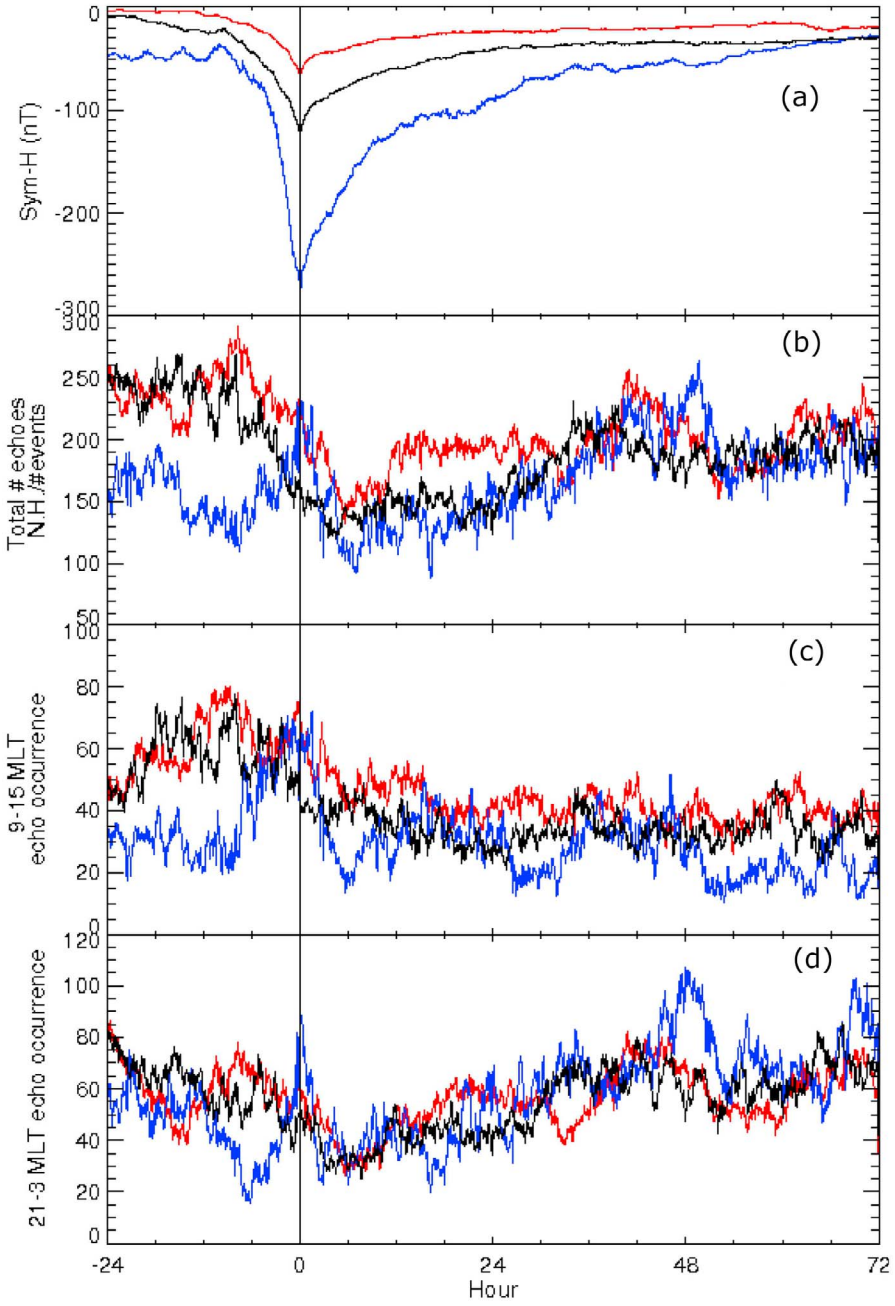

Figure 4. The superposed epoch plots of SuperDARN echo occurrence for the three storm classes. Intense storms are plotted in blue, strong storms are plotted in black, and weak–moderate storms are plotted in red. (a) The mean Sym-H index profile. (b) The mean echo occurrence from all Northern Hemisphere radars for each geomagnetic storm category for all MLTs and latitudes. (c) The mean echo occurrence for the 09–15 MLT (noon) region for each storm class. (d) The mean echo occurrence for the 21–03 MLT (midnight). The zero epoch reference marker is shown by the black vertical line at t = 0 h.

moderate storms in red. In Figure 4b we present the average number of ionospheric echoes for each storm class, recorded by all available northern SuperDARN radars. Prior to the onset of the initial phase of the intense storms (blue) the average echo occurrence remains relatively steady between 150 and 200 echoes per 2 min. Around $t = -15$ h there is a reduction in the echo occurrence to between 100 and 150 echoes per 2 min. The averaged main phase onset occurs at roughly $t = -7$ h, when a gradual increase in echo occurrence begins, from about 120 echoes. This increase continues until a peak is reached, roughly 200–240 echoes, at the end of the main phase at $t = 0$ h. During the recovery phase the echo occurrence decreases to approximately 100 approximately 7 h after recovery phase onset. Over the next 3 days there is a gradual return of the SuperDARN echo occurrence to prestorm levels, around 100 echoes per 2 min.

For strong (black) and weak–moderate (red) storms the echo occurrence is high, roughly 250 echoes, before the onset of the main phase at $t = -8$ h. The echo occurrence then drops to between 100 and 150 echoes by $t = 6$ h, well into the recovery phase, at which time it begins to slowly recover to prestorm values, roughly 200 echoes per 2 min.

[28] To examine dayside and nightside echo occurrence separately, we considered a subset of the mean Northern Hemisphere SuperDARN data in two large MLT sector sections: "noon" (9–15 MLT) and "midnight" (21–03 MLT). The noon sector data are presented in Figure 4c, and the midnight sector data are in Figure 4d.

[29] In the noon sector prior to $t = -8$ h the echo occurrence for intense storms is steady near 30 echoes. The echo occurrence increases from 30 $\sim$ 50 echoes rather abruptly at the onset of the main phase of the intense storms, gradually increasing to about 70 echoes by the end of the main phase at t = 0 h. In contrast, the strong (black) and weak–moderate (red) storms remain relatively stable between 60 to 80 echoes in the noon sector prior to $t = 0$ h. Following $t = 0$ h, the intense storms have a large decrease in the noon sector echo occurrence early in the recovery phase, to $\sim$20, while the noon echo occurrence for the strong and weak–moderate storm classes remain higher between 40 and 60. The noon echo occurrence for all storm classes then slowly converges to prestorm values during the recovery phase, to around 40 echoes per 2 min. It is important to note that there seems to be a 24 h periodicity evident in the noon sector of the intense storm class when the echo occurrence drops below 40. This is potentially due to a nonuniformity of SuperDARN radars for the 22 events in that class.

[30] In contrast to the dayside data, the echo occurrence in the midnight sector does not seem to be as closely linked to the development of the Sym-H profile during storms. For the intense storms, there is a sharp decrease in the echo occurrence at the beginning of the main phase, from 60 to 20 echoes. The number of echoes then increases quickly, during the next 6 h, to more than 80, at the end of the main phase. At the start of the recovery phase, the echo occurrence quickly drops to main phase values, of $\sim$30, and then slowly increases to prestorm values during the recovery phase. In the midnight sector the strong and weak–moderate storms experienced a decrease from about 70 to 60 echoes before the main phase. This would correspond to an initial phase for many of the storms, but the variable delay between the SSC and the end of the main phase tends to minimize the appearance of the initial phase when the zero epoch time is chosen to be at the end of the main phase. The echo occurrence for the strong and weak–moderate storms drops steadily, at a rate of roughly 5 counts per hour, during the main phase until about $t = 6$ h, when it begins recovering to prestorm values.

4.3. Ionospheric Convection During Storms

[31] While our approach is fairly straightforward for count statistics, we devised a novel strategy to study the evolution of the ionospheric convection velocity during storms. We wanted to stay as close as possible to the original measured line-of-sight SuperDARN velocity data and avoid the spherical harmonic expansion that is commonly used to produce global convection maps. This convection mapping technique [*Ruohoniemi and Baker*, 1998] interpolates data, filling any gaps in the global SuperDARN viewing area, and it also parametrizes the statistical *a priori* convection pattern, which is used as the starting point for the convection map fitting algorithm, according to the orientation of the IMF. Data gaps can be substantial at times, and, as evident in Figure 4, the number of available echoes changes throughout the storm evolution.

[32] We use line-of-sight velocity components placed into an equal area grid measured in MLT/magnetic latitude. The direction of the measured line-of-sight velocity components is determined entirely by the pointing direction of a radar beam. It was therefore important to consider carefully the direction of ionospheric flow relative to the fixed look direction. Note that the radars also rotate under the convection pattern, thus changing their geographically fixed look directions relative to the convection pattern, throughout the storms. We subdivided the line-of-sight velocity data into two groups: those with a component in the $+x$ GSM direction (sunward) and those in the $-x$ GSM direction (antisunward). Antisunward flows were defined as "negative," while sunward flows were defined as "positive." The determination of flow direction (sunward or antisunward) was assigned regardless of the degree to which a vector had a sunward or antisunward component. In this paper we are taking a first step toward examining sunward and antisunward flow statistics. While this method is relatively crude, it has revealed important information about the ionospheric convection velocity during storms.

[33] With the magnitude and flow direction of each line-of-sight measurement, we performed a superposed epoch analysis of the SuperDARN velocity data sets for the three storm classes. The results for the intense, strong, and weak–moderate storms are presented in Figures 5–7, respectively. For comparison purposes, we included the Sym-H index, the IMF B_z, the IMF B_y, and the solar wind pressure in Figures 5a–5c, 6a–6c, and 7a–7c. In Figures 5d, 5e, 6d, 6e, 7d, and 7e the echo occurrence is arranged in line-of-sight velocity bins measured by the Northern Hemisphere radars at "noon" (9 to 15 MLT) and "midnight" (21 to 3 MLT), respectively. In each graph, the velocity distribution from -1.5 km/s to 1.5 km/s, measured in 50 m/s bins, is displayed in epoch time, as before. The color bar on the right hand side of each graph displays the log of the total counts of echoes at each velocity magnitude. The red color indicates a large number of echoes while the blue color indicates relatively few echoes. In Figure 5 we display the noon and midnight ionospheric drift speeds for the intense storms. In the noon sector, in Figure 5d, we find the flow to be predominantly antisunward. However, starting at $t = -7$ h, there is an intensification of the antisunward line-of-sight velocities with high counts (red) and speeds in excess of 500 m/s. The maximum occurrence of fast flows is at $t = -2$ h, the same time at which the IMF B_z reaches its most negative value. The IMF B_y is near zero until the start of the main phase where it becomes positive, reaching a maximum value of near 10 nT, at the same time the IMF B_z is most negative, before returning to near zero values by $t = 12$ h. This slightly positive behavior is not seen in the other storm categories where it remains near zero for the entire interval. The dayside fast flows disappear 3 h after zero epoch, after which time the velocity distributions return to prestorm values. In the midnight sector, in Figure 5e, before the start of the

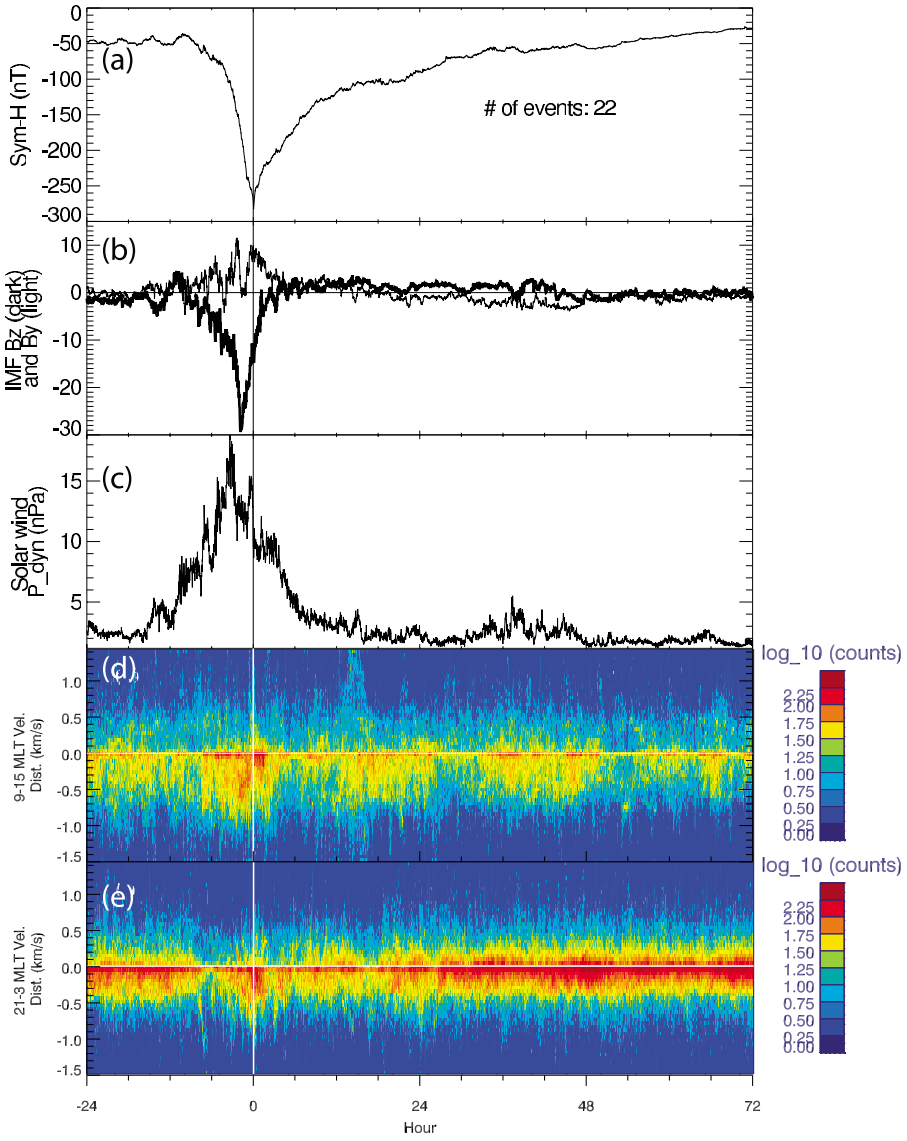

Figure 5. The mean IMF and SuperDARN parameters for 22 intense (Sym-H < −180 nT) storms. (a) The Sym-H profile, (b) the mean IMF B_z (dark line) and B_y (light line), and (c) the solar wind dynamic pressure. The SuperDARN line-of-sight (LOS) velocity distributions for the (d) 09–15 MLT (noon) and (e) 21–03 MLT (midnight) regions. LOS velocities are binned in 50 m/s bins. Sunward velocity flows are positive, and antisunward flows are negative. The zero epoch time is highlighted by the vertical line at t = 0 h.

main phase there is a marked predominance of antisunward flows slower than 500 m/s. At $t = -7$ h there is an almost complete disappearance of flows in excess of 100 m/s. After this, both the number and magnitudes of antisunward velocities gradually increase. The largest antisunward line-of-sight velocity magnitudes are seen near zero epoch. This coincides with the maximum in the nightside occurrence rate for intense storms.

[34] In Figure 6 we display the velocity distributions for the strong storms. In the noon sector, in Figure 6d, there is a high occurrence of fairly fast antisunward flows between $t = -20$ and 0 h. At $t = 0$ h the number of echoes with antisunward flows between 0.5 km/s and 0 km/s decreases markedly and remains low for the remainder of the epoch interval. In the midnight sector, in Figure 6e, before $t = 0$ h the number of sunward flows gradually decreases. Leading up to $t = 0$ there are increasing numbers of faster antisunward flows in the midnight sector. The largest asymmetry between sunward and antisunward flows is found near $t = 0$ h, with faster drifts in the midnight sector. By $t = 3$ h both sunward and antisunward flows are particularly slow, after which time there is a return to prestorm values. The largest differences between the noon and midnight sectors are between $t = 0$ and $t = 3$ h, with strong antisunward flows in the midnight sector but not in the noon sector.

[35] In Figure 7 we display velocity distributions for the weak–moderate storms. In the noon sector, in Figure 7d, we

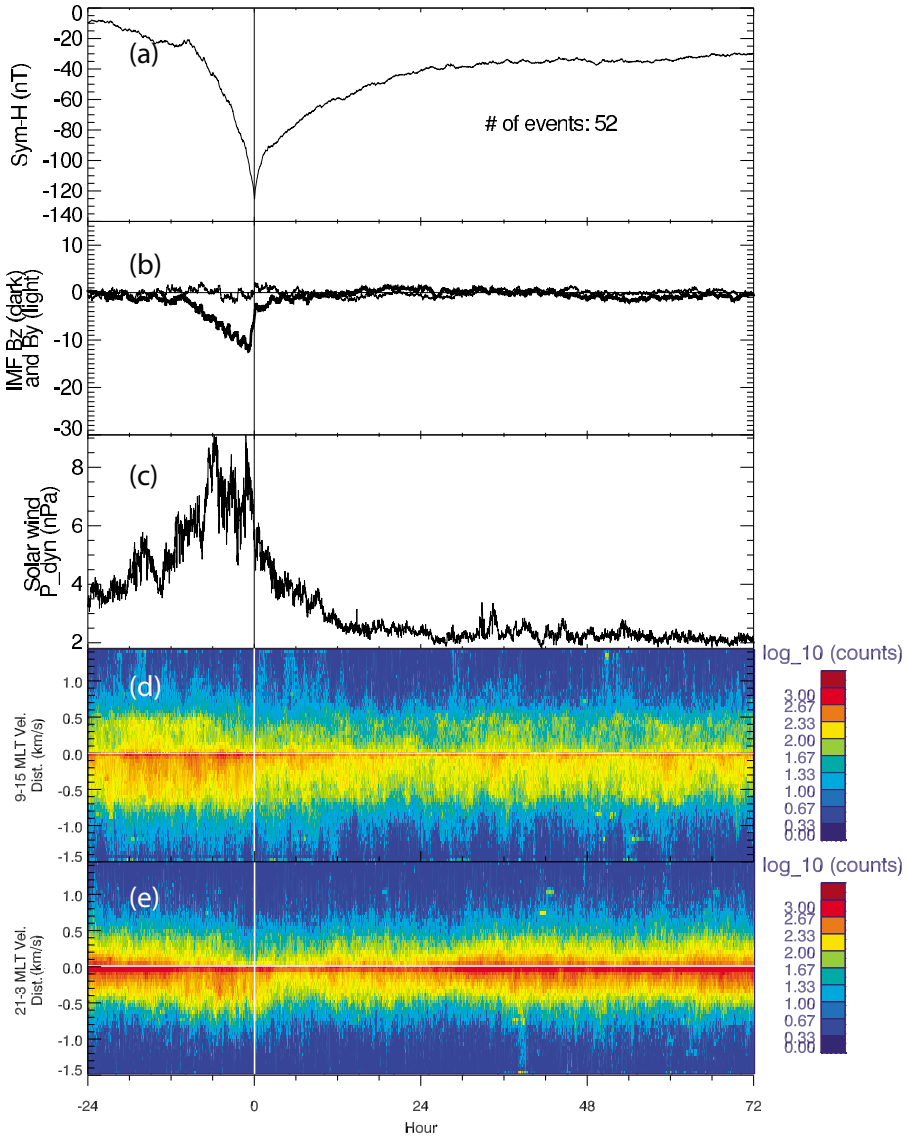

Figure 6. The mean IMF and SuperDARN parameters for 52 strong (-180 nT $\leq$ Sym-H < -100 nT) storms. (a) The Sym-H profile, (b) the mean IMF B_z (dark line) and B_y (light line), and (c) the solar wind dynamic pressure. The SuperDARN line-of-sight (LOS) velocity distributions for the (d) 09–15 MLT (noon) and (e) 21–03 MLT (midnight) regions. LOS velocities are binned in 50 m/s bins. Sunward velocity flows are positive, and antisunward flows are negative. The zero epoch time is highlighted by the vertical line at t = 0 h.

see a greater number of antisunward velocities between $t = -24$ and $t = 0$ h. Between $t = -12$ and $t = -7$ h there is a sudden increase in slow antisunward flows (an expansion of the red and orange regions), with line-of-sight velocities less than 0.5 km/s. In the midnight sector, shown in Figure 7e, we find a high concentration of antisunward line-of-sight velocities less than 0.25 km/s between $t = -24$ h and $t = -12$ h. Between $t = -12$ h and $t = 0$, there is a gradual increase in the higher (0.5 to 1 km/s) antisunward flows, and a reduction in slow moving (less than 0.5 km/s) sunward flows. At $t = 0$ the number of antisunward flows decreases and a symmetric distribution of slow moving sunward and antisunward flow occurrence resumes at $t = 6$ h, which resembles the prestorm distributions. Much like in the previous case, there is a strong reduction in the magnitude of flows, both sunward and antisunward in the midnight sector, around $t = 3$ h.

5. Discussion

5.1. Interpreting the SuperDARN Scattering Properties

[36] We are interested in the ionospheric convection response to geomagnetic storms of varying intensities. We divided the geomagnetic storms into three classes based on storm intensity and undertook a superposed epoch analysis. From our superposed epoch analysis we have seen that the

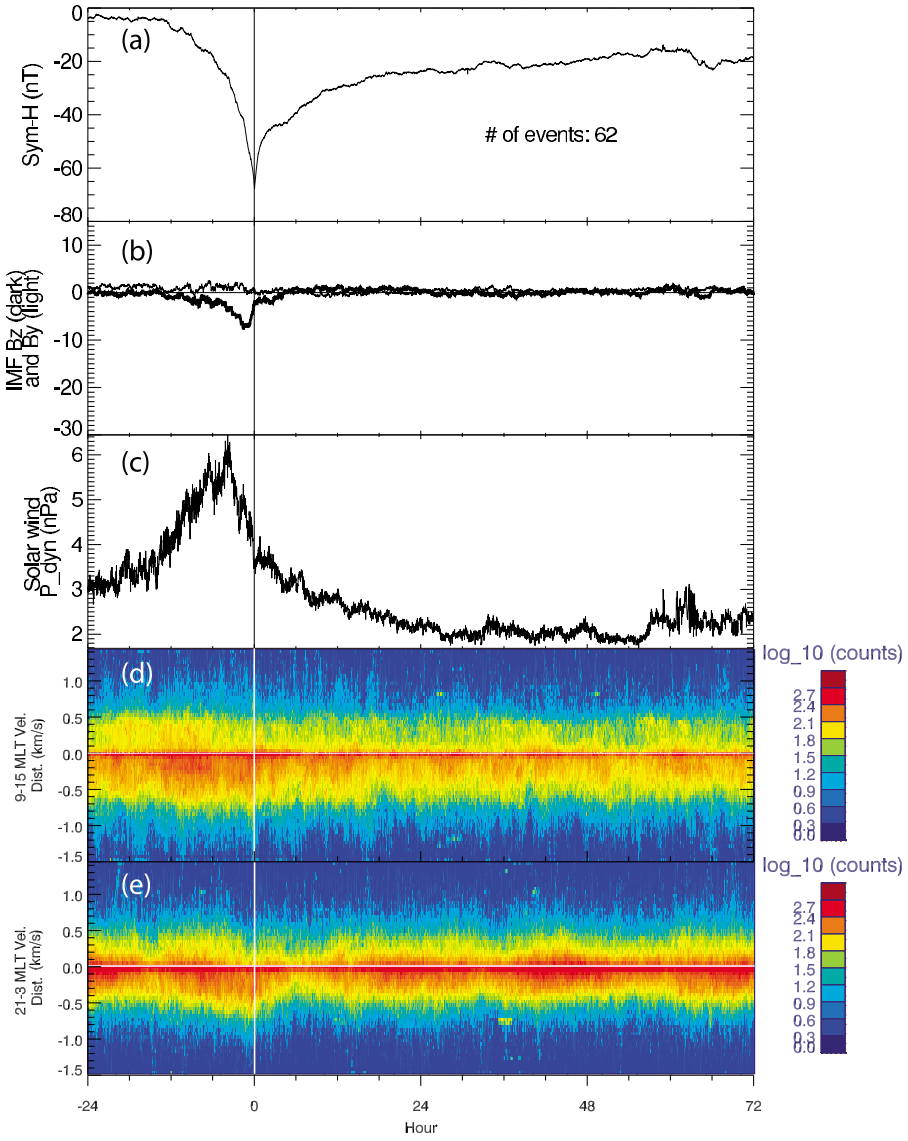

Figure 7. The mean IMF and SuperDARN parameters for 62 weak–moderate (-100 nT $\leq$ Sym-H < -30 nT) storms. (a) The Sym-H profile, (b) the mean IMF B_z (dark line) and B_y (light line), and (c) the solar wind dynamic pressure. The SuperDARN line-of-sight (LOS) velocity distributions for the (d) 09–15 MLT (noon) and (e) 21–03 MLT (midnight) regions. LOS velocities are binned in 50 m/s bins. Sunward velocity flows are positive, and antisunward flows are negative. The zero epoch time is highlighted by the vertical line at t = 0 h.

storm phases affect both the Doppler shift of SuperDARN echoes and their number. The processes that affect the number of echoes were discussed at length by *Kane and Makarevich* [2010]. A strong storm can reduce the number of echoes in two ways. One way relies on particle precipitation that is energetic enough to produce enough D region ionization to absorb the HF waves or collisionally damp them until there is no meaningful signal coming back to the radars [*Hargreaves*, 1969]. This effect is particularly pronounced during solar proton events [e.g., *Van Allen et al.*, 1964; *Stauning*, 1996] when the radar echoes in the polar regions virtually disappear at all local times for prolonged periods of times. Polar cap absorption (PCA) events can also prevent the propagation of HF radio signals. However, PCA produce a global blackout of echoes for an extended period of time. This would not explain the reduction in echoes which we see isolated to the nightside limited to the 2–3 h time scale which we discussed previously. The second way involves changes in the ionospheric plasma density due to auroral particle precipitation that can eliminate viable ray paths for the HF radars to achieve scatter of the signal back to the receiver, thereby reducing the number of recorded echoes [*Gauld et al.*, 2002]. Even without precipitation this can become an issue during the "negative storms" [e.g., *Danilov and Morozova*, 1985; *Schunk and Sojka*, 1996], when the F region peak is strongly depleted through the influence of large electric fields. The electric fields increase the ion temperature through friction, thereby dramatically increasing the rate at which O^+ ions are converted into NO^+ ions. This is followed by a quick dissociative recombination of the latter

[*Schunk and Sojka*, 1996]. Depending on the electric field strength, it can take as little as 20 min for the F region to become strongly depleted through this process. Even without the screening effect of the E region, the smaller F region densities affect the strength of the received signal, which is proportional to the change in ionospheric density, such that $\Delta N^2 = N^2|\Delta N/N|^2$, where N is the ionospheric density [e.g., *Ponomarenko et al.*, 2009]. Thus, for a given electric field strength, and therefore for a given fractional change in plasma density $|\Delta N/N|$, an ambient density that decreases by one order of magnitude will decrease the signal strength (power) by two orders of magnitude (20 dB).

[37] The strong electric fields that are observed during storms are a factor that increases rather than decreases the echo occurrence. The most widely accepted mechanism for the production of F region irregularities is the gradient drift (or interchange) instability. The growth rate for the structures increases linearly with the electric field strength. The ~10 m plasma waves probed by the SuperDARN HF radars correspond to 50 mV/m electric fields. Electric fields of this magnitude should be large enough to overcome diffusion and excite the irregularity structures directly. Most of the time, however, a plasma wave with a larger wavelength is destabilized, maybe at scales as large as several 100 m. Cascading (or mode coupling) will then transfer the energy to smaller wavelengths. The smaller the electric field is, the more cascades are required and the smaller the amplitude of the 10 m plasma waves that are able to scatter radio waves back to the SuperDARN radars, to the point that the signal might not be detectable by the ground-based radars.

[38] Considering the evolution of the SuperDARN line-of-sight velocities during a storm presented in section 4.3, one notes that the more frequent noon sector echoes usually observed in the early stages of the storms also have larger Doppler speeds and therefore correspond to larger electric fields. This corroborates the notion that strong electric fields are an effective way to trigger decameter irregularities. Specifically, in the noon sector, the plasma is either sunlit or has recently been sunlit, so that the effects of plasma recombination related to strong electric fields are not as important as on the nightside, where the only plasma production mechanism is soft electron precipitation. Another option to consider is the potential transport of dense F region plasma from lower latitudes into the polar cap as the main phase electric field initiates as suggested by *Foster et al.* [2005]. This consists of a polar tongue of ionization considered to be a continuous stream of cold dense plasma confined to the global convection pattern. During storm time, the enhanced density is convected from lower latitudes on the dayside by the subauroral disturbance electric field [*Foster et al.*, 2005].

[39] Another factor to consider is the changing conditions for radio wave propagation during a storm. In particular, the position of the auroral oval relative to the SuperDARN radars changes during the development of a storm. The strongly negative IMF B_z component leads to the production of a large amount of open magnetic flux on the dayside, which increases the area of the polar cap [*Milan et al.*, 2009]. As the storm progresses, the auroral oval will expand, moving equatorward over the SuperDARN radar sites, particularly in the midnight sector. As the regions of bright aurora move equatorward over the radars, they experience a depletion in echoes, due to radio wave absorption and the reduction of viable raypaths [*Gauld et al.*, 2002]. Note that for the intense storms, in particular, the echo occurrence rate drops dramatically both early in the main phase and after the end of the main phase of the storms (see Figures 4d and 5e). This is consistent with the auroral zone moving equatorward over the radars during the main phase and then contracting poleward once the dayside loading of open flux in the polar cap is reduced (when the IMF B_z component is no longer strongly southward). The very strong antisunward flows observed between these two reductions in echoes are consistent with the strong electric fields that are expected on the nightside, in the footprint of strong magnetic reconnection that is closing a substantial amount of magnetic flux in the tail. It is therefore possible that large electric fields exist during the times when the number of echoes is reduced, but we are unable to confirm this with the data sets used in the present study. Electric field data from additional instruments will be required to do so.

5.2. Evolution of Plasma Flows During Storms

5.2.1. Intense Storms

[40] We have presented the details of the sunward and antisunward ionospheric plasma drift during the main and recovery phases of storms in section 4.3. For the intense storms the fastest antisunward flows occur on the dayside when the IMF B_z reaches its most negative value, rather than at the end of the main phase when the Sym-H is at its lowest value. The increased reconnection electric field on the dayside therefore appears to be controlling the dayside plasma drifts, with strong antisunward flows entering the dayside polar cap, as expected.

[41] A second feature of interest is the strong antisunward flows, lasting for 1 to 2 h, and which are registered later in the midnight sector, just after the Sym-H index reaches its most negative value at the end of the main phase. The Sym-H minimum is itself delayed by about 2 h from the most negative IMF B_z excursion. Reconnection in the tail that injects particles into the ring current is expected to be delayed, with the maximum unloading of flux on the nightside delayed by at least as long as the time for the plasma to convect over the polar cap from the reconnection region on the dayside. It is important to note that there are also potential instrumental issues related to the polar cap size and radio wave absorption and propagation, so that the timing with SuperDARN is not as precise as desired. It does, however, appear that the nightside flow speeds are fastest at the end of the main phase. The IMF B_z component returns to prestorm values in about 4 h, while the intensified ring current, as indicated by the Sym-H data, takes more than 48 h to return to prestorm values.

5.2.2. Strong Storms

[42] In the strong storm category, again the sunward flows in the noon sector disappear, and the nightside fast antisunward flows are delayed by 2 h from the minimum in Sym-H. The noon sector flows are strong throughout the main phase of the storm, and the fast antisunward flows disappear as soon as the IMF B_z increases to small negative values. The strong class storms have more echoes on the dayside than the intense storms (see Figure 4c) prior to the main phase, and the velocity distribution in Figure 6d reveals that these flows are relatively fast, compared with the intense storms. Both

prior to the main phase and at the end of the main phase, the mean IMF B_z component was near zero, but the dayside antisunward plasma drift speeds were much higher before the main phase than they were near the end of the storm. The dayside drift speeds after the southward turning of the IMF reach much lower values, on average, than those that existed prior to the IMF turning southward. The fast antisunward flows seen prior to the southward turning of the IMF may be associated with a sharp compression of the magnetosphere during the initial phase of the storms [*Boudouridis et al.*, 2007]. The selection of the reference time as the end of the main phase leads to the initial phase of storms being offset relative to each other in the epoch analysis such that a clear initial phase is not apparent in the Sym-H profile. However, the averaging of increased antisunward velocities during offset initial phases could lead to an averaged picture with strong antisunward flows without a corresponding strongly negative IMF B_z. Note that the averaged solar wind dynamic pressure is elevated during this time (e.g., see Figure 6c).

[43] Finally, we note that after the recovery phase starts, the fast antisunward flows persist for approximately 2 h longer in the midnight sector than in the noon sector, where the strong antisunward flow terminates as soon as the IMF B_z increases to small negative values. There is also a persistence in the fast antisunward flows in the midnight sector for the intense storms for approximately 2 h after the start of the recovery phase, but the significance of this is not clear at this point. Detailed case studies will be required to understand the delays between the dayside and the nightside responses.

5.2.3. Weak–Moderate Storms

[44] Interestingly, the antisunward flows in the weak–moderate storms are as large as in the other classes and are more sustained. Like the other storm classes, the weak–moderate storms also have a reduction in the magnitude of the dayside antisunward flows when the IMF B_z becomes less negative. The nightside reduction in flows and echo occurrence, which is so clear in the intense and strong storm classes, is much more gradual for the weak–moderate storm class. There is a gradual reduction in the tailward (antisunward) flow speeds and the echo occurrence about 6 h after the onset of the recovery phase. This could, like the intense and strong storm classes, correspond to the auroral oval contracting poleward over the radar sites, but the precipitation might not be intense enough in this class as to cause such extreme disruption of radio wave propagation.

6. Conclusions

[45] We have performed a statistical analysis of SuperDARN velocities measured during geomagnetic storms. We separated the storm events into three classes: intense, strong, and weak–moderate. Based on previous studies [e.g., *Borovsky and Denton*, 2006], this subdivision was intended to separate CME- and CIR-driven storms. While the intense storm class consisted of predominately CME-driven storms, CME-driven storms occurred in all three storm classes. The most striking difference between the storm classes was that the intense storms had much larger solar wind speed and dynamic pressure preceding them.

[46] Our work has demonstrated that rather than separate classes, there is a continuum of storm intensities, as the Sym-H index appears to respond predictably to the strength of the southward IMF, regardless of storm driver. The most negative value of IMF B_z immediately preceding the end of the main phase (by several hours) is linearly correlated with the intensity of the Sym-H at the end of the main phase. The correlation was discussed by *Echer et al.* [2008], but they considered only events corresponding to our intense storm class. The continuum of storm intensity in our study suggests that their division is arbitrary. For example, it is not possible to discern distinct classes of storms in Figure 3.

[47] The superposed epoch presentation of the Sym-H index and IMF data (Figure 2) revealed that, if one uses the end of the main phase as the zero epoch time, the duration of the main phase was nearly identical for all storm classes. This is closely related to the IMF B_z driver, which also had a similar duration of the southward turning for all storm classes. The recovery phases of the three storm classes were also of similar duration, so it appears that regardless of the intensity of the driver, the ring current has a characteristic time scale with which it decays. This decay time has previously been established by *Burton et al.* [1975] to be $T = 7.7$ h [*Burton et al.*, 1975; *Søraas et al.*, 2002]. Burton et al. chose 30 intervals of constant pressure and northward IMF, plotted the decay rate (time derivative of the Dst) versus the Dst (normalized to a constant solar wind dynamic pressure), and fitted a slope of $-0.13\ \mathrm{h}^{-1}$ which corresponds to a decay time of 7.7 h. We performed an analogous study utilizing the Sym-H index with no solar wind restrictions placed on our events. However, by producing a similar plot of the derivative of the Sym-H versus the Sym-H, and calculating the slope for each storm category, we found decay times of: $T = 9.4$ h for the intense storms, $T = 6.8$ h for the strong storms, and $T = 5.1$ h for the weak–moderate storms. The strong storms were most similar to the magnitudes used in Burton et al.'s study. As mentioned earlier, the continuum in storm response suggests that storm division by magnitude is arbitrary. We calculated the decay time of all 136 storms and found the decay time to be $T = 7.2$ h which is in good agreement with Burton et al.'s value of $T = 7.7$ h. Despite the dissimilarities between the two studies, the apparent agreement between the two decay times is quite encouraging and warrants further investigation.

[48] Two SuperDARN data parameters were analyzed: the amount of ionospheric echoes recorded by the radars in the Northern Hemisphere and the ionospheric plasma drift components measured along the radar beams. All three storm classes had a reduction in the number of ionospheric echoes early in the recovery phase. The overall number of echoes in the strong and weak–moderate storm classes also decreased during the main phase, but the intense storm class behaved differently. For intense storms there was a reduction in the number of echoes prior to the main phase, which recovered gradually to prestorm values by the end of the main phase. This is expected to be related to the large SSCs and the initial phases of the intense storms. The strong and weak–moderate storm classes include more gradually commencing storms without SSC.

[49] Plasma convection over the polar cap, from the dayside to the nightside, was observed during the entire epoch interval studied. In the noon sector (9–15 MLT) both the number and the speed of the antisunward flows increased in tandem with the IMF B_z. The large southward IMF B_z leads to increased reconnection on the dayside magnetopause, and

therefore to faster antisunward flows in the noon sector ionosphere flowing into the polar cap. Faster flows were also observed in the midnight sector (21–3 MLT), but the number of recorded ionospheric echoes remain unchanged. The exception to this is the intense storm class, where there was a reduction in the midnight echoes early in the main phase, but changes in radar propagation and backscatter conditions, which are particularly erratic in the midnight sector, make it difficult to link these variations to the storms. The number of echoes is determined by the state of the ionosphere, in particular by its plasma density and the presence of irregularities. These factors are modified during the storm, so the changes in the SuperDARN data are ultimately a result of the storm. The challenge arises with their interpretation. For example, the reduction in the measured plasma drift (e.g., early in the main phase for intense storms, as presented in Figure 4d) may be due to a reduction in the plasma drift speed or a change in the direction of the drift relative to the SuperDARN radar beam. The reduction in echo occurrence may also be due to a loss of radar backscatter related to changing radio wave propagation conditions as the F region loses ionization and the E region density becomes enhanced. The plasma drifts may still be strong, but the transmitted radio waves may not be able to reach the irregularity targets and be scattered back to the receiver. A more detailed study of the radar data during storms is required, in particular in the midnight sector.

[50] Other future work will involve a better characterization of direction of the ionospheric plasma drifts. More sophisticated methods will be required to analyze the radar look directions. A study of the degree to which a radar is pointing in a direction can be implemented. This will assist in relating the plasma drifts in other local time sectors to the storm evolution, and it will also allow for an analysis of azimuthal drifts in the noon and midnight sectors.

[51] **Acknowledgments.** We thank the SOHO LASCO CME Team. This CME catalog is generated and maintained at the CDAW Data Center by NASA and the Catholic University of America in cooperation with the Naval Research Laboratory. SOHO is a project of international cooperation between ESA and NASA. We would like to thank the principal investigators of the SuperDARN radars used in this study: G. Sofko (Saskatoon, Prince George), M. Lester (Hankasalmi, Pykkvibaer), J. M. Ruohoniemi (Goose Bay, Kapuskasing), A. Marchaudon (Stokkseyri), T. Nagatsuma (King Salmon), and W. Bristow (Kodiak). We acknowledge the support of the Canadian Space Agency (CSA) and the Natural Sciences and Engineering Research Council (NSERC) to the Canadian component of the SuperDARN ground-based radar system. CUTLASS is supported by the Radio and Space Plasma Physics Group (RSPP) at the University of Leicester with support from the PPAC. Support for the Goose Bay and Kapuskasing radars are provided by the NSF and NASA. We would also like to thank the World Data Center in Kyoto, Japan, for providing the Sym-H indices. This research has been supported in part by the EU Marie Curie Early Stage Training in Space, Planetary, and Astrophysical Sciences (SPARTAN)Program and in part by the University of Saskatchewan. We acknowledge and thank NASA GSFC's Space Physics Data Facility's OMNIWeb (or CDAWeb or ftp) service for the use of OMNI data.

[52] Masaki Fujimoto would like to thank two anonymous reviewers for their assistance in evaluating this paper.

References

Akasofu, S.-I., and S. Chapman (1963a), The development of the main phase of magnetic storms, *J. Geophys. Res.*, *68*(1), 125–129, doi:10.1029/JZ068i001p00125.

Akasofu, S.-I., and S. Chapman (1963b), Magnetic storms: The simultaneous development of the main phase (DR) and of polar magnetic substorms (DP), *J. Geophys. Res.*, *68*(10), 3155–3158, doi:10.1029/JZ068i010p03155.

Baker, J. B. H., R. A. Greenwald, J. M. Ruohoniemi, K. Oksavik, J. W. Gjerloev, L. J. Paxton, and M. R. Hairston (2007), Observations of ionospheric convection from the Wallops SuperDARN radar at middle latitudes, *J. Geophys. Res.*, *112*, A01303, doi:10.1029/2006JA011982.

Baker, K. B., and S. Wing (1989), A new magnetic coordinate system for conjugate studies at high latitudes, *J. Geophys. Res.*, *94*(A7), 9139–9143, doi:10.1029/JA094iA07p09139.

Borovsky, J. E., and M. H. Denton (2006), Differences between CME-driven storms and CIR-driven storms, *J. Geophys. Res.*, *111*, A07S08, doi:10.1029/2005JA011447.

Boudouridis, A., L. R. Lyons, E. Zesta, and J. M. Ruohoniemi (2007), Dayside reconnection enhancement resulting from a solar wind dynamic pressure increase, *J. Geophys. Res.*, *112*, A06201, doi:10.1029/2006JA012141.

Burton, R. K., R. L. McPherron, and C. T. Russell (1975), An empirical relationship between interplanetary conditions and Dst, *J. Geophys. Res.*, *80*(31), 4204–4214, doi:10.1029/JA080i031p04204.

Chisham, G., et al. (2007), A decade of the Super Dual Auroral Radar Network (SuperDARN): Scientific achievements, new techniques and future directions, *Surv. Geophys.*, *28*, 33–109, doi:10.1007/s10712-007-9017-8.

Correia, E., and R. V. de Souza (2005), Identification of solar sources of major geomagnetic storms, *J. Atmos. Sol. Terr. Phys.*, *67*, 1702–1705, doi:10.1016/j.jastp.2005.03.007.

Danilov, A. D., and L. D. Morozova (1985), Ionospheric storms in the F2 region—Morphology and physics (review), *Geomagn. Aeron.*, *25*, 593–605.

Denton, M. H., J. E. Borovsky, R. M. Skoug, M. F. Thomsen, B. Lavraud, M. G. Henderson, R. L. McPherron, J. C. Zhang, and M. W. Liemohn (2006), Geomagnetic storms driven by ICME- and CIR-dominated solar wind, *J. Geophys. Res.*, *111*, A07S07, doi:10.1029/2005JA011436.

Echer, E., W. Gonzalez, B. Tsurutani, and A. Gonzalez (2008), Interplanetary conditions causing intense geomagnetic storms ($Dst \leq -100$ nT) during solar cycle 23 (1996–2006), *J. Geophys. Res.*, *113*, A05221, doi:10.1029/2007JA012744.

Foster, J. C., et al. (2005), Multiradar observations of the polar tongue of ionization, *J. Geophys. Res.*, *110*, A09S31, doi:10.1029/2004JA010928.

Gauld, J. K., T. K. Yeoman, J. A. Davies, S. E. Milan, and F. Honary (2002), SuperDARN radar HF propagation and absorption response to the substorm expansion phase, *Ann. Geophys.*, *20*, 1631–1645.

Gonzalez, W. D., B. T. Tsurutani, and A. L. Clúa de Gonzalez (1999), Interplanetary origin of geomagnetic storms, *Space Sci. Rev.*, *88*, 529–562, doi:10.1023/A:1005160129098.

Greenwald, R. A., W. A. Bristow, G. J. Sofko, C. Senior, J.-C. Cerisier, and A. Szabo (1995), Super Dual Auroral Radar Network radar imaging of dayside high-latitude convection under northward interplanetary magnetic field: Toward resolving the distorted two-cell versus multicell controversy, *J. Geophys. Res.*, *100*(A10), 19,661–19,674, doi:10.1029/95JA01215.

Grocott, A., J. A. Wild, S. E. Milan, and T. K. Yeoman (2009), Superposed epoch analysis of the ionospheric convection evolution during substorms: Onset latitude dependence, *Ann. Geophys.*, *27*, 591–600.

Hargreaves, J. K. (1969), Auroral absorption of HF radio waves in the ionosphere: A review of results from the first decade of riometry, *Proc. IEEE*, *57*, 1348–1372.

Hutchinson, J. A., D. M. Wright, and S. E. Milan (2011a), Geomagnetic storms over the last solar cycle: A superposed epoch analysis, *J. Geophys. Res.*, *116*, A09211, doi:10.1029/2011JA016463.

Hutchinson, J. A., D. M. Wright, S. E. Milan, A. Grocott, and P. D. Boakes (2011b), A new way to study geomagnetic storms, *Astron. Geophys.*, *52*, 4.20–4.23, doi:10.1111/j.1468-4004.2011.52420.x.

Kane, T. A., and R. A. Makarevich (2010), HF radar observations of the *F*-region ionospheric plasma response to storm sudden commencements, *J. Geophys. Res.*, *115*, A07320, doi:10.1029/2009JA014974.

Loewe, C. A., and G. Prölss (1997), Classification and mean behavior of magnetic storms, *J. Geophys. Res.*, *102*(A7), 14,209–14,213, doi:10.1029/96JA04020.

Milan, S. E., J. Hutchinson, P. D. Boakes, and B. Hubert (2009), Influences on the radius of the auroral oval, *Ann. Geophys.*, *27*, 2913–2924.

Perreault, P., and S.-I. Akasofu (1978), A study of geomagnetic storms, *Geophys. J. R. Astron. Soc.*, *54*, 547–573, doi:10.1111/j.1365-246X.1978.tb05494.x.

Ponomarenko, P. V., J.-P. St.-Maurice, C. L. Waters, R. G. Gillies, and A. V. Koustov (2009), Refractive index effects on the scatter volume location and Doppler velocity estimates of ionospheric HF backscatter echoes, *Ann. Geophys.*, *27*, 4207–4219.

Richardson, I. G., E. W. Cliver, and H. V. Cane (2001), Sources of geomagnetic storms for solar minimum and maximum conditions during 1972–2000, *Geophys. Res. Lett.*, *28*(13), 2569–2572.

Richardson, I. G., et al. (2006), Major geomagnetic storms ($Dst \leq -100$ nT) generated by corotating interaction regions, *J. Geophys. Res.*, *111*, A07S09, doi:10.1029/2005JA011476.

Ruohoniemi, J. M., and K. B. Baker (1998), Large-scale imaging of the high-latitude convection with Super Dual Auroral Radar Network HF radar observations, *J. Geophys. Res.*, *103*(A9), 20,797–20,811, doi:10.1029/98JA01288.

Sandanger, M., F. Søraas, K. Aarsnes, K. Oksavik, and D. S. Evans (2007), Loss of relativistic electrons: Evidence for pitch angle scattering by electromagnetic ion cyclotron waves excited by unstable ring current protons, *J. Geophys. Res.*, *112*, A12213, doi:10.1029/2006JA012138.

Schunk, R. W., and J. J. Sojka (1996), Ionosphere-thermosphere space weather issues, *J. Atmos. Terr. Phys.*, *58*, 1527–1574.

Søraas, F., K. Aarsnes, K. Oksavik, and D. S. Evans (2002), Ring current intensity estimated from low-altitude proton observations, *J. Geophys. Res.*, *107*(A7), 1149, doi:10.1029/2001JA000123.

Søraas, F., K. Oksavik, K. Aarsnes, D. S. Evans, and M. S. Greer (2003), Storm time equatorial belt: An "image" of RC behavior, *Geophys. Res. Lett.*, *30*(2), 1052, doi:10.1029/2002GL015636.

Stauning, P. (1996), Investigations of ionospheric radio wave absorption processes using imaging riometer techniques, *J. Atmos. Terr. Phys.*, *58*, 753–764.

Tsurutani, B. T., and W. D. Gonzalez (1997), The interplanetary causes of magnetic storms: A review, in *Magnetic Storms*, *Geophys. Monogr. Ser.*, vol. 98, edited by B. T. Tsurutani et al., pp. 77–89, AGU, Washington, D. C.

Usanova, M. E., et al. (2010), Conjugate ground and multisatellite observations of compression-related EMIC Pc1 waves and associated proton precipitation, *J. Geophys. Res.*, *115*, A07208, doi:10.1029/2009JA014935.

Van Allen, J. A., W. C. Lin, and H. Leinbach (1964), On the relationship between absolute solar cosmic ray intensity and riometer absorption, *J. Geophys. Res.*, *69*(21), 4481–4491, doi:10.1029/JZ069i021p04481.

Wang, C., J. B. Liu, H. Li, Z. H. Huang, J. D. Richardson, and J. R. Kan (2009), Geospace magnetic field responses to interplanetary shocks, *J. Geophys. Res.*, *114*, A05211, doi:10.1029/2008JA013794.

Wanliss, J. A., and K. M. Showalter (2006), High-resolution global storm index: *Dst* versus SYM-H, *J. Geophys. Res.*, *111*, A02202, doi:10.1029/2005JA011034.

Weimer, D. R. (2004), Correction to "Predicting interplanetary magnetic field (IMF) propagation delay times using the minimum variance technique," *J. Geophys. Res.*, *109*, A12104, doi:10.1029/2004JA010691.

Weimer, D. R., D. M. Ober, N. C. Maynard, M. R. Collier, D. J. McComas, N. F. Ness, C. W. Smith, and J. Watermann (2003), Predicting interplanetary magnetic field (IMF) propagation delay times using the minimum variance technique, *J. Geophys. Res.*, *108*(A1), 1026, doi:10.1029/2002JA009405.

Wild, J. A., and A. Grocott (2008), The influence of magnetospheric substorms on SuperDARN radar backscatter, *J. Geophys. Res.*, *113*, A04308, doi:10.1029/2007JA012910.

Zhang, J., et al. (2007), Solar and interplanetary sources of major geomagnetic storms ($Dst \leq -100$ nT) during 1996–2005, *J. Geophys. Res.*, *112*, A10102, doi:10.1029/2007JA012321.

D. M. Gillies, K. A. McWilliams, and J.-P. St. Maurice, Institute of Space and Atmospheric Science, University of Saskatchewan, 116 Science Place, Saskatoon, SK S7N 5E2, Canada. (megan.gillies@usask.ca)

S. E. Milan, Department of Physics and Astronomy, University of Leicester, University Road, Leicester LE1 7RH, UK.

Chapter 6

Near-space and global-scale observations during SC events

6.1 Introduction

The research presented in this chapter is based upon the following publication:

- Gillies, D. M., J.-P. St.-Maurice, K. A. McWilliams, and S. E. Milan (2011),Global Scale Observations of Ionospheric Convection Variation in Response to Sudden Increases in the Solar Wind Dynamic Pressure,
  J. Geophys. Res.,*117*(A04209), doi:10.1029/2011JA017255.

In Chapter 5, we investigated the ionospheric convection and SuperDARN echo occurrence during 136 geomagnetic storms occurring during the declining phase of solar cycle 23. Solar wind dynamic pressure pulses are prominent features in CME-driven solar wind, and to a lesser extent, CIR-driven structures (*Borovsky and Denton*, 2006). This paper investigates geoeffective solar wind dynamic pressure pulses resulting in SI or SSC events. During the interval 2000 to 2007, inclusive, 206 SC type events were analyzed. Ionospheric properties such as convection patterns, velocity distributions, and echo occurrence rates were investigated superposed relative to the onset of the SC event as seen by ground based magnetometers.

6.2 Results

We present in this chapter one of the first statistical studies of SC events from an ionospheric perspective. We used a superposed epoch analysis to study 205 Sudden

Commencement (SC) events between the years 2000 and 2007. We noticed that the relationship between the solar wind dynamic pressure and the Sym-H index was the same, regardless of whether the event was classified as an SI or SSC. The magnetospheric response to the sudden impulse appears to be unrelated to whether the SC was followed by a magnetic storm or not. That being said, the magnitude of the Sym-H response resulting from SSCs is greater than that observed from SI events. Data obtained from SuperDARN showed both the ionospheric plasma drift speed and the number of echoes increasing in the noon sector at SC onset. During this reduction in data, the average drift speed in the midnight sector also increased. One important result of this work was the idea that the ionosphere and ring current evolve differently in response to the solar wind pressure pulses. The Sym-H index, used to identify the SC events, responds to changes in both the magnetopause and ring currents. In the case of SI events, after the initial abrupt increase in Sym-H (due to the magnetopause current), it rapidly returns to pre-SC values. The SuperDARN data, however, were affected for a much longer time. The implication is that the ring current reacts to a sudden compression of the magnetosphere on a time scale of 10 minutes, while the convection pattern itself is affected for as long as the increase in solar wind dynamic pressure is sustained, or until a geomagnetic storm was triggered, as is the case in the SSC subset of events. The onset of the SC resulted in changes in the ionospheric velocity distribution and echo occurrence patterns. As mentioned above, this increase in echo occurrence was maintained for longer than the increased Sym-H component, with the large echo occurrence being sustained for as long as the high solar wind dynamic pressure was sustained. Also noted was a change in the velocity distribution of the ionospheric F-region plasma in the noon sector, with a clear increase in the number and strength of antisunward flows. The noon sector SuperDARN data were most clearly affected by the arrival change in solar wind dynamic pressure. However, there was also a measurable reduction in echo occurrence in the midnight sector for both SIs and SSCs. Another observation from the present study was that the use of the SC onset time for epoch reference time was ideal for monitoring the effect of pressure increases on the magnetosphere.

6.3 Published Paper

Global-scale observations of ionospheric convection variation in response to sudden increases in the solar wind dynamic pressure

D. M. Gillies,[1] J.-P. St.-Maurice,[1] K. A. McWilliams,[1] and S. Milan[2]

Received 11 October 2011; revised 23 February 2012; accepted 24 February 2012; published 11 April 2012.

[1] We have used a superposed epoch analysis to study 205 sudden commencement (SC) events detected with ground-based magnetometers between the years 2000 and 2007. The strength of the SC events was clearly correlated to the magnitude of the jump in the solar wind dynamic pressure, regardless of whether or not the SC events were followed by a magnetic storm. Data from the Super Dual Auroral Radar Network (SuperDARN) demonstrated that both the ionospheric plasma drift speed and the number of echoes increased in the noon sector in response to the increase in solar wind dynamic pressure. In contrast, the number of SuperDARN echoes in the midnight sector decreased as the solar wind dynamic pressure increased, even though the average drift speed in the midnight sector also increased. We also uncovered that the ionosphere and ring current evolve differently in response to the pressure pulses. The *SYM-H* index, which represents changes in both the magnetopause and ring currents, responded immediately and either rapidly returned to pre-SC values or progressed into the main phase of a geomagnetic storm. In contrast, the ionospheric convection data were affected for a much longer time. The implication is that the ring current reacts to a sudden compression of the magnetosphere on a time scale of 10 min, while the convection pattern itself is affected for as long as the increase in solar wind dynamic pressure is sustained, or until a geomagnetic storm was triggered, as is the case in the sudden storm commencement (SSC) subset of events.

Citation: Gillies, D. M., J.-P. St.-Maurice, K. A. McWilliams, and S. Milan (2012), Global-scale observations of ionospheric convection variation in response to sudden increases in the solar wind dynamic pressure, *J. Geophys. Res.*, *117*, A04209, doi:10.1029/2011JA017255.

1. Introduction

[2] Variations in the solar wind properties are known to produce a wide range of consequences in the Earth's magnetosphere and ionosphere. Known triggers are sudden changes in the solar wind dynamic pressure and changes in the orientation and strength of the interplanetary magnetic field (IMF) carried by the solar wind. The former often triggers a sudden change in the magnetic field value registered at ground stations, while the latter often influences the development of geomagnetic storms or substorms. For instance, a strong southward IMF is known to produce a geomagnetic storm, while a northward IMF of the same value generally does not [*Akasofu and Chapman*, 1963a, 1963b; *Gonzalez et al.*, 1994, 1999].

[3] It has been shown that geomagnetic storms can occur from multiple solar wind phenomena [*Huttunen and Koskinen*, 2004; *Borovsky and Denton*, 2006; *Zhang et al.*, 2007]. *Huttunen and Koskinen* [2004] have identified geomagnetic storms resulting from magnetic clouds, coronal mass ejections (CMEs), corotating interaction regions (CIRs), and "postshock streams." They showed that postshock streams and sheath regions create intense and long-term disturbances of the high-latitude magnetosphere. They are not typically reported as geomagnetic storms because they have little to no impact on the low-latitude magnetosphere which is monitored by *Dst* or *SYM-H*. An important finding in that study was that events that affected high-latitude activity could be followed by low-latitude activity (*SYM-H* and *Dst*) several hours later.

[4] *Gillies et al.* [2011] presented a detailed analysis of the evolution of the ionospheric plasma drift and ground magnetic field strength during storms. The focus of the present paper is to quantify ionospheric convection and echo occurrence changes triggered by sudden increases in the solar wind dynamic pressure. These particular changes in the solar wind are normally triggered by interplanetary coronal mass ejections (ICMEs) and CIRs [*Borovsky and Denton*, 2006; *Zhang et al.*, 2007], where shocks are produced by fast solar wind plasma catching up with slower solar wind plasma as it travels through interplanetary space. At distances

[1]Institute of Space and Atmospheric Studies, University of Saskatchewan, Saskatoon, Saskatchewan, Canada.
[2]Department of Physics and Astronomy, University of Leicester, Leicester, UK.

0148-0227/12/2011JA017255

greater than 1.5 AU this will create a shock formation in the solar wind. At distances of roughly 1 AU, shocks in CIR-driven solar wind are not typically seen. Instead, discontinuities defined as abrupt increases or decrease in the solar wind velocity and density are observed [*Alves et al.*, 2006; *Heber et al.*, 1999].

[5] At its most basic, a sudden increase in the solar wind dynamic pressure compresses the magnetosphere on the dayside until the magnetic pressure in the magnetosphere matches the plasma pressure in the magnetosheath [*Shue et al.*, 1997]. The magnetopause current also therefore increases with the increase in the geomagnetic field strength. This sudden enhancement of the dusk-to-dawn magnetopause current creates a sudden northward deflection of the magnetic field at the Earth's surface.

[6] Changes in the geomagnetic field are recorded on the ground by arrays of low to polar latitude magnetometers. Following suitable data assimilation and processing, they emerge as the 1 h disturbed storm time (*Dst*) index and its 1 min counterpart, the symmetric H component (*SYM-H*) index [*Wanliss and Showalter*, 2006]. The indices are used to monitor magnetic activity on a global scale and are often used for tracking the intensity and duration of magnetic storms. A sudden increase in the *Dst* or *SYM-H* index from a low stable value is called a sudden commencement (SC), and this signature is usually associated with the jumps in the solar wind dynamic pressure that we wish to study [*Akasofu and Chapman*, 1963a, 1963b]. SCs followed by a large *Dst* decrease within a few hours are considered part of a magnetic storm and are referred to as storm sudden commencements, or SSCs. In contrast, if the storm signature is not present and if the elevated *Dst* returns to the pre-impulse level, the SC is labeled as a sudden impulse (SI). Our interest in the present paper is twofold. We will (1) assess the response of the ionosphere during SCs, in general, and (2) examine whether there are any significant differences between SSCs and SIs, keeping in mind that the two phenomena ultimately diverge once a magnetic storm unfolds a few hours after a SSC.

[7] In the present study we focus on the global-scale ionospheric response to SCs using the Super Dual Auroral Radar Network (SuperDARN) [*Greenwald et al.*, 1995; *Ruohoniemi and Baker*, 1998; *Chisham et al.*, 2007]. These radars detect decameter-scale magnetic field-aligned ionospheric irregularities and, through them, observe the *F* region ionospheric plasma drift, namely, the $\mathbf{E} \times \mathbf{B}$ drift imposed by the interaction of the solar wind with the magnetosphere. The SuperDARN radars are capable of producing unprecedented global views of the ionospheric circulation, with convection maps produced every 1–2 min. The SuperDARN radars are very responsive to changes in the ionospheric convection pattern. However, like any instrument they do have their limitations. One is that they are sensitive to changes in ionospheric density due to auroral precipitation, which can absorb the radio waves or deflect them away from the regions where scattering of the radio waves back to the radars occurs [*Gauld et al.*, 2002]. In conjunction with the fact that there are gaps in coverage due to the location of the radars themselves, this introduces data gaps that can be important at times. A fact that may mitigate these limitations is that stronger electric fields are, according to linear plasma instability theory, more capable of generating intense plasma structures than weak fields. For weak electric fields one source of irregularities could be structured precipitation, which requires that there be precipitation in the first place, and this may limit the coverage to a small subset of the field of view. One way or the other, the cusp region on the dayside tends to be a region of strong echoes [*Milan et al.*, 1998]. Keeping these advantages and limitations in mind, we have used an epoch study described in more detail below to identify how the ionosphere responds during SCs. The response was clearest on the dayside, both in terms of plasma drift and of irregularity detection.

[8] This is not the first time that the effect of SCs on SuperDARN radar echoes has been studied. *Coco et al.* [2005] investigated the response of 256 pressure pulses in the solar wind dynamic pressure and concluded that an increase in the solar wind dynamic pressure caused a decrease in the number of SuperDARN echoes, and vice versa. *Coco et al.* [2005] also studied the "mean rate of scattering" (MRS) in various magnetic local time sectors and concluded that for geomagnetic quiet periods, the MRS was higher on the dayside. The events that were studied occurred under a variety of IMF B_z conditions. They concluded that the behavior of the MRS was due to SI-related physics rather than to a particular orientation of the IMF. In another study, *Boudouridis et al.* [2007] presented three case studies in which they concluded that abrupt increases in solar wind dynamic pressure resulted in strong increases in the magnitude of the dayside convection velocities recorded by SuperDARN. These solar wind dynamic pressure pulses had SSCs associated with them. *Boudouridis et al.* [2007] noted a 4 min delay between the solar wind dynamic pressure pulse and the corresponding maximum in flow magnitude on the dayside.

[9] *Kane and Makarevich* [2010] studied the *F* region ionospheric plasma response during SSCs and the ensuing storms, using a superposed epoch analysis of a small subset of SuperDARN radar data from a 5 year period. This approach was similar to a study performed by *Wild and Grocott* [2008], which focused on substorms. Compared to quiet time diurnal variations, *Kane and Makarevich* [2010] found a dramatic increase in the number of SuperDARN echoes shortly after the onset of the SSC and subdivided the echo occurrence into three distinct phases surrounding the SSC: (1) quiet levels just prior to SSC, (2) a sharp increase in echo occurrence 1 to 2 h into the main phase of the ensuing storm, and (3) a gradual return to prestorm echo conditions during the storm recovery phase. They noted a significant decrease, on average, in echo occurrence beginning approximately 12 h after the SSC, which lasted for at least 2 days. They also concluded that the initial echo response to the SSC was instantaneous, i.e., within 1 min, and that for the radars used in their study, they could not detect a latitudinal or MLT dependence.

[10] Given the somewhat contradictory results from these studies, as well as their relatively limited scopes, we have undertaken a more comprehensive study focusing on the local and global ionospheric responses to a sudden increase in the solar wind dynamic pressure. That is to say, we have used all the Northern Hemisphere SuperDARN radar data and all catalogued SCs from ground-based magnetometers during the time period 2000 to 2007 inclusive to investigate the ionospheric response to a sudden increase in the solar

wind dynamic pressure as a function of magnetic latitude and MLT. The increase in the solar wind dynamic pressure was confirmed by satellite data for all SC (both SSC and SI) events. Finally, to redress any data gaps, particularly with the unevenly spaced SuperDARN array of radars, we employed a statistical epoch study.

2. Methodology

2.1. Data Sets

[11] Three data sets are at the core of the present study. They support a broad description of the SSC and SI behavior from both an interplanetary and an Earth-based view point. For the magnetic disturbance index, we have opted for *SYM-H* rather than *Dst*, owing to the higher temporal resolution of *SYM-H*. The *SYM-H* index, which indicates the strength of the symmetric H component of the geomagnetic field, is often used instead of *Dst* [*Wanliss and Showalter*, 2006]. The *SYM-H* index is provided by the World Data Center for Geomagnetism, Kyoto (http://wdc.kugi.kyoto-u.ac.jp/), and is calculated with a 1 min resolution using data from six magnetometers at low latitudes to midlatitudes [*Iyemori*, 1990; *Wanliss and Showalter*, 2006]. The 1 min resolution of the *SYM-H* compares favorably with the 2 min resolution of the SuperDARN data and the 1 min resolution in the solar wind data.

[12] The interplanetary solar wind and IMF data were provided by the Operating Missions as Nodes (OMNI) Web-based database (http://nssdc.gsfc.nasa.gov/omniweb/). The IMF and solar wind data from OMNI were time shifted to 17 R_E upstream of the Earth, using the phase front propagation technique of *Weimer et al.* [2003; see also *Weimer*, 2004] in order to enable consistent temporal comparisons of upstream measurements and ground-based observations.

[13] To quantify the ionospheric behavior during geomagnetic storms, we have utilized the Northern Hemisphere SuperDARN radars [*Greenwald et al.*, 1995; *Ruohoniemi and Baker*, 1998; *Chisham et al.*, 2007]. SuperDARN monitors plasma convection in the midlatiude to high-latitude ionosphere and provides global ionospheric convection maps for the Northern and Southern Hemispheres. The SuperDARN radars are synchronized, and the entire network performs a complete scan every 1 or 2 min, depending on the scan mode. The signal received by the radars occurs from the scattering of radio waves from decameter-size plasma irregularities that are aligned with the geomagnetic field lines. Figure 1 shows the FOV of the radars used in the study. In 2000, eight of the nine radars were operational: Saskatoon, Goose Bay, Kapuskasing, Stokkseyri, Hankasalmi, Pykkvibaer, Prince George, and Kodiak. In 2001, the King Salmon radar became operational. The locations of the nine radars are outlined in Table 1. Radio waves scatter back to the radars from decameter ionospheric irregularities that are aligned with the geomagnetic field lines. The Doppler shift of the received radar signal provides an estimate of the line-of-sight (LOS) component of the $\mathbf{E} \times \mathbf{B}$ plasma convection velocity. The LOS velocity data from all radars can be assimilated and processed, and global-scale convection patterns are produced every 1 or 2 min [*Baker and Wing*, 1989; *Ruohoniemi and Baker*, 1998].

2.2. Processing of the SuperDARN Data

[14] We processed the SuperDARN data using the method presented by *Gillies et al.* [2011]. Our statistical epoch study used LOS velocities from all available Northern Hemisphere SuperDARN radars. Only *F* region ionospheric echoes (ranges in excess of 630 km) were included in our study. Near-range ionospheric echoes were excluded to reduce the likelihood of including *E* region echoes because the LOS velocities in the *E* region are not always a result of $\mathbf{E} \times \mathbf{B}$ drift [*Koustov et al.*, 2005]. We opted to use the directly measured LOS velocities from the SuperDARN radars rather than the reconstructed global convection maps. The convection mapping technique determines the convection pattern from spherical harmonic functions that fit best with the measured LOS velocity components, and it uses a statistical convection pattern as an a priori starting point for the algorithm. These statistical convection patterns are parameterized by the IMF orientation, and the convection maps can influence the resulting best fit convection pattern if the data are too sparse. For this reason we opted not to use fitted convection map velocity data. Instead, we used the measured LOS velocity components. It is important to note, however, that the LOS pointing directions are fixed by a radar field-of-view geometry. To take that into account, we used the standard data assimilation techniques that are part of the convection mapping process [*Ruohoniemi and Baker*, 1998], given that this procedure is done prior to any adjustment of the LOS data through the fitting routines. The data assimilation technique places LOS velocity data from all available radars into an equal-area grid. This grid is defined by a spatial scale of 1° of latitude. We classified gridded LOS velocities based on their direction along the Earth-Sun line. We defined antisunward flows to be negative and sunward flows as positive. In this very simple classification, the flow direction (sunward or antisunward) does not include information about the degree to which a vector has a sunward or antisunward component. This is only a first step toward quantifying the ionospheric convection response during SCs, more refined techniques will be devised in the future.

2.3. Event Selection and Epoch Analysis

[15] In this study SCs, which can be SSCs or SIs, are characterized by the *SYM-H* data. At a SI onset, the *SYM-H* increases in step-function-like manner and can remain above the pre-SI value for up to several hours [*Perreault and Akasofu*, 1978; *Loewe and Prölss*, 1997]. After the SI, the *SYM-H* index will return to predisturbed conditions. In the case of a SSC, the sharp increase in *SYM-H* is defined as the onset of the initial phase of a magnetic storm, during which time the *SYM-H* remains elevated for up to several hours. The initial phase is followed by the main phase of a storm, made manifest by a sharp drop in *SYM-H* of much greater magnitude than the increase seen in the initial phase. During the final recovery phase of the storm, which can last several days, the *SYM-H* index gradually returns to the levels seen before the start of the storm.

[16] Our event list was established using the list of SSC and SI events produced by Observatorio del Ebro, Roquetas, Spain (SSC tables, http://www.obsebre.es/php/geomagnetisme/variaciorap.php). The list identified 106 SSC

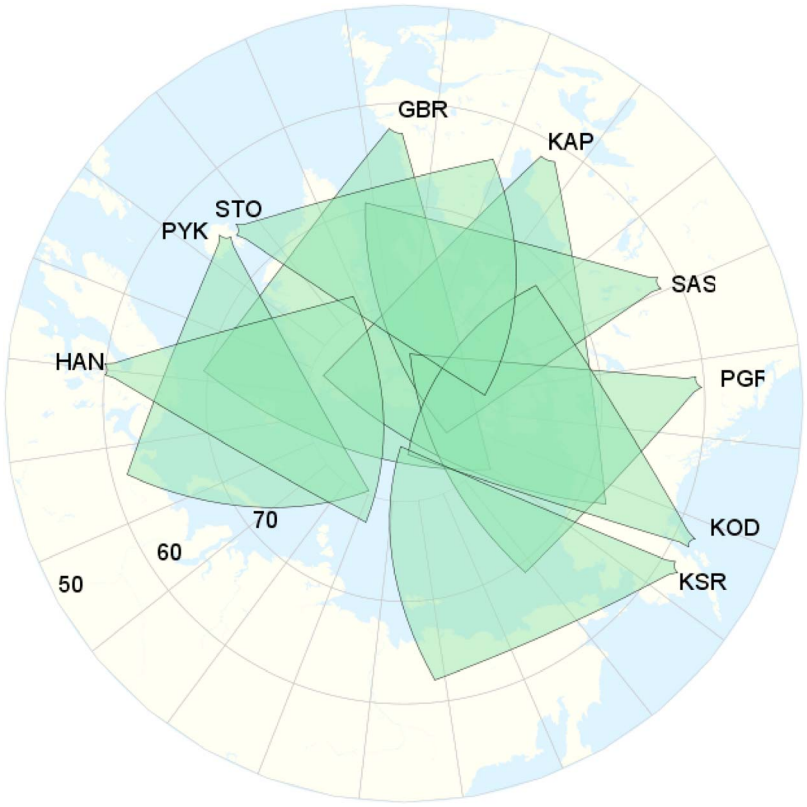

Figure 1. Field of view (FOV) of the nine Northern Hemisphere SuperDARN radars considered during this study. Solid gray lines represent concentric lines of magnetic latitude starting at 50°, 60°, and 70°. Radars correspond to Saskatoon (SAS), Goose Bay (GBR), Kapuskasing (KAP), Stokkseyri (STO), Hankasalmi (HAN), Pykkvibaer (PYK), Prince George (PGR), Kodiak (KOD), and King Salmon (KSR).

and 99 SI events between 2000 and 2007, inclusive. We used the sudden increase in *SYM-H* at the start of a SI or SSC as our zero reference marker for the epoch studies, and we examined the data during the interval starting 24 h prior to and ending 72 h after the SC.

[17] Our choice of the zero reference marker can be contrasted with our recent geomagnetic storm study [*Gillies et al.*, 2011], where we chose the zero epoch time to be at the end of the storm main phase, i.e., when the *SYM-H* reached its most negative value during the storm. Storms that have SSCs, and therefore have initial phases, have variable delays between the SSC and the end of the main phase. Selecting the end of the main phase as the reference time was appropriate for the previous study that investigated storm main and recovery phases. Using the SSC marker as the zero reference point for a storm study tends to offset the storm profiles and can blur the averaged main and recovery phase profiles of the storm [*Loewe and Prölss*, 1997]. The initial phase was of lesser importance to the storm study of *Gillies et al.* [2011]. In contrast, a study focused on the pressure pulses should use for its zero marker the stepwise increase in the *SYM-H*.

[18] Our study is based on a comparison of the *SYM-H* index, the IMF, the solar wind dynamic pressure and flow speed, and the SuperDARN ionospheric echo occurrence and LOS velocity data.

Table 1. Geographic and Geomagnetic Coordinates for the Nine Northern Hemisphere SuperDARN Radars Operating Between 2000 and 2007 Inclusive

		Geographic Coordinates		Geomagnetic Coordinates	
Radar Station	Start Year	Latitude (deg)	Longitude (deg)	Latitude (deg)	Longitude (deg)
Goose Bay	1993	53.32N	60.46W	61.94N	23.02E
Kapuskasing	1993	49.39N	82.32W	60.06N	9.22W
Saskatoon	1993	52.16N	106.53W	61.34N	45.26W
Prince George	2000	53.98N	122.59W	59.88N	65.67W
Kodiak	2000	57.60N	152.2W	57.17N	96.28W
Pykkvibaer	1995	63.86N	19.20W	64.59N	69.65E
Hankasalmi	1995	62.32N	26.61E	59.78N	105.53E
King Salmon	2001	58.68N	156.65W	57.43N	100.51E
Stokkseyri	1994	63.9N	22.0W	65.0N	67.3E

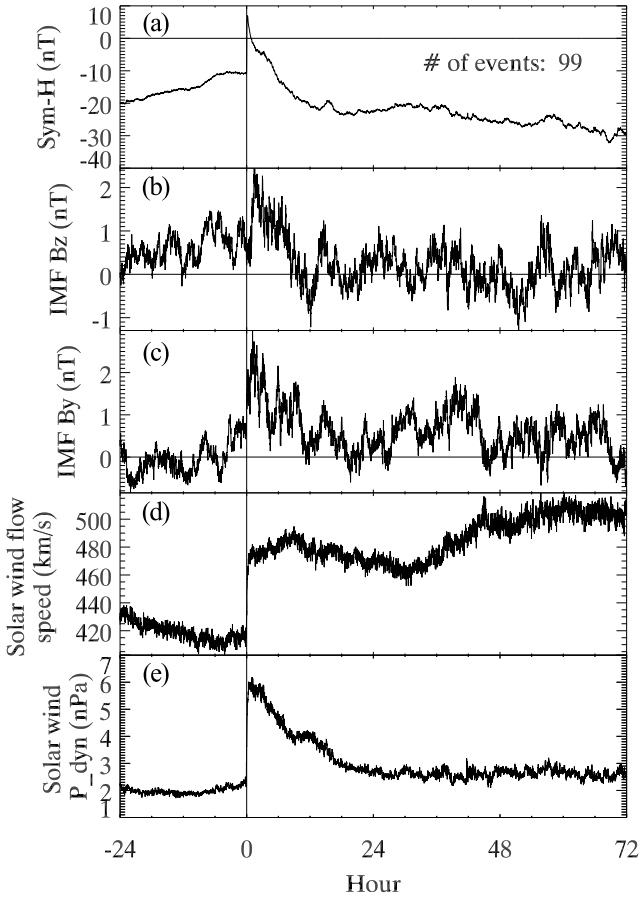

Figure 2. Solar wind and geomagnetic data for 99 SI events as a function of epoch time, in hours, relative to the onset of the SI at $t = 0$. (a) Mean *SYM-H* profile, (b) mean IMF B_z (GSM), (c) mean IMF B_y (GSM), (d) mean solar wind flow speed, and (e) solar wind dynamic pressure. The black vertical line at $t = 0$ marks the onset of the SC events.

[19] We applied the superposed epoch analysis separately to the SI and the SSC events to explore possible differences between the two types of events. Of particular interest are any differences in the upstream solar wind and IMF conditions that may determine whether a SC becomes a SI or a SSC, that is to say, whether a SC is followed by a storm or not.

3. Results of Storm Sudden Commencement Events

[20] We have performed the analysis of the SuperDARN data using two time scales. We have examined the data over the longer term (a few days), as well as over a much shorter time scale (2 h).

3.1. Sudden Impulse Events From the Longer Time Perspective

[21] For the 99 SI events between 2000 and 2007, inclusive, we performed a longer-term epoch analysis, including 24 h prior to the SI onset time to 72 h after the onset time. This 4 day time period allows us to investigate prestorm IMF, solar wind, and SuperDARN data, as well as any prolonged effects on the ionosphere following the SI, particularly in the SuperDARN data.

3.1.1. SI Solar Wind and IMF Parameters

[22] Figure 2 presents the superposed geomagnetic and solar wind data for the 99 SI events. Figure 2 includes, from top to bottom, the *SYM-H* index (Figure 2a), the IMF B_z and B_y GSM components (Figures 2b and 2c), the solar wind proton flow speed (Figure 2d) and the solar wind dynamic pressure (Figure 2e). The solar wind dynamic pressure in nPa was obtained by computing $P_{dyn} = 2 \times 10^{-6} N_p V_p^2$, where N_p is the proton density in cm^3 and V_p is the proton speed in km s^{-1}. The vertical black line centered on the epoch time $t = 0$ marks the SI onset.

[23] Figure 2a is a trace of the superposed *SYM-H* index for all SI events. Starting approximately 7 h prior to the SI, the *SYM-H* index steadily increases from −20 to −10 nT. At $t = 0$ there is, by definition, a sharp jump in *SYM-H* to +10 nT. A gradual decline to approximately −20 nT occurs over the next 20 h, after which the *SYM-H* undergoes no important change for the remainder of the epoch time interval.

[24] The average IMF B_z component, presented in Figure 2b, is weak and oscillates between 0 and 1 nT for the 24 h preceding the SI. It is small (a fraction of 1 nT) at the SI onset, but in the hour that follows the SI, the average value of B_z increases to 2 nT. It remains strongly positive, above 1 nT for approximately 8 h following the onset. After $t = 12$ h, the mean IMF B_z fluctuates between −1.5 and 1.5 for the remainder of the selected interval. Given that a superposition of diverse events is involved, the most significant feature is that B_z reaches its largest positive value of +2 nT 1 h after the SI onset. The other noticeable feature is the total absence of a trend for a southward IMF, which is consistent with the lack of a magnetic storm after this particular type of SC [*Gillies et al.*, 2011].

[25] The behavior of the mean IMF B_y component, which is presented in Figure 2c, is similar to the B_z behavior, but there is a sharp transition to elevated values that last for 1–2 h after the SI onset. Shortly after the SI, the IMF B_y reaches ∼3 nT before decreasing gradually over several hours. Through most of the epoch interval, the IMF B_y component oscillates between ±1 nT. As was the case for B_z, the main feature that stands out is the maximum positive value attained 1 to 2 h after the SI onset. We also notice the tendency for a persistent weak positive B_y for the days that follow the SI.

[26] The mean solar wind flow speed (Figure 2d) is relatively steady at 420 km s^{-1}, with a slow progression toward lower values, for 24 h prior to the SI. At $t = 0$ h there is a sharp jump to approximately 480 km s^{-1}. The speed is gradually increasing to 500 km s^{-1} by $t = 40$ h, where it remains for the rest of the selected interval. For the 24 h prior to SI, the solar wind dynamic pressure, shown in Figure 2e, is steady at approximately 2 nPa. A sharp jump to approximately 6 nPa occurs at $t = 0$, strongly suggesting that the trigger mechanism for the sharp jump in the *SYM-H* that defines the SI is the dynamic pressure. The dynamic pressure retains its maximum value for about 4 h before gradually decreasing to 3 nPa by $t = 20$ h where it remains for the next 48 h.

3.1.2. Echo Occurrence and Convection Velocity

[27] In Figure 3, we present the superposed SuperDARN echo occurrence. The echo occurrence is calculated as the total number of ionospheric echoes recorded by all northern

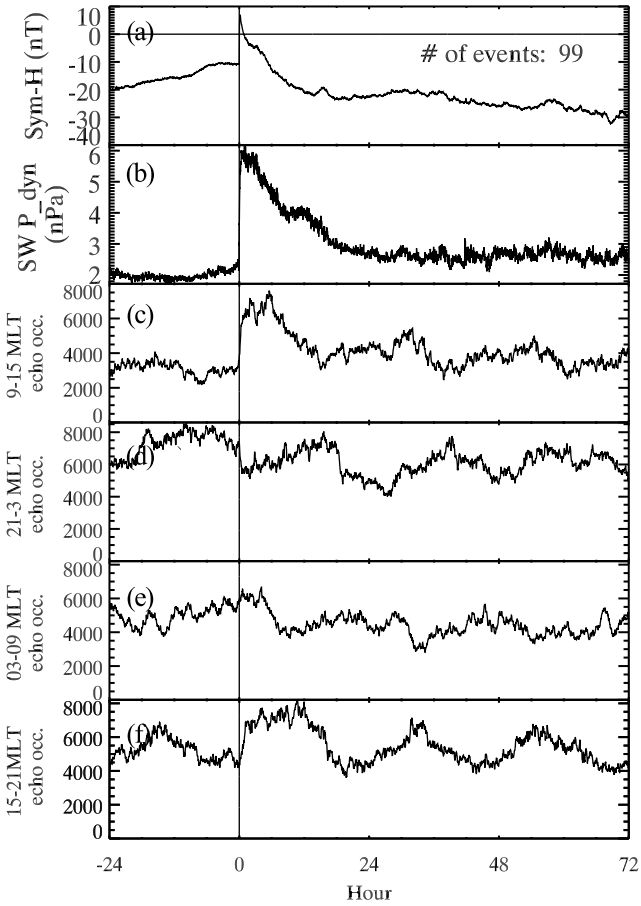

Figure 3. SuperDARN echo occurrence for SI events as a function of epoch time, in hours, relative to the onset of the SI at $t = 0$. (a) Mean *SYM-H* profile, (b) solar wind dynamic pressure, (c) noon SuperDARN echo occurrence, (d) midnight SuperDARN echo occurrence, (e) dawn SuperDARN echo occurrence, and (f) dusk SuperDARN echo occurrence.

SuperDARN radars during a 2 min interval. In Figures 3a and 3b, we repeat the presentation of the *SYM-H* and dynamic pressure data for comparison. We have subdivided the SuperDARN echo occurrence into for four MLT sectors shown in Figure 3. "Noon" includes data between 9 and 15 MLT, "midnight" between 21 and 3 MLT, "dawn" between 3 and 9 MLT, and "dusk" between 15 and 21 MLT. SuperDARN echo occurrence from noon and midnight are presented in Figures 3c and 3d, respectively, while the dawn and dusk SuperDARN echo occurrence data are presented in Figures 3e and 3f.

[28] Figure 3c indicates that in the noon sector the number of SuperDARN echoes is relatively constant until $t = 0$, at which point the echo occurrence more than doubles. Interestingly, at the same time, the number of echoes in the midnight sector, in Figure 3d, suddenly decreases, though by not as significant an amount. Following the jumps at $t = 0$, the number of echoes takes approximately 12 h to gradually return to its original level in both the noon and midnight sectors. After that time, the numbers oscillate with an apparent 24 h cycle. The midnight occurrence peaks when the noon occurrence is at a minimum and vice versa. The 24 h trend reflects the lack of uniformity in radar coverage, combined with a tendency for this set of SI events to preferentially occur between 10:00 and 18:00 UT (not shown). With the radar coverage being uneven, when the coverage is at its best in the midnight sector, it is simultaneously far from ideal near noon. The preferred UT start time results in a 1 day oscillation. The effect does not apply, however, to sharp changes of the kind that are taking place at $t = 0$, which indicate a large genuine increase in the number of noon echoes in simultaneity with a measurable decrease in midnight echoes at SI onset.

[29] The dawn and dusk sector echo occurrence in Figures 3e and 3f also demonstrates a noticeable antiphase, again with about a 24 h periodicity for the same reasons that were discussed for the noon and midnight sectors. There is some weak indication of an increase in the dusk sector at $t = 1$ h. While this increase occurs during the peak of the 24 h periodicity, the echo occurrence in the 15 h following the SI is markedly higher than the rest of the interval. The enhancement in the number of echoes in the dusk sector may well be related to the asymmetric tendency for a positive IMF B_y in the few days that follow the SI onset.

[30] The long-term superposed SuperDARN LOS velocity distributions are shown in Figure 4. Figures 4a and 4b are for the *SYM-H* and the solar wind dynamic pressure plots from Figure 2 for comparison purposes. Figures 4c and 4d display the velocity distributions measured by the northern SuperDARN radars in the noon and midnight sectors, respectively. The velocity distributions are not normalized, so the total number of echoes in a particular 2 min time bin adds up to the total shown in Figure 3. Velocities from -1.5 to 1.5 km s^{-1} are displayed on the vertical axis. Negative velocities indicate LOS velocities with an antisunward component, and vice versa. The color scale is logarithmic and indicative of the total number of echoes in each velocity bin. Red indicates a high number of echoes while blue indicates relatively few echoes. As in Figures 2 and 3, the vertical line located at $t = 0$ marks the SI onset.

[31] The noon sector velocity distributions in Figure 4c are asymmetric at all times, with a predominance of antisunward flows. This is consistent with antisunward plasma drifts over the polar cap. Recall the marked increase in the noon sector echo occurrence in Figure 3c at $t = 0$. The velocity distribution in Figure 4c demonstrates a systematic increase in the magnitude of antisunward velocities following $t = 0$, particularly during the first 5 h following SI onset.

[32] Following the SI onset, the number of noon sector echoes decreases on a time scale of hours. This decrease therefore occurs more slowly than the decrease in the *SYM-H* data in Figure 4a, having a time scale more like that of the decrease in the solar wind dynamic pressure in Figure 4b. While the noon echo occurrence decreases to pre-SI values within about 1 day, the faster antisunward flows persist for the remainder of the interval. In summary, the effect of the SI on the noon sector velocity distribution is to double the number of radar echoes during the period of increased solar wind dynamic pressure. The increase is proportionately greater for antisunward flows.

[33] The effects of the SI events on the midnight sector are far more subtle. Aside from the decrease in the number of echoes at $t = 0$ already reported in Figure 3, there is a hint in the few hours that follow the SI for a decrease in the number

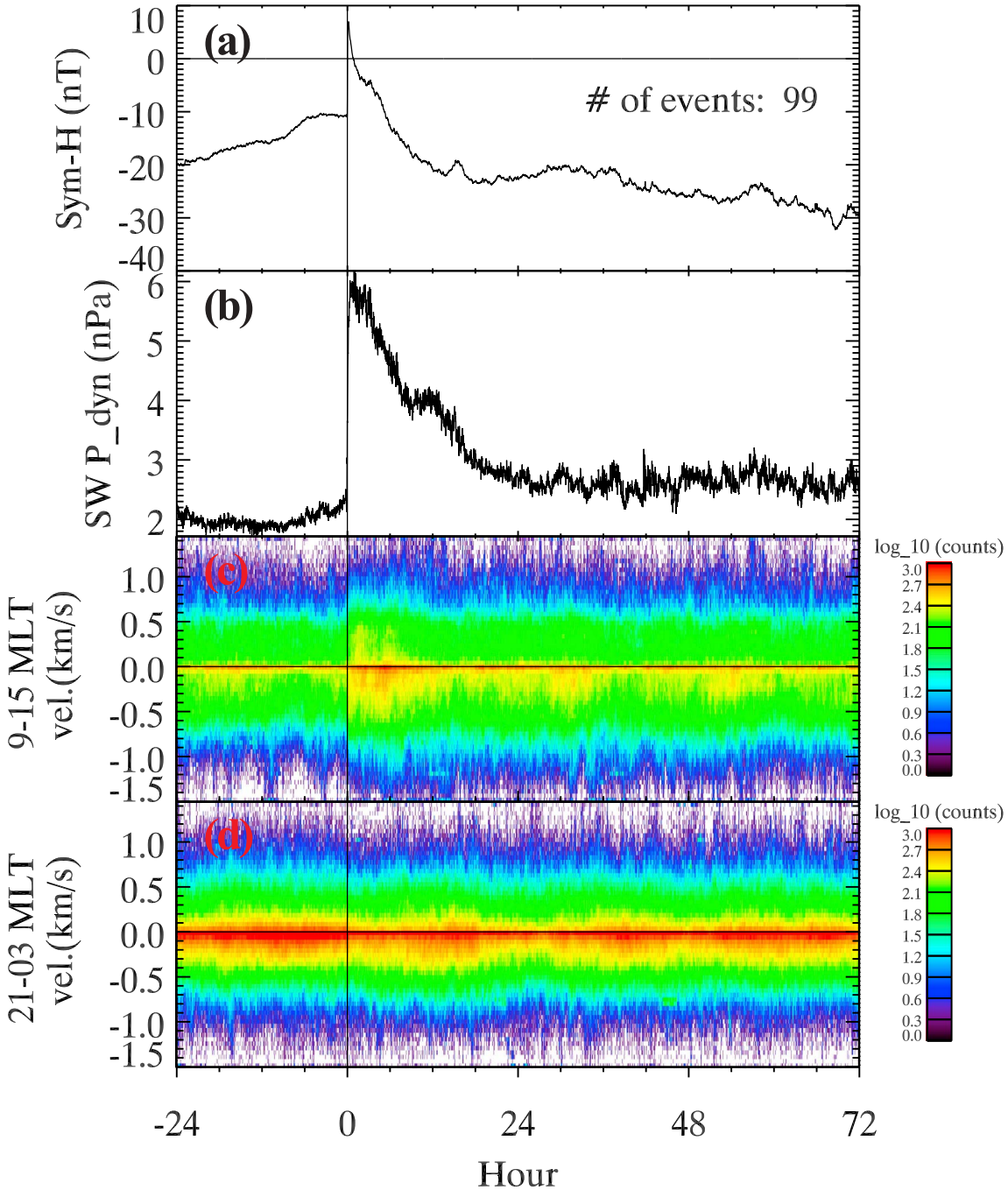

Figure 4. SuperDARN velocity distributions for SI events, relative to the onset of the SI at $t = 0$. (a) Mean *SYM-H*, (b) mean solar wind dynamic pressure, (c) noon sector (9–15 MLT) line-of-sight velocity distributions, and (d) midnight sector (21–3 MLT) line-of-sight velocity distributions. Line-of-sight velocities in 50 m s^{-1} bins. Sunward (antisunward) LOS velocities are positive (negative).

of slow velocities, both sunward and antisunward. A closer look is provided below, when analyzing the velocity distributions within an hour of the SI onset.

3.2. Storm Sudden Commencement Events From the Longer Time Perspective

3.2.1. SSC Solar Wind and IMF Parameters

[34] In fashion similar to the SI case, Figure 5a shows the superposed *SYM-H* index the 106 SSC events. Prior to the SSC, *SYM-H* is steady around −10 nT. A sharp jump to +20 nT occurs at the SSC. Following the SSC, the mean *SYM-H* decreases rapidly to a large negative value of −80 nT over the next 12 h. The *SYM-H* index then begins a gradual recovery nearly to pre-SSC values over the next 72 h. The mean IMF B_z component (Figure 5b) fluctuates near 0 nT prior to the SSC. At $t = 0$ there is relatively strong southward turning of the IMF, with the largest negative value of about −4.5 nT reached at about $t = 5$ h. The IMF B_z

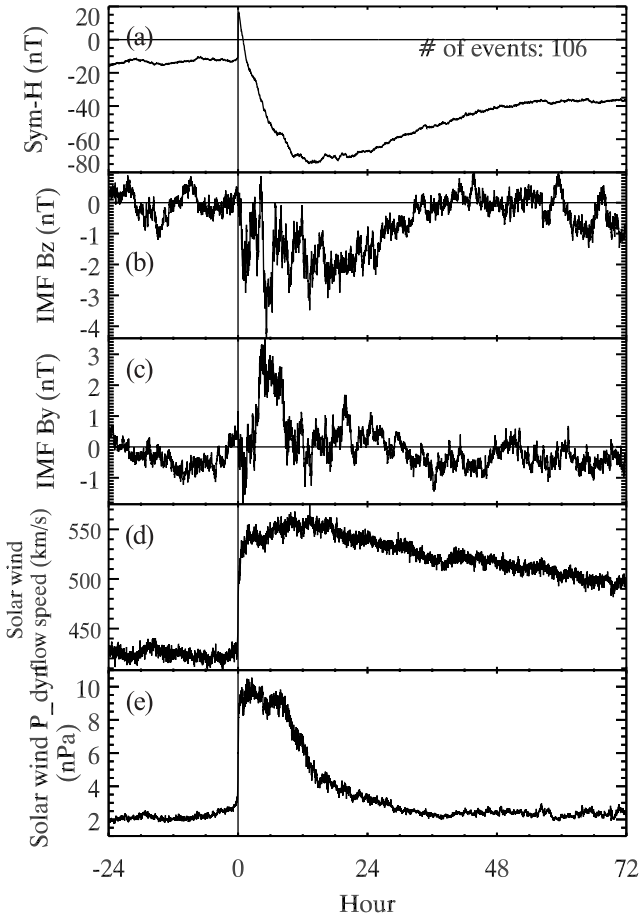

Figure 5. Solar wind and geomagnetic data for 106 SSC events in the same format as Figure 2. (a) Mean *SYM-H* profile, (b) mean IMF B_z (GSM), (c) mean IMF B_y (GSM), (d) mean solar wind flow speed, and (e) solar wind dynamic pressure. The black vertical line at $t = 0$ marks the onset of the SC events.

component then fluctuates between −3 and 0 nT until approximately $t = 24$ h, after which time it returns to values near zero, as it was prior to the SSC. Unlike the weakly positive IMF B_z following the SI that was presented in Figure 2b, the strongly negative IMF B_z and the large drop in *SYM-H* following the SSC is consistent with the development of a storm, which is required by definition for this type of SC [*Gillies et al.*, 2011].

[35] The IMF B_y component (Figure 5c) is near zero prior to SSC. After a brief negative excursion, reminiscent of a similar feature in the B_z component, it undergoes a sharp reversal and increases to 4 nT where it remains high until the solar wind dynamic pressure begins to decrease. By $t = 8$ h the B_y component returns to near zero where it fluctuates for the remainder of the interval of interest. By contrast to the SI events, the SSCs in this study experience a short interval (about 6 h) of relatively large sustained positive IMF B_y, rather than the weakly positive values that persist for 72 h after the SI. For the SSCs the IMF B_y component returns to near zero values and remains there.

[36] The solar wind flow speed (Figure 5d) is steady at 420 km s^{-1} for 24 h prior to SSC. At the SSC there is a sharp jump to approximately 550 km s^{-1}. The flow speed retains this value for 24 h before gradually decelerating to 500 km s^{-1} by $t = 72$ h. Note that the solar wind flow speed never drops back down to pre-SSC values by the end of the 72 h interval.

[37] For 24 h prior to SSC, the solar wind dynamic pressure (Figure 5e) is steady at 2 nPa. At $t = 0$ h, there is a sharp jump to 10 nPa, which is nearly double the increase for the SIs. The dynamic pressure stays near 10 nPa for the next 9 h before gradually decreasing to 3 nPa by $t = 24$ h, where it remains for the next 48 h. The reduction in the solar wind dynamic pressure is largely due to a decrease in the solar wind number density (not shown), since the solar wind velocity remains elevated.

3.2.2. Echo Occurrence and Convection Velocity

[38] The superposed SuperDARN echo occurrence for SSC events is presented in Figure 6 using a format identical to that used to present the SI data (Figure 3). The data are separated into the four MLT sectors: noon and midnight in Figures 6c and 6d, respectively, and dawn and dusk in Figures 6e and 6f, respectively.

[39] Prior to the SSC, the noon sector SuperDARN echo occurrence (Figure 6c) is relatively steady near 4000 echoes.

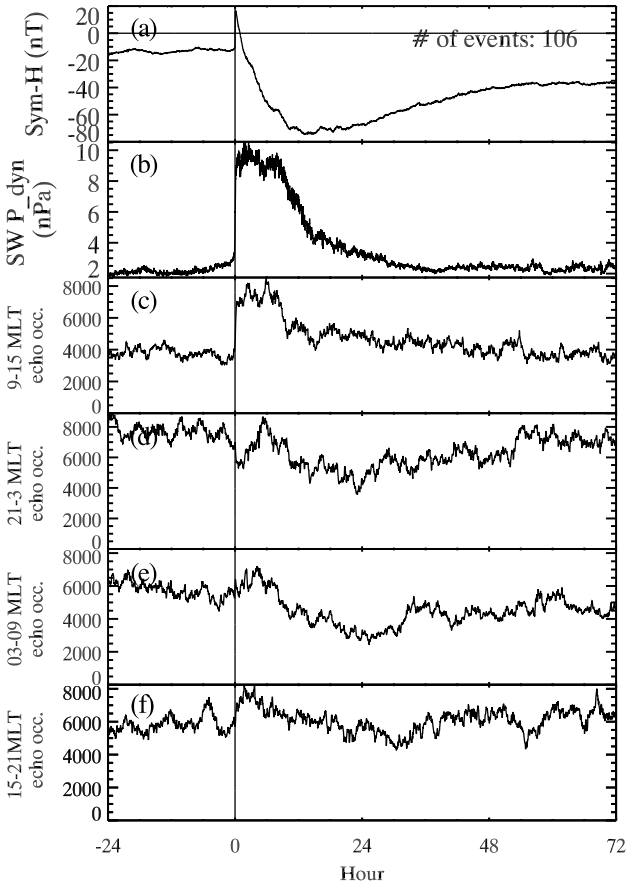

Figure 6. SuperDARN echo occurrence for SSC events in the same format as Figure 3. (a) Mean *SYM-H* profile, (b) solar wind dynamic pressure, (c) noon SuperDARN echo occurrence, (d) midnight SuperDARN echo occurrence, (e) dawn SuperDARN echo occurrence, and (f) dusk SuperDARN echo occurrence.

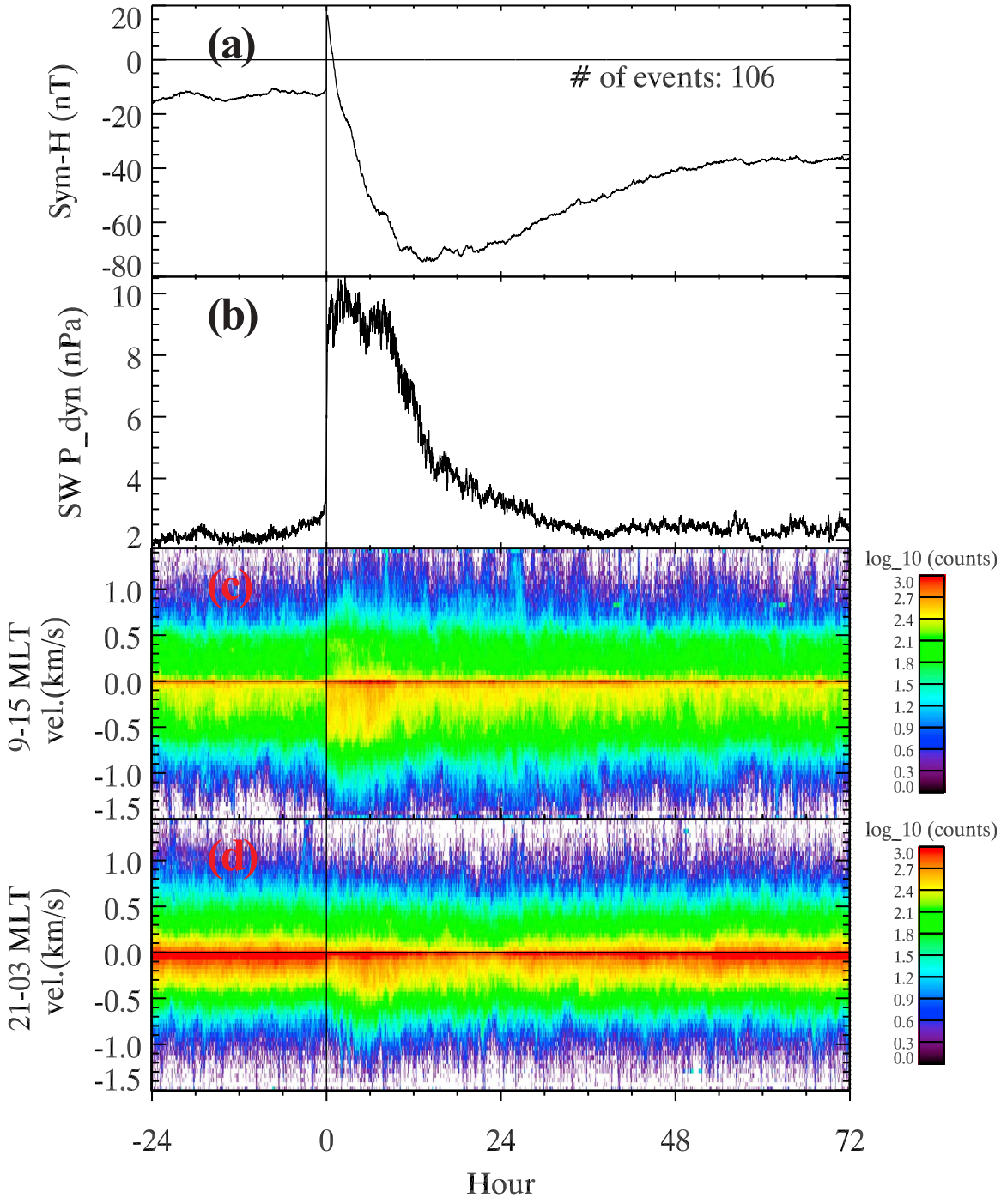

Figure 7. SuperDARN velocity distributions for SSC events, in the same format as Figure 4. (a) Mean *SYM-H*, (b) mean solar wind dynamic pressure, (c) noon sector (9–15 MLT) line-of-sight velocity distributions, and (d) midnight sector (21–3 MLT) line-of-sight velocity distributions. Line-of-sight velocities are in 50 m s^{-1} bins. Sunward (antisunward) LOS velocities are positive (negative).

The echo occurrence increases sharply at $t = 0$ to nearly 8000 echoes. The increase is sustained until the solar wind dynamic pressure decreases nearly to pre-SSC values, approximately 12 h later. After this time, the noon echo occurrence drops quickly to a level slightly higher than that observed before $t = 0$. This lasts for approximately 2 days during which time the noon echo occurrence slowly diminishes to pre-SSC values.

[40] As was the case for SI events, the behavior of the data in the midnight sector is more subtle than that in the noon sector. The number of echoes in the midnight sector decreases by a small but detectable amount at $t = 0$, as seen in Figure 6d. This is followed by a temporary increase back to the pre-SSC level at around $t = 10$ h. Aside from this brief excursion, the midnight sector echo occurrence is low compared to pre-SSC levels for the duration of the storm.

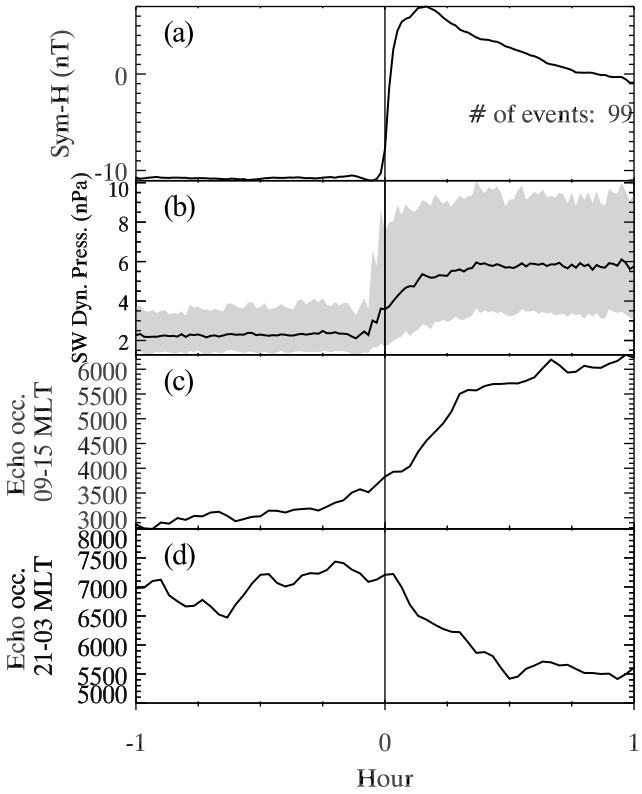

Figure 8. High time resolution superposed epoch data for SI events. (a) *SYM-H* index, (b) solar wind dynamic pressure (the shaded gray area represents the spread in the data), (c) noon sector (9–15 MLT) line-of-sight velocity distributions, and (d) midnight sector (21–3 MLT) line-of-sight velocity distributions.

The echo occurrence recovers gradually as the *SYM-H* returns to prestorm levels. The existence of a drop in the SuperDARN echo occurrence near midnight for both SSCs and SIs suggests that this feature is significant, even though this drop is small and comparable to the random fluctuations during the epoch interval.

[41] The dusk and dawn echo occurrences are shown in Figures 6e and 6f. Prior to SSC, both the dawn and dusk sectors maintain a small descending trend in echo occurrence and have very similar values. There is a temporary increase in the echoes at both dawn and dusk during the 6 h that follow the SSC, after which time the echo occurrence in the dawn sector becomes depleted by comparison to the dusk sector and the prestorm levels. No clear trend emerges in the dusk sector, which maintains an echo occurrence similar to the prestorm level. Broadly speaking, the dawn sector echo occurrence is more similar to the midnight echo occurrence, and the dusk sector echo occurrence is more similar to the noon echo occurrence.

[42] In contrast to the SI events, there is less evidence of a 24 h periodicity of echo occurrence for the SSC events. Unlike the SI events, there was no preferred UT start time for SSCs. In the superposed epoch interval this effectively creates uniform SuperDARN coverage over all local times.

[43] Comparing the SSC and SI echo occurrence, a few additional features stand out. First, while the dynamic pressure jump is much larger, on average, for SSCs than for SIs, the jump in the SuperDARN echo occurrence in the noon sector is similar. The echo occurrence rises sharply in the noon sector by a factor of slightly less than 2 for both SSCs and SIs. We also note the similarity between the noon echo occurrence and the period of high solar wind dynamic pressure for both SIs and SSCs. Finally, for both types of events, the echo occurrence in the dusk sector following the SSCs and SIs is larger than the echo occurrence in the dawn sector.

[44] The SuperDARN velocity distributions are shown for the SSC events in Figure 7, using the same presentation format as described for the SI events (Figure 4). The velocity distributions prior to the SSC are very similar to those prior to the SI. On the dayside (Figure 7c), the majority of pre-SSC SuperDARN echoes have a LOS velocity component that is less than 0.5 km s^{-1}. Antisunward plasma drifts, as for SIs, are more frequent than their sunward counterparts. After $t = 0$, there is not only a sharp increase in the total echo occurrence in the noon sector but also a large increase in the antisunward plasma drift speeds. In particular, during the first 12 h that follow the onset (namely, until the dynamic pressure begins to decrease rapidly) there is a dramatic increase in the noon sector of all antisunward velocities between 0 and 1.5 km s^{-1}. In the midnight sector (Figure 7d), the most noticeable features are the decrease in velocities of both sunward and antisunward speeds of all magnitudes

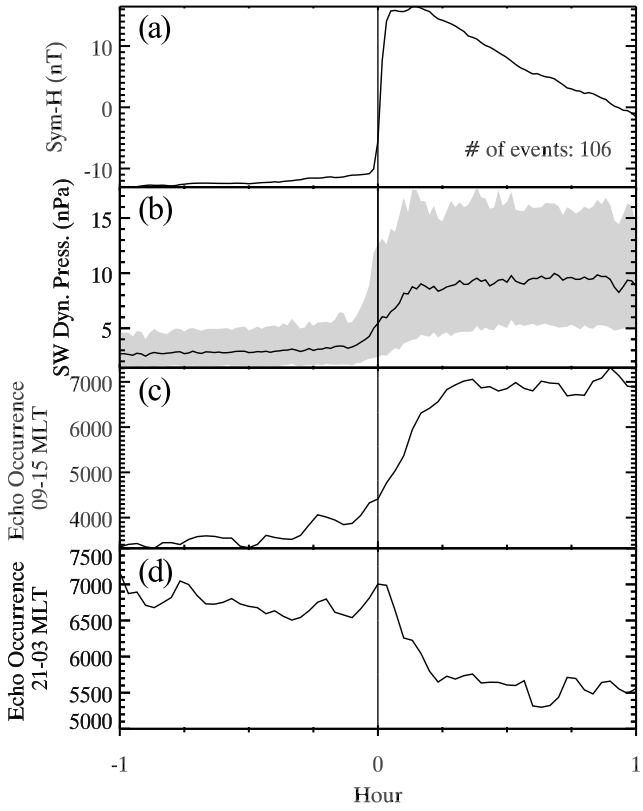

Figure 9. High time resolution superposed epoch data for SSC events. (a) *SYM-H* index, (b) solar wind dynamic pressure (the shaded gray area represents the spread in the data), (c) noon sector (9–15 MLT) line-of-sight velocity distributions, and (d) midnight sector (21–3 MLT) line-of-sight velocity distributions.

at $t = 0$, followed by the increase in antisunward velocities 6 h later. These large antisunward velocities in the midnight sector are typical of storm flows [*Gillies et al.*, 2011]. In other words, the noon sector behavior was quite similar for both SI and SSC events, while fast flows in the midnight sector following SSCs are likely related to the development of the main phase of a storm [*Gillies et al.*, 2011].

3.3. Sudden Commencements From a Shorter Time Perspective

[45] Further insights into the ionospheric response during SCs can be gained if we examine the data with a finer time resolution. We focus in on the time interval from 1 h before the SC onset until 1 h after. Figure 8 includes the *SYM-H* index, the solar wind dynamic pressure, and the noon and midnight echo occurrence for the SI events. For the SI events the variation of the number of SuperDARN echoes is more similar to changes in the solar wind dynamic pressure than it is to changes in *SYM-H*. In the noon sector the number of echoes increases when the dynamic pressure increases, and the number of echoes plateaus as the dynamic pressure plateaus. A similar picture emerges in the midnight sector, except that the number of echoes decreases as the dynamic pressure increases. By contrast, the increase in *SYM-H* at the SI onset is very sharp, and it starts to decrease very soon after reaching its maximum value, even though the dynamic pressure continues to increase, albeit at a slower rate than in the earlier stages. Both the increase in SuperDARN echo occurrence and the increase in *SYM-H* can be explained by the increase in the solar wind dynamic pressure, as described in section 1. The *SYM-H* index, however, increases only in the first 10 min. It then appears that a geomagnetic storm begins, thereby causing the *SYM-H* to decrease, even as the solar wind dynamic pressure continues to increase. Initially, the SI produces an enhancement of the magnetopause current, and the geomagnetic field increases earthward of the magnetopause. The drop in *SYM-H* suggests that the ring current, which is diamagnetic in nature, begins to counteract the increase in the dayside magnetic field strength on a 10 min time scale.

[46] A remarkably similar evolution is found in SSC events, which are presented in Figure 9 in the same format. We find similar trends for a dramatic increase in *SYM-H* at the same time as the more gradual change in the solar wind dynamic pressure and in the noon and midnight SuperDARN echo occurrence. A similar percentage change in the number of echoes occurs in both the noon and midnight sectors after $t = 0$, and both values level off once the dynamic pressure has leveled off. Just like the SI case, the *SYM-H* index also begins to decrease approximately 10 min after the SSC at $t = 0$.

[47] This being stated, SSCs and SIs exhibit some distinct differences. As evident from Figures 8b and 9b, the solar wind dynamic pressure rises more quickly for the SSC events than the SI events. In addition, SSCs are associated with stronger solar wind dynamic pressure pulses than SIs. There are also minor differences in the echo occurrence in the noon (9–15 MLT) sector. As shown in Figures 8c and 9c, the echo occurrence for SIs tends to rise more gradually, reaching a peak over the course of approximately 30 min. SSCs, on the other hand, reach a peak occurrence value after 15 min.

[48] The short time scale LOS velocity distributions are presented in Figures 10 and 11 for SIs and SSCs, respectively. The velocity distributions are shown as both the total echo occurrence in Figures 10a, 10c, 11a and 11c and as normalized echo occurrence in Figures 10b, 10d, 11b and 11d. The distributions are normalized by dividing the distribution in each 2 min interval by the total number of echoes in that interval. The noon sector distributions are in Figures 10a, 10b, 11a and 11b and the midnight sector distributions in Figures 10c, 10d, 11c and 11d. Note that the velocity scales range from -1500 to $+1500$ m s^{-1} for the noon sector, and from -750 to $+750$ m s^{-1} for the midnight sector.

[49] The noon sector data (Figures 10, 10b, 11a and 11b) are very similar for both the SI and SSC events. Following a brief decrease in the intensity of antisunward flows just before $t = 0$, there is a smooth and relatively rapid increase in the intensity of the antisunward flows for about 10–15 min, after which time both the total and the normalized velocity distributions stop evolving. The changes in the midnight sector are more subtle but are still very similar for both SI and SSC events. Following $t = 0$, there is a weak enhancement in the antisunward flows overall, as well as a decrease of the sunward flows. The fastest antisunward flows occur approximately 5 min after onset. After approximately $t = 15$ min there is very little evolution of the total and normalized velocity distributions.

4. Discussion

4.1. The *SYM-H* Response to Increases in Dynamic Pressure

[50] Our study originated with the identification of SCs through their *SYM-H* magnetic signatures, based on L'Observatori de l'Ebre (SSC tables, http://www.obsebre.es/php/geomagnetisme/variaciorap.php) database. We found that SI and SSC events were both clearly related to sudden increases in the solar wind dynamic pressure. This is expected due to the nature of the compression of the magnetosphere caused by the increased plasma pressure in the bow shock. The magnetopause moves closer to Earth when the dynamic pressure increases. The geomagnetic field increases in response to this compression which in turn induces an increase in the magnetopause current to compensate. The jump in the magnetic field strength downstream from the magnetopause boundary layer produces the observed increase in the *SYM-H* index.

[51] We also found that in response to the increase in dynamic pressure, there were important morphological differences between the evolution of the *SYM-H* trace and the SuperDARN echo characteristics. The jump in the number of echoes and the increase in the intensity of the antisunward flows in the noon sector SuperDARN data followed very closely the changes in the solar wind dynamic pressure. In contrast, the *SYM-H* index peaked within 10 min of the arrival of the solar wind dynamic pressure pulse, after which time it began to decay despite the continued increase of the solar wind dynamic pressure (see Figures 7 and 8). Another interesting difference that stands out in our comparative superposed epoch study is that the jump in the *SYM-H* index was stronger, on average, for the SSC events than for the SI events.

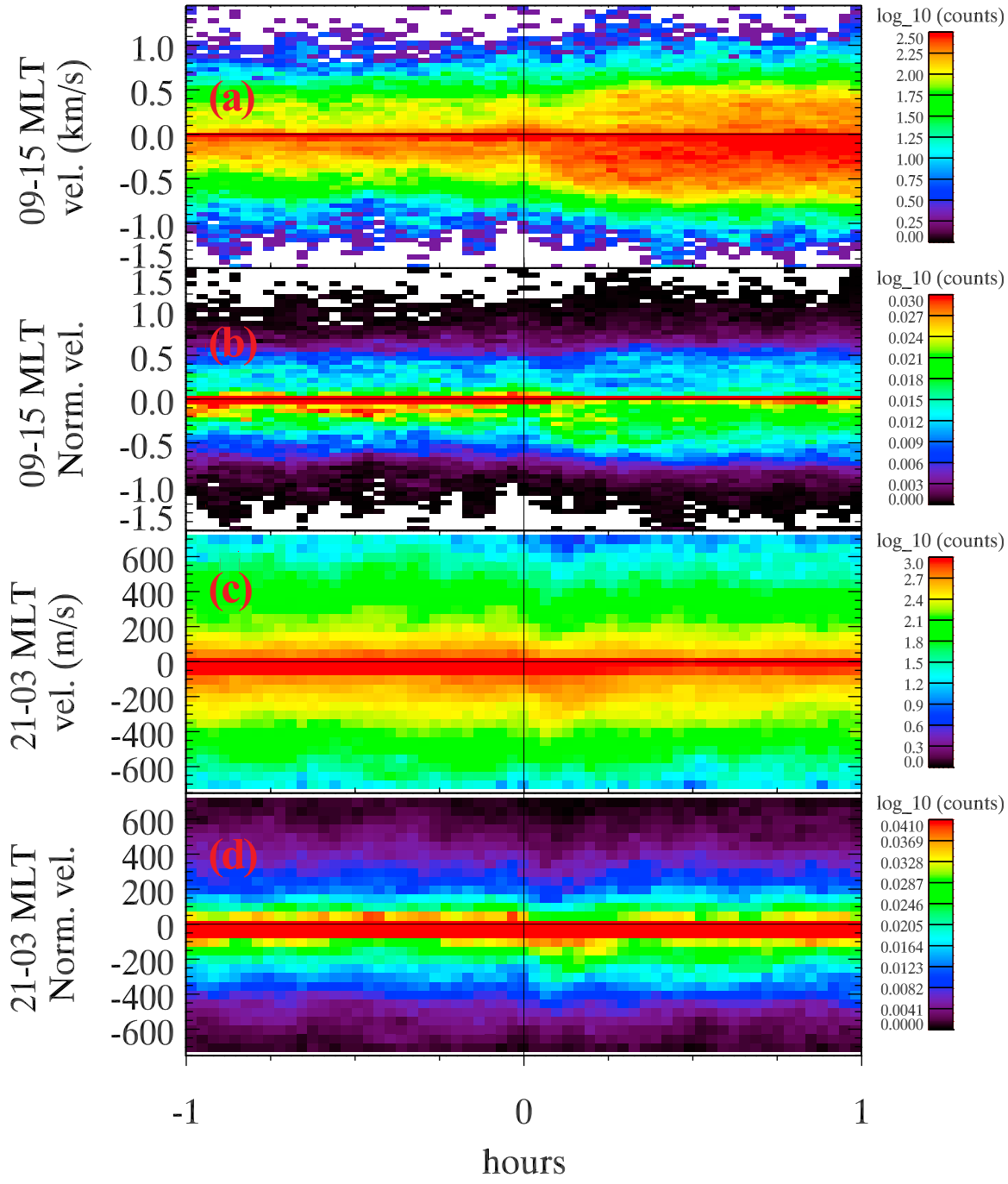

Figure 10. High time resolution SuperDARN LOS velocity distributions for SI events. (a) Moon sector LOS velocity distributions, (b) normalized noon sector LOS velocity distributions, (c) midnight sector LOS velocity distributions, and (d) midnight sector normalized LOS velocity distributions. Velocity bins, velocity sign conventions, and the vertical marker at $t = 0$ are the same as in Figure 4.

[52] Clearly, while the jump in the dynamic pressure had an immediate effect on both the *SYM-H* index and on the radar echoes, the morphological differences between the two following the impact imply that the dynamic pressure pulses affect the system in multiple ways. This led us, in particular, to probe more deeply into the *SYM-H* response. Our aim was to gain more insight into the reason for a larger response for SSC events and to consider why the *SYM-H* typically decays 10 min after the jump in dynamic pressure even though the pressure increase is sustained for much longer.

4.1.1. Comparison of the *SYM-H* jumps in SIs and SSCs

[53] We first scrutinized the connection between the magnitude of the solar wind dynamic pressure jump and the magnitude of the jump in the *SYM-H* index. The amplitude of the SC at the Earth's surface is linearly related to the

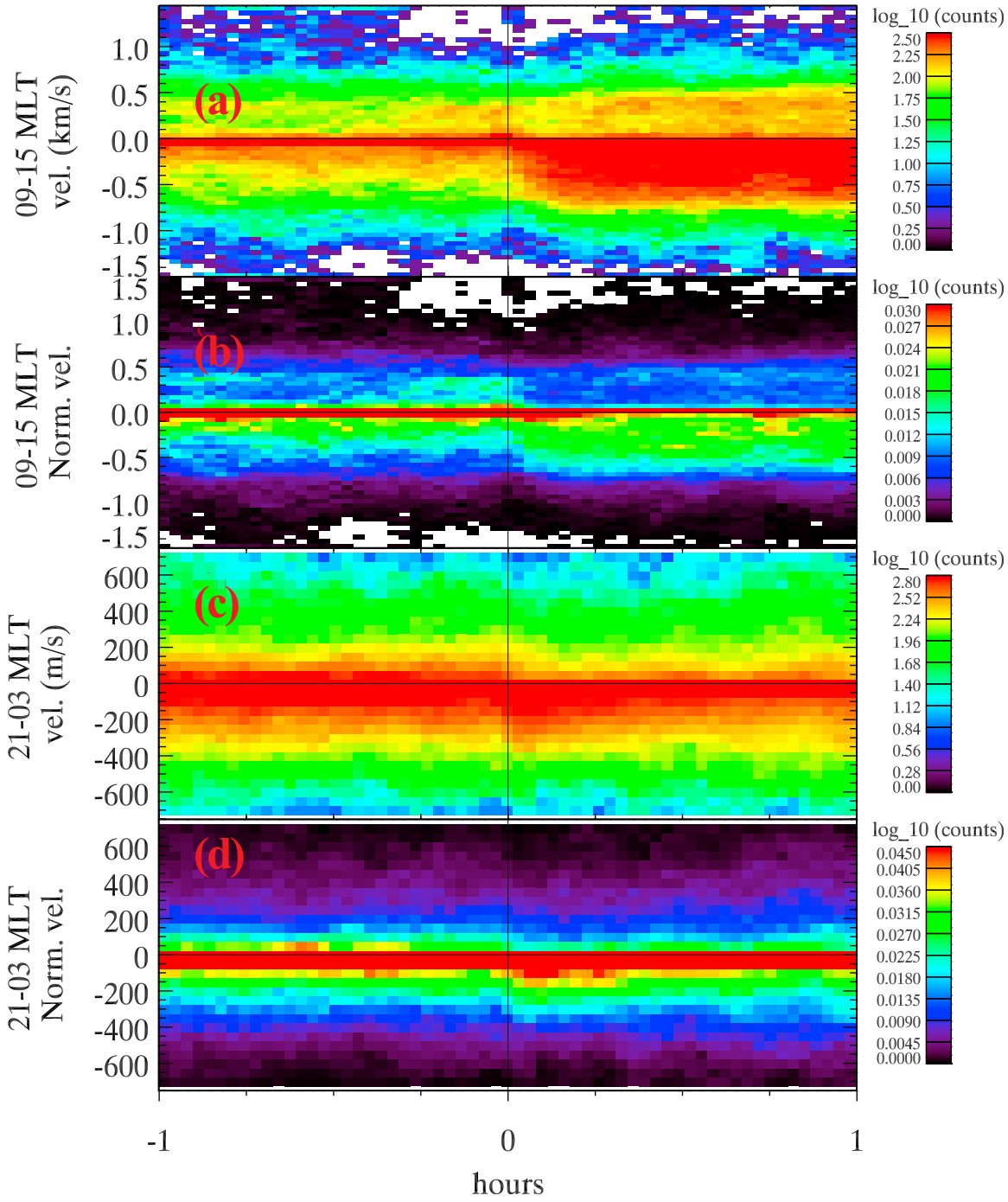

Figure 11. High time resolution SuperDARN LOS velocity distributions for SSC events. (a) Noon sector LOS velocity distributions, (b) normalized noon sector LOS velocity distributions, (c) midnight sector LOS velocity distributions, and (d) midnight sector normalized LOS velocity distributions. Velocity bins, velocity sign conventions, and the vertical marker at $t = 0$ are the same as in Figure 7.

square root of the solar wind dynamic pressure [*Siscoe et al.*, 1968; *Burton et al.*, 1975; *Echer et al.*, 2008, 2005]. A clear relationship between the two emerged, as illustrated in Figure 12a, where we produced a scatterplot of the change in *SYM-H* versus the change in the square root of the dynamic pressure across the impulse for all available SI and SSC events. Since the transition was not always instantaneous, we calculated the magnitude of the maximum difference of the parameters within 30 min of the *SYM-H* jump. Due to gaps in solar wind and IMF data only 135 of 205 events could be included in Figure 12a. Figure 12a establishes that there was, overall, a high degree of correlation between the jumps in *SYM-H* and the jumps in the solar wind dynamic pressure, as expected from the basic magnetopause boundary layer physics. When we separate the data according to whether they are SI or SSC events, however, an interesting

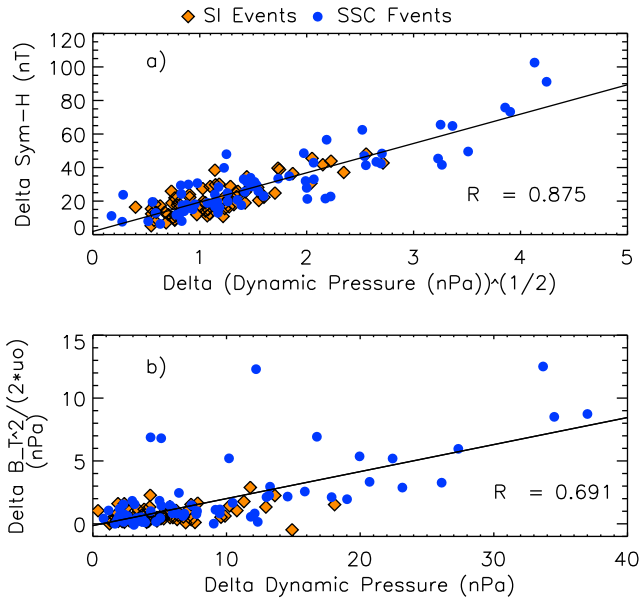

Figure 12. Scatterplots of (a) the magnitude of the jump in the *SYM-H* index and (b) the solar wind magnetic pressure as a function of the jump in the solar wind dynamic pressure. SI events are indicated by diamonds, and SSC events are indicated by solid circles. Due to gaps in the solar wind data, only 135 of the 205 SC events are included.

trend emerged. All SCs with dynamic pressure jumps larger than about 20 nPa were exclusively SSC events, even though for dynamic pressure jumps below about 15 nPa the SI and SSC data points were indistinguishable and both data sets taken together were clustered similarly around a single best fit line.

[54] The above result is curious, in the sense that with possibly a few exceptional events, it is highly unlikely that one might be able to deduce whether the initial impulse will be a SI or a SSC event. Whether or not a magnetic storm emerges is determined by what happens well after the initial impulse. A strong magnetic storm will develop only if there is a strong and sustained southward turning of the IMF B_z component [*Akasofu and Chapman*, 1963a, 1963b; *Gillies et al.*, 2011]. Only then will the event be classified as a SSC. Conversely, if the strong southward IMF orientation does not develop, the likelihood of a storm is much smaller, and the impulse will be classified as a SI event.

[55] Another important factor to consider is the magnitude of the IMF around dynamic pressure jumps. While the north-south orientation of the IMF appears to be unpredictable, there is a correspondence between the magnitude of the dynamic pressure jump and the magnitude of the change in the IMF before and after the SC. This is demonstrated in Figure 12b, which is a scatterplot of the jump in the magnetic pressure of the IMF versus the jump in the solar wind dynamic pressure. We conclude from Figure 12b that larger dynamic pressure jumps are accompanied by larger excursions in the IMF magnetic pressure and therefore in the IMF magnitude. This is consistent with the most extreme SSC events occurring when the solar wind and IMF are also extreme.

[56] It should be kept in mind that while a substantial jump in magnetic pressure is accompanied by a substantial jump in dynamic pressure, it does not follow that all jumps in dynamic pressure will bring large jumps in the magnetic pressure. A jump in the solar wind dynamic pressure is, in that sense, a necessary but not a sufficient condition for a large jump in magnetic pressure. Many of the SC events with small or negligible jumps in IMF magnitude correspond to large rotational discontinuities.

[57] We conclude that the largest *SYM-H* jumps (above 20 nT), which are produced by the largest solar wind dynamic pressure jumps, were a necessary condition for the occurrence of a magnetic storm several hours after the arrival pressure pulses. While not all dynamic pressure jumps were associated with jumps in the IMF magnitude (such as rotational discontinuities), the likelihood of observing a storm after the impulse is largest when both the dynamic pressure and the magnetic pressure jumps are large. The *SYM-H* response was larger, on average, for SSCs than for SIs, and this is likely due to the extreme solar wind conditions during which storms tend to occur.

4.1.2. The Quick Decay of the *SYM-H* and Its Possible Origin

[58] As seen in Figures 7 and 8, and contrary to what was seen in the dynamic pressure and SuperDARN data, the averaged *SYM-H* began to decrease 10 min after the arrival of the dynamic pressure pulse in both SI and SSC events. There was no SuperDARN echo occurrence signature to match this decrease in *SYM-H*. The *SYM-H* responds to both the the magnetopause currents and to the ring current. Had the enhancement of the magnetopause current been the only mechanism affecting the *SYM-H* index in SC events, *SYM-H* should have remained elevated for as long as the solar wind dynamic pressure remained high and the magnetosphere remained compressed. The different responses by the *SYM-H* index and SuperDARN echo occurrence therefore indicate that the ionosphere and the ring current respond differently to the SC. Furthermore, this difference has no relation to the orientation of the IMF, namely, to the amount of dayside reconnection occurring after the SC. On average, the IMF B_z component was positive after SIs and negative after SSCs (see Figures 2 and 5), implying that the *SYM-H* decrease 10 min after the impulse, which was the same for SIs and SSCs, has nothing to do with dayside reconnection.

[59] The sudden increase in the solar wind dynamic pressure increases the magnetic field strength inside the magnetosphere through the magnetopause currents, particularly up front. The magnetosphere system must respond in some way to counteract the magnetic field intensification and to reduce the magnetic field strength quickly thereafter. This can be accomplished through an intensification of the ring current. Qualitatively, the ring currents can be viewed in this context as a diamagnetic system. When such a system experiences an increase in the magnetic field strength, such as that produced by the enhanced magnetopause current, the diamagnetic current will respond in such a manner as to reduce the changing magnetic flux through the system. Increasing the magnitude of the ring current will produce southward magnetic flux through the ring, in opposition to the extra northward magnetic flux associated with the enhanced magnetopause current. This ring current enhancement produces the registered decrease in *SYM-H*. Though the issue is beyond the scope of the present paper, we note that the 10 min response time is consistent, for instance,

with the time expected for the running pulse of increased solar wind dynamic pressure to travel tailward and to compress the entire magnetosphere [e.g., see *Mann and Wright*, 1999]. When the magnetosphere is compressed, the intensity of the ring current must increase adiabatically, with ions and electrons moving faster through a smaller volume element. This is analogous to an incompressible flow that would increase when passing through a smaller cross-sectional area. Enhancements in energetic neutral atom (ENA) emissions after pressure pulses have been explained through this compression effect [*Lee et al.*, 2007] and were particularly clear for SI events. Advanced numerical models of the system also now exist to document more precisely how the currents react to the sudden pressure changes and, later on in SSC cases, to a southward IMF orientation [e.g., *Sitnov et al.*, 2010].

4.2. Possible Interpretation of the Noon and Midnight Radar Results

[60] In the end, the SuperDARN data are more closely linked to the upstream solar wind, in particular the dynamic pressure, than to the *SYM-H* or the ring currents, particularly in the noon sector. As discussed above in relation to Figures 10 and 11, in the first 10 min following the impulse, for both SIs and SSCs, the antisunward flows in the noon sector become gradually larger. The fastest antisunward velocity components are reached in these first 10 min, after which the velocity distribution remains broad and very steady for at least 12 h. This occurs for both SIs and SSCs, regardless of the IMF B_z component (and therefore independent of the convection triggered by dayside reconnection) or of the occurrence of a storm later on.

[61] Previous work by *Milan et al.* [2004] has shown that the polar cap contracts and there is no new open flux (essentially have a closed system) in the cap after the arrival of a solar wind shock. The initial buildup of the antisunward flows can be explained by the quick poleward progression of the polar cap boundary, as the polar cap becomes smaller [*Boudouridis et al.*, 2007]. The initial increase in the antisunward flows is consistent with this explanation, since the frozen-in ionospheric plasma cannot flow across the boundary where reconnection does not occur (the adiaroic boundary) [*Siscoe and Huang*, 1985]. On the other hand, this does not fully explain why we observe persistent fast flows for the 12 h that follow both SIs and SSCs. This feature is observed regardless of the sign of the IMF B_z, and regardless, therefore, of the presence of reconnection-driven flows into the polar cap on the dayside, or of storm-induced flows out of the polar cap on the nightside. Clearly, a much more sophisticated analysis of SuperDARN velocities will be required to address this puzzle.

[62] In addition to the increased convection speeds (and therefore increased convection electric fields) in the noon sector, the number of SuperDARN echoes also rises. The simplest explanation for this connection is that the decameter structures scattering the radio waves are frequently associated with a gradient drift instability, which depends on the strength of the electric field for its growth [*Kelley*, 1989]. Since the stronger flows must be connected to stronger electric fields, the increase in echo occurrence may therefore well be related to the increase in the electric field in the noon sector.

[63] We finally note that for both SI and SC events, the number of echoes in the midnight sector sharply drops just a few minutes after the SC (e.g., Figures 7 and 8). The magnitude of the drop is small relative to other variations throughout the 4 day epoch interval, but the coincidence of similar data rate drops in both SIs and SSCs indicates that this is a geophysical response.

[64] Many factors could be responsible for a decrease in echo occurrence, making it difficult with the current analysis to identify the mechanism. For instance, a poleward motion of the shrinking polar cap boundary in response to the impulse could affect the position of the auroral boundaries. The majority of the SuperDARN radars are located only marginally equatorward of the auroral oval and are therefore scanning across the auroral boundaries. There could be fewer echoes because of a reduction in the electric field strength, or because of an increase in HF absorption or *E* region deflection of the radar rays [*Gauld et al.*, 2002]. The former appears unlikely since the flow speed, equivalently the electric field strength, was increasing while the number of echoes was diminishing. The latter mechanism, in contrast, would actually be helped by enhanced electric field because, in the absence of photoionization in the midnight sector, an increase in the electric field strength must lead to a depletion in the *F* region plasma density through increased molecular ion production as a result of the ion temperature increase that accompanies strong electric fields [*Schunk and Nagy*, 2000]. Lower *F* region densities make it less likely that the HF radar waves can refract to and be scattered from field-aligned irregularities, particularly if the *E* region through which the radar waves are moving is itself enhanced by precipitation (possibly, in this case, just through a poleward motion of the auroral boundary).

4.3. Impacts on the Dawn and Dusk Sectors

[65] In general, the dusk sector response was more like the noon response, and the dawn sector response was more like the midnight response. There was an increase in total number of echoes in the dusk sector immediately after both the SI and the SSC events, on average. In contrast with the response in the noon sector, however, the increase in the number of dusk echoes was more delayed, in the sense that it took 2–3 h to reach a peak echo occurrence in the dusk sector. There was likewise a hint of a broad increase in echo occurrence in the dawn sector in the SSC case, but the time delay was of the order of 5 to 6 h. In the context of the background fluctuations in echo occurrence, it is not possible to know if there was a response in echo occurrence in the dawn sector in the SI case. Overall, we can conclude that within the 5 or 6 h that followed the SC onset, there was a relatively sluggish increase in the total number of dusk echoes and an even more sluggish increase in the dawn sector, if at all. The increases in both cases were followed by a decrease in echo occurrence a few hours later.

[66] On a longer time scale, in the SSC case there was a clear and prolonged reduction in the total number of SuperDARN echoes in the dawn sector throughout the duration of the storm that followed the SSC. The number of echoes was also systematically higher in the dusk sector than in the dawn sector during the storm itself. This offset was found to persist for at least 72 h after the SSC. This contrast in echo occurrence between the dawn and dusk sectors may

be a common feature of the SuperDARN data, overall, or it may be related to the significantly positive IMF B_y that occurs after both SIs and SSCs. We note that the dawn-dusk asymmetry occurs here only after the SCs and not before. Asymmetries in the dawn and dusk particle precipitation may lie at the root of the contrast. Like in the midnight sector, as discussed above, in the presence of hard electron precipitation, the *E* and *D* region densities increase to the point when the radar rays are either absorbed in the *D* region or deflected by intense *E* region gradients so that the radar waves cannot reach the *F* region [*Gauld et al.*, 2002]. Both effects reduce the amount of SuperDARN *F* region echoes. In the dawn sector, upflowing region 2 field-aligned currents are carried by energetic electrons on the equatorward side of the auroral oval. This contrasts with the dusk sector, where the electrons precipitate at higher latitudes in the region 1 currents. The upward currents therefore lie closer in latitude to the SuperDARN radars in the dawn sector. This offset in latitude means that the likelihood of a reduction in the number of SuperDARN echoes may be related to the structure and size of the auroral oval, making for possible dawn-dusk differences in radio wave propagation and absorption, as well as in production of irregularity targets for the radio waves. It is more likely on average for the dawn echo occurrence to drop during strong auroral conditions, simply owing to the position and nature of the energetic precipitation relative to the radars. Since the feature is associated with the presence of active conditions, the decrease in the number of echoes is expected to be greater during magnetic storms and substorms when stronger precipitating conditions are expected to prevail.

5. Conclusion

[67] We studied 99 SI events and 106 SSC events between 2000 and 2007, inclusive. In a superposed epoch study of the SuperDARN response to solar wind impulses, we examined relevant solar wind, IMF, *SYM-H* and SuperDARN data from 24 h prior to until 72 h after the impulses. We specifically studied the ionospheric echo occurrence and LOS velocities recorded by SuperDARN and found the following.

[68] 1. The solar wind dynamic pressure and *SYM-H* data behaved in a very similar manner during both SI and SSC events. The response in the magnetosphere to the initial impulse seemed to be unrelated to whether the SC would be followed by a magnetic storm (and therefore become classified as SSC, rather than SI).

[69] 2. There is an immediate and large increase in the noon sector in the number of ionospheric echoes recorded by SuperDARN for both SI and SSC events. The increase in echo occurrence is maintained for longer than the increased *SYM-H* component, with the large echo occurrence being sustained for as long as the high solar wind dynamic pressure was sustained.

[70] 3. There was a measurable change in the velocity distribution of the ionospheric *F* region plasma in the noon sector, with a clear increase in the number and strength of antisunward flows. These increases suggest that the mechanism behind the generation of ionospheric structures in the noon sector is an increase in the electric field magnitude, which appears to be produced, at least at first, by the motion of the polar cap boundary triggered by the impulse. The persistence of strong antisunward flows on the dayside for about 12 h, regardless of the IMF B_z, remains a mystery, however.

[71] 4. Although the noon sector SuperDARN data were most clearly affected by the increase in solar wind dynamic pressure, there was also a measurable reduction in echo occurrence in the midnight sector for both SIs and SSCs.

[72] 5. The midnight sector response could have been due to an increase in the electric field strength leading to a partial depletion in *F* region densities in a region where little or no photoionization can replenish the plasma density, making 10 m irregularities more difficult for SuperDARN to detect. The reduction could also be due to changing propagation paths of the radar waves, as the high- and low-density regions moved through the radar's fields of view, as the polar cap area changed.

[73] 6. The echo occurrence was equal in the dawn and dusk sectors prior to the arrival of the solar wind dynamic pressure increase. For a few hours after the arrival of the shock, the number of echoes increased progressively in both sectors. From that point on, the echo occurrence decreased significantly and did so particularly in the dawn sector in the SSC case. This may well be related to the relative position of electron precipitation regions in the regions 1 and 2 field-aligned currents. It might also be a result of the dominant positive IMF B_y that followed both SIs and SSCs. More sophisticated analysis is required to explore this question further.

[74] It is clear from the SuperDARN and *SYM-H* data that the HF radar echoes in both types of SC events were affected by the dynamic pressure impulse of the solar wind, rather than by the enhancement of the ring current made evident in the *SYM-H* signature. We attribute the enhancement of the ring current 10 min after the arrival of the impulse to the compression suffered by the whole magnetosphere after the arrival of the shock. Several mechanisms are possible. For instance, the ring current enhancement may be due to a compression of the ring current cross section and an adiabatic increase in the intensity of the currents without additional current carriers. It is also possible that the ring current is enhanced due to a burst of reconnection in the plasma sheet brought about by the impulsive compression of the magnetotail.

[75] Finally, it should be clear from the present study that the use of the SC onset time for epoch reference time was ideal for monitoring the effect of pressure increases on the magnetosphere. In contrast, however, this reference time would be far from ideal for monitoring the ensuing magnetic storms in SSC cases. The reason is simply that the duration of the initial phases of storms is highly variable, and the offsets can result in a "smearing out" of the storms main and recovery phases. The end of the main phase of a storm, when the *SYM-H* index reaches its most negative value, is clearly determined by the time at which the IMF B_z component reaches its most negative value during the storm [*Echer et al.*, 2008; *Gillies et al.*, 2011]. Hence, for the few hours after the arrival of a solar wind dynamic pressure pulse, we can study the effect of the dynamic pressure increase of SSCs on the magnetosphere and ionosphere without the additional complications added by the occurrence of storms. Conversely, the SSC is a poor marker for the study of storms

because the time evolution and intensity of the IMF B_z component, rather than the initial jump in dynamic pressure at the SSC, determine the response of the system.

[76] The current study and a previous study [*Gillies et al.*, 2011] noted a difference in the magnitude of the geomagnetic activity response for SIs and SSCs. This was accompanied by a difference in the magnitude of the solar wind dynamic pressure pulse, with SSCs resulting in a higher magnitude jump in dynamic pressure than SIs. This suggests that statistically there are stronger shocks, or discontinuities, before storms. Indeed, *Gillies et al.* [2011] showed that the strongest storms resulted from ICMEs. This feature will be a topic of our future studies.

[77] **Acknowledgments.** We would like to thank the World Data Center in Kyoto, Japan, for providing the *Dst* and SYMbH indices. The SC list was obtained from the International Service on Rapid Magnetic Variations published by the Observatorio de l'Ebre, in Roquetes, Spain, in association with International Association of Geomagnetism and Aeronomy (IAGA). This research has been supported by The Marie Curie SPARTAN Fellowship for early stage researchers training, University of Saskatchewan, and indirectly by Natural Sciences and Engineering Research Council of Canada (NSERC). We acknowledge and thank NASA GSFC's Space Physics Data Facility's OMNIWeb (or CDAWeb or ftp) service for the use of OMNI data. We would also like to thank the SuperDARN PIs for providing the data from the Northern Hemisphere radars. The authors would also like to thank Luis F. Alberca for his helpful discussions.

[78] Robert Lysak thanks the reviewers for their assistance in evaluating this paper.

References

Akasofu, S.-I., and S. Chapman (1963a), The development of the main phase of magnetic storms, *J. Geophys. Res.*, *68*(1), 125–129, doi:10.1029/JZ068i001p00125.

Akasofu, S.-I., and S. Chapman (1963b), Magnetic storms: The simultaneous development of the main phase (*DR*) and of polar magnetic substorms (*DP*), *J. Geophys. Res.*, *68*(10), 3155–3158, doi:10.1029/JZ068i010p03155.

Alves, M. V., E. Echer, and W. D. Gonzalez (2006), Geoeffectiveness of corotating interaction regions as measured by *Dst* index, *J. Geophys. Res.*, *111*, A07S05, doi:10.1029/2005JA011379.

Baker, K. B., and S. Wing (1989), A new magnetic coordinate system for conjugate studies at high latitudes, *J. Geophys. Res.*, *94*(A7), 9139–9143, doi:10.1029/JA094iA07p09139.

Borovsky, J. E., and M. H. Denton (2006), Differences between CME-driven storms and CIR-driven storms, *J. Geophys. Res.*, *111*, A07S08, doi:10.1029/2005JA011447.

Boudouridis, A., L. R. Lyons, E. Zesta, and J. M. Ruohoniemi (2007), Dayside reconnection enhancement resulting from a solar wind dynamic pressure increase, *J. Geophys. Res.*, *112*, A06201, doi:10.1029/2006JA012141.

Burton, R. K., R. L. McPherron, and C. T. Russell (1975),An empirical relationship between interplanetary conditions and *Dst*, *J. Geophys. Res.*, *80*(31), 4204–4214, doi:10.1029/JA080i031p04204.

Chisham, G., et al. (2007), A decade of the Super Dual Auroral Radar Network (SuperDARN): Scientific achievements, new techniques and future directions, *Surv. Geophys.*, *28*, 33–109, doi:10.1007/s10712-007-9017-8.

Coco, I., E. Amata, M. F. Marcucci, M. De Laurentis, J.-P. Villain, C. Hanuise, and M. Candidi (2005), Effects on SuperDARN HF radar echoes of sudden impulses of solar wind dynamic pressure, *Ann. Geophys.*, *23*(5), 1771–1783.

Echer, E., W. D. Gonzalez, A. Dal Lago, L. E. A. Vieira, F. L. Guarnieri, A. L. C. Gonzalez, and N. J. Schuch (2005), Interplanetary shocks and sudden impulses during solar maximum (2000) and solar minimum (1995–1996), *Adv. Space Res.*,*36*(12), 2313–2317, doi:10.1016/j.asr.2005.04.030.

Echer, E., W. D. Gonzalez, B. T. Tsurutani, and A. L. C. Gonzalez (2008), Interplanetary conditions causing intense geomagnetic storms ($Dst \leq -100$ nT) during solar cycle 23 (1996–2006), *J. Geophys. Res.*, *113*, A05221, 10.1029/2007JA012744.

Gauld, J. K., T. K. Yeoman, J. A. Davies, S. E. Milan, and F. Honary (2002), SuperDARN radar HF propagation and absorption response to the substorm expansion phase, *Ann. Geophys.*, *20*, 1631–1645.

Gillies, D. M., K. A. McWilliams, J.-P. St. Maurice, and S. E. Milan (2011), Global-scale observations of ionospheric convection during geomagnetic storms, *J. Geophys. Res.*, *116*, A12238, doi:10.1029/2011JA017086.

Greenwald, R. A., W. A. Bristow, G. J. Sofko, C. Senior, J.-C. Cerisier, and A. Szabo (1995), Super Dual Auroral Radar Network radar imaging of dayside high-latitude convection under northward interplanetary magnetic field: Toward resolving the distorted two-cell versus multicell controversy, *J. Geophys. Res.*, *100*(A10), 19,661–19,674, doi:10.1029/95JA01215.

Gonzalez, W. D., J. A. Joselyn, Y. Kamide, H. W. Kroehl, G. Rostoker, B. T. Tsurutani, and V. M. Vasyliunas (1994), What is a geomagnetic storm?, *J. Geophys. Res.*, *99*(A4), 5771–5792, doi:10.1029/93JA02867.

Gonzalez, W. D., B. Tsurutani, and A. Clúa de Gonzalez (1999), Interplanetary origin of geomagnetic storms, *Space Sci. Rev.*, *88*(3), 529–562, doi:10.1023/A:1005160129098.

Heber, B., T. R. Sanderson, and M. Zhang (1999), Corotating interaction regions, *Adv. Space Res.*, *23*(3), 567–579, doi:10.1016/S0273-1177(99)80013-1.

Huttunen, K. E. J., and H. E. J. Koskinen (2004), Importance of post-shock streams and sheath region as drivers of intense magnetospheric storms and high-latitude activity, *Ann. Geophys.*, *22*, 1729–1738, doi:10.5194/angeo-22-1729-2004.

Iyemori, T. (1990), Storm-time magnetospheric currents inferred from mid-latitude geomagnetic field variations, *J. Geomagn. Geoelectr.*, *42*(11), 1249–1265.

Kane, T. A., and R. A. Makarevich (2010), HF radar observations of the *F* region ionospheric plasma response to storm sudden commencements, *J. Geophys. Res.*, *115*, A07320, doi:10.1029/2009JA014974.

Kelley, M. C. (1989), *The Earth's Ionosphere*, 371 pp., Academic, San Diego, Calif.

Koustov, A. V., D. W. Danskin, R. A. Makarevitch, and J. D. Gorin (2005), On the relationship between the velocity of *E*-region HF echoes and $\mathbf{E} \times \mathbf{B}$ plasma drift, *Ann. Geophys.*, *23*, 371–378, doi:10.5194/angeo-23-371-2005.

Lee, D.-Y., S. Ohtani, P. Brandt, and L. R. Lyons (2007), Energetic neutral atom response to solar wind dynamic pressure enhancements, *J. Geophys. Res.*, *112*, A09210, doi:10.1029/2007JA012399.

Loewe, C. A., and G. Prölss (1997), Classification and mean behaviour of magnetic storms, *J. Geophys. Res.*, *102*(A7), 14,209–14,213, doi:10.1029/96JA04020.

Mann, I. R., and A. N. Wright (1999), Diagnosing the excitation mechanisms of Pc5 magnetospheric flank waveguide modes and FLRs, *Geophys. Res. Lett.*, *26*(16), 2609–2612.

Milan, S. E., T. K. Yeoman, and M. Lester (1998), The dayside auroral zone as a hard target for coherent HF radars, *Geophys. Res. Lett.*, *25*(19), 3717–3720, doi:10.1029/98GL02781.

Milan, S. E., S. W. H. Cowley, M. Lester, D. M. Wright, J. A. Slavin, M. Fillingim, C. W. Carlson, and H. J. Singer (2004), Response of the magnetotail to changes in the open flux content of the magnetosphere, *J. Geophys. Res.*, *109*, A04220, doi:10.1029/2003JA010350.

Perreault, P., and S.-I. Akasofu (1978), A study of geomagnetic storms, *Geophys. J. R. Astron. Soc.*, *54*, 547–573, doi:10.1111/j.1365-246X.1978.tb05494.x.

Ruohoniemi, J. M., and K. B. Baker (1998), Large-scale imaging of the high-latitude convection with Super Dual Auroral Radar Network HF radar observations, *J. Geophys. Res.*, *103*(A9), 20,797–20,811, doi:10.1029/98JA01288.

Schunk, R. W., and A. F. Nagy (2000), *Ionospheres: Physics, Plasma Physics, and Chemistry*, Cambridge Univ. Press, Cambridge, U. K.

Shue, J.-H., J. K. Chao, H. C. Fu, C. T. Russell, P. Song, K. K. Khurana, and H. J. Singer (1997), A new functional form to study the solar wind control of the magnetopause size and shape, *J. Geophys. Res.*, *102*(A5), 9497–9511, doi:10.1029/97JA00196.

Siscoe, G. L., and T. S. Huang (1985), Polar cap inflation and deflation, *J. Geophys. Res.*, *90*(A1), 543–547, doi:10.1029/JA090iA01p00543.

Siscoe, G. L., V. Formisano, and A. J. Lazarus (1968), Relation between geomagnetic sudden impulses and solar wind pressure changes—An experimental investigation, *J. Geophys. Res.*, *73*(15), 4869–4874, doi:10.1029/JA073i015p04869.

Sitnov, M. I. , N. A. Tsyganenko, A. Y. Ukhorskiy, B. J. Anderson, H. Korth, A. T. Y. Lui, and P. Brandt (2010), Empirical modeling of a CIR-driven magnetic storm, *J. Geophys. Res.*, *115*, A07231, doi:10.1029/2009JA015169.

Wanliss, J. A., and K. M. Showalter (2006), High-resolution global storm index: *Dst* versus *SYM-H*, *J. Geophys. Res.*, *111*, A02202, doi:10.1029/2005JA011034.

Weimer, D. R. (2004), Correction to "Predicting interplanetary magnetic field (IMF) propagation delay times using the minimum variance technique," *J. Geophys. Res.*, *109*, A12104, doi:10.1029/2004JA010691.

Weimer, D. R., D. M. Ober, N. C. Maynard, M. R. Collier, D. J. McComas, N. F. Ness, C. W. Smith, and J. Watermann (2003), Predicting interplanetary magnetic field (IMF) propagation delay times using the minimum variance technique, *J. Geophys. Res.*, *108*(A1), 1026, doi:10.1029/2002JA009405.

Wild, J. A., and A. Grocott (2008), The influence of magnetospheric substorms on SuperDARN radar backscatter, *J. Geophys. Res.*, *113*, A04308, doi:10.1029/2007JA012910.

Zhang, J., et al. (2007), Solar and interplanetary sources of major geomagnetic storms ($Dst \leq -100$ nT) during 1996–2005, *J. Geophys. Res.*, *112*, A10102, doi:10.1029/2007JA012321.

D. M. Gillies, K. A. McWilliams, and J.-P. St.-Maurice, Institute of Space and Atmospheric Science, University of Saskatchewan, 116 Science Pl., Saskatoon, SK S7N 5E2, Canada. (megan.gillies@usask.ca)

S. Milan, Department of Physics and Astronomy, University of Leicester, University Road, Leicester LE1 7RH, UK.

Chapter 7

Conclusions

The goal of this thesis was to determine how changes in the ionospheric convection velocities and SuperDARN echo occurrence rates are affected by the arrival of geoeffective CMEs and CIRs. During these times of increased magnetic activity, solar wind and IMF conditions were analyzed to quantify interplanetary conditions. The CMEs and CIRs are considered to be geoeffective if their interaction with the magnetosphere results in a magnetic activity enhancement at the Earth's surface, due to a SC or geomagnetic storm. In the case of geomagnetic storms, the geoeffective CMEs and CIRs were identified using the 1-hour resolution Dst index. The geomagnetic activity profiles of the CMEs and CIRs were analyzed with the higher resolution Sym-H index. SC events were obtained from the list compiled by the Observatori de l'Ebre (*Observatori de l'Ebre*) using the method described in Section 3.2.3. A superposed epoch analysis of solar wind and IMF conditions from 24 hours prior to the initial magnetic activity enhancement to 72 hours later was performed. CME and CIR interactions with the magnetosphere led to changes in the ionospheric convection pattern, SuperDARN echo occurrence rates, and magnetospheric currents. Connection of the data to the upstream solar wind dynamic pressure or the IMF orientation that initiated the magnetic disturbance was clearly established. Two main studies were performed. The first study focused on the ionospheric response during the main and recovery phases of geomagnetic storms. The second study concentrated on the abrupt change in ionospheric and geomagnetic activity associated with increases in solar wind dynamic pressure.

7.1 Ionospheric response to the arrival of CMEs and CIRs resulting in geomagnetic storms

7.1.1 Results from the geomagnetic storms study

Chapter 5 detailed one of the first statistical studies involving ionospheric convection velocities and SuperDARN echo occurrence rates during geomagnetic storms. A total of 136 geomagnetic storms from the declining phase of solar cycle 23 were analyzed. This thesis used the higher resolution Sym-H index instead of the more traditional Dst index when analyzing the geomagnetic activity levels during geomagnetic storms.

As described in Chapter 3, previous studies used the depth of the negative excursion of the Dst or Sym-H at the end of the main phase to introduce geomagnetic storms classes. The relationship between the negative extremum of the Sym-H at the end of the main phase and the peak negative IMF B_z preceding the geomagnetic storm was investigated. This study showed that Sym-H responded in a predictable manner to the intensity of the southward IMF. This confirmed a previous study of the relationship between the Dst (rather than the Sym-H) and IMF B_z (*Echer et al.*, 2008). The current study included all magnitude storms with Sym-H minima from -30 nT to below -300 nT. By including geomagnetic storms of all magnitudes, a continuum of storm intensities became evident, questioning the need to define distinct classes (*Tsurutani and Gonzalez*, 1997). A very good correlation between the minimum Sym-H at the end of the main phase and the minimum IMF B_z that occurred roughly 1 hour earlier was found. A comparison between the IEF and Sym-H produced an excellent correlation as well.

Previous studies calculated a maximum strength for CIR-driven geomagnetic storms (*Richardson et al.*, 2006; *O'Brien and McPherron*, 2000). According to their studies, the Dst during the main phase of the storm would not descend below -181 nT. The geomagnetic storms in the current study were divided into the three classes suggested by *Tsurutani and Gonzalez* (1997) with the intent of identifying a class consisting solely of CME-driven storms. However, while the intense class of

storms consisted only of CME-driven events, CME-driven storms were prevalent in all three storm classes. The intense storms had a larger solar wind speed and solar wind dynamic pressure preceding the main phase. Also, regardless of the solar wind driver the strength of the storm depended on the depth of the IMF B_z minimum. CIR-driven storms were only found in the strong and weak-moderate storm classes where the lower limit at the end of the main phase was Sym-H =-180 nT. This agreed with the *O'Brien and McPherron* (2000) theoretical limit of -181 nT for CIR-driven geomagnetic storms. Curiously, the strongest CIR-driven storm in solar cycle 23 (for years 1996-2006) only reached $\sim$ -120 nT in magnitude. A related study by *Richardson et al.* (2006) found the strongest CIR-driven storm in the previous solar cycle (1972-1995) only reached a Dst = -161 nT. Based on the current work relating geomagnetic storm magnitude to the strength of the IMF B_z, the apparent reduction in the magnitude of CIR-driven storms over the two previous solar cycles reflects a reduction in the IMF B_z strength. This supports the notion of a weakening solar magnetic field structure over the last century proposed by *Penn and Livingston* (2010).

All three storm classes had a reduction in SuperDARN echo occurrence rates early in the recovery phase. In the weak-moderate and strong storms, the reduction in echo occurrence began with the main phase. All three storm classes exhibited an increase in the speed of the antisunward flows in the noon (09-15 MLT) and midnight (21-03 MLT) sectors in the presence of a southward IMF B_z. This was likely due to enhanced reconnection on the dayside magnetosphere that led to faster flows from the noon sector into the polar cap. The weak-moderate and strong storms had a reduction in the number of northern hemisphere echoes beginning in the main phase. In contrast, the intense storms had a marked reduction in the number of echoes early in the main phase in the 09-15 MLT sector. At the same time in the 21-03 MLT sector there was a sharp reduction in the number of echoes.

It was observed that the recovery phase for the three storm classes were similar in duration regardless of strength of the storm or of the solar wind driver. This confirmed the characteristic time scale over which the ring current decays (*Burton*

et al., 1975). This decay time has been established to be T = 7.7 hours (*Burton et al.*, 1975; *Söraas et al.*, 2002). In the present work the Sym-H index was used instead of the Dst and there were no restrictions on pressure nor was a northward IMF required during the recovery phase. Decay times of T = 9.4 hours for the intense storms, T = 6.8 hours for the strong storms, and T = 5.1 hours for the weak-moderate storms were calculated. The strong storms were most similar to the magnitudes used in the *Burton et al.* (1975) study. With the previously established notion that storm divisions were arbitrary due to the continuum in storm response, the category divisions were removed and the time decay of the recovery phase was recalculated using all 136 events. This yielded a decay time of T = 7.2 hours that was in good agreement with the *Burton et al.* (1975) value of T = 7.7 hours. Despite the dissimilarities between the two studies, the apparent agreement between the decay times was quite interesting and warrants further investigation.

7.1.2 Future work involving geomagnetic storms

The SuperDARN convection analysis presented in this thesis used for the first time a superposed epoch study of abrupt changes in geomagnetic activity and the resulting changes in ionospheric convection velocities and echo occurrence rates. The decomposition of the l-o-s velocity in terms of the sunward and antisunward components was a first step in a process that can be further refined. The next iteration of the analysis will be to decompose the line-of-sight velocity into component towards/-away from 6 MLT. This will enable a more detailed study of the convection pattern. With finer resolution on the l-o-s direction it may be possible to identify features such as the Harang discontinuity. The algorithm used in this thesis did not include magnetic latitude dependence but could easily include it in the future. Although echo occurrence as a function of magnetic latitude has been studied by *Hutchinson et al.* (2011b), a comparison between the two studies may yield interesting results.

This thesis revealed a systematic positive IMF B_y during the main phase of storms that also warrants further investigation. The present work focused on solar maximum and the declining phase of solar cycle 23. The solar wind and IMF data

should be expanded to include the entire solar cycle to see if this positive tendency is maintained. If maintained, it would warrant investigating whether this feature is specific to solar cycle 23 or if it is present in previous solar cycles as well. Further expanding this study to look at solar cycles 21 and 22 may yield information regarding IMF orientation during the main phase of geomagnetic storms.

7.2 Ionospheric response to sudden commencements resulting from discontinuities in solar wind dynamic pressure

7.2.1 Results from the sudden commencement (SC) study

Chapter 6 detailed the first study to establish a clear MLT dependence to SCs and the ionospheric convection velocity and HF radar echo response. The SC appears to be the result of an abrupt increase in solar wind dynamic pressure. Both SIs and SSCs are step function-like increases in the Sym-H index, and they both occurred in tandem with a solar wind dynamic pressure pulse.

The magnetospheric current response indicated by Sym-H was stronger for SCs which were later categorized as SSCs. These events produced a stronger positive perturbation of the Sym-H index and solar wind dynamic pressure, by approximately a factor of 2. Irrespective of whether or not the SC was followed by a geomagnetic storm, there was excellent correlation between the strength of SC events and the magnitude of the jump in the solar wind dynamic pressure.

The SuperDARN echo occurrence increased in tandem with the solar wind dynamic pressure pulse and SC. This response was particularly clear in the noon sector. While the period of increase geomagnetic activity following the SC seen in the Sym-H profile was maintained on the order of 10-20 minutes, the increase in echo occurrence occurred for a longer time period, on the order of hours, which was consistent with the duration of the enhanced solar wind dynamic pressure after the initial pulse. The

increase in echo occurrence was similar, regardless of whether the event was a SI or a SSC. It is not known how the ionospheric convection was maintained in relation to the solar wind dynamic pressure pulse. Further study is needed to determine how these two processes are coupled. There was an immediate decrease in SuperDARN echo occurrence in the midnight sector in response to the SC. This decrease was quite brief, on the order of 1/2 hour, after which time the echo occurrence recovered to pre-SC values. Case studies are needed to fully understand what was occurring in that time sector.

The SuperDARN echo occurrence rates and convection velocity orientation in the dawn and dusk sectors were similar prior to the arrival of the pressure pulse but differed afterward. This could potentially be a result of the IMF B_y asymmetry or a result of the R1/R2 current systems.

Geomagnetic storms are defined based upon their Dst profile. The initial phase of a storm is now known to be the result of a compression of the magnetopause, which causes an intensification of the magnetopause current. This compression is the result of an enhancement of the solar wind dynamic pressure, often caused by a CME or a CIR. The main phase of the geomagnetic storm results from a different process. When the IMF turns southward, a global depression of the geomagnetic field at the Earth's surface occurs which is defined as the main phase of a geomagnetic storm. When the IMF turn to a northward orientation, dayside reconnection slows. Particles then begin to leave the ring current region and the global geomagnetic field begins to recover. The present work has shown that SuperDARN echo occurrence and F-region ionospheric plasma convection for SCs (and subsequent the recovery phase) was different than that of the main phase. The present work also showed that ionospheric parameters such as SuperDARN echo occurrence and convection responded in a similar manner to a SC regardless of the SI or SSC distinction. The present work therefore suggests that the initial phase, initiated by the SC, should no longer be included in the definition of geomagnetic storm (i.e., 'standard' type geomagnetic storm). Instead, it should be considered that geomagnetic storms can be preceded by a SC, but a SC may occur as an isolated event.

7.2.2 Future work involving discontinuities in the solar wind resulting from solar wind dynamic pressure pulses

Solar wind dynamic pressure pulses that were geoeffective (i.e, resulting in a SC) were shown in this thesis to greatly affect SuperDARN convection velocities and echo occurrence rates. Examination of the solar wind parameters yielded pressure pulses that did not result in a SC. During a three year time span, *Coco et al.* (2005) identified 236 solar wind dynamic pressure pulses. During this same time span, the Observatori de l'Ebre recorded 106 SC events. This discrepancy prompts the question of what is required to produce a geoeffective solar wind dynamic pressure pulse. Further investigation into the IMF orientation and solar wind parameters is needed to determine why some pressure pulses result in a significant geomagnetic disturbance and some do not. This work focused on increases in solar wind dynamic pressure. A look at reductions in solar wind dynamic pressure (jump from high to low pressure) is suggested.

The approach used in this thesis has yielded some interesting results in the midnight sector. The brief reduction in echo occurrence and SuperDARN convection velocities is of particular interest. It might be useful to investigate case studies with good SuperDARN coverage. The dawn and dusk sectors were only briefly analyzed in this work. However, their response to the arrival of solar wind dynamic pressure pulses should be investigated further.

7.3 Summary

The research involved in this thesis helped to establish the response of the ionospheric convection and SuperDARN echo occurrence to CME- and CIR-driven solar wind. A first statistical analysis of the SuperDARN echo occurrence and ionospheric convection velocities corresponding to abrupt changes in geomagnetic activity levels was performed. For the first time it could be established that there was a clear MLT dependence to significant increases in SuperDARN echo occurrence and ionospheric

convection velocities coinciding with a SC. A computer algorithm was developed that successfully determined if gridded line-of-sight velocity vectors were antisunward or sunward. This useful tool could be used in future studies of F-region SuperDARN echo occurrence and ionospheric convection velocities. The algorithm is currently undergoing further refinement to provide higher spatial resolution. There was a continuum in the strength of geomagnetic storms, suggesting the traditional division of storms into classes was arbitrary and unnecessary. The ring current decay time calculated in this thesis, using a high time resolution geomagnetic index was found to be in good agreement with the classic *Burton et al.* (1975) value. Two SuperDARN data parameters were analyzed: the number of ionospheric echoes recorded by the radars in the Northern Hemisphere and the ionospheric plasma drift components measured along the radar beams. All three storm classes had a reduction in the number of ionospheric echoes early in the recovery phase. The overall number of echoes in the strong and weak–moderate storm decreased during the main phase. The intense storms behaved differently with a reduction of echoes occurring early in the main phase in the 21-03 MLT sector. In the noon sector (09-15 MLT) the number of antisunward flows increased with the southward turning of the IMF B_z. Abrupt changes in geomagnetic activity levels, classified as SCs, were also studied. It was found that the geomagnetic activity response of SIs and SSCs was identical in nature. On average, the SSCs had a higher magnitude jump in Sym-H and dynamic pressure than the SIs. Using the Sym-H index provided a high temporal resolution look at how the magnetospheric current, SuperDARN echo occurrence rates, and the geomagnetic activity levels developed. By using the Sym-H index, the SuperDARN echo occurrence and ionospheric convection velocities were established to initially respond to the SC. Once the ring current intensified, providing a reduction in the Sym-H, the SuperDARN echo occurrence remained enhanced. The SuperDARN echo occurrence rates remained enhanced for the duration of the solar wind dynamic pressure pulse, long after the initial geomagnetic perturbation had ceased.

Appendix A
Copyright Agreements

A.1 American Geophysical Union

Date: **Wed, 11 Jan 2012 13:55:20 +0000**
From: "Michael Connolly" <MConnolly@agu.org> **Block Address**
To: "dmh987@mail.usask.ca" <dmh987@mail.usask.ca>
Subject: **permission**

Reply | Reply All | Forward | Print | Delete

We are pleased to grant permission for the use of the material requested for inclusion in your thesis provided that the original publication be appropriately cited. Permission is restricted to the use stipulated. Further reproduction or distribution is not permitted.

The standard credit line for the citation is, "Author(s), title, publication, volume number, issue number, page number(s), date. Copyright [year] American Geophysical Union." The following must also be included, "Reproduced/modified by permission of American Geophysical Union."

If an article was placed in the public domain, in which case the words "Not subject to U.S. copyright" appear on the bottom of the first page or screen of the article, please substitute "published" for the word "copyright" in the credit line mentioned above.

For permission for any other use, please contact the AGU Publications Office at AGU, 2000 Florida Ave., N.W., Washington, DC 20009.

Michael Connolly
Program Manager, Journals
American Geophysical Union
+1.202.777.7365
MConnolly@agu.org
www.agu.org

AGU galvanizes a community of Earth and space scientists that collaboratively advances and communicates science and its power to ensure a sustainable future.

Support the American Geophysical Union!
Visit the AGU Blogosphere

Get the latest information on Facebook and tweet us at #AGU11!

Reply | Reply All | Forward | Print | Delete

References

Akasofu, S.-I., and S. Chapman (1963a), The development of the main phase of magnetic storms, *J. Geophys. Res.*, *68*(1), 125–129, doi:10.1029/JZ068i001p00125.

Akasofu, S.-I., and S. Chapman (1963b), Magnetic storms: The simultaneous development of the main phase (DR) and of polar magnetic substorms (DP), *J. Geophys. Res.*, *68*(10), 3155–3158, doi:10.1029/JZ068i010p03155.

Alves, M. V., E. Echer, and W. D. Gonzalez (2006), Geoeffectiveness of corotating interaction regions as measured by Dst index, *J. Geophys. Res.*, *111*(A07S05), doi:10.1029/2005JA011379.

Baker, J. B. H., R. A. Greenwald, J. M. Ruohoniemi, K. Oksavik, J. W. Gjerloev, L. J. Paxton, and M. R. Hairston (2007), Observations of ionospheric convection from the Wallops SuperDARN radar at middle latitudes, *J. Geophys. Res.*, *112*(A01303), doi:10.1029/2006JA011982.

Baker, K. B., and S. Wing (1989), A new magnetic coordinate system for conjugate studies at high latitudes, *J. Geophys. Res.*, *94*(A7), 9139–9143, doi:10.1029/JA094iA07p09139.

Baumjohann, W., and R. A. Treumann (2006), *Basic Space Plasma*, Fourth Ed., Imperial College Press, 57 Shelton Street, Covent Garden, London WC2H 9HE, 2006.

Borovsky, J. E., and M. H. Denton (2010), Solar wind turbulence and shear: A superposedepoch analysis of corotating interaction regions at 1 AU, *J. Geophys. Res.*, *115*(A10101), doi:10.1029/2009JA014966.

Borovsky, J. E., and M. H. Denton (2006), Differences between CME-driven storms and CIR-driven storms, *J. Geophys. Res.*, *111*(A07S08), doi:10.1029/2005JA011447.

Boudouridis, A., L. R. Lyons, E. Zesta, and J. M. Ruohoniemi (2007), Dayside reconnection enhancement resulting from a solar wind dynamic pressure increase, *J. Geophys. Res.*, *112*(A06201), doi:10.1029/2006JA012141.

Brueckner, G., and J.-D. F. Bartoe (1983), Observations of high-energyjets in the corona above the quiet sun, the heating of the corona, and the acceleration of the solar wind, *The Astrophysical Journal*, *272*, 329–248.

Burton, R. K., R. L. McPherron, and C. T. Russell (1975), An empirical relationship between interplanetary conditions and Dst, *J. Geophys. Res.*, *80*(31),4204–4214, doi:10.1029/JA080i031p04204.

Cairns, I. H., D. H. Fairfield, R. R. Anderson, V. E. H. Carlton, K. I. Paularena, and A. J. Lazarus (1995), Unusual locations of Earth's bow shock on September 24 - 25, 1987: Mach number effects, *J. Geophys. Res.*, *100*(A1), 47-62, doi: 10.1029/94JA01978.

Carlson, H. C., T. Pedersen, S. Basu, M. Keskinen, and J. Moen (2007), Case for a new process, not mechanism, for cusp irregularity production, *J. Geophys. Res.*, *112*(A11304), doi:10.1029/2007JA012384.

Chisham, G., et al., (2007), A decade of the Super Dual Auroral Radar Network (SuperDARN): scientific achievements, new techniques and future directions, *Surv. Geophys.*, *28*, 33–109, doi:10.1007/s10712–007–9017–8.

Chisham, G., I. J. Coleman, M. P. Freeman, M. Pinnock, and M. Lester (2001), Ionospheric signatures of split reconnection X-lines during conditions of IMF Bz < 0 and |By| $\sim$ |Bz|: Evidence for the antiparallel merging hypothesisjournal, *J. Geophys. Res.*, *107*(1323), doi:10.1029/2001JA009124.

Cliver, E. W., and A. G. Ling (2001),Coronal Mass Ejections Open Magnetic Flux and Cosmic-Ray Modulation, *The Astrophysical Journal*, *556*(1), 432, doi: 10.1086/321570.

Coco, I., E. Amata, M.F. Marcucci, M. De Laurentis, J.-P. Villain, C. Hanuise, and M. Candidi (2005), Effects on SuperDARN HF radar echoes of sudden impulses of solar wind dynamic pressure, *Ann. Geophys.*, *23*(5), 1771–1783, 2005.

Correia, E., and R. V. de Souza (2005), Identification of solar sources of major geomagnetic storms, *J. Atmos. and Solar-Terr. Phys.*, *67*, 1702–1705, doi: 10.1016/j.jastp.2005.03.007.

Cowley, S. W. H. (2000), Magnetosphere-Ionosphere Interactions: A Tutorial Review, *Magnetospheric Current Systems*, *Geophysical Monograph*, *118*, 91–106.

Danilov, A.D. and L.D. Morozova (1985), Ionospheric storms in the F2 region. Morphology and Physics (Review), *Geomag. Aeron.*, *25*, 593–605.

Denton, M. H., J. E. Borovsky, R. M. Skoug, M. F. Thomsen, B. Lavraud, M. G. Henderson, R. L. McPherron, J. C. Zhang, and M. W. Liemohn (2006), Geomagnetic storms driven by ICME- and CIR-dominated solar wind, *J. Geophys. Res.*, *111*(A07S07), doi:10.1029/2005JA011436.

Echer, E., W. Gonzalez, B. Tsurutani, and A. Gonzalez (2008), Interplanetary conditions causing intense geomagnetic storms (Dst $\leq$ -100 nT) during solar cycle number 23 (1996-2006), *J. Geophys. Res.*, *113*(A05221), doi:10.1029/2007JA012744.

Foster, J. C., et al. (2005), Multiradar observations of the polar tongue of ionization, *J. Geophys. Res.*, *110*(A09S31), doi:10.1029/2004JA010928.

Gauld, J. K., T. K. Yeoman, J. A. Davies, S. E. Milan, and F. Honary (2002), SuperDARN radar HF propagation and absorption response to the substorm expansion phase, *Ann. Geophys.*, *20*, 1631–1645.

Gillies, D., K.A. McWilliams, J.-P. St.-Maurice, and S. Milan (2011), Global-scale observations of ionospheric convection during geomagnetic storms, *J. Geophys. Res.*, *116*(A12238), doi:10.1029/2011JA017086.

Gillies, D. M., J.-P. St.-Maurice, K. A. McWilliams, and S. Milan (2012), Global-scale observations of ionospheric convection variation in response to sudden increases in the solar wind dynamic pressure, *J. Geophys. Res.*, *117*(A04209), doi: 10.1029/2011JA017255.

Green, D. L., C. L. Waters, B. J. Anderson, and H. Korth (2009), Seasonal and interplanetary magnetic field dependence of the field-aligned currents for both Northern and Southern Hemispheres, *Ann. Geophys.*, *27*, 1701-1715

Greenwald, R. A., W. A. Bristow, G. J. Sofko, C. Senior, J.-C. Cerisier, and A. Szabo (1995), Super Dual Auroral Radar Network radar imaging of dayside high-latitude convection under northward interplanetary magnetic field: Toward resolving the distorted two-cell versus multicell controversy, *J. Geophys. Res.*, *100*(A10), 19661–19674, doi:10.1029/95JA01215.

Grocott, A., J. A. Wild, S. E. Milan, and T. K. Yeoman (2009), Superposed epoch analysis of the ionospheric convection evolution during substorms: onset latitude dependence, *Ann. Geophys.*, *27*, 591–600.

Hargreaves, J. (1992), *The solar-terrestrial environment*, Cambridge Atmospheric and Space Science Series, Press Syndicate of the University of Cambridge, 40 West 20th Street, New York, New York, 10011-4211, USA, 1992.

Hargreaves, J.K. (1969), Auroral absorption of HF radio waves in the ionosphere: A review of results from the first decade of riometry, *Proc. IEEE*, *57*, 1348–1372.

Heber, B., T.R Sanderson, and M. Zhang (1999), Corotating interaction regions, *Advances in Space Research*, *23*(3),567–579, doi:10.1016/S0273–1177(99)80013–1.

Hughes, W.J (1997), *edited by: Margaret G. Kivelson and Christopher T. Russell*, Introduction to Space Physics, *Cambridge University Press*, *Third Edition*, 227–287.

Hutchinson, J. A., D. M. Wright, and S. E. Milan (2011), Geomagnetic Storms over the Last Solar Cycle: A Superposed Epoch Analysis, *J. Geophys. Res.*, *116*(A09211), doi:10.1029/2011JA016463.

Hutchinson, J. A., D. M. Wright,S. E. Milan, A. Grocott and P. D. Boakes (2011), A new way to study geomagnetic storms, *Astronomy & Geophysics*, *52*, 4.204.23. doi: 10.1111/j.1468–4004.2011.52420.x.

Iijima, T., and T. Potemra (1978), Large-scale characteristics of field-aligned currents associated with substorms, *J. Geophys. Res.*, *83*(A2), doi: 10.1029/JA083iA02p00599.

Illing, R. M. E., and A. J. Hundhausen (1983), Possible observation of a disconnected magnetic structure in a coronal transient, *Geophysical Research Letters*, *88*(A12), 10,210–10,214.

Johansson, T., G. Marklund, T. Karlsson, S. Lilo, P.-A. Lindqvist, H. Nilsson, and S. Bucherte (2007), Scale sizes of intense auroral electric elds observed by Cluster , *Ann. Geophys.*, *23*(5), 2413–2425, 2007.

Kane, T. A., and R. A. Makarevich (2010), HF radar observations of the F-region ionospheric plasma response to storm sudden commencements, *J. Geophys. Res.*, *115*(A07320), doi:10.1029/2009JA014974.

Kane, R.P. (2001), Did Predictions of the Maximum Sunspot Number for Solar Cycle 23 Come True?, *Solar Physics*, *202*(2), 395–406, doi:10.1023/A:1012211803591.

Kelley, M.C. (1989), *The Earth's Ionosphere*, Page 371, Academic Press Inc., San Diego, California 92101, 1989.

Keskinen, M., and S. L. Ossakow (1982), Nonlinear evolution of plasma enhancements in the auroral ionosphere 1. long wavelength irregularities, *J. Geophys. Res.*, *87*(A1), 144-150, doi:10.1029/JA087iA01p00144.

Koustov, A. V., D. W. Danskin, R. A. Makarevitch, and J. D. Gorin (2005), On the relationship between the velocity of E-region HF echoes and ExB plasma drift, *Annales Geophysicae*, *23*, 371–378, doi:10.5194/angeo–23–371–2005.

Lee, D.-Y., S. Ohtani, P. Brandt, and L.R. Lyons (2007), Energetic neutral atom response to solar wind dynamic pressure enhancements, *J. Geophys. Res.*, *112*(A09210), doi:10.1029/2007JA012399.

Loewe, C. A., and G. Prölss (1997), Classification and mean behavior of magnetic storms, *J. Geophys. Res.*, *102*(A7), 14209–14213, doi:10.1029/96JA04020.

Mann, I.R., and A.N. Wright (1999), Diagnosing the excitation mechanisms of Pc5 magnetospheric flank waveguide modes and FLRs, *Geophys. Res. Lett.*, *26*(16), 2609–2612.

McPherron, R.L. (1997), *edited by: Margaret G. Kivelson and Christopher T. Russell*, Introduction to Space Physics, *Cambridge University Press*, *Third Edition*, 400–458.

Menvielle, M., T. Iyemori, A. Marchaudon, and M. Nosé (2011), Geomagnetic indices in Geomagnetic Observations and Models, *IAGA Special Sopron Book Series*, *5*, 183–228, doi:10.1007/978–90–481–9858–0_8.

Milan, S. E., J. Hutchinson, P. D. Boakes, and B. Hubert (2009), Influences on the radius of the auroral oval, *Ann. Geophys.*, *27*, 2913-2924

Milan, S. E., S. W. H. Cowley, M. Lester, D. M. Wright, J. A. Slavin, M. Fillingim, C. W. Carlson, and H. J. Singer (2004), Response of the magnetotail to changes in the open flux content of the magnetosphere, *J. Geophys. Res.*, *109*(A04220), doi:10.1029/2003JA010350.

Milan, S.E., T.K. Yeoman, and M. Lester (1998), The dayside auroral zone as a hard target for coherent HF radars, *Geophys. Res. Lett.*, *25*(19), 3717–3720, doi: 10.1029/98GL02781.

Newbury, J., C. T. Russell, J. L. Phillips, and S. P. Gary (1998), Electron temperature in the ambient solar wind: Typical properties and a lower bound at 1 AU, *J. Geophys. Res.*, *103*(A5), 9553–9566, doi:10.1029/98JA00067.

O'Brien, T. P., and R. L. McPherron (2000), An empirical phase space analysis of ring current dynamics: Solar wind control of injection and decay, *J. Geophys. Res.*, *105*(A4), 7707–7719, doi:10.1029/1998JA000437.

Observatori de l'Ebre, Spain, SC tables, *http://www.obsebre.es/php/ geomagnetisme/variaciorap.php*.

Ohtani, S.-I. (2004), Flow bursts in the plasma sheet and auroral substorm onset: observational constraints on connection between midtail and near-earth substrom processes, *Space Science Reviews*, *113*, 77–96, doi: 10.1023/B:SPAC.0000042940.59358.2f.

OMNIweb: NASA/GSFC's Space Physics Data Facility's OMNIWeb (or CDAWeb or ftp) service, OMNI, *http://nssdc.gsfc.nasa.gov/omniweb*.

Penn, M., and W. Livingston (2010), Long-term Evolution of Sunspot Magnetic Fields, *arXiv eprints*, *arXiv:1009.0784v1*.

Perreault, P., and S.-I. Akasofu (1978), A study of geomagnetic storms, *Geophys. J. R. Astr. Soc.*, *54*, 547–573, doi:10.1111/j.1365-246X.1978.tb05494.x.

Ponomarenko, P.V., J.-P. St-Maurice, C.L. Waters, R.G. Gillies, and A.V. Koustov (2009), Refractive index effects on the scatter volume location and Doppler velocity estimates of ionospheric HF backscatter echoes, *Ann. Geophys.*, *27*, 4207–4219.

Priest, E.R. (1997), *edited by: Margaret G. Kivelson and Christopher T. Russell*, Introduction to Space Physics, *Cambridge University Press*, *Third Edition*, 58–90.

Quest, K. B. (1998), Theory and simulation of collisionless parallel shocks, *J. Geophys. Res.*, *93*(A9), 9649–9680, doi:10.1029/JA093iA09p09649.

Richardson, I. and H. Cane (2010), Near-Earth Interplanetary Coronal Mass Ejections During Solar Cycle 23 (19962009): Catalog and Summary of Properties, *Solar Physics*, *264*(1), 189–237.

Richardson, I. G., et al. (2006), Major geomagnetic storms (Dst $\leq$ -100 nT) generated by corotating interaction regions, *J. Geophys. Res.*, *111*(A07S09), doi: 10.1029/2005JA011476.

Richardson, I. G., (2004). Energetic particles and corotating interaction regions in the solar wind, *Space. Sci.*, *111*, 267-376.

Richardson, I. G., E. W. Cliver, and H. V. Cane (2001), Sources of geomagnetic storms for solar minimum and maximum conditions during 1972-2000, *Geophys. Res. Lett.*, *28*(13), 2569–2572, doi:10.1029/2001GL013052.

Richmond, A. D., and J. P. Thayer (2000), Magnetosphere-Ionosphere Interactions: A Tutorial Review, *Magnetospheric Current Systems*, *Geophysical Monograph*, *118*, 131–146.

Ruohoniemi, J. M., and K. B. Baker (1998), Large-scale imaging of the high-latitude convection with Super Dual Auroral Radar Network HF radar observations, *J. Geophys. Res.*, *103*(A9), 20797–20811, doi:10.1029/98JA01288.

Sandanger, M., F. Sraas, K. Aarsnes, K. Oksavik, and D. S. Evans (2007), Loss of relativistic electrons: Evidence for pitch angle scattering by electromagnetic ion cyclotron waves excited by unstable ring current protons, *J. Geophys. Res.*, *112*(A12213), doi:10.1029/2006JA012138.

Schunk, R.W., and A.F. Nagy (2000), *Ionospheres: Physics, Plasma Physics, and Chemistry*, Cambridge University, 2000.

Schunk, R.W. and J.J. Sojka (1996), Ionosphere-thermosphere space weather issues, *J. Atmos. Terr. Phys.*, *58*, 1527–1574.

Shue, J.-H. J.K. Chao, H.C. Fu, C.T. Russell, P. Song, K.K. Khurana, and H.J. Singer (1997), A new functional form to study the solar wind control of the magnetopause size and shape, *J. Geophys. Res.*, *102*(A5), 9497–9511, doi: 10.1029/97JA00196.

Siscoe, G.L., and T.S. Huang (1985), Polar cap inflation and deflation, *J. Geophys. Res.*, *90*(A1), 543–547, doi:10.1029/JA090iA01p00543.

Sitnov, M. I. , N.A. Tsyganenko, A.Y. Ukhorskiy, B.J. Anderson, H. Korth, A.T.Y. Lui, and P. Brandt (2010), Empirical modeling of a CIR-driven magnetic storm, *J. Geophys. Res.*, *115*(A07231), doi:10.1029/2009JA015169.

SOHO, Courtesy of SOHO/EIT and SOHO/LASCO consortium. SOHO is a project of international cooperation between ESA and NASA.

Söraas, F., K. Aarsnes, K. Oksavik, and D. S. Evans (2002), Ring current intensity estimated from low-altitude proton observations, *J. Geophys. Res.*, *107*(A7), *1149*, doi:10.1029/2001JA000123.

Söraas, F., K. Oksavik, K. Aarsnes, D. S. Evans, and M. S. Greer (2003), Storm time equatorial belt - an 'image' of RC behavior, *Geophys. Res. Lett.*, *30(2)*, *1052*, doi:10.1029/2002GL015636.

Stauning, P. (1996), Investigations of ionospheric radio wave absorption processes using imaging riometer techniques, *J. Atmos. Terr. Phys.*, *58*, 753–764.

St.-Maurice, J.-P., and A. M. Hamza (2009), Small scale irregularities at high latitudes. *In "Characterising the Ionosphere", ed. G. Wyman; Technical Report RTO-TR-IST-051*, *1*(p70), *http://www.rto.nato.int/abstracts.aspx*.

St.-Maurice, J.-P., and A. M. Hamza (2001), A new nonlinear approach to the theory of E region irregularities,*J. Geophys. Res*, *106*, 1751–1759.

Sudan, R. N. (1983), Unified Theory of Type I and Type II Irregularities in the Equatorial Electrojet, *J. Geophys. Res.*, *88*(A6).

Temmer, M., A. M. Veronig, E. P. Kontar, S. Krucker and B. Vršnak (2010), Combined STEREO/RHESSI Study of Coronal Mass Ejection Acceleration and Particle Acceleration in Solar Flares, *The Astrophysical Journal*, *712*, 1410, doi: 10.1086/0004-637X/712/2/1410.

Tokman, M., and P. Bellan (2002), Three-dimensional model of the structure and evolution of coronal mass ejections, *The Astrophysical Journal*, *567*, 2002.

Tsurutani, B. T., and W. D. Gonzalez (1997), The interplanetary causes of magnetic storms: A review, *in Magnetic Storms, Geophys. Monogr. Ser.*, *98*, edited by B. T. Tsurutani, W. D. Gonzales, Y. Kamide, and J. K. Arballo, pg 77, AGU, Washington, D.C., 1997.

Usanova, M. E., et al. (2010), Conjugate ground and multisatellite observations of compression-related EMIC Pc1 waves and associated proton precipitation, *J. Geophys. Res.*, *115*(A07208), doi:10.1029/2009JA014935.

Van Allen, J.A., W.C. Lin, and H. Leinbach (1964), On the Relationship between Absolute Solar Cosmic Ray Intensity and Riometer Absorption, *J. Geophys. Res.*, *69*(21), 4481–4491, doi:10.1029/JZ069i021p04481.

Walker, R. J., and C. T. Russell (1997), *edited by: Margaret G. Kivelson and Christopher T. Russell*, Introduction to Space Physics, *Cambridge University Press*, *Third Edition*, 164–182.

Walter D. Gonzalez, e. al. (1999), Interplanetary origin of geomagnetic storms, *Space Science Reviews*, *88*, 529–562, doi:10.1023/A:1005160129098.

Wang, C., J. B. Liu, H. Li, Z. H. Huang, J. D. Richardson, and J. R. Kan (2009), Geospace magnetic field responses to interplanetary shocks, *J. Geophys. Res.*, *114*(A05211), doi:10.1029/2008JA013794.

Wanliss, J. A., and K. M. Showalter (2006), High-resolution global storm index: Dst versus Sym-H, *J. Geophys. Res.*, *111*(A02202), doi:10.1029/2005JA011034.

Webb, D. F., and R. A. Howard (1994), The Solar Cycle Variation of Coronal Mass Ejections and the Solar Wind Mass Flux, *J. Geophys. Res.*, *99*(A3), 42014220, doi:10.1029/93JA02742.

Weimer, D. R. (2004), Correction to predicting interplanetary magnetic field (IMF) propagation delay times using the minimum variance technique, *J. Geophys. Res.*, *109*(A12104), doi:10.1029/2004JA010691.

Weimer, D. R., D. M. Ober, N. C. Maynard, M. R. Collier, D. J. McComas, N. F. Ness, C. W. Smith, and J. Watermann (2003), Predicting interplanetary magnetic field (IMF) propagation delay times using the minimum variance technique, *J. Geophys. Res.*, *108*(A11026), doi:10.1029/2002JA009405.

Wilcox, J. M. and N. F. Ness (1967), Sector Structure of the Quiet Interplanetary Magnetic Field, *Science*, *148*(3677),1592–1594, doi:10.1126/science.148.3677.1592.

Wild, J. A., and A. Grocott (2008), The influence of magnetospheric substorms on SuperDARN radar backscatter, *J. Geophys. Res.*, *113*(A04308), doi: 10.1029/2007JA012910.

Wolf, R.A (1997), *edited by: Margaret G. Kivelson and Christopher T. Russell*, Introduction to Space Physics, *Cambridge University Press*, *Third Edition*, 288–329.

World Data Center (WDC) for Geomagnetism, Kyoto, Japan, *http://wdc.kugi.kyoto u.ac.jp/*

Zhang, J., et al. (2007), Solar and interplanetary sources of major geomagnetic storms (Dst $\leq$ -100 nT) during 1996-2005, *J. Geophys. Res.*, *112*(A10102), doi: 10.1029/2007JA012321.

Zirker, J. B. (1997), Coronal holes and high-speed wind streams, *Reviews of Geophysics and Space Physics*, *15*(3), 257–269, 1977.